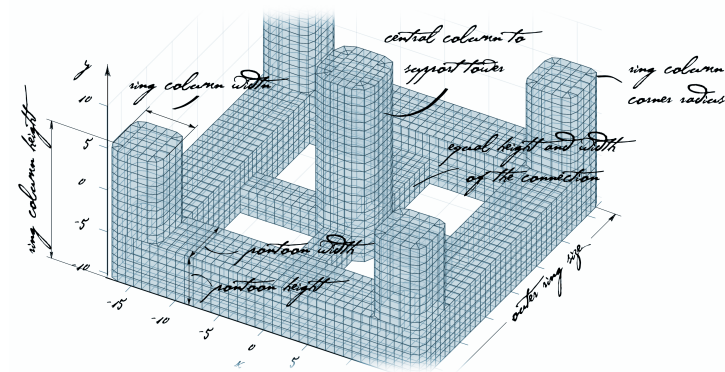


UNIVERSIDADE DE LISBOA
INSTITUTO SUPERIOR TÉCNICO



**A System for the Hydrodynamic Design of Floating
Wind Turbine Platforms**

Cihan Emre Uzunoglu

Supervisor: Doctor Carlos António Pancada Guedes Soares

**Thesis approved in public session to obtain the PhD Degree in
Naval Architecture and Ocean Engineering
Jury final classification: Pass with Distinction**

UNIVERSIDADE DE LISBOA
INSTITUTO SUPERIOR TÉCNICO

**A System for the Hydrodynamic Design of Floating
Wind Turbine Platforms**

Cihan Emre Uzunoglu

Supervisor: Doctor Carlos António Pancada Guedes Soares

**Thesis approved in public session to obtain the PhD Degree in
Naval Architecture and Ocean Engineering
Jury final classification: Pass with Distinction**

Jury

Chairperson: Doctor Luís Manuel Calado de Oliveira Martins, Instituto Superior Técnico, Universidade de Lisboa

Members of the committee:

Doctor Carlos António Pancada Guedes Soares, Instituto Superior Técnico, Universidade de Lisboa

Doctor Antonio Souto-Iglesias, Escuela Técnica Superior de Ingenieros Navales, Universidad Politécnica de Madrid, Spain

Doctor Constantine Michailides, Faculty of Engineering and Technology, Cyprus University of Technology, Cyprus

Doctor Manuel Filipe Simões Franco Ventura, Instituto Superior Técnico, Universidade de Lisboa

Título Sistema para o projeto hidrodinâmico de plataformas de turbinas eólicas flutuantes

Nome Cihan Emre Uzunoglu

Doutoramento em Engenharia Naval e Oceânica

Orientador Carlos António Pancada Guedes Soares

Resumo

Este trabalho propõe criar uma ponte entre as fases iniciais e avançadas do projeto hidrodinâmico de um flutuador, fornecendo um sistema rápido, flexível e interligado. Centra-se no cenário de “folha em branco”, onde todas as variáveis são desconhecidas. Este caso difere dos estágios posteriores que podem estudar variações de uma propriedade particular depois de assumir um conjunto de constantes. Existem dois problemas aparentes nas fases iniciais: Alternativas simplificadas, como folhas de cálculo, são imprecisas em relação aos dados baseados em geometria, especialmente para formas mais complexas (por exemplo, matriz de massa, coeficientes hidrodinâmicos, propriedades hidrostáticas). O uso de múltiplos softwares comerciais é necessário para uma solução confiável, mas no entanto, a falta de conexão torna-se num segundo problema.

Esses assuntos são abordados aqui iniciando o projeto diretamente no espaço tridimensional e utilizando um modelo paramétrico de multiuso. Desenvolve-se uma configuração integrada com os componentes necessários e a sua sistematização. Em seguida, o problema hidrodinâmico é resolvido sem a necessidade de interação humana além de um único modelo da ideia inicial. A abordagem sugere o uso de soluções no domínio da frequência do tempo com uma maior eficiência. Para este propósito, as informações extraídas no domínio de frequência são estendidas e os computacionalmente exigentes códigos do domínio do tempo são reservados para verificação adicional da resposta dinâmica. O sistema é demonstrado com uma plataforma de pernas de tensão para energia eólica, considerando a dinâmica acoplada entre o flutuador e a turbina. O projeto é realizado com o objetivo de evitar ocorrências de perda de tensão da amarração num conjunto de condições ambientais; esta situação realça um caso difícil de cobrir com cálculos manuais. O projeto no domínio de frequência, o dimensionamento da plataforma e as fases de verificação no domínio de tempo são discutidos.

No geral, a realocação do recurso humano do cálculo para a parte de inovação do processo de projeto implica uma maior precisão, economia de tempo e um número reduzido de erros. O sistema descrito também está aberto ao desenvolvimento futuro, adicionando módulos à estrutura e estendendo a sua funcionalidade.

Palavras-chave: estruturas offshore; plataforma de pernas de tensão; hidrodinâmica; energia renovável; energia eólica

Abstract

This work proposes to bridge the gap between the initial and the advanced phases of a floater's hydrodynamic design by providing a fast, flexible, and interconnected system. It focuses on a "blank-sheet" scenario where all variables are unknown. This case differs from the later stages that can study variations of a particular property after assuming a set of constants. There are two apparent problems at early phases: Simplified alternatives such as spreadsheets and hand calculations are imprecise regarding the geometry-based data especially for complex shapes (e.g., mass matrices, hydrodynamic coefficients, hydrostatic properties). The use of multiple commercial software is required for a reliable solution, but their lack of connectedness poses the second problem.

These issues are addressed here by starting the design directly in the three-dimensional space and using a multi-purpose parametric model. An integrated configuration is developed with the necessary components and their systematisation. Following that, the hydrodynamic problem is solved without the need for human interaction beyond a single model of the initial idea. The approach advocates using both frequency and time domain solutions with higher efficiency. For this purpose, the information extracted in the frequency domain is extended and computationally demanding time domain codes are reserved to further verification of motion dynamics. The system is demonstrated on a tension leg platform for wind energy, considering the coupled dynamics between the floater and the turbine. The design is carried out with the aim of avoiding slack mooring occurrences in a set of environmental conditions; it underlines a case difficult to cover with hand calculations. The frequency domain stage, platform sizing, and the time domain verification phases are discussed.

Overall, relocating the human resource from the calculation to the innovation part of the design process implies increased precision, significant time savings, and reduced number of errors. The described system is also open to future development by adding modules to the framework and extending its functionality.

Keywords: offshore structures; tension-leg platform; hydrodynamics; renewable energy; wind energy

Acknowledgments

I first met Prof. Carlos Guedes Soares in Istanbul, 2008. That day marked a personal milestone as I moved to Portugal for a master's degree. In the following years, his insights, experience, and the opportunities he provided turned my ideas into the reality you are reading. Simply said, a few of my life's major events including this dissertation would not exist without him.

A doctoral degree is a long journey. On that road, Prof. Yordan Garbatov's guidance has put matters into perspective when I had doubts. I am grateful to him for sparing the time to share his thoughts; our conversations brought me wisdom.

If a dissertation could have a second author, that would have been Prof. Dunja Legović. She had to, willingly and sometimes unwillingly, listen to my talks on ocean platforms for long hours as I thought out loud. It was she who turned my napkin drawings into the beautiful illustrations that you will see in the following pages.

I exchanged opinions with almost all my colleagues at CENTEC while developing this work. Baran Yeter, Shan Wang, and Mesut Tekgöz have especially been essential in helping me see things from different angles. Outside the university, Celal Çelikkaya's outlook was much appreciated on topics that required an understanding beyond theory.

When needed, I found constant support from my family. My father Hayri Uzunoğlu, mother Füsün Uzunoğlu, and aunt Ferda Kalegasioğlu were always there. I also have to acknowledge Aysun Uygun's role: Apparently, some help offered at the right time can have a far reach. At last, after so many years of friendship, I do not need a particular reason to include Emre Emanetoğlu here.

This thesis is dedicated to my grandparents Hatice and Sadık Kalegasioğlu who were pivotal in my early years. After all, I can trace the ideas in here back to my grandfather's –a maths teacher– 1960s hand-drawn geometrical shapes that I admired as a child.

Contents

Resumo	iii
Abstract	v
Acknowledgments	vii
List of Tables	xv
List of Figures	xix
Glossary	xxiii
1 Introduction	1
1.1 Offshore wind turbine platform concepts	3
1.1.1 Waterplane area stabilized platforms	3
1.1.2 Mooring stabilized platforms	5
1.1.3 Deep ballast stabilized platforms	7
1.1.4 Hybrid platforms and multi-turbine concepts	8
1.2 Evaluation of platform concepts	9
1.2.1 DeepCwind Consortium	9
1.2.2 Collaborative comparison studies in Japan	11
1.3 Numerical analysis of platform motions	12
1.4 Floating wind turbine projects	13
1.5 Design of offshore platforms	14
1.5.1 Design standards	14

1.5.2	Design and optimisation studies	15
1.6	Motivation and objectives	16
1.7	Layout	17
2	Theoretical Background	19
2.1	Ocean waves	19
2.2	Representation of sea states in the frequency and time domain	20
2.3	Hydrostatics and upright stability	22
2.4	Potential flow theory	24
2.5	Calculation of wave loads on the structure	26
2.5.1	The Morison Equation	26
2.5.2	Hydrodynamically compact structures	27
2.6	Wind loads	28
2.6.1	Wind resource	28
2.6.2	Wind loads on the rotor and tower	29
2.7	Mooring line dynamics	30
2.8	Coupled motion dynamics of wind turbine platforms	31
3	Comparison of time domain simulations and experimental data for a semi-submersible	33
3.1	Introduction	33
3.2	An overview of FAST	34
3.3	Turbine description and parameter calibration	34
3.3.1	The wind turbine and the blades	34
3.3.2	Airfoil setup and the wind turbine performance	35
3.3.3	Tower properties and vibration modes	37
3.3.4	Platform and the mooring system	39
3.4	Validation of the model with the experimental data	40
3.4.1	Responses under steady wind forces	40
3.4.2	Responses under regular waves	42
3.5	Concluding remarks	43

4	Influence of geometric modelling simplifications on platform motion predictions	45
4.1	Introduction	45
4.2	Methodology	46
4.3	Comparison of hydrodynamic coefficients and wave exciting forces	47
4.3.1	Added masses	47
4.3.2	Damping coefficients	48
4.3.3	Exciting Forces	49
4.4	Time domain evaluation	49
4.4.1	System identification	50
4.4.2	Platform responses in waves	51
4.4.3	Coupled system dynamics	52
4.5	Concluding remarks	53
5	Model uncertainty of wave induced platform motions and mooring loads	55
5.1	Introduction	55
5.2	Assessment of model uncertainty	56
5.2.1	Description of the initial data set and preliminary considerations	57
5.2.2	Obtaining the model uncertainty	57
5.2.3	Filtering the data set	58
5.3	Platform model, load case, and the final participants	59
5.4	Hydrodynamic models	60
5.4.1	Combined low-frequency and wave frequency ranges	63
5.4.2	Wave frequency range	66
5.4.3	User errors and differences in modelling practices	68
5.5	Mooring models	68
5.6	Concluding remarks	69

6	Automation of the time domain code for model building and sequential simulations	71
6.1	Introduction	71
6.2	System setup for automation	72
6.2.1	Advantages and disadvantages of text-based input and output	73
6.2.2	Systematising FAST's input-output procedure	73
6.3	Pre-processing	74
6.3.1	Load case matrix	75
6.3.2	Altering the primary data format	76
6.3.3	Altering the tabular data format	76
6.4	Post-processing	77
6.4.1	Output processing	78
6.4.2	Plotting	79
6.4.3	Response amplitude operators	80
6.4.4	Assessment of static equilibrium	80
6.4.5	Input backup	81
6.5	Application: linear regression based volume calibration process	82
6.6	Concluding remarks	82
7	Multi-purpose parametric modelling for hydrodynamic calculations	85
7.1	Introduction	85
7.2	On modelling practices for hydrodynamic calculations	86
7.3	Representation of a 3D geometry with quadrilaterals	87
7.3.1	Radius based approach	88
7.3.2	Face based approach	91
7.3.3	Rotation and translation in 3D space	95
7.3.4	Multi-body models, symmetry, and the consolidated input format	96
7.4	Calculation of the mass properties of the mesh	97
7.4.1	Centre of gravity and weight	97
7.4.2	Inertia	99
7.4.3	Volume	100
7.5	Examples of application	101

7.5.1	Examples of application for the radius based models	101
7.5.2	Examples of application for the face based models	104
7.6	Validation of mass property calculations and the panel method model	107
7.6.1	Volume	109
7.6.2	Centre of gravity, weight and inertia	110
7.6.3	Panel method calculations	110
7.7	Performance assessment	111
7.8	Concluding remarks	112
8	Application of the design system on a tension leg platform	115
8.1	Introduction	115
8.2	Design practices and considerations	116
8.3	System development	117
8.3.1	Mass properties	117
8.3.2	The hydrostatic restoring matrix and the hydrodynamic panel model	118
8.3.3	Mooring setup	121
8.3.4	Platform motion dynamics	122
8.3.5	Building a parametric model and systemising the design process	127
8.4	Motions under linear excitation in frequency and time domain	132
8.4.1	Static equilibrium and the platform eigenfrequencies	132
8.4.2	Motion dynamics	134
8.5	Assessing responses in stochastic environments	136
8.6	Design criteria evaluation and platform sizing	138
8.7	Time requirements for design space evaluation	140
8.8	Concluding remarks	142

9 Pitch actuator fault induced yaw motion in storms	145
9.1 Introduction	145
9.2 The system and the environmental conditions	146
9.2.1 Description of the turbine, tower, and the platform	146
9.2.2 Environmental conditions	148
9.3 Motion responses in fault-free storm conditions	149
9.4 Blade pitch actuator fault induced yaw motion	153
9.4.1 Responses of the platform in fault condition	153
9.4.2 Yaw motion in lower wind speeds and partial brake failure	157
9.5 Factors that contribute to the yaw motion	161
9.6 Concluding remarks	164
10 Conclusions	167
10.1 Suggestions for future research	169
10.2 Author's publications	170
10.2.1 On offshore platforms	170
10.2.2 On other topics	172
References	175

List of Tables

1.1 Platform types classified according to their stability and motion compliance, (C) and (R) indicate compliant and restricted modes respectively [31]	9
3.1 Experimental implementation of the NREL 5MW turbine	35
3.2 Settings of the simple generator model	36
3.3 Experimental and numerical thrust differences as a function of wind speed	37
3.4 Normalised root mean square error of the comparison between 6 th and 9 th order polynomials representing the tower modes	38
3.5 Summary of semisubmersible's properties	40
3.6 Platform viscous damping coefficients	40
4.1 Updated viscous damping values	46
4.2 NREL 5MW turbine design values	47
4.3 System identification load cases	50
4.4 Load cases with only waves and no wind	51
4.5 Load cases with waves and wind	52
5.1 Platform surge RMS values of all attending participants	59
5.2 Viscous damping coefficients used in the OC4 Phase II	60
5.3 Load case 2.6 data included in the uncertainty study and their respective figure markings	61
5.4 Low-frequency and wave frequency combined range comparisons inside identical primary hydrodynamics groups	64

5.5	CoV values of low-frequency and wave frequency comparisons between the mean RMS values of the primary hydrodynamics groups	64
5.6	CoVs of all hydrodynamic models in low and wave frequency ranges	65
5.7	Wave frequency range comparisons inside identical primary hydrodynamics groups	66
5.8	CoV values of wave frequency comparisons between the mean RMS values of the primary hydrodynamics groups	66
5.9	CoV of all hydrodynamic models in wave frequency range	67
5.10	CoV values of the users of NREL's FAST	68
5.11	Mean RMS values of the mooring models	68
5.12	CoV of the mean RMS values of the mooring models	69
6.1	Sample load case matrix representing the platform related variables of the OC4 Code Comparison studies	75
6.2	Pseudocode for input editing	77
6.3	A sample of suggested output format for numerical verification of static equilibrium	81
6.4	Pseudocode for mode calibration	83
7.1	Comparisons of volume measurements between Rhino3D and ParMod	109
7.2	Weight calculations of the box and the frustum	110
7.3	Structural inertia calculations of the frustum about the origin and the centre of gravity (CoG)	111
7.4	Structural inertia calculations of the box about the origin and the centre of gravity (CoG)	111
7.5	Performance breakdown of the modules in seconds	113
7.6	Total run times with (W) and without (WO) performance measurement in seconds	113
8.1	The properties of spiral strand mooring line material as a function of its diameter	121
8.2	Tower and RNA mass properties as modelled and documented	127
8.3	Parameters used for the platform dimensions	131
8.4	Hydrostatic calculations of WAMIT and ParMod, CoB stands for the centre of buoyancy	132
8.5	Static equilibrium assessment	133
8.6	Platform eigenfrequency estimations of the three numerical models [s]	133
8.7	Wave only RAOs for a 10s period regular wave	134
8.8	Motions of the TLP under 11.4 m/s linear wind excitation	135

8.9 Platform responses to regular wave height of 4 m and a period of 10 seconds, with a linear wind of 11.4 m/s	136
8.10 Occurrences of sea states and related wind speeds during the period of January 2008 to December 2010 in Galicia (H_s in m, U_w in m/s, T_p in s)	136
8.11 Safety margin estimations between a linear wind / regular waves case and a stochastic case, wind speed is 11.4 m/s and wave height and period are 4 m at 10 s	137
8.12 Platform's compliance with the 25% safety margin. (T+W) signifies compliance with a running the turbine and. (W) signifies that the platform can comply only with a parked turbine. (H_s in meters, T_p in seconds)	138
8.13 Lowest mooring line tension attained in a 1200-second time domain simulation	138
8.14 Turbine's probable operational conditions in response to the sea states of Galicia during the period of January 2008 to December 2010	139
8.15 Frequency domain evaluation criteria	139
8.16 Finalized platform properties after evaluation	140
8.17 Performance breakdown of the modules and codes used inside the design process of a single variation	142
9.1 Properties of the semisubmersible platform	147
9.2 Viscous damping coefficients	147
9.3 Hydrostatic and mooring restoring forces	147
9.4 Natural frequencies of the structure [Hz]	148
9.5 Summary of the environmental conditions	150
9.6 The effect of the faulty blade position on the yawing motion in NS_A environment [deg]	155
9.7 Thrust forces on the rotor in intact and faulty conditions [kN]	157
9.8 Yaw motion as a function of the blade starting position [deg]	158

List of Figures

1.1	Average water depth, distance to shore of bottom-fixed, offshore wind farms by development status in 2016. The size of the bubble indicates the overall capacity of the site. [5]	2
1.2	The primary of stabilization methods of common offshore platform types	4
1.3	Examples of semisubmersible platforms	5
1.4	A SeaStar family tension leg platform	6
1.5	A SPAR platform	8
1.6	The platform geometries developed by the DeepCwind consortium [38]	10
1.7	Natural frequencies of the DeepCwind platforms [43]	11
1.8	The TLP, the semisubmersible, single point mooring (SPM) semisubmersible, and the SPAR platforms developed in collaborative studies in Japan [25]	12
2.1	The axes, coordinates and the numbering system used to represent the platform motions about the centre of gravity (CG)	24
3.1	NACA 64 Profile comparison between experimental data and reference 5MW Turbine	36
3.2	Turbine and generator evaluation at 21.80 m/s wind speed	37
3.3	Normalized mode shapes as a function of tower height	38
3.4	An illustration of the DeepCwind semisubmersible wind turbine platform	39
3.5	Responses of the DeepCwind platform under steady wind loading	41
3.6	Responses of the DeepCwind platform under regular wave loading	43

4.1	The underwater geometry of the semisubmersible model with and without the connecting braces	47
4.2	Added mass coefficients of the braceless and full models	48
4.3	Potential damping coefficients of the braceless and complete models	49
4.4	Wave exciting forces of the braceless and complete models	50
4.5	Free decay motions of the platform in surge, heave, and pitch	51
4.6	Load case 2.1, Responses of the platform to regular waves	51
4.7	RAOs as a response to white noise amplitude of 1 m ² /Hz between 0.05 Hz and 0.25 Hz, described in load case 2.2	52
4.8	Platform responses in regular waves with wind, described in load case 3.1	53
4.9	RAOs of surge, heave and pitch motions in turbulent wind and irregular waves, described in load case 3.2	53
4.10	RAOs for white noise amplitude of 1 m ² /Hz between 0.05 Hz and 0.25 Hz and linear wind of 8 m/s, described in load case 3.3	54
5.1	Spectral density of the wave frequency	62
5.2	Platform pitch responses	63
5.3	Platform surge and heave responses	63
5.4	Spectral density of the tension at fairline 1	69
6.1	Flowchart systematization of the I/O process	74
6.2	Time series plot of a wave; the headers and units are taken from the FAST output file	79
7.1	Origin, axis, surface normals, and vertex ordering	88
7.2	Simplified models of a disc and a cylinder quadrant	90
7.3	Flowchart of radial based modelling	92
7.4	A quadrilateral face composed of three sub-faces	93
7.5	Flowchart of face based modelling	95
7.6	Triangulation of a quadrilateral	98
7.7	Frustum	102
7.8	Sphere	103
7.9	Torus rotated 45 degrees in Y and X axes	104
7.10	Glass	105

7.11 The DeepCwind semisubmersible floating wind turbine platform	105
7.12 A rectangular prism with 6 faces	106
7.13 Midship section of a tanker	107
7.14 Hull geometry of a ship	108
7.15 Brunnelleshi's Octagonal Dome in Florence	108
7.16 Simplified models of a disc and a cylinder quadrant	110
7.17 Comparison of hydrodynamic coefficients of a cylinder, obtained with WAMIT.	112
7.18 Comparison of hydrodynamic coefficients of the semisubmersible platform, obtained with WAMIT.	113
8.1 Contribution of an individual panel to the model's centre of buoyancy	118
8.2 Truncating an individual quadrilateral panel from the waterline ($Z=0$), the subscripts e and n denote eliminated sections and new quadrilaterals respectively.	119
8.3 The mass, hydrodynamics, and waterplane area models illustrated on the OC4 semisubmersible platform	120
8.4 Spline interpolation of heave and pitch added masses calculated with 0.5-second intervals by WAMIT	123
8.5 Tension leg platform dynamics in set down	125
8.6 Interaction between the modules throughout the design cycle, dark grey shaded components represent external codes	128
8.7 Interaction between ParMod's modules in the development and assessment of the multi-purpose model	129
8.8 The model of the platform, tower and the RNA. The meshed components are considered as distributed mass	130
8.9 The parameterised dimensions of the platform	131
8.10 Mooring line responses in a time domain simulation with a wave height of 6.74 meters at a period of 7 seconds	135
8.11 Motion responses, mooring line setup and tensions of the 231 TLP variations	141
8.12 Platform mass and the total mass including the RNA for the 231 TLP variations	142
8.13 Time domain responses of the platform with 19.25 meters outer ring size and 13 meters of keel depth to 8 meters of significant wave height and 22 m/s of stochastic wind	143
9.1 The hub-centred coordinate system and the blade numberings	148
9.2 Platform responses and tower base side-to-side moments in operational conditions	151

9.3	Platform responses and tower base side-to-side moments in storm conditions	152
9.4	Time series of the yaw motion caused by the blade feathering fault under IEC, North Sea and Portuguese coast storm conditions	154
9.5	Comparison of the blade 1 azimuth angle, platform motions, and the HSS-brake behaviour in the North Sea Storm (NS ₅₀) conditions. Feathered blades and actuator fault are denoted by (fb) and (af) respectively.	156
9.5	continued, Comparison of the blade 1 azimuth angle, platform motions, and the HSS-brake behaviour in the North Sea Storm (NS ₅₀) conditions. Feathered blades and actuator fault are denoted by (fb) and (af) respectively.	157
9.6	Behaviour of the platform influenced by the blade feathering fault and applied HSS brake in PT ₅₀ conditions	159
9.7	Yaw motion induced by reduced maximum HSS brake torque in PT ₅₀ conditions. Blade 1 initial azimuth angle is zero degrees.	160
9.8	Forces acting on the platform in roll motion	163
9.9	Blade 1 azimuth angles in NS ₅₀ between 2000 and 3000 seconds. The peaks used for frequency measurements are marked in diamond shapes	164

Mathematical notation

A_{ij}	added mass coefficient in the modes denoted by the subscript
A_{wp}	waterplane area
BM	distance between the metacentre and the centre of buoyancy
BM_L	distance between the longitudinal metacentre and the centre of buoyancy
B_{ij}	damping coefficient in the modes denoted by the subscript
C	restoring coefficient
CG	centre of gravity
C_h	hydrostatic restoring matrix
C_m	mooring restoring matrix
$CoB(x, y, z)$	location of the center of buoyancy
C_t	restoring matrix as a sum of mooring and hydrostatic matrices
EA	Young's modulus multiplied by the cross sectional area
F_a	aerodynamic forces
F_b	increase in mooring line tension due to the change in buoyancy force
F_{break}	mooring line breaking tension
F_h	hydrodynamic forces
F_{line}	mooring line tension
F_{loss}	Loss of mooring line tension
F_{s_m}	change in mooring line tension due to surge
F_t	total force on

GM	metacentric height
GM_L	longidinal metacentric height
H	wave height
H_o	operational wave height
H_s	significant wave height
I_{ij}	structural inertia about the subscript axes
$I_{xx,yy,xy}^w$	waterplane inertia about the subscript axes
KB	distance between the keel and the centre of buoyancy
KG	distance between the keel and the centre of gravity
L_m	stretched length of the mooring line
L_u	unstretched length of the mooring line
M_t	mass matrix of a structure as a sum of its components
S_b	underwater hull surface area
TI	turbulence intensity
$T_{turbine}$	Turbine thrust
$U(z_r)$	wind speed at reference height
$U(z)$	wind speed at height z
V_{x,y,z_b}	coordinates of the centre of buoyancy in x , y , or z axis as defined by the subscript
d	diameter of the TLP tendons
g	gravitational acceleration
k	wave number
m	mass
n_t	total number of mooring lines
t	time
x	Cartesian component
x_{33}	amplitude of the motion at the fairlead due to heave
x_{55}	amplitude of the motion at the fairlead due to pitch
x_f	location of the centre of floatation in x axis
x_g	location of the center of mass in x axis
x_l	mooring line fairlead location in x axis
y	Cartesian component

y_f	location of the centre of floatation in y axis
y_g	location of the center of mass in y axis
y_l	mooring line fairlead location in y axis
z	Cartesian component
z_g	location of the center of mass in z axis
z_l	mooring line fairlead location in z axis
F_m	total change in mooring line tension
Φ	fluid velocity potential
Φ^D	diffraction potential
Φ^I	radiation potential
Φ^R	radiation potential
ϵ	phase shift
η	wave amplitude
γ	peak enchantment factor
μ	mean value
∇	hull volume
ω	wave frequency
ω_o	operational wave frequency
ω_p	peak wave frequency
φ_{ts5}	sum platform pitching angle due to wind and waves
φ_{wave55}	platform pitching angle due to waves
φ_{wind55}	platform pitching angle due to wind
ρ	density
σ	standard deviation
θ	turbine's angle with the horizontal axis

Variables used in geometric modelling

A_p	surface area of a quadrilateral panel
$A_{PROJ_{x,y,z}}$	projection area of a panel onto the axis defined by the subscripts x, y, or, z
A_{tri}	surface area of a triangle
$C_G(x_g, y_g, z_g)$	centre of gravity of the model
C_M	centre of mass of a quadrilateral panel
$C_{quad}(x_c, y_c, z_c)$	geometric centre of a quadrilateral in 3D space

$C_{tri}(x_C, y_C, z_C)$	geometric centre of a triangle in 3D space
[G]	global matrix
\vec{l}_B	second defined edge increment
\vec{l}_T	first defined edge increment
$I_{xx,yy,zz,yz,zx,zy}$	structural inertia of the model about the axes defined in the subscript
[L]	local matrix
M_p	mass of a quadrilateral panel
$O_{R(x,y,z)}$	origin of rotations in Cartesian axes x,y, and z
$O_{axis_{x,y,z}}$	surface normal orientation in the given axis subscript x, y, or z
$O(X_0, Y_0)$	origin of the Cartesian coordinate system
[P]	panel matrix
R_O	order of rotations about the Cartesian axes (e.g., x, z, then y)
$R_{x,y,z}$	rotation angle in the Cartesian axis defined by the subscript
T	translation distance in Cartesian coordinates
$V(x, y, z)$	vertex location in Cartesian axes
V1	vertex number 1 of a given quadrilateral
V14	an arbitrary intermediate vertex between the vertices 1 and 4 of a given quadrilateral
V2	vertex number 2 of a given quadrilateral
V23	an arbitrary intermediate vertex between the vertices 2 and 3 of a given quadrilateral
V3	vertex number 3 of a given quadrilateral
V4	vertex number 4 of a given quadrilateral
Vol_{k_t}	total volume of the model integrated in the k axis
W_t	mass of the model
Z	z-axis coordinate
Z_{inc}	depth increment
m	number of bodies of constituting the structure
n	number of edges in a body
\vec{n}_s	inverse of the surface normal
n_{sub}	subsurface number
\vec{n}	surface normal vector
r	radius

r_i	radius of edge i
r_{inc}	radius increment
s_1	number of sections of the first defined edge of the quadrilateral
s_2	number of sections of the second defined edge of the quadrilateral
s_p	number of arc segments
s_r	number of radius segments
s_z	number of sections in the vertical axis
t	plate thickness
x_m	translation distance in x axis in 3D space
$x'_{x,y,z}$	the new value of the Cartesian x-coordinate after being rotated about the axis defined by the subscript
y_m	translation distance in y axis in 3D space
$y'_{x,y,z}$	the new value of the Cartesian y-coordinate after being rotated about the axis defined by the subscript
z_m	translation distance in z axis in 3D space
$z'_{x,y,z}$	the new value of the Cartesian z-coordinate after being rotated about the axis defined by the subscript
χ	mathematical function defined as flipping the first 3 columns of a matrix upside down
φ_i	sweep (polar) angle of the edge i
φ_{inc}	polar (sweep) increment
θ	rotation angle in 3D space

List of acronyms

3D	three-dimensional
ABS	American Bureau of Shipping
BEM	boundary element method
BV	Bureau Veritas
CAD	computer aided design
ClassNK	Nippon Kaiji Kyokai
CoV	coefficient of variation

DNV	Det Norske Veritas
FAST	Fatigue, Aerodynamics, Structures, and Turbulence
FE/DYN	finite elements dynamic
FFT	fast Fourier transform
FMEA	Failure Modes and Effects Analysis
GL	Germanischer Lloyd
GWEC	Global Wind Energy Council
HSS Brake	high speed-shaft brake
IEA	International Energy Agency
IEC	International Electrotechnical Commission
IP	instantaneous position
ISSC	International Ship and Offshore Structures Congress
IWL	instantaneous water level
JONSWAP	Joint North Sea Wave Observation Project
LM/DYN	lumped mass dynamic
MAP++	Mooring Analysis Program
MARIN	Maritime Institute of the Netherlands
ME	Morison Equation
ME + PF	Morison Equation combined with the potential flow theory
NREL	National Renewable Energy Laboratory
NURBS	non-uniform rational basis spline
OC	Offshore code comparison collaboration

PF + QD	potential flow theory combined with quadratic damping
PSD	power spectral density
QS	quasi-static
R&D	research and development
RAO	response amplitude operator
RMS	root mean square
RNA	rotor nacelle assembly
RSD	relative standard deviation
SPAR	single point anchor reservoir
SPM	single point mooring
SWL	still water level
TLP	tension leg platform

CHAPTER 1

Introduction

Industrialization brought forward an increased need for energy which was primarily covered by the oil and gas industry in the last century. As its effects on the environment became clear, the world's focus shifted towards cleaner resources. Within a list that includes alternatives such as solar and wave energies, wind power emerged as one of the major solutions to tackle the problem.

Using wind for energy production is a well-established idea, with roots dating back to the first windmills. The application of this concept to electricity originates from the Brush turbine which produced a mere 12 kW in 1888 [1, 2]. Since then, the idea progressed immensely. The Global Wind Energy Council (GWEC) states that in 2001 the global installed wind power was 23,900 MW. In 2016, this number increased to approximately 486,000 MW: a 20-fold increase over 15 years [3]. In 2016 alone, there was a cumulative market growth of 11 percent, and an average rate of 21 percent in the last decade. These totals above include both onshore and the offshore capacities with the GWEC report of 2017 listing an offshore share of 4,117 MW in 2011. Subsequently, it tripled to 14,384 MW in 2016, reaching 18,814 MW in 2017 [4].

Offshore wind brings a set of advantages over the onshore installations. The open space over the ocean results in a more consistent wind resource and the visual impact is reduced. On the other hand, it introduces economical challenges and hydrodynamic complexities. The progression of offshore wind power resembles the early days of the oil & gas industry. In the beginning of the 20th century, the first search for oil in the sea was in shallow waters using fixed bottom foundations. Over the years, floating platforms made it possible to exploit higher depths. The first offshore wind

Published in: E. Uzunoglu, D. Karmakar, and C. Guedes Soares. Floating Offshore Wind Platforms. In L. Castro-Santos and V. Diaz-Casas, editors, *Floating Offshore Wind Farms*, chapter 4, pages 53–76. Springer International Publishing, Switzerland, 1st edition, 2016. ISBN 978-1-138-00124-4. doi: 10.1007/978-3-319-27972-5.4

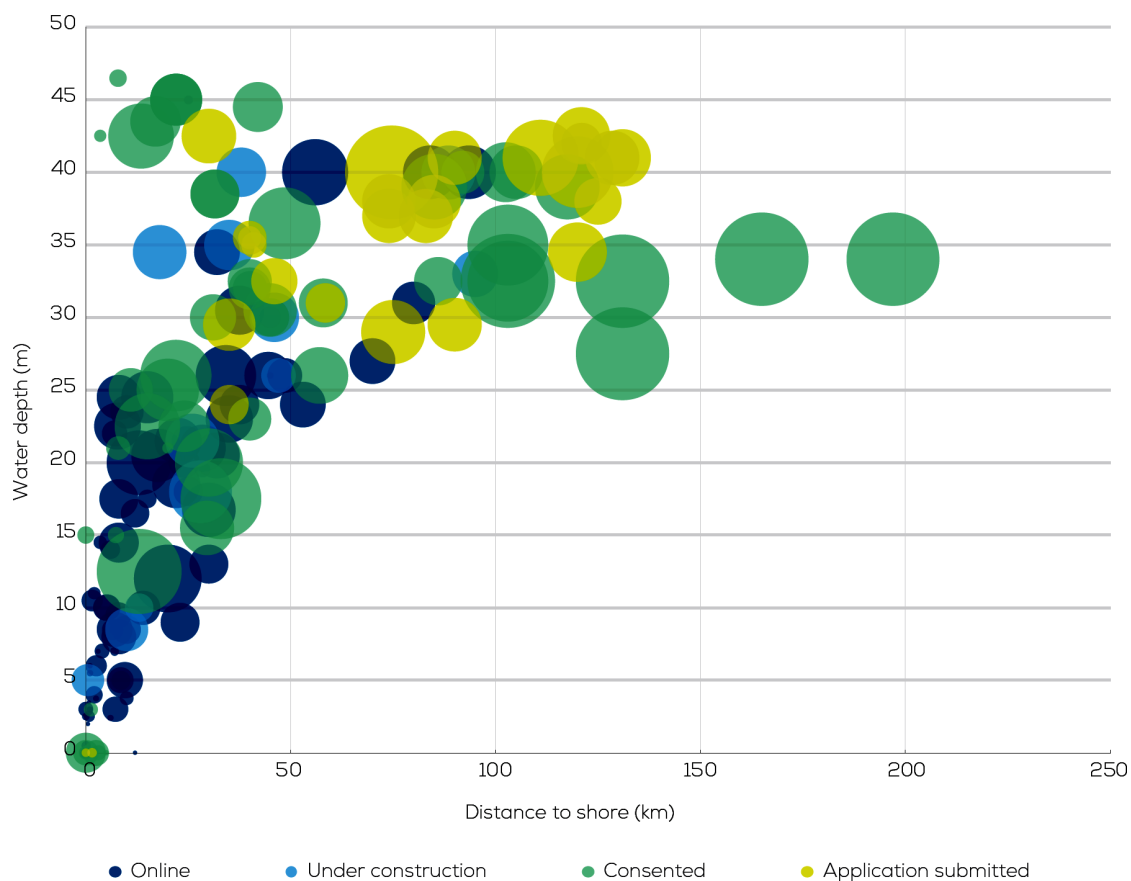


Figure 1.1: Average water depth, distance to shore of bottom-fixed, offshore wind farms by development status in 2016. The size of the bubble indicates the overall capacity of the site. [5]

installation was the Vindeby farm in Denmark, inaugurated in 1991 and decommissioned in 2017. Since then, the turbine sizes of 450 kW have reached 7-8 MW.

GWEC states that 90 percent of these offshore installations are in European waters. China, Japan, South Korea, Taiwan, and the USA show growth, underlining the global interest in the topic. The status of offshore installations reveals that the wind farms have moved further from shore and into deeper waters. By the end of 2016, the average water depth of operating wind farms was 29.2 m, and the average distance to shore 43.5 km which is a significant increase from 16 m and 29 km in 2013 [5]. Figure 1.1 shows the state of offshore wind power in 2016. This progress implicates floating alternatives will be considered more frequently as fixed bottom solutions may become disadvantageous in deeper waters.

The platform is the defining element of floating wind turbines. Ultimately, the motions and loads on the floater are the two factors that set floating and fixed bottom structures apart. The fundamental knowledge on offshore platforms is based on the experiences of the oil and gas industry. However, the additional aerodynamic loading signifies that the motion behaviour is different in this newer field of wind power. Consequently, the knowledge needs to be updated and re-evaluated to focus on this combined loading. In this regard, recent research and demonstration projects mainly study

semisubmersibles, tension leg platforms (TLPs), and single point anchor reservoir (SPAR) buoys. To understand why these platforms differ from each other, it is necessary to understand their dynamics.

1.1 Offshore wind turbine platform concepts

As the offshore wind turbine industry evolved to meet the demand, the number of proposed platforms increased considerably. Each one of these solutions employs a different configuration classified with various approaches. Overall, they can be categorised into three groups depending on their method of stabilisation: “buoyancy”, “ballast” and “mooring” stabilised platforms [6]. In practice, any given structure relies on a combination of these methods. Regardless, the prominent factor in attaining stability identifies the type.

Semi-submersibles and barges provide examples of “buoyancy stabilised” structures in this classification. They are similar in the sense that they both depend on buoyancy. However, the distribution of volume differs. The barge generally has a larger waterplane area and a shallower draft. Conversely, the semi-submersible combines ballasting with a smaller waterplane area. Hence, the semisubmersible is often referred as a “column-stabilised” unit in stability rulebooks [7]. Revising “buoyancy-stabilized” as “waterplane area stabilized” allows to clarify this distinction regarding the volume distribution.

The TLP requires the support of its tendons to become stable, which classifies it as a “mooring stabilised structure”. The SPAR has a column-shaped hull that requires heavy ballast placed at a deep draft to overcome tipping moments. With these considerations, the primary platform types can be placed on a stability triangle as in Figure 1.2. While variations to these four alternatives (e.g., heave restrained TLP [8]) exist, they relate closely to the concepts explained below.

1.1.1 Waterplane area stabilized platforms

Between the barge and the semi-submersible, the semi-submersible is prevalent in both oil & gas, and wind power sectors due to their favourable motion dynamics. They have been in use by the oil and gas industry since the 1960s, which are referred as the first generation. Over time, their design has evolved and the 6th generation is now in discussion. Hence, it's possible to state that the semi-sub is a well-studied platform type. They are preferred for their stability in waves, particularly against heave and pitch motion. While the platform sizes and encountered loads differ between the offshore wind and oil gas industry, this type is still considered as one the major concepts.

A semi-submersible comprises columns and pontoons that provide the main volume under water. Connecting braces secure the structural integrity of the system. The oil-and-gas industry uses large volume pontoons and columns that pierce the water level to carry the deck: a setup that has its origins in submersible hull forms. In a passage to wind turbine platforms, this concept evolved to suit the specific needs of the industry. Since the payload of wind turbines is lower and the required

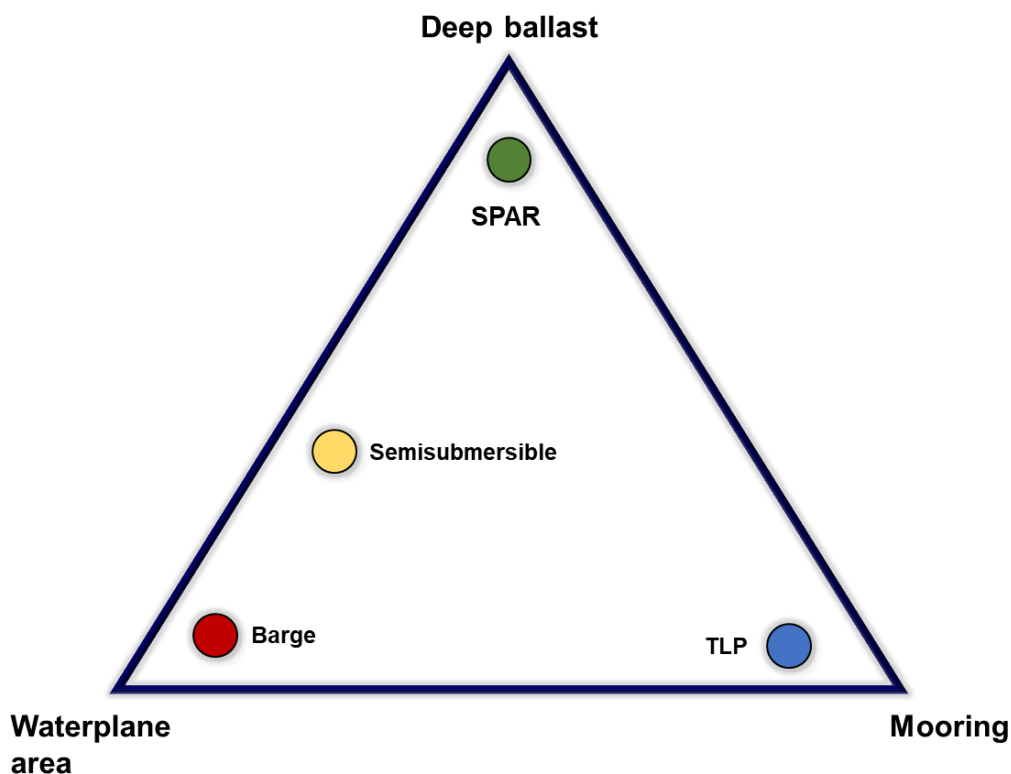


Figure 1.2: The primary of stabilization methods of common offshore platform types

deck space is equally reduced, lowering the volume of the platform became essential in achieving economic feasibility [9].

The number of columns of the semi-sub varies between concepts. Considering the setup, the distance between columns affects the structure's hydrostatic stiffness. The loads on the bracings and the structural integrity are also functions of the moments and forces coming from each column. The multi-body setup provides different ballasting options to counter pitch and roll motions. Heave motion may be reduced by adding plates of large radii at the lower extremity of the structure [10, 11]. The platform offers a relatively small waterplane area; therefore, the eigenfrequency of heave usually falls outside the wave frequencies except for extreme weather conditions. Heave, pitch and roll are counteracted by the hydrostatic restoring. Surge, sway, and yaw are dealt with by catenary mooring.

Design decisions include column properties (e.g., rectangular vs cylindrical) and the placement of the tower and turbine. Some variations are exemplified in Figure 1.3. For instance, the WindFloat platform [12, 13] is one of the early adopters of floating wind turbine technology. It brings together three columns connected by braces. The turbine is hosted on one of them. The semi-submersible designed by the DeepCwind consortium features a different solution, utilising four columns where one is placed in the centre, supporting the wind turbine. DeepCwind and the WindFloat feature similar characteristics regarding column shapes and connecting braces. Braceless models use entirely different configurations. Fukushima Shimpuu [14, 15] utilises three rectangular columns connected by pontoons and laid out in a V-shape. The turbine is placed on the bottom tip of the V.

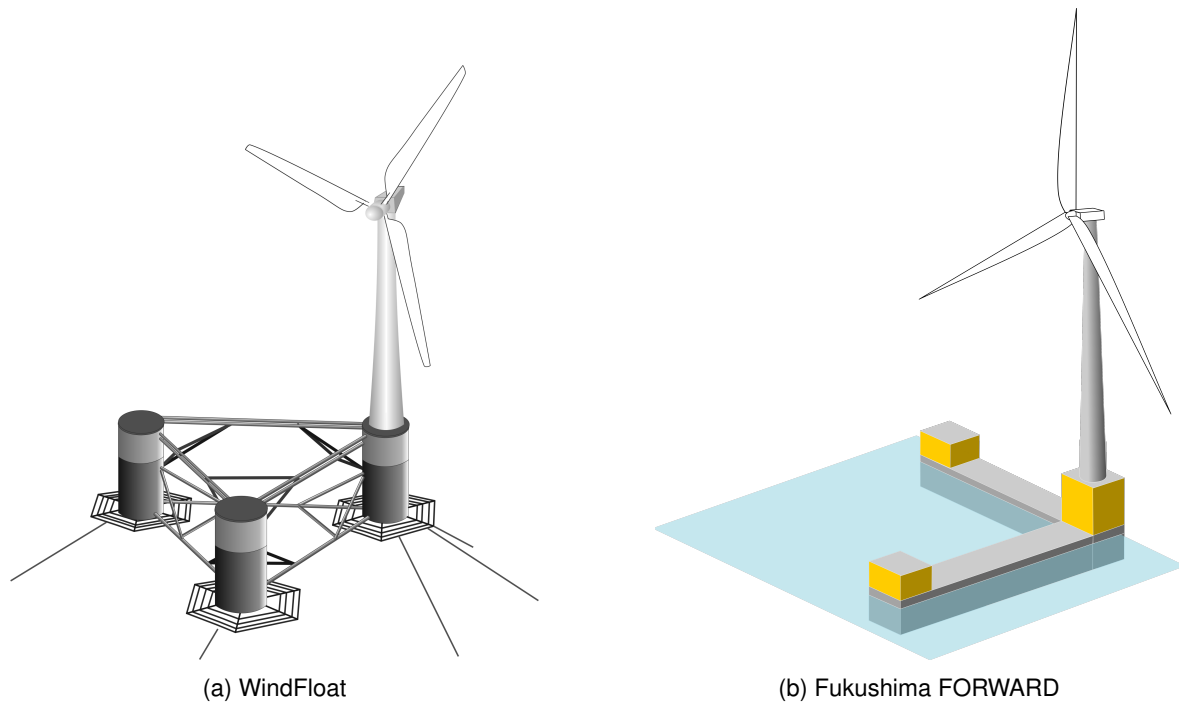


Figure 1.3: Examples of semisubmersible platforms

One of the main advantages of semi-submersibles comes from their installation procedures. As a hydrostatically stable structures, they may be towed to the deployment site after being built onshore. Mooring system and design complexity are lower in comparison to tension leg platforms as they are not a factor in stabilising the structure. The variety of hull geometry options, therefore the draught, suggests these platforms can be flexible regarding installation depths.

1.1.2 Mooring stabilized platforms

The oil-and-gas industry initially developed the TLP concept as a cost-effective way of exploiting deeper water dating back to 1970s. The first working installation, the Hutton TLP, was successfully deployed by Conoco in the North Sea in the 1980s [16, 17]. The main feature of tension leg platforms lies in their stabilisation characteristics. Instead of relying on a balance of forces between the buoyancy resulting from the underwater geometry and aptly distributed weight, the stability depends on taut mooring lines. This setup provides resistance to motions due to the extra stiffness coming from the tendons, resulting in highly restricted roll, pitch, and heave modes. These platforms behave more like a fixed structure regarding these motions. The minimal pitching response is an advantage in terms of power production as it is a major factor that affects the aerodynamic performance [18, 19]. The generated power is accordingly defined by the specifications of the turbine in the absence of large amplitude motions.

In oil and gas platforms, the hull shape can resemble semisubmersibles with surface piercing columns like the Hutton TLP. In this case, there are ring type pontoons underwater, connecting the columns. However, the volume and the surface area of TLPs are overall lower than semi-

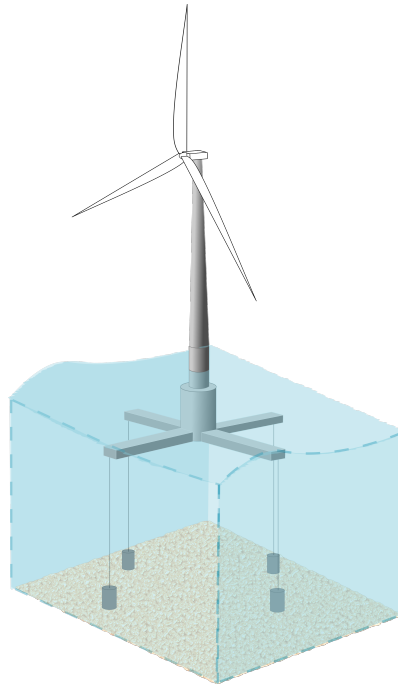


Figure 1.4: A SeaStar family tension leg platform

submersibles. This setup reduces the loads from incoming waves. It also turns into an advantage in terms of corrosion resistance, which occurs at the waterline. An alternative geometry aims to minimise the structural weight by employing arms (spokes) connected to a single column that carries the deck. This type, the SeaStar design, was developed in the 90s [20, 21]. The number of spokes and the angle between them varies depending on the configuration; however, it's common to see three or four. Figure 1.4 represents the underwater geometry of a TLP platform mirroring National Renewable Energy Laboratory (NREL) designed MIT/NREL TLP [22].

The TLP's optimisation parameters are the shape of the spokes (e.g., rectangular vs cylindrical), the placement of extra weight, and the general hull form. The distance of the tendons from the main body alters the moments provided by the lines. Compared to catenary mooring, the tendon length is shorter, equalling the direct distance from the fairlead (tendon's connection point to the hull) to the seabed. The connections can be tension piles, gravity anchors, and suction buckets. In wind turbine platforms, the tendons need to counteract the aerodynamic loading coming from the turbine besides the wave exciting forces. Therefore, there is an increase in total mooring loads.

The rigid-like behaviour of the platform in certain modes brings forward concerns about high-frequency excitation. Accordingly, the design of the hull and the mooring lines is highly coupled (i.e., changing one will cause fundamental alterations in the setup or responses of the other component.) Two failure modes are of particular importance: the breaking of a mooring line may cause stability failure. On the other hand, the loss of tension at the mooring line (termed as going slack) leads to high snatch loads when it comes back into tension causing by a zipper effect with a high probability of structural failure. Therefore, slack moorings are considered as a limit state in the design of tension leg platforms.

In installation phases, added weights can provide temporary stability to the platform during the tow to the deployment site. For this purpose, the structure is ballasted in the pre-installation phase, and the ballast is removed following the installation of the anchors on-site. If the structure cannot be towed, it will need to be carried to the location by other means such as installation barges [23]. This case is also valid for maintenance procedures if the turbine needs to be relocated to the port. Despite these disadvantages, on average, the tension leg platform offers the lightest alternative to wind platforms regarding steel weight (i.e., one of the primary drivers of monetary cost) when compared to other platform types [24].

1.1.3 Deep ballast stabilized platforms

SPARs are the main ballast stabilised platform type. Designed initially as buoys that gather oceanographic information, they were used by the oil and gas industry in the 1990s in the Oryx Neptune field. Since then, alternative forms have been developed, focusing on slightly different applications. The main idea stayed unchanged. SPAR resembles a slender cylinder. Heavy ballast is used at the lower extremity of the platform, to reduce the centre of gravity below the centre of buoyancy and ensure stability. Catenary mooring lines provide station keeping.

Figure 1.5 represents the underwater geometry of a SPAR platform. SPARs are deep-water platforms as they necessitate the placement of a ballast low enough to achieve the desired restoring moment. The added weight at the bottom of the cylinder also counters the rotational motions of pitch and roll. The relatively small waterplane area provides the restoring forces in heave and characterises the SPAR as a platform that has low stiffness in this mode. Due to the symmetry and the small size, hydrodynamic excitation enforces only negligible yaw motion on the body of the cylinder. On the other hand, when used for wind turbines, aerodynamic loads induce yaw motion through the applied moments on the blades [25]. The mooring lines should counteract these forces. However, when catenary mooring lines are attached directly to the body of the platform, they introduce a limited amount of yaw restoring moment. Alternative configurations try to increase the distance between the mooring fairleads and the hull to address this problem. As these platforms are intended for higher depths, the mooring lines need to be longer, and this may reflect in costs. In contrast, the hull represents a simple-to-produce form that may be economical.

The simplicity of the hull form makes the SPAR susceptible to a phenomenon called vortex-induced vibration (VIV). As the cylinder heaves, it creates vortices, changing the pressure distribution along the surface, and the flow becomes irregular. This pressure change leads to low-frequency vortex-induced vibrations, causing higher mean current forces and leading to fatigue [26]. Various methods are available to eliminate the cause of VIVs. An example to common practice is to employ streaks at the cost of increased drag and total mass. Considering the significant underwater body of the platform, water currents may need to be taken into account when designing a SPAR. There are substantial advantages regarding corrosion effectiveness as the waterplane area is small. In sum-

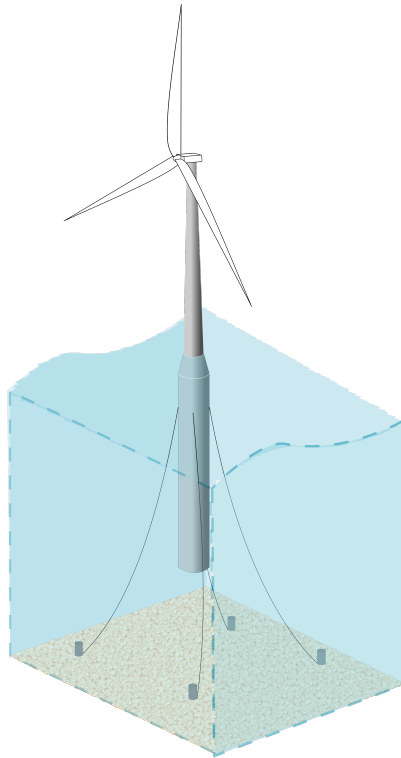


Figure 1.5: A SPAR platform

mary, the SPAR provides a simple shaped platform that has slow and limited motions due to its low waterplane area. It may become economically disadvantageous due to its higher depth requirement.

1.1.4 Hybrid platforms and multi-turbine concepts

In most cases, a platform can be included in one of the classifications provided above. However, alternatives to better accommodate the turbine and tower are always under consideration. Such structures employ a combination of the stabilisation methods to reap the advantages of each approach while bringing them together. Heave restrained TLP and SPAR configurations compliant in other modes but restrained in heave are examples of hybrid structures [27]. There are also concepts that aim to integrate other forms of energy such as wave into a single system [28, 29].

As an alternative to platforms that can host a single turbine, integrating multiple turbines together has its advantages and disadvantages. The benefits include using a single grid connection and a mooring system for multiple turbines. There is also the possibility of having a common service area. The difficulties arise mainly due to the proximity of the turbines. As in the fixed-bottom offshore wind farms, floating structures also have to be installed in numbers to provide a significant amount of energy. Their placement affects the performance of the surrounding turbines due to the wake phenomena behind the blades. This case may also mean that the nacelle yaw motion may not mitigate the wake effect and rotating the platform may be necessary to face the wind. All multi-turbine solutions have to be evaluated for such effects. As an example, the Swedish company Hexicon proposes a concept that hosts four turbines on a single platform [30].

Table 1.1: Platform types classified according to their stability and motion compliance, (C) and (R) indicate compliant and restricted modes respectively [31]

Platform	Stability	Surge-Sway	Heave	Pitch-Roll	Yaw
SPAR	Deep ballast	C	C	C	C
Semi sub	Waterplane	C	C	C	C
TLP	Mooring	C	R	R	C

1.2 Evaluation of platform concepts

The platforms can be categorised as compliant or restrained in each mode of motion according to their global responses. A summary of these conditions is presented in International Ship and Offshore Structures Congress (ISSC) 2012 [31]. Table 1.1 couples this information with the primary means of stabilising the platforms [32]. Compliant modes significantly respond to the forces coming from the environment while restrained modes show small responses (i.e., measured in centimetres). The reduced motions are limited by the mooring line elasticity.

While the tabular information on restrained modes provides a general understanding of motion characteristics of platforms, further probing is necessary for details. The effect platform on system dynamics may be isolated by keeping the other variables identical (i.e., turbine, blade, and tower assembly) and changing only the platform. Experimental works of this nature that examine a scaled model of a 5MW reference turbine [33] mounted on different platforms are discussed below.

1.2.1 DeepCwind Consortium

The USA based DeepCwind consortium carried out the testing of three platforms: a TLP, a semi-submersible and a SPAR. The study aimed to exclude proprietary information to provide the researchers open access to data. The experimental program was carried out at the Maritime Institute of the Netherlands (MARIN).

The semi-submersible was designed by the DeepCwind consortium [34]. It features a four-column design with the turbine placed in the middle and three buoyancy columns that form a triangle. The TLP concept follows the form of Glosten Associates' PelaStar [35]. The SPAR is based on the Hywind platform, which was also the subject of an earlier code comparison study [36, 37]. They are presented in Figure 1.6. The findings are summarised in [38] and an account follows below.

A scale of 1/50 was utilised to prepare the model and the environment, using Froude scaled wind, and wave loads. It was explained that the main difficulty in experiments arises from making a suitable model for Froude scaling while adhering to similar Reynolds numbers. In this way, both wind and wave forces are scaled correctly. This difficulty was circumvented by designing a thrust-equivalent turbine for experiments [39] with different blade geometries. As in this case, scaling laws play a significant role in the experiments, and they are discussed in [40] and [41].

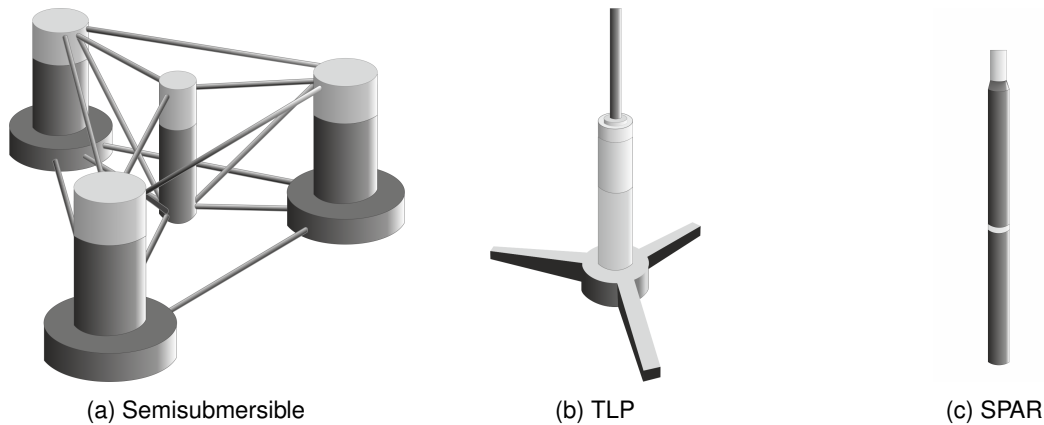


Figure 1.6: The platform geometries developed by the DeepCwind consortium [38]

The test procedure is explained in [42]. According to this method, the natural frequencies of the platforms are identified using hammer tests, followed by the determination of the static equilibrium position. Hydrodynamic characteristics such as viscous damping are evaluated through free decay tests. After the platform behaviour is examined in the absence of external forces, wind and waves are evaluated separately. Hydrodynamic studies include regular and irregular waves. Wind responses concern steady and dynamic wind loads. The last stage focuses on coupled wind and wave loading.

The natural frequencies of the platforms are summarized in Figure 1.7 [43]. Cross-comparing the platform types and considering the first-order wave excitation range (4 to 25 seconds [44]) provides an idea of the motion dynamics. The semisubmersible's surge natural periods are significantly longer than the TLP and the SPAR. Due to symmetry, sway is almost identical to the surge in all platforms. The TLP identifies itself in heave, pitch, and roll by proving to be a stiff structure with short natural periods (under 5 seconds). Other platforms deliver lower frequencies closer to 30 seconds. Yaw period is different for all platforms. The SPAR provides short yaw periods, resembling a restrained structure. TLP's yaw period is slightly above the wave frequency (WF) region, and the semisubmersible delivers longer periods compared to the other two platforms. These results clarify the required methods of avoiding resonance, either by going above or staying below the exciting frequencies. It was also noted that the platform alters the bending frequencies of the tower as it changes the total stiffness of the system.

The results have shown that under steady wind loading, surge responses of the TLP and the semi-submersible turned out to be similar. Their motion amplitudes were larger than those of the SPAR. Neglecting the wave forces, the small surface area exposed to wind provides an advantage to the SPAR in surge mode. Conversely, the semisubmersible delivered the highest surge motion overall, which may be reasoned to result from the same disadvantage.

The SPAR-buoy's pitching motion was the highest, as only the ballast counteracts pitching and rolling. As expected, the TLP showed limited responses due to the restrictions enforced by the mooring system. For this set of experimental models, the semi-submersible delivered pitch amplitudes that equal approximately the half of SPAR's values. It is important to add as a reminder that go-

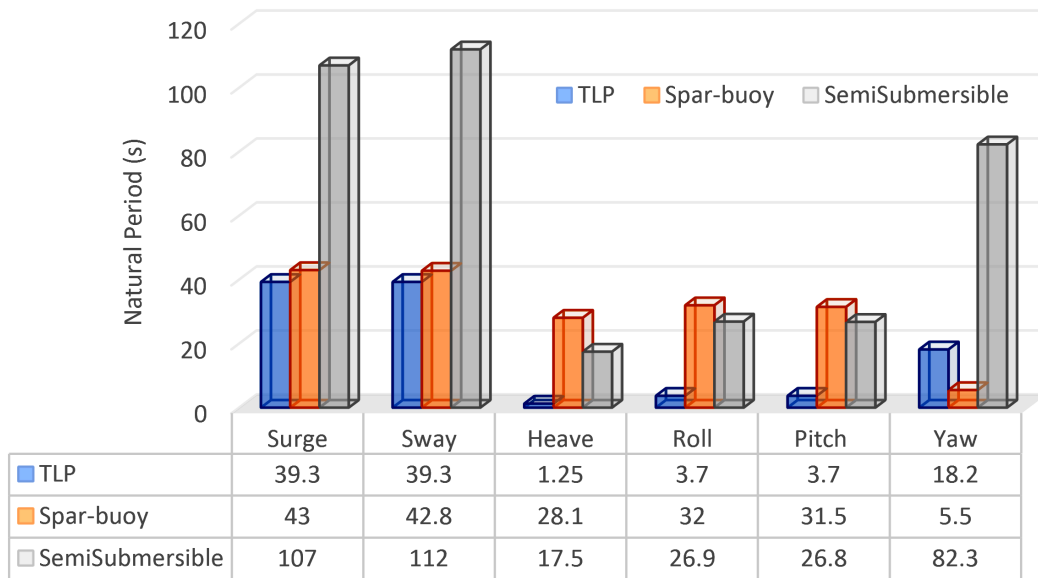


Figure 1.7: Natural frequencies of the DeepCwind platforms [43]

ing beyond certain angles in this mode limits the aerodynamic performance of the turbine. Angles beyond 4 degrees result in considerable differences in aerodynamic calculations [19]. This design constraint is imposed in other projects that design new platforms, such as the INNWIND, by keeping the maximum pitch amplitude below 3.5 degrees [45]. Higher pitch angles also result in increased tower base bending moment due to the weight of the nacelle-rotor assembly on the top of the tower.

Experimental data showed that the response amplitude operators (RAOs) of combined wind/wave loading were similar to responses to waves without the wind. These findings outlined waves as the primary driver of platform motions in all modes, as opposed to wind. Nevertheless, dynamic effects from aerodynamics, especially thrust, are significant in platform motions. The work presented an experimental confirmation for the presence of motions outside the wave excitation range. Higher-order sum frequency effects were identified in all platform types. However, the semi-submersible delivered by far the highest responses outside the wave frequency region.

1.2.2 Collaborative comparison studies in Japan

Japan shifted their focus to clean energy after the Fukushima nuclear disaster in 2011. To speed up this process, a comparative study was carried out with the joint effort of Osaka Prefecture, Yokohama National, Nihon, and Osaka Universities [25]. Contributors provided their platform design, to be coupled with a 5MW scaled turbine and a tower of 90 meters. A TLP, two semisubmersibles and a SPAR type platform with a scale of 1/100 were evaluated, illustrated in Figure 1.8. The leftmost model shows similarities to the DeepCwind TLP. Three mooring lines with 120 degrees of spread are present; however, a longer fairlead distance is seen. Two alternative semisubmersible platforms were studied. One of the suggested hulls uses a single point mooring (SPM) system and places the turbine on one of the three columns. The second model employs a 4-column approach with the

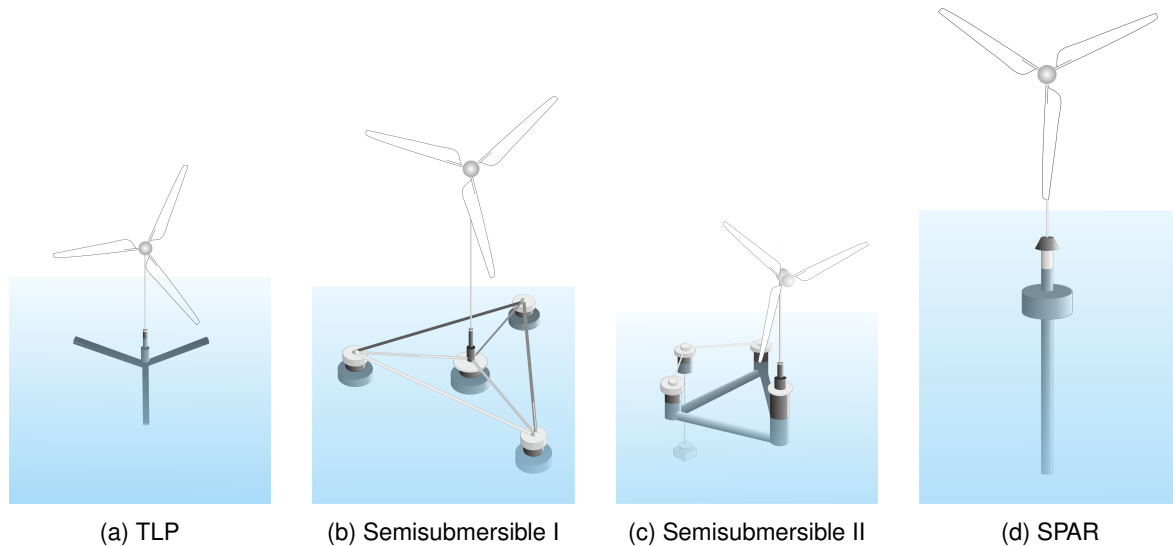


Figure 1.8: The TLP, the semisubmersible, single point mooring (SPM) semisubmersible, and the SPAR platforms developed in collaborative studies in Japan [25]

turbine at the centre. The SPAR platform presents an alternative to the standard cylindrical model. There is an additional disc placed at 15% of the total draft below the water level.

The findings of this study concur with the DeepCwind studies concerning platform characteristics. Their study classified TLP favourably for providing stability in pitch, roll, and heave motion. SPAR was identified to show the highest acceleration values and motions in most environmental conditions. Considering that high acceleration would affect the crew working at the nacelle level, they have proposed that the platform may induce difficulties regarding maintenance. In addition to wave and wind-induced motions of the platforms, the work has reported significant yaw motion of the SPAR which was attributed to the gyroscopic effect of the rotor. The small moment of inertia of the platform was listed as another factor. Their conclusion concerning the coupled motions also states waves as the primary driver of platform responses. The single point moored semi-submersible design provided an exception to this trend.

1.3 Numerical analysis of platform motions

The response dynamics of floating wind turbines involves significant coupling between the aerodynamics of the turbine and the hydrodynamics of the platform. The loads on the turbine, waves, and the moorings all contribute to the global response of the system. There are two ways to approach this problem. A validated hydrodynamic tool may be extended to include the aerodynamics of the turbine, or an aerodynamic code may be extended to include the hydrodynamics of the platform. In both cases, to fully capture the non-linearity of the responses in wind turbine platforms, a time-domain analysis is preferred as opposed to frequency domain approaches [46]. In hydrodynamic calculations, the main difference between codes lies in the basis of theories employed to estimate the motions. The Morison equation, the potential theory, or a hybrid approach combining

both are applicable. In most cases, the main approach is altered to include other factors such as the instantaneous water line or position [47].

One of the most prominent works in numerical tool development is the Offshore code comparison collaboration (OC) studies. The collaboration brings different codes to provide comparative results. The International Energy Agency (IEA) Task 23 (OC3), Phase IV involved a study on the Hywind SPAR platform [36] as a joint work of multiple groups using seven different codes. On a continuation study, a semi-submersible was analysed in OC4 Task 30 Phase II [48] with an increased number of collaborators. The results were published in [49]. These studies have contributed to the understanding of the validity of various modelling approaches and their application.

Code-to-code studies are significant in understanding the effect of theories on the motions; however experiment-to-code studies are essential in validating the tools. To address this topic, comparisons of numerical data from NREL's simulation code "Fatigue, Aerodynamics, Structures, and Turbulence (FAST)" [50] and experimental data for the DeepCwind semisubmersible were published in [51]. The offshore code comparison project's fifth iteration, OC5 Phase II, includes the experiment to numerical data comparisons of the DeepCwind semisubmersible [52]. 19 participants from 11 countries were involved in the study. These works are significant in identifying areas where the codes need improvement, such as the mooring models as discussed in [53, 54].

1.4 Floating wind turbine projects

The exploration on floating wind turbines by project teams and consortia is progressing, and most of them have invested in research and development (R&D) projects. Globally, companies such as Vestas, Siemens, Areva, Mitsubishi and Fuji Heavy Industries are present in the field [55]. The involvement of these large groups shows that the floating wind turbine technology has emerged from a limited R&D status and is moving towards deployment worldwide.

In Europe, most of the offshore floating foundation technologies under development are led by the countries that have deep-water offshore potential. The European Union has set targets to obtain 20% of its energy requirements from renewables by 2020 [56, 57]. Examples to the companies working on concept development may be listed as Blue H from the Netherlands, Nass et Wind of France, GICON of Germany [58], Poseidon of Denmark, IDEOL of France, HiPRWind of Spain, Winflo of France, Hexicon of Sweden [30], and Statoil of Norway. In Japan, there are a variety of concepts considered, and most research projects are government funded [14]. In 2011, the first scale model was launched in Hakata Bay in Kyushu [59]. In 2013, a 2MW full-scale SPAR wind turbine was deployed off Choshi at the entrance of Tokyo Bay [60]. The U.S government plans to develop wind turbine technology for power generation to cover 20% of energy requirements by 2030 [61]. In the intermediate and deep-water depths, the company Principle Power, based in Seattle, is involved in the development of the WindFloat semi-submersible floating foundation concept [13, 12]. In early 2011, it was deployed at the Portuguese coast with a Vestas 2MW turbine.

1.5 Design of offshore platforms

1.5.1 Design standards

Design standards evolve according to the needs and the status of the industry. When this is considered, it is as expected that the standards dealing with offshore wind turbines are significantly new. It should be noted that offshore wind turbines differ from their onshore counterparts regarding the encountered loads. They experience significantly different environment-related conditions such as hydrodynamic loads, sea ice and extended periods of standby. Additionally, they differ from offshore oil rig platforms due to wind loads, increased shallow water effects, and also operate unmanned. For these reasons, they have to be considered accordingly, addressing all of these issues to improve confidence in their implementation.

Det Norske Veritas (DNV) and Germanischer Lloyd (GL) published the first editions of their standards for offshore wind turbines in 2004 and 2005 to address these concerns, which have been subsequently updated [44, 62]. International Electrotechnical Commission (IEC) standard IEC-61400-3 was first published in 2009 [63] as the result of a 10-year study, with a development process that started in 1999. The American Bureau of Shipping (ABS) published ABS standard #176 in 2010 [64].

Following the trend in the industry, the previous set of rules was mainly applicable to fixed-bottom offshore structures. However, they have served as a precursor to evaluating their applications for floating wind turbines as in the case of DNV standard OS-J101 [65]. Bureau Veritas (BV) issued a note concerning offshore floating wind turbines in 2010 [66] (updated in 2015 [67]), mainly addressing IEC-61400-3 and defining load cases to be tested out.

From 2012 onwards, the focus shifted to floating platforms and class societies have undertaken work to develop standards concerning floating wind turbines. DNV introduced OS-J103 [27] in 2013 with ABS providing ABS #195 guide [68]. Following the events of the Fukushima nuclear disaster in 2011, Nippon Kaiji Kyokai (ClassNK) introduced their set of rules in 2012 [69]. The work of DNV is a result of a Joint Industry Project that was initiated in September 2011 with Statoil, Navantia, Iberdrola, Alstom Gamesa, Sasebo Heavy Industries, Nippon Steel Corporation, STX, Principle Power and Glosten Associates to bring together a wider range of experience in the field [70]. IEC has also extended the standard to define design requirements for floating wind turbines [71]. The revised version aims to address the differences between floating and fixed bottom wind turbines. Considerations such as hydrostatic stability and the effect of second-order hydrodynamics on the platforms are taken into account [72, 73, 74].

For floating wind turbines, the system suffers from multiple load types that need to be accommodated while providing stability. Consequently, class societies consider that the factors in their design differ from the topics covered for bottom-fixed foundations. For instance, the hydrodynamics of the platform will need to be evaluated thoroughly in installation, operation, and accidental cases. Depending on the area, shallower water may result in higher order wave effects becoming prominent.

Longer time simulations may also be needed to capture non-linearities and slowly varying responses of the platform.

Along with these complications, one of the challenges in floating wind turbines continues to be economical [9]. To lower the costs, the need for more efficient designs becomes inevitable. For this reason, the classification standards try to incorporate cost-benefit analysis and reliability into the design process [75]. The life-cycle assessment also takes a critical part where cyclic loads lead to fatigue problems [76, 77]. As the industry gathers more experience in the field, the standards will be subsequently updated to address the concerns of safety and operation.

1.5.2 Design and optimisation studies

While the principal type (i.e., the method of stabilisation) defines the overall behaviour, the real task is revising the hull form to obtain suitable characteristics for the function and safety of the platform. In settled industries such as oil & gas, the cumulative knowledge coming from previous installations scales down the design space. In novel fields, this information does not exist. The number of possible configurations (e.g., connecting braces of a semisubmersible) is limitless, making design a rather broad topic to investigate.

Novel designs in areas such as wind energy present similar challenges faced by the offshore oil and gas industry in its earlier years. For instance, a comparison of second generation semisubmersibles to the fifth gives an idea on how the hulls have consolidated to their current form over a 50-year period. A similar progression is possible for wind turbine platforms. However, at this stage, there is a significant number of unknowns, and the most appropriate solution is undecided. The industry lacks the experience as the number of installations is limited, and the proposed platform designs show considerable differences. As examples, the WindFloat semisubmersible is based on three cylindrical columns joined with braces [13, 12] while a braceless V-shaped alternative with prismatic columns is studied in [15]. Similarly, there have been numerous studies on single column variations [78, 79] with pontoons based on the SeaStar design [20, 21]. Conversely, the GICON TLP [58] and the model presented in [80] focus on forms where the hull is closer to the four column tension-leg designs with certain modifications and adaptations.

At the early design stages where the number of unknowns is rather high, [81] advocates the use of spreadsheet-type calculations and closed-form equations to avoid dealing with complicated computer aided design (CAD) systems. Several authors follow this advice in design [79, 45], and up-scaling [82, 83] studies. It is a reasonable approach considering that obtaining the values of necessary variables often requires multiple commercial software (e.g., a finite element model for the mass matrix and a panel method code for hydrodynamics) that will deliver the three-dimensional (3D) hydrodynamic model. This significant investment of time and resources may not pay off for that design. Still, a shortcoming of this method is that the precision is lower barring basic hull shapes with known analytical solutions.

For optimisation processes of a hull form, the initial works using parametrised dimensions as inputs to panels methods presented in 1996 [84] have evolved in years [85] as the computational power increased. These studies in oil & gas platforms have also been applied as a solution to wind turbine platforms [86] and used particularly for a tension leg platform [78]. In this approach, several parameters (e.g., platform depth, member diameter) are selected as variables and the hull shape is altered inside the design space with the defined constraints. Then, a series of geometries are created to evaluate the desired performance characteristics. In most cases, there are simplifications introduced to make the model manageable such as omitting the connecting braces of multi-body structures [87]. With the advance in computer sciences, a third alternative emerged: using genetic algorithms [88] and variations of other similar approaches [89]. The primary advantage stated by this third method is the lower computational requirement compared to loop-type calculations [88].

An aspect seen in the previously published hydrodynamic design studies is that they do not emphasize the changes in mass and inertia values due to the alterations of the hull form (e.g., [84, 90, 91]). The weight is addressed partially through assumptions since it is easier to calculate without CAD software compared to inertial values of arbitrary shapes. Hence, research focuses solely on the heave mode (e.g., [85, 92, 93]). However, the responses of the platform are reliant on the six by six mass matrix with the inertial values being particularly important in determining the tendon tensions of a TLP. The pitch and roll modes are associated with the change in mooring forces and moments: a miscalculation in the mass matrix will clearly lead to errors in the estimations of motions and loads. This topic is partially addressed in a simplistic manner. A study published in 2015 includes the structural weight as an optimisation variable through statistics-based calculations for a semisubmersible, while inertia is not mentioned [93]. Both mass and inertia are discussed in [92], taken as a percentage of the main dimensions without explaining the rationale. Similarly, the centre of gravity is chosen with an assumption. It should also be stressed that statistics aren't available in novel fields such as wind turbine platforms as the number of installations is rather low and hull forms differ significantly. These topics are revisited when evaluating the design practices with the discussion expanded to include the limits in motion predictions.

1.6 Motivation and objectives

Novel areas such as the floating wind turbine platforms are open to the development of new concepts. Conversely, in settled industries such as the oil and gas, optimisation to improve the performance of existing hull forms is in focus. As most software is built with the latter goal in mind, they leave a substantial gap between these two cases which needs to be attended.

This dissertation addresses the topic by developing a flexible, fast, and integrated framework that covers the requirements of a platform's hydrodynamic design. The use of three dimensional models from the beginning is suggested for that purpose. When necessary, external codes will be implemented to solve particular problems. In those cases, the system is to act as a moderator to arrange the platform configuration, calculate and provide the input data, and deal with the exchange of infor-

mation. The setup will comprise several modules where each one can be updated and extended to cover alternative solutions. This approach will make it possible to add new modules to extend areas of application. The outcome is to offer higher precision, reduced probability of errors, and lower time investment in the stages from the conception of an idea to getting the motion dynamics. Removing the human factor from the calculation part of the design will allow relocating this resource to creativity and innovation.

1.7 Layout

Following the introduction, Chapter 2 gives the concepts and theoretical background that form a basis of knowledge. Ocean wave kinematics, hydrodynamic theories, and wind loads are discussed. The implementation of mooring line dynamics into the numerical models is explained along with the coupled system analysis. The section helps to understand the necessities for the design process by identifying the required variables.

After providing the theory, the time domain code is introduced in Chapter 3 by comparing numerical results to experimental data for a semisubmersible platform. The comparison serves to understand the accuracy of the code's estimations. Once this information is known, Chapter 4 looks at the possibility of geometrical simplifications of the platform to clarify the level that they can be implemented in early design stages.

Chapter 5 evaluates the level of uncertainty in the motion predictions regarding the hydrodynamic and mooring models. User's role in possible errors is also discussed. This topic is addressed through the removal of blunder-type mistakes in Chapter 6 where the method of automating the time domain code's functions for model building and sequential simulations is presented.

The development of a multi-purpose 3D model for mass properties and hydrodynamic calculations is explained in Chapter 7. The description starts by discussing geometry development in a format compatible with potential flow calculations. Then, it goes through the estimation of mass properties from the same multi-purpose mesh. The results are validated using specialised commercial software. This tool is integrated into the system in Chapter 8 on a worked example for a tension leg platform with a 5 MW turbine. The platform's development stage is illustrated in a step-by-step approach. Both frequency and time domain assessments are provided, and their differences are evaluated. The responses of the TLP in an installation area are studied taking safety into consideration.

Chapter 9 discusses a specific problem of floating wind turbines under damage. As floaters are compliant in more modes compared to fixed-bottom counterparts, they can be subjected to loads that result in unexpected large amplitude responses. This case is exemplified through the yaw motions of the semisubmersible platform in aligned head seas and wind. Emphasising the effect of likely damage here serves to remind that the initial design should also be made robust to counter these complications. The final discussion in Chapter 10 concludes the work and evaluates future possibilities.

Theoretical Background

The study of a floating wind turbine's behaviour is a multidisciplinary area that encompasses aerodynamics, structural mechanics, hydrodynamic responses, and mooring line dynamics. The coupling between the methods of calculation is as crucial as their individual performances. A sophisticated code for the calculation of wave forces will not serve the purpose if it cannot be integrated with the other components. Hydrodynamics, aerodynamics, and mooring line dynamics should be covered conjointly. The following section is discussed from this point of view. First, an account of the ocean waves, hydrostatics, and hydrodynamics is given. Then, wind turbine aerodynamics and wind forces are examined, and methods to calculate the mooring line responses are summarised. At the platform's design stage, some of these components become input parameters. The floater is designed to host a known rotor nacelle assembly (RNA) and tower. Hence, the target is to accommodate a defined setup and provide favourable operational conditions for power generation.

2.1 Ocean waves

Several wave theories describe the behaviour of ocean waves. Their regions of applicability depend on the relative depth and wave height as summarized in [94]. The Airy waves [95] (linear theory) and higher order Stokes Finite Amplitude are common applications for offshore structures (e.g.[96]). The list includes others such as Cnoidal and solitary waves.

The linear theory describes a regular sine wave. Hence, the crest and the trough amplitudes are equal. The free surface profile of the a wave (η) as a function of space (x) and time (t) is given with the following equation:

$$\eta(x, t) = \frac{H}{2} \sin(kx - \omega t) \quad (2.1)$$

In Equation 2.1, H represents the wave height equal to twice the wave amplitude (η). The wave frequency is ω and k is wave number. Their formulations depend on the relative water depth. By differentiating Equation 2.1 with respect to time, the velocities and the accelerations of the wave can be calculated and related to the forces acting on the structure.

The linear theory allows to represent the sea states of irregular waves as a linear sum of i regular components through superposition [97]. The phase shift of each component is represented by ϵ_i :

$$\eta(t) = \sum_i \eta_i \sin(\omega t - k_j x + \epsilon_i) \quad (2.2)$$

When the wave height to water depth ratio increases, the behaviour changes and the crest amplitude becomes larger in comparison to troughs. At higher steepness, the Stoke's higher order wave theories [98] replace the linear theory. In the case of a second-order representation, each wave component contains first and second order terms. The particle accelerations and velocities are calculated accordingly.

Ultimately, the choice of the theory depends on the relative wave height, water depth, and the case at hand. Airy waves have the advantage of being a linear solution, making an arbitrary superposition of multiple components possible. The seaway and the associated response effects can be decomposed into harmonic components and spectral analysis can be applied. The linear theory can also be modified through wave stretching formulations to represent waves above the mean water level with alteration such as the Wheeler's stretching [99]. Higher order waves are recommended for mooring and riser analysis, drag dominated structures, storm waves, and air gap analysis [81]. Linear theory is given as a preference in low sea states, fatigue analysis, long-term statistics, and inertia dominated structures.

2.2 Representation of sea states in the frequency and time domain

The sea state needs to be represented as a power spectrum to carry out the calculations in the frequency domain. The spectral amplitude per oscillation period characterises the wave conditions. The Pierson-Moskowitz, ISSC, and Joint North Sea Wave Observation Project (JONSWAP) [100] are well-known single peaked spectra in this regard. In the simultaneous presence of swell and wind sea or when a changing wind direction creates a developing wave system, double peaked alternatives represent the sea states better [101, 102].

In this list, the Pierson-Moskowitz and the JONSWAP models are closely related. The latter uses a peak enhancement factor (γ) to express sea states that are not fully developed with the following formulation:

$$S_i(\omega) = \frac{\alpha g^2}{\omega^5} \exp \left[-\frac{5}{4} \left(\frac{\omega_p}{\omega_i} \right)^4 \right] \gamma^r \quad (2.3)$$

$$r = \exp \left[-\frac{(\omega_i - \omega_p)^2}{2\sigma^2\omega_p^2} \right] \quad (2.4)$$

$$\alpha = 0.076 \left(\frac{U_{10}^2}{xg} \right)^{0.22} \quad (2.5)$$

$$\omega_p = 0.076 \left(\frac{xg}{U_{10}^2} \right)^{\frac{1}{3}} \quad (2.6)$$

The α parameter in Equation 2.3 is 0.07 when the ω is smaller than the peak frequency (ω_p) or 0.09 otherwise. The fetch is x , and U_{10} is the wind velocity 10 meters above the sea surface. The parameters of the JONSWAP spectra depend on the significant wave height and peak periods. For a fully developed sea, the JONSWAP spectra equal to the Pierson-Moskowitz using a peakedness factor of unity ($\gamma = 1.0$).

Time domain calculations and frequency domain spectra relate to each other through Fourier transforms. The Cooley-Tukey fast Fourier transform (FFT) is an algorithm for this purpose, with examples of application in software such as the SIMO-Riflex [103]. This work utilises NREL's FAST [50] for the time domain solution which explains its FFT implementation as follows [104]:

$$\eta(t)|_{t=n\delta t} = \frac{1}{N} \sum_{k_s=-\frac{N}{2}+1}^{N/2} W[k_s] \sqrt{\frac{2\pi}{\delta t} S_{\eta}^{2\text{-sided}}(\omega)|_{\omega=k\Delta\omega}} e^{j\frac{2\pi k_s n}{N}} \quad (2.7)$$

In Equation 2.7, j is the imaginary number $\sqrt{-1}$. To represent the sea state in time domain simulations, n and k_2 are the discrete-time-step and discrete-frequency-step counters. The number of discrete steps is N . Sampling theory defines the relation between them:

$$N = \frac{2\pi}{\Delta t \Delta \omega} \quad (2.8)$$

Accordingly, the length of simulation time and the detail that is obtained from a frequency-domain analysis are related.

2.3 Hydrostatics and upright stability

The hydrostatic restoring force provides stability in catenary moored structures. It is also relevant to the platform motions and the natural frequencies as it contributes to the overall stiffness. The buoyancy force on a floating structure acts on the centroid of the displaced fluid. Assume that the structure can be decomposed into n partial volumes:

$$\nabla = \sum_{i=1}^n \nabla_i \quad (2.9)$$

The centroids of the volumes in x , y , and z axes can be calculated with reference to the keel (K) to find the position of the centre of buoyancy:

$$(x_b, y_b, z_b) = \left(\frac{\sum_{i=1}^n \nabla_i x_i}{\nabla}, \frac{\sum_{i=1}^n \nabla_i y_i}{\nabla}, \frac{\sum_{i=1}^n \nabla_i z_i}{\nabla} \right) \quad (2.10)$$

In static equilibrium, the buoyancy force opposes the weight acting at the centre of gravity G , and both forces act on the same vertical line. As the structure rotates, the underwater geometry changes and the centre of buoyancy is displaced. The new action line of the buoyancy force intersects the previous one at the metacentre M . The distance between this point and the centre of gravity, GM , shows the initial stability of the structure. When the value is positive, the floater is stable in its given position. When this value is negative, the structure will rotate until a static equilibrium point is reached unless it is held in position with other factors such as the mooring lines. The metacentric height is defined using the following parameters:

$$\overline{GM} = \overline{KB} + \overline{BM} - \overline{KG} \quad (2.11)$$

The Equation 2.11 requires the knowledge of the position of the centre of gravity $CG = (x_g, y_g, z_g)$. The BM depends on the inertia of the waterplane and is calculated as follows:

$$BM = \frac{I_{ij}^w}{\nabla} \quad (2.12)$$

In Equation 2.12, the term I_{ij}^w represents the waterplane area moments after replacing the subscript ij with xx for rolling and yy for pitching. The x and y -axes are defined as the longitudinal and transverse axes respectively. If the intersection of the waterplane and the structure results in a cross-section with an elementary shape (e.g., a disc or a rectangle), they can be calculated through analytical formulae. Conversely, a generalised numerical solution requires a different approach. When it is possible to define the waterplane as a closed polygon with known vertices $V(x_i, y_i)$, the second moment of an area can be calculated with:

$$I_{xx} = \frac{1}{12} \sum_{i=1}^n (y_i^2 + y_i y_{i+1} + y_{i+1}^2) (x_i y_{i+1} - x_{i+1} y_i) \quad (2.13)$$

$$I_{yy} = \frac{1}{12} \sum_{i=1}^n (x_i^2 + x_i x_{i+1} + x_{i+1}^2) (x_i y_{i+1} - x_{i+1} y_i) \quad (2.14)$$

$$I_{xy} = \frac{1}{12} \sum_{i=1}^n (x_i^2 + x_i x_{i+1} + x_{i+1}^2 + y_i^2 + y_i y_{i+1} + y_{i+1}^2) (x_i y_{i+1} - x_{i+1} y_i) \quad (2.15)$$

The hydrostatic forces also affect the motions of the structure through the restoring coefficients. When a unit normal to the hull surface is defined as $n = (n_1, n_2, n_3)$ and the wetted area is defined as S_b , the restoring coefficients at the equilibrium position are calculated in a generalised form [105]:

$$C_{33} = \rho g \iint_{S_b} n_3 dS \quad (2.16)$$

$$C_{34} = \rho g \iint_{S_b} y n_3 dS \quad (2.17)$$

$$C_{35} = -\rho g \iint_{S_b} x n_3 dS \quad (2.18)$$

$$C_{44} = \rho g \iint_{S_b} y^2 n_3 dS + \rho g \nabla z_b - mg z_g \quad (2.19)$$

$$C_{45} = -\rho g \iint_{S_b} x y n_3 dS \quad (2.20)$$

$$C_{46} = -\rho g \nabla x_b + mg x_g \quad (2.21)$$

$$C_{55} = \rho g \iint_{S_b} x^2 n_3 dS + \rho g \nabla x_b - mg z_g \quad (2.22)$$

$$C_{56} = -\rho g \nabla y_b + mg y_g \quad (2.23)$$

In Equation 2.16, the heave, roll, pitch, and yaw are denoted by the subscripts 3, 4, 5, and 6 respectively. Figure 2.1 clarifies the numbering in relation to the Cartesian coordinates. The remaining hydrostatic restoring terms are zero. The waterplane area and inertial terms, the centre of gravity, and the submerged volume are required variables to obtain the restoring matrix. The coupling between roll and yaw (C_{46}) for structures with a longitudinal offset between the centres of gravity and buoyancy should be noted. This case holds true for most horizontal wind turbine systems (e.g., NREL 5 MW turbine on any of the DeepCwind platforms [33]).

The prominence of the restoring terms in the motion dynamics of the structure depends on its type. For semisubmersibles and SPARs that rely on buoyancy and ballast, the hydrostatic restoring and upright stability are critical. In a tension leg platform, while they still play a role, the stiffness in restricted modes is mostly provided by the mooring lines.

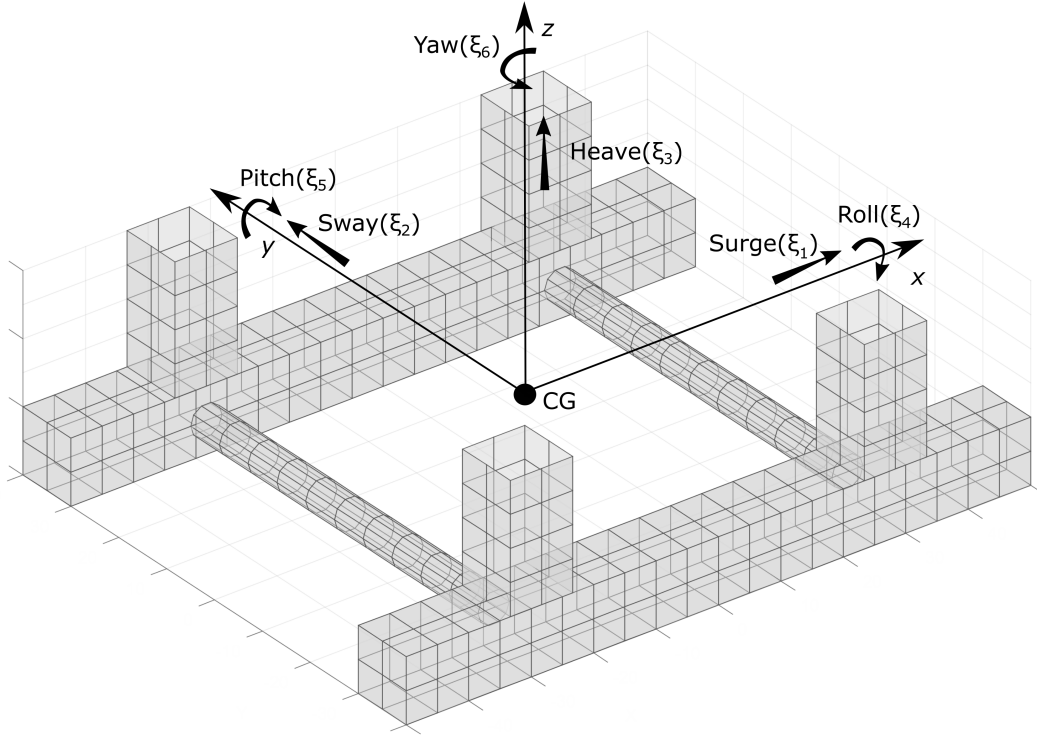


Figure 2.1: The axes, coordinates and the numbering system used to represent the platform motions about the centre of gravity (CG)

2.4 Potential flow theory

The potential flow hypothesis considers specific boundary values to solve the hydrodynamic problem. It is a set of simplifications over the real flow of a fluid. While higher order solutions are available, at concept design stages, the linearised solution can provide the preliminary information to assess the behaviour of a structure in waves [106]. Certain conditions apply to the water properties and kinematics to reduce the problem and manage complexity. The variability of the density can be omitted to define an incompressible and homogeneous fluid. It may also be assumed that the fluid is inviscid, imposing no vorticity. This approach is justified since water viscosity is small and the flow irrotational over a large extent of the domain of the hydrodynamic problem. For smaller waves, the ripples on the surface of the water are also small and will not cause significant hydrodynamic forces. For larger waves, the prominent factor is replaced by gravity. Hence, the surface tension is of low practical importance and can be neglected. Considering these limitations, the following formulations emerge:

- If the fluid is homogeneous and incompressible then the equation of conservation of mass reduces to the equation of continuity:

$$\frac{\partial u}{\partial x} + \frac{\partial v}{\partial y} + \frac{\partial w}{\partial z} = 0 \quad (2.24)$$

where u , v and w are the fluid velocity vectors in x , y , and z axes.

- If the fluid is inviscid then it is also irrotational (i.e. there is no vorticity, or it remains constant) and the fluid velocity vector may be represented by a scalar function: the velocity potential. In Equation 2.25, ∇ stands for the gradient operator, \vec{V} is the velocity vector and Φ is the velocity potential:

$$\vec{V} = \nabla\Phi \quad (2.25)$$

Under these assumptions, the hydrodynamic problem is formulated in terms of the potential flow theory. This means that the velocity vector of the fluid particles may be represented by the gradient of a velocity potential as in Equation 2.25. The fluid velocity potential reduces the continuity equation to the Laplace equation:

$$\nabla^2\Phi(\vec{x}_0, t) = \frac{\partial^2\Phi}{\partial x^2} + \frac{\partial^2\Phi}{\partial y^2} + \frac{\partial^2\Phi}{\partial z^2} = 0 \quad (2.26)$$

Once the velocity potential is known, the determination of the fluid pressure may be carried out according to the Bernoulli equation:

$$p(\vec{x}_0, t) = -\rho \left(\frac{\partial\Phi}{\partial t} + \frac{1}{2}|\nabla\phi|^2 + gz_0 \right) \quad (2.27)$$

In the Equation 2.27, $p(\vec{x}_0, t)$ represents the fluid pressure, ρ shows the fluid specific mass and g is the acceleration of gravity. Integration of fluid pressures over the wetted surface results in the hydrodynamic forces acting on the hull.

The solution for the Laplace equation can be obtained when the boundary conditions are defined. The rigid-body surface boundary condition states that the fluid does not penetrate the hull and there are no void spaces between the fluid and the surface. The free surface boundary condition defines that the velocity potential must satisfy the kinematic and dynamic boundary conditions. The kinematic boundary condition implies that on this free surface, the vertical velocity of the fluid has to equal to the velocity of the same surface. There's no splashing of the water, and all particles on the surface have the same velocity. The dynamic free surface boundary condition states that the fluid pressure at the sea surface is given by the dynamic equation (or the Bernoulli Equation) for irrotational flow. The sea bottom boundary conditions state that the seabed is at a long distance from the free surface. Therefore, it is not affected by the motions. It is also defined as the deep water condition. The radiation conditions at infinity state that the effect of the movements of the fluid at an infinite distance from the vessel tends to zero, and therefore it may be taken as zero. To obtain a linear solution, $\Phi(\vec{x}_0, t)$, is divided into two components, namely the steady flow ($\bar{\Phi}$) and the oscillatory flow ($\tilde{\Phi}$) and expressed as:

$$\Phi(\vec{x}_0, t) = \Phi(x + Ut, y, z, t) = \bar{\Phi}(\vec{x}) + \tilde{\Phi}(\vec{x}, t) \quad (2.28)$$

The unsteady term ($\tilde{\Phi}(\vec{x}, t)$) can be linearised and decomposed into incident (incoming) waves (Φ^I), diffracted waves (Φ^D) and radiated waves (Φ^R):

$$\tilde{\Phi} = \Phi^I + \Phi^D + \Phi^R \quad (2.29)$$

The radiation potential is related to each of the six oscillatory motions:

$$\Phi^R = \sum_{j=1}^6 \Phi_j^R, \quad j = [1, 6] \quad (2.30)$$

After the linearisation, application of the boundary conditions and the Bernoulli equation, the forces on the structure are obtained using an appropriate method. The exciting (F^E), radiation (F^R) and the hydrostatic forces (F^H) are then deducted for motion calculations.

2.5 Calculation of wave loads on the structure

The hydrodynamic forces are a vector superposition of their components found by integrating the water pressure field over the hull using a suitable approach. The selection of the method depends on the relative size of the structure compared to the wavelength, and the flow regime. The Morison Equation [107] is an empirical formulation that assumes the structure is small enough to not disturb the wave field around it. For larger structures, the diffraction/radiation components need to be considered as the presence of the platform will change the wave field. A breakdown of the pressure effects on floating structures may be listed:

1. The Froude-Krylov force: due to the undisturbed incident waves;
2. Radiation component and their related hydrodynamic added mass and potential damping forces: due to the relative acceleration and velocity between water particles and structural components in an ideal fluid;
3. Diffraction component: caused by the diffracted waves due to the presence of the structure.

When the exciting forces and the hydrodynamic coefficients acting on the structure are known, they are included in the equations of motion obtain the responses.

2.5.1 The Morison Equation

Structures that are assumed to not disturb the wave field around them can be referred as “hydrodynamically transparent” bodies. In such cases, the diffraction component in Equation 2.29 becomes negligible, the pressure distribution due to waves on the surface becomes complex, and the flow forms vortices in the vicinity. Morison’s empirical formulation serves to calculate the loads on these

structures by presenting them as a breakdown of their drag and inertia components. For a unit length of vertical pile, the formula is given as follows:

$$F = \rho C_M \frac{\pi D^2}{4} \dot{u} + \frac{1}{2} \rho C_D |u| u \quad (2.31)$$

where D is the pile diameter, F is the horizontal force per unit length, and u is the horizontal water particle velocity. The over-dot signifies differentiation with respect to time. The C_M and the C_D are the empirical inertia and drag coefficients. Their values depend on several factors such as the member shape, flow regime, and surface roughness. The flow regime is evaluated by the use of two dimensionless parameters: the Keulegan-Carpenter (KC) and the Reynolds (Re) numbers. While the Reynolds number represents the ratio of the inertial and viscous forces, the KC number describes the relative importance of the drag over inertia forces. Accordingly, the total force can be classified as inertia or drag dominant. The following formulae define the KC and Re numbers:

$$Re = \frac{uD}{\nu} \quad (2.32)$$

$$KC = \frac{uT}{D} \quad (2.33)$$

where ν is the kinematic viscosity of the water, T is the oscillation frequency and D is the member diameter. Sarpkaya and Keulegan [108, 109] published the hydrodynamic coefficients under various conditions through a series of experiments on scaled models. Once these values and the water kinematics are known, the forces are calculated through Equation 2.31. For members with inclination angles this formula needs to be generalised to include relevant particle velocities and accelerations [96]. For smooth cylinders, earlier experimental results state that the Morison equation can obtain accurate results [110]. However, recent studies also discuss discrepancies in floating wind platforms [58] as the hull sizing inevitably increases with the turbine's power.

2.5.2 Hydrodynamically compact structures

The solution proposed by Morison assumes that the structure (or the structural member) is small enough to allow undisturbed passage to the wave. These types of structures can be described as hydrodynamically transparent. The diffraction parameter clarifies whether this is the case:

$$\frac{\pi D}{L_w} \quad (2.34)$$

where L_w is the wavelength. For diffraction parameters larger than 0.5 the flow separates from the structure, and the Morison Equation is applicable for the calculations, and the potential flow assumption is rendered invalid. The Keulegan-Carpenter and the Reynolds numbers define the flow regime as drag or inertia dominant.

Conversely, the structure can be considered as hydrodynamically compact when the diffraction parameter is above 0.5. Under this scenario, the flow remains attached to the surface of the structure. Hence, it makes it possible to obtain a solution to the pressure field by breaking it down into the wave scattering, radiation, and diffraction components as given in Equation 2.29.

Calculations that assume the structure does not distort the wave field (i.e., the undisturbed incident wave) give the Froude-Krylov force acting on it. However, in practice, when a comparably large object encounters the wave, it alters its form in the vicinity. This type of flow behaviour fits the limitations given by the potential flow theory. Approaches such as the boundary element method (BEM) method provide a numerical solution to the problem. They require a 3D description of the underwater geometry up to the mean water level. The body can be discretized using panels described by the coordinates of their vertices. Once the geometry and the velocity potential are known, the pressure at the geometric centre of each panel is obtained from the linear term of the Bernoulli equation. The pressure field leads to the forces and moments in the six degrees of freedom, computed as an integration over the structure's surface.

Along with the diffracted and scattered waves, the moving structure causes the surrounding water to form radiating waves. The resulting pressure fields on the surface are associated with each mode of motion. Similar to the diffraction potential, when these forces are integrated over the body of the structure, their respective forces lead to the added mass and damping coefficients. The component in phase with the velocity relates to the potential damping value while the term in phase with the acceleration gives the added mass. Their magnitudes depend on the oscillation frequency.

The discretization of a body signifies that the number of panels needs to be adequate for the calculations to converge. The Haskind relationship provides what is known as a far-field solution for verification. The exciting force is calculated from the radiation potential, and the agreement between the near and far field solutions serve as an accuracy checkpoint.

2.6 Wind loads

Wind loading on turbines and the related control dynamics have a complex interaction. At a platform's concept design stage, the most relevant factors are the ones that directly affect the coupled hydrodynamic behaviour. For instance, the study of the blade pitching angles in turbulent wind is essential for control systems. However, their reflection on the platform dynamics are functions of the resulting thrust and wind forces due in the implemented setup. In this sense, the pitch angles of the blades themselves assume a secondary position. The following sections examine the wind loads from this point of view.

2.6.1 Wind resource

Inter-annual, annual, diurnal, and short-term (gust and turbulence) are categories that characterize the change of wind speed in time [111]. Inter-annual variations occur over time scales greater

than one year and are important in assessing the long-term wind resource in an area. There are also changes in wind speeds in an annual time frame as a result of seasonal deviations. Similarly, on land, an increase in wind speeds at day times, and a decrease at night time is common as a reflection of diurnal differences. The largest daily changes occur in spring and summer. Short-term fluctuations include turbulence and gusts and refer approximately to a 10 minute time interval. Turbulence explains continuous random wind speed changes in time while gusts are discrete events within the wind field. In turbulence, the wind can have a relatively constant mean value over time periods for an hour or more. Conversely, within shorter timescales of a minute or less, it is variable.

Turbulence intensity (TI) is an elementary measure of the wind behaviour. It is given as the ratio of standard deviation of the wind speed (σ_u) to its mean value (U):

$$TI = \frac{\sigma_u}{U} \quad (2.35)$$

Frequently, its value is between 0.1 to 0.4 where lower wind speeds result in higher turbulence intensity. Similar to waves and other stochastic processes, the wind can be represented in the form of a power spectrum. The DNV guidelines suggest [27] Kaimal's formulation to simulate wind turbine loads. Another well-known definition of wind behaviour is based on the von Karman spectrum which was first discussed in the 1957 NACA report [112].

In a 3D wind field, the speeds vary as a function of space and time where the velocity increases with the altitude. This change is described with the logarithmic and power laws with the latter being formulated as:

$$\frac{U(z)}{U(z_r)} = \left(\frac{z}{z_r} \right)^\alpha \quad (2.36)$$

In Equation 2.36 the $U(z)$ term is the wind speed at height z and the $U(z_r)$ term is the wind speed at z_r . The power law exponent is denoted by α .

2.6.2 Wind loads on the rotor and tower

The Blade Element Momentum and Generalised Dynamic Wake theories are two of the prominent approaches in modelling the wake for turbine aerodynamics. The Blade Element Momentum theory has its roots at the beginning of the 20th century and is implemented into NREL's FAST [113] also in its recent version. It is a combination of the blade element and momentum theories that assumes the blades can be divided into several elements along its span. The aerodynamic forces on these sections can be calculated based on the local flow conditions. These values are integrated along the blade to obtain the forces and moments acting on the turbine. The effect of the momentum loss and the induced velocities are considered through the momentum part of the theory, and included in the summed forces. The two theories are coupled to provide the total aerodynamic loads and induced velocities near the rotor. One theoretical limitation is the assumption that the blade is two-dimensional

which overlooks the spanwise flow. Additionally, the airfoil induced velocities are accepted to be instantaneous while, in reality, include a delay [114]. Some of these simplifications are revised through adding corrections such as the Prandtl model to adjust for the hub and tip losses [115].

In operation, the complexity of wind turbine aerodynamics and control systems also give rise to instantaneous dynamic problems. In a turbulent wind field, the momentary change in the lift and drag coefficients due to the varying angles of attack is explained as the dynamic stall phenomenon. Beddoes-Leishmann [116] proposed a semi-empirical model to account for these variations.

Besides the turbine and the rotor, the tower also influences the airflow behind it. This is a significant effect for downwind turbines. In upwind turbines, the flow changes as each of the blades passes in front of the tower. Additionally, the tower is exposed to wind pressure, especially in storm conditions. The resulting force is termed the tower drag. It can be treated with the use of a drag coefficient.

2.7 Mooring line dynamics

The mooring lines provide the station-keeping capabilities of the wind turbine platforms, and their behaviour affects the motion dynamics. Ultimately, the connection between the seabed and the fairleads should counteract the wind, wave, and current loads for the structure to remain in position. There are two main types of mooring line configurations: catenary and taut.

Catenary mooring lines hang freely from the fairleads and are subjected to low vertical tension. They carry horizontal loads since a part of the line lies on the seabed. They provide limited restoring term contribution to platform motions. Without external loads, the mooring force applied to the platform is equal to the force required to revert the lines to their free-hanging position. The restoring provided by catenary lines has limited contribution to the platform's stability. Hence, catenary moored structures should rely on either ballasting or hydrostatic restoring terms. The mooring lines' initial shape can be altered by adding weights and buoys along its length. In this case, their dynamics become more complex. The connection to the seabed may rely on drag type anchors.

As opposed to the catenary mooring, taut lines carry significant vertical and horizontal tension. Their contribution to the total restoring force is a function of their elasticity properties. In heave, pitch, and roll this addition to hydrostatic restoring may be high enough to result in platform behaviour that resembles fixed structures. The natural frequencies of the structure increase in the restricted modes of motion. Compared to catenary applications, taut mooring provides an advantage in deeper waters as shorter lines are required. A disadvantage is the complexity of the anchors that connect to the seabed. Piles, suction buckets, and plate anchors are recommended anchoring options.

The mooring line material can be metallic, or synthetic. Steel chains and wire ropes are regularly used in offshore platforms. As the depth increases, the weight of the steel chains may start to

present a problem. In that case, the lighter rope-type material comprising strands become preferable. Compared to metal, these synthetic materials have the advantage of providing better corrosion resistance.

The mooring's responses can be obtained through quasi-static and dynamic approaches. The basic premise of the quasi-static calculations is negligible inertial forces and seabed friction [117]. Only the normal drag forces are considered while tangential drag along the line is neglected. It is accepted that the Morison Equation suffices to describe the hydrodynamic drag forces on the mooring line elements. One implementation in Mooring Analysis Program (MAP++) used in NREL FAST is a multi-segmented quasi-static model [118]. In dynamic models, the lines are expressed as a sum of segments where the inertia and drag forces on each element are taken into consideration. Therefore, added mass and damping both become factors in response calculations [119]. Finite elements method (e.g., [120]) and lumped mass [54] are both implementations available in FAST. The differences between these models have been evaluated by various authors over the years [121, 47] and revealed that dynamic applications fare better against experimental data [122].

2.8 Coupled motion dynamics of wind turbine platforms

The coupled motions of the floater require the knowledge of exciting forces and the hydrodynamic coefficients. Hydrostatic and restoring stiffness will constitute the restoring terms. The platform motions can be obtained as a six degree of freedom system:

$$m_k \ddot{x}_k + \sum_{l=1}^6 (A_{lk} \ddot{x}_l + B_{lk} \dot{x}_l + C_{lk} x_l) = F_k \exp(-i\omega t); \quad k = 1, 2, \dots, 6 \quad (2.37)$$

In Equation 2.37, the mass matrix is denoted by m_k . The added mass and damping coefficients are A_{lk} and B_{lk} respectively. The restoring matrix C_{lk} is a sum of hydrostatic and external terms. For a linear solution to the problem, the motions and forces are accepted to be harmonic. For a motion amplitude X_k with a phase of ϵ_k , the solution is written:

$$\sum_{l=1}^6 [-\omega^2 (m_{kl} + A_{kl}) - i\omega B_{kl} + C_{kl}] X_l \exp(i\epsilon_l) = F_k; \quad k = 1, 2, \dots, 6 \quad (2.38)$$

Decomposing Equation 2.38 list the variables of the design stage. The inertial terms require the 6×6 mass matrix. For a floating wind turbine, the significant components of the total mass (m_s) are the masses of the platform (m_p), nacelle (m_n), rotor (m_r), and the tower (m_t) including their coupling terms.

$$[m_s]_{6 \times 6} = [m_r]_{6 \times 6} + [m_p]_{6 \times 6} + [m_n]_{6 \times 6} + [m_t]_{6 \times 6} + [m_c]_{6 \times 6} \quad (2.39)$$

The added masses can be obtained from tabular data for a hydrodynamically transparent structure. For hydrodynamically compact structures, a possible solution to the radiation problem is using a viable approach such as the panel method. The damping term includes the potential and viscous components. For structures that contain larger and smaller structural elements, a hybrid approach may be developed by adding the contributions of Morison-elements to the values of potential flow calculations.

The total restoring terms of the matrix C_t are a sum of the stiffness provided by the hydrostatic C_h forces and the mooring lines C_m . They are written in their matrix forms including their couplings:

$$[C_t]_{6 \times 6} = [C_h]_{6 \times 6} + [C_m]_{6 \times 6} \quad (2.40)$$

Considering symmetry, both components will have zero value terms. The sum of external forces F_t will contain the excitation from the aerodynamics F_a and hydrodynamics F_h :

$$[F_t]_{6 \times 6} = [F_a]_{6 \times 6} + [F_h]_{6 \times 6} \quad (2.41)$$

There are additional possibilities such as ice loading, earthquakes, and accidental loads. While their presence is acknowledged, these cases are not discussed. Hence, the minimal requirements obtain the motions are summarised as follows:

1. The mass matrix
2. Aerodynamic and hydrodynamic exciting forces
3. Hydrostatic restoring terms
4. Mooring system stiffness
5. Hydrodynamic coefficients

Having these values, the wind turbine platform responses can be evaluated in both frequency and time domains. The time domain solution opens up the possibility of treating the variables non-linearly while frequency domain approaches offer faster solutions to the problem.

Comparison of time domain simulations and experimental data for a semi-submersible

3.1 Introduction

This chapter compares numerical and experimental data for a semi-submersible offshore wind turbine, in partial repetition of the data published by [39]. The differences are emphasised when necessary. The primary goal of the chapter is to verify the implementation and model building practices as opposed to validating the time domain code (FAST) itself. Regarding FAST, which is used in this work, the latter is a topic that is readily available in the literature [51, 123].

The floater is the DeepCwind semi-submersible [48]; however, the turbine setup is different than the reference NREL 5MW turbine [33]. It is explained in [39] that building a scaled geometric model of the NREL 5 MW system led to differences in aerodynamics due to scaling problems of the Reynolds number. The authors of that study addressed the problem by making a thrust-equivalent turbine that forgoes geometric similarity of the blades. The rationale behind this approach is that having an accurate model of the forces at the rotor leads to similar platform motion dynamics.

The data set includes the isolated linear wind and regular wave effects to evaluate the aerodynamic and hydrodynamic subroutines of the time domain code in a controlled manner. These conditions form the basis for stochastic environments and clarify the standing of the code in terms of motion prediction capabilities. For this work, the hydrodynamics module of the time domain code was modified to include the viscous damping values measured at MARIN, taken from the reference

Published in: E. Uzunoglu and C. Guedes Soares. Comparison of numerical and experimental data for a DeepCwind type semi-submersible floating offshore wind turbine. In C. Guedes Soares, editor, *Renewable Energies Offshore*, pages 747–754. Taylor & Francis Group, London, UK, 2015. ISBN 978-1-138-02871-5

study [39]. It is also examined whether the vibration mode shapes of the tower need to be redefined with higher order polynomials to represent experimental data accurately.

3.2 An overview of FAST

FAST is a time domain aeroelastic computer-aided engineering tool for horizontal axis wind turbines, developed by the National Renewable Energy Laboratory (NREL) in the USA [124]. It brings together different modules that deal with aerodynamics, hydrodynamics, structural models and control systems in a framework referred as FAST.

Up to the seventh version, the hydrodynamic and aerodynamic calculations were carried out by the HydroDyn and AeroDyn, respectively. The portion of the code that evaluated the servo-elastic dynamics was termed FAST. It also acted as a driver code that provided the interaction between the other modules. As of the eighth version of FAST, this is no longer the case. The FAST module itself is reduced to a driver code, and each part of the calculation is carried out by its respective submodule. This approach helps codes regarding flexibility, maintenance, and upgradeability. Each part can be worked on and verified separately. In programming terms, this case may be seen as an application of loose coupling and is beneficial for future development.

FAST's ElastoDyn is utilized for structural dynamics of the rotor, drivetrain, nacelle, tower, and the platform. As input, the calculated degrees of freedom are set along with the turbine configuration. It solves the motion dynamics. The aerodynamics is dealt by the AeroDyn subroutine that receives the instantaneous structural positions, orientation, and velocities. Wind properties at a given time and the motions are used to calculate the aerodynamic loads on the blade and tower nodes. The wind flow is assessed by the InflowWind module while the turbine's reaction regarding servo dynamics (e.g. blade pitch) is calculated through ServoDyn. If the wind turbine is installed offshore, HydroDyn assesses the loads acting on the platform due to waves. MAP++, MoorDyn, and FEAMooring are available to represent the dynamics of the mooring lines.

3.3 Turbine description and parameter calibration

The following sections present the results in full-scale correspondents of a 1/50 model. The scaling laws for conversion are listed in [41]. The drag and lift properties of the airfoils are the primary differences between the experimental model and the hypothetical NREL 5MW turbine.

3.3.1 The wind turbine and the blades

The model is an upwind horizontal-axis wind turbine with three blades. The tower height and the rotor hub diameter are 90 and 126 meters, respectively. The additional instrumentation present in the experimental setup (e.g., cables and sensors), causes a higher tower top weight compared to the reference turbine [125]. Table 3.1 provides a list of gross properties used in the numerical model. In

Table 3.1: Experimental implementation of the NREL 5MW turbine

Variable	Data
Turbine configuration	Upwind 3 blade
Rotor hub diameter	126.0
Hub height over SWL	90 m
Overhang	-10.58 m
Shaft tilt	0°
Precone	0°
Tower top mass	397,160 kg
Nacelle mass	274,940 kg
Hub mass	72,870 kg

experimental setup, the blades have no precone angles, and the shaft is laid out horizontally without tilting.

The blades have a total mass of 16,450 kg with the length of each blade reaching 61.5 meters. Their centre of mass is located at 23.4 meters from the blade root. Their flexibility is neglected, and they are assumed to be rigid. Accordingly, the blade's flapwise and edgewise degrees of freedom are turned off in the numerical model and the complexity is reduced. The pitch angles were taken as fixed values and the controller wasn't simulated. The rotational speed of the turbine was also defined as a constant value in each environmental condition.

3.3.2 Airfoil setup and the wind turbine performance

The airfoil designations represent the biggest difference between the NREL 5MW reference turbine and the current experimental setup mirrored from [39]. The Froude-scaled environment leads to Reynolds numbers that are three orders of magnitude lower than the required full-scale values. Hence, the airfoils used in the numerical calculations are not a geometric model of the 5MW turbine. Instead, the drag and lift coefficients were adjusted to match the thrust generated by the numerical model's rotor. Compared to unmodified versions of the airfoils, the current set provides lower lift and higher drag. The NACA64 profile which constitutes the final airfoil towards the tip of the blade (from 44.5 to 61.5 meters), is presented in Figure 3.1. The wind speeds are reduced by a multiplier of 0.952, with the wind shear exponent of 0.0912 to match the reported thrust at hub height.

The generated power does not affect the overall response of the system. With this reasoning, a simple generator model that matches the power in the rated region of the turbine (11.4 rpm at low-speed shaft) is used here. This model captures the power generation at rated speeds but underestimates it at lower rpm. It also disregards the experimental drop in higher revolutions. The method to calculate this generator model's variables is explained in [126]. The results comparing the experimental data for the generated power and numerical estimation are available in Figure 3.2a. The wind speed was adjusted to 21.80 m/s for this set of results. Table 3.2 lists the generator parameters.

Unlike the generated power, the thrust applied by the turbine affects the hydrodynamic responses. The forces and moments encountered on the tower are also altered. The running turbine causes a

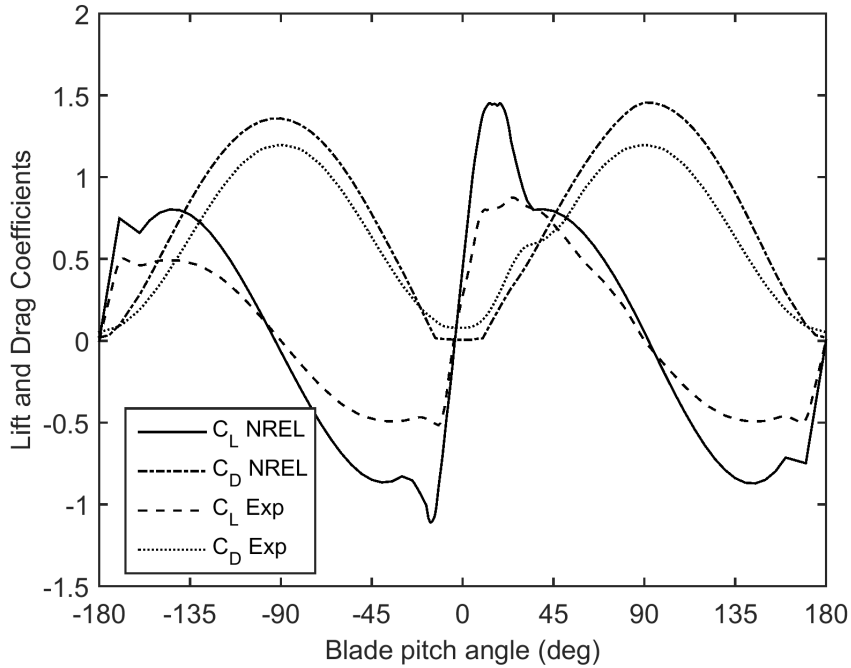


Figure 3.1: NACA 64 Profile comparison between experimental data and reference 5MW Turbine

Table 3.2: Settings of the simple generator model

Variable	Data
Model	Simple
Rated Speed (rpm)	1193 rpm
Rated torque in region 3	20954 N.m
Rated torque constant in region 2 ^{1/2}	0.0147 (N.m/rpm) ²
Rated slip percentage in region 2 ^{1/2}	16.87 %

large force that drives the platform pitching motion; therefore, it is essential to match the experimental values to predict the responses. Figure 3.2b shows the thrust between 3 to 14 rpm at the wind speed of 21.80 m/s. The average difference between the numerical and the experimental results are 5.3% between 3 to 12 rpm, and the numerical values are higher. The experiments show a reduction in the force between 12 to 14 rpm where the differences increase to 11.2 percent.

The thrust values for a series of wind and rotor speed combinations are given in Table 3.3. In all cases apart from the 30.5 m/s wind speed, the blade pitch is set to 6.4 degrees. Above the turbine's operational range, the 30.5 m/s wind velocity, the blades are feathered to 85 degrees. In this table, the most significant differences are seen at 7.32 m/s and 11.23 m/s of wind speed. Under these conditions, the values are underestimated and overestimated by approximately 25 percent, respectively. The best match is obtained at 21.8 m/s where the model calibration was carried out.

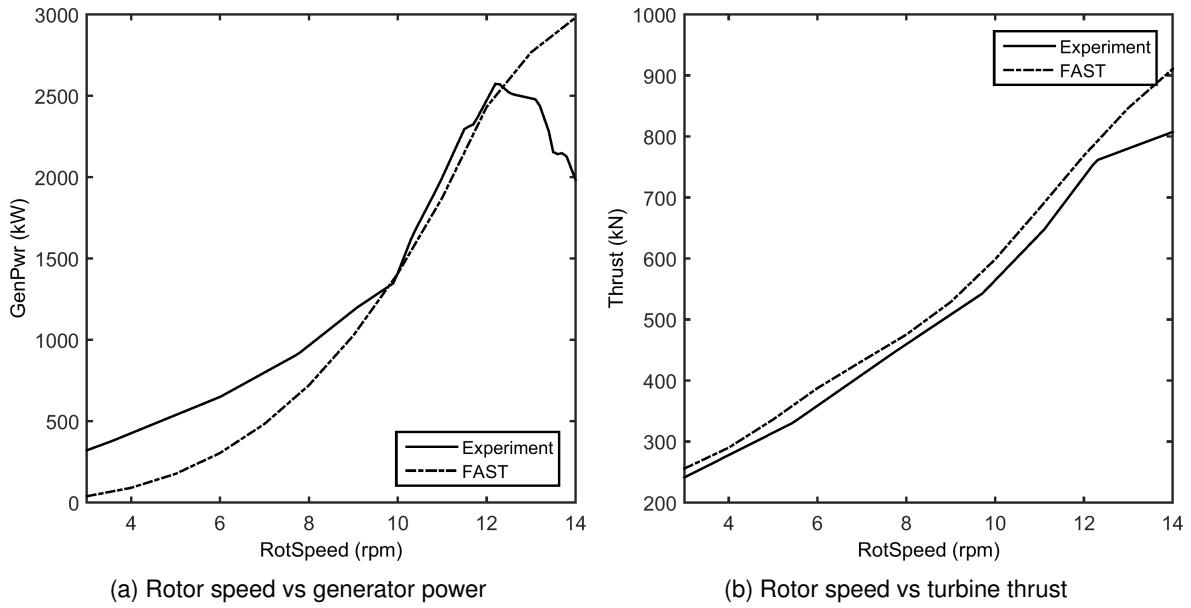


Figure 3.2: Turbine and generator evaluation at 21.80 m/s wind speed

Table 3.3: Experimental and numerical thrust differences as a function of wind speed

Wind Speed m/s	Rotor Speed rpm	Exp. Thrust kN	Num. Thrust kN	Difference %
7.32	4.95	126.1	97.7	-22.5
8.94	5.66	156.9	142.6	-9.1
11.23	7.78	202.7	249.3	23.0
16.11	9.19	381.7	434.7	13.9
21.80	12.3	749.8	793.2	5.8
30.50	0	156.8	141.8	-9.6

3.3.3 Tower properties and vibration modes

The tower-top mass of this model is higher than the reference NREL turbine due to the installed instrumentation. Accordingly, its vibration mode shapes needed to be redefined. FAST utilises two mode shapes to model the tower fore-aft and side-to-side bending modes. 6th order polynomials represent the deflection with respect to normalised height. It is stated in [39] that the 6th order polynomials do not reflect the mode shapes with high accuracy. As an alternative, it is suggested to utilise 9th order polynomials. In an attempt to see if any significant changes occur through the use of the FAST's standard approach, it was preferred to simplify the mode shapes. Remodelling was carried out by reconstructing the 9th order polynomials into 1000 data points along the tower's length. The discrete data was redefined with a 6th order polynomial adhering to a list of constraints defined by FAST and physics:

- The 0th and the 1st term of the polynomials are always zero to set the origin correctly.

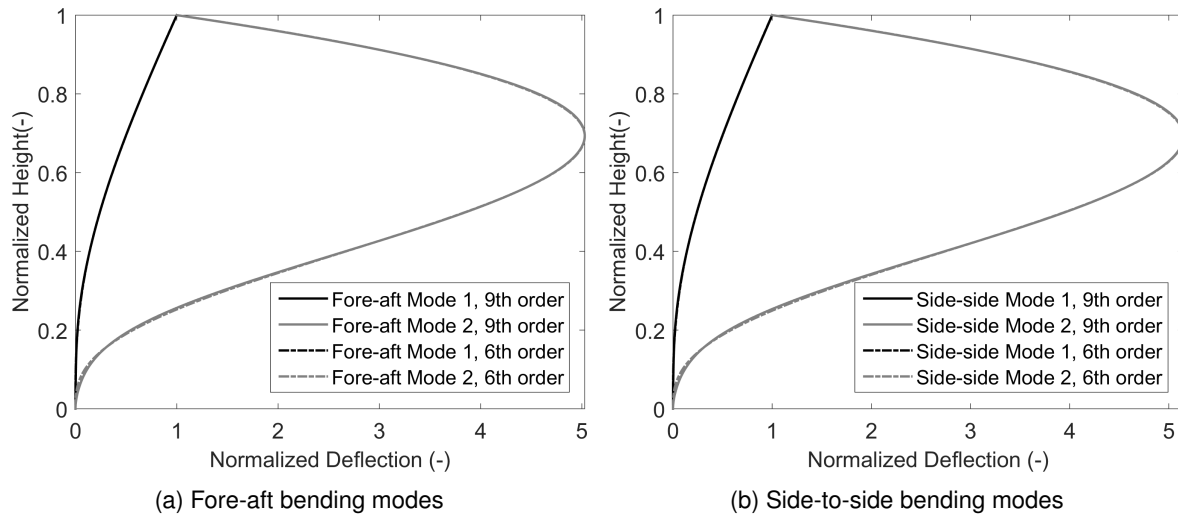


Figure 3.3: Normalized mode shapes as a function of tower height

Table 3.4: Normalised root mean square error of the comparison between 6th and 9th order polynomials representing the tower modes

Fore-aft Mode 1	Fore-aft Mode 2	Side-side Mode 1	Side-side Mode 2
0.999	0.999	0.999	0.999

- The deflection and the slope at the height of zero meters should equal zero to represent the cantilevered base of the tower.
- At the top of the tower, the deflection must have a normalized value equal to unity.
- The sum of the polynomial coefficients must add up to unity.

In addition to the items above, two additional conditions were enforced to ensure similarity between the polynomials:

- The locations of the maximum deflection were matched for the 6th and the 9th order polynomials. This condition was only required for the second mode as the first mode always has the maximum value at the top of the tower.
- Constraints were added to match the discretized value of the 9th order polynomials at arbitrary normalized heights. (0.15/1 and 0.50/1).

The comparison of tower fore-aft (Figure 3.3a) and side-to-side (Figure 3.3b) mode shapes reveal that the 6th order polynomials are significantly good representatives of their counterparts. The largest deviation occurs below 1/10th of the height. Table 3.4 presents an evaluation of the goodness of fit using normalized mean square error. According to this data, all mode shapes and tower motions show the same deviation.

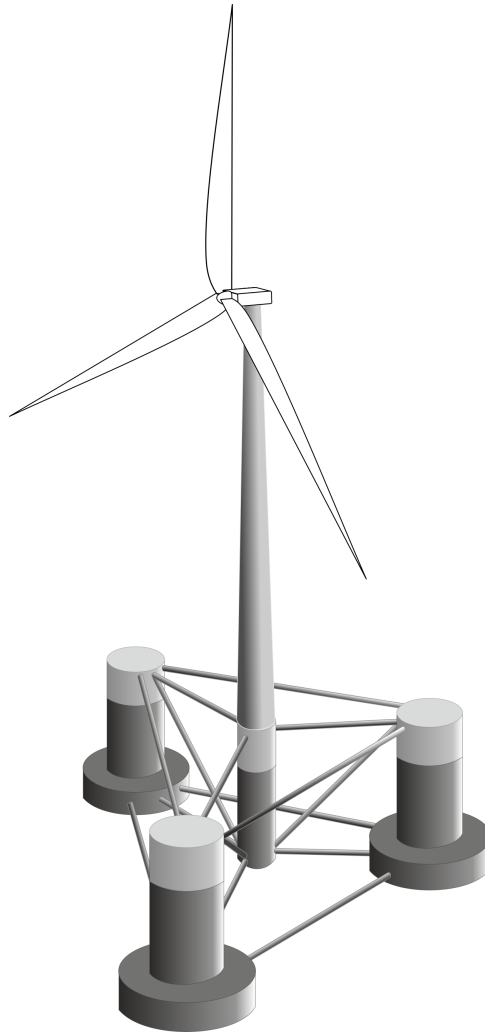


Figure 3.4: An illustration of the DeepCwind semisubmersible wind turbine platform

3.3.4 Platform and the mooring system

The OC4 semisubmersible, given in Figure 3.4, is composed of four columns. Three buoyancy columns help to stabilise the structure and the central column houses the tower-turbine assembly. A set of cross-braces provides structural integrity. Three catenary mooring lines are used for station keeping. The mooring model disregards the experimental variations of the line tension's mean values described in [52]. Accordingly, equal lengths and initial tensions were used for the three lines set at 60, 120 and 180 degrees. The properties of the platform and the mooring are listed in Table 3.5. The measurements are given at the still water level (SWL) and CM stands for the semisubmersible's centre of mass.

The numerical model includes the viscous damping component in 6 uncoupled modes (i.e., non-diagonal values of the matrix are zero) added into a recompiled version of FAST v7. Their values are given in Table 3.6. [39] lists an additional surge stiffness of 7.39 kN/m to account for the experimental equipment. However, this value was omitted. The omission does not seem to change the results as discussed when comparing responses.

Table 3.5: Summary of semisubmersible's properties

Variable	Data
Depth of platform base below SWL (total draft)	20 m
Elevation of main column (tower base) above SWL	10 m
Elevation of offset columns above SWL	12 m
Length of upper columns	26 m
Length of base columns	6 m
Depth to top of base columns below SWL	14 m
Diameter of the main column	6.5 m
Diameter of offset (upper) columns	12 m
Diameter of base columns	24 m
Diameter of pontoons and cross braces	1.6 m
Platform mass, including ballast	1.344E+7 kg
Platform CM location below SWL	14.40 m
Platform roll inertia about CM	8.011E+9 kg·m ²
Platform pitch inertia about CM	8.011E+9 kg·m ²
Platform yaw inertia about CM	1.391E+10 kg·m ²
Number of mooring lines	3
Angle between adjacent lines	120°
Depth to anchors below SWL (water depth)	200 m
Depth to fairleads below SWL	14 m
Radius to anchors from platform centreline	837.6 m
Radius to fairleads from platform centreline	40.868 m
Unstretched mooring line length	835.5 m
Mooring line diameter	0.0766 m
Equivalent mooring line mass density	113.35 kg/m
Equivalent mooring line mass in water	108.63 kg/m
Equivalent mooring line extensional stiffness	7.536E+8 N

Table 3.6: Platform viscous damping coefficients

Surge Ns ² /m ²	Sway	Heave	Roll Nms ² /rad ²	Pitch	Yaw
1.25E+6	0.95E+6	3.88E+6	3.35E+10	3.35E+10	1.15E+10

3.4 Validation of the model with the experimental data

This section focuses on two validation studies: linear wind without waves, and regular waves without wind. If both cases match experimental values, the combined wind-wave loading will also yield acceptable results provided that the code's coupling performance is satisfactory.

3.4.1 Responses under steady wind forces

Steady wind load cases were run in FAST for 2600 seconds. The final 100 seconds of the data were averaged to get the values presented in the proceeding figures. At the last segment of the time series, the transient motions subside, leaving only small oscillations. Averaging the last seconds of simulation delivers the steady state solution in non-oscillatory loads. As discussed, the wind speeds denoted in the figures were multiplied by 0.952 at hub height, and a power law profile with

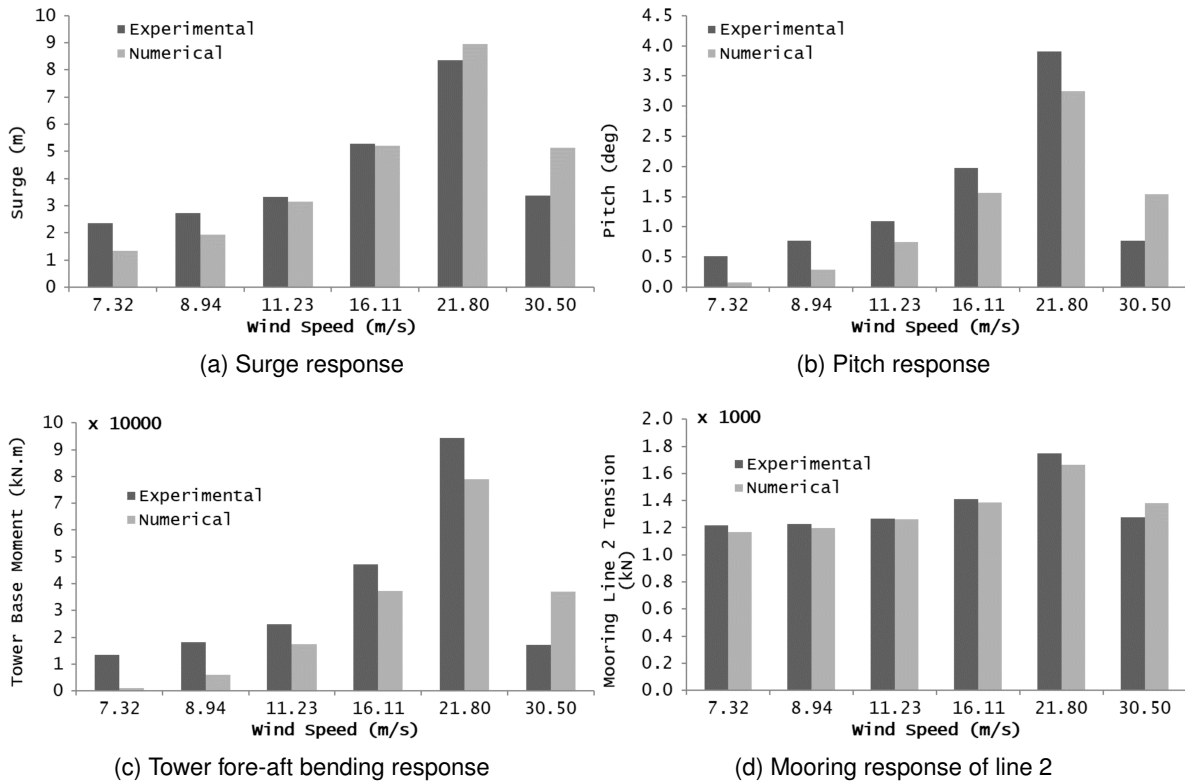


Figure 3.5: Responses of the DeepCwind platform under steady wind loading

the exponent of 0.0912 was applied. In all cases apart from the wind speed of 30.5, the blade pitch angles are fixed at 6.4. At this wind speed, the blade pitch is set to 85 degrees. The rotor speed at the low-speed shaft adheres to the values in Table 3.3.

The turbine thrust make surge and the pitch the primary responses in Figures 3.5a and 3.5b in the absence of waves. The conformity between the numerical predictions and the experiments depends on the mode of motion. The surge is generally predicted well. At 7.32 m/s and 8.94 m/s wind, the experimental value is larger. The results are almost identical at a wind speed of 16.11 m/s, and slightly higher at 21.80 m/s. For the idling turbine, the estimated numerical value is significantly larger than the experimental data. Figure 3.5c and Figure 3.5d show the tower base bending moments and the tension at the second mooring line respectively. While the mooring responses are captured, the tower's bending moments are underestimated. The discrepancies increase in lower wind speeds.

These sets of results are related to the differences between the thrust values presented in Table 3.3. At 7.32 m/s wind speed, the modelled thrust is approximately 20 percent lower than the experimental value. At 21.80 m/s it is 6% higher. The surge motion reflects this trend, providing lower surge amplitude at lower wind speeds and slightly higher surge amplitude at 21.80 m/s.

In the pitch mode, there is an overall tendency to underestimate the motion (Figure 3.5b). This case is mostly apparent in low wind speeds. Pitching is one of the primary causes of high tower base bending moments; consequently, their values in Figure 3.5c follow the differences in pitch predictions.

Figure 3.5d compares of the mooring line tensions of the experimental data and the numerical simulations for line 2 (i.e., incoming wind/wave direction). Regardless of the wind speed and the motions of the platform, the predictions are close to the experimental values. They do not show to be significantly affected by the platform motions. The main contributor to the fairlead tension seems to be the static loading on the platform and the line weight.

When the wind speed is increased to 21.80 m/s, the tension increases both numerically and experimentally. In this case, the surge and pitch motions are significantly high in comparison to the other wind speeds. Therefore, it is reflected as an increase in the mooring line tension, which is captured correctly by FAST.

3.4.2 Responses under regular waves

This section examines the motions of the platform under regular waves, in the absence of wind. The simulations were run for 2600 seconds from which the initial 600 seconds were removed as transient stages. The remaining time series were analysed for the RAOs. In post-processing, the numerical wave frequency was found to be 4 percent higher than defined. This difference was neglected.

In this simulation set, the blades were feathered to 85 degrees. Head waves were investigated with the heights of 1.92, 7.58, 7.14, 10.3, 10.74 and 11.12 meters. The periods are 7.5, 12.1, 14.3 and 20 seconds. Equal periods with several wave heights were investigated to assess the non-linearity of the RAOs. Period to wave height pairings are stated in the horizontal axis of the figures.

Figure 3.6a presents results for the surge motion of the platform in seven wave period-height pairs. Numerical results are close to experimental values. It was previously stated that this work does not account for the extra surge stiffness due to the experimental equipment. The comparison between these results and the set published by [39] shows that the motion is not affected by this simplification.

Figure 3.6b shows the heave mode. The general trend is to underestimate the motions with the difference in the 20 second period being significant. This area is close to the heave natural frequency of the platform at 17.5 seconds. It is possible to state that the motion is underestimated at resonance areas. Both 14.3 seconds and 20 seconds are at approximately equal distances to the heave natural period and are underestimated. The differences change from 25 to 50 percent compared to the experimental responses. Wave heights of 7.58 and 7.14 meters are similar values that differ in terms of their periods (12.1 and 14.3 seconds respectively). However, their results diverge significantly. This finding shows that the prediction quality relies on the periods. Additionally, it should be considered that viscous damping is largely non-linear. See for instance [127] and [128] exemplifying the treatment of free decay curves and overall change of hydrodynamic coefficients due to motions. For such reasons, including values for several excitation amplitudes may provide a better estimations in large responses.

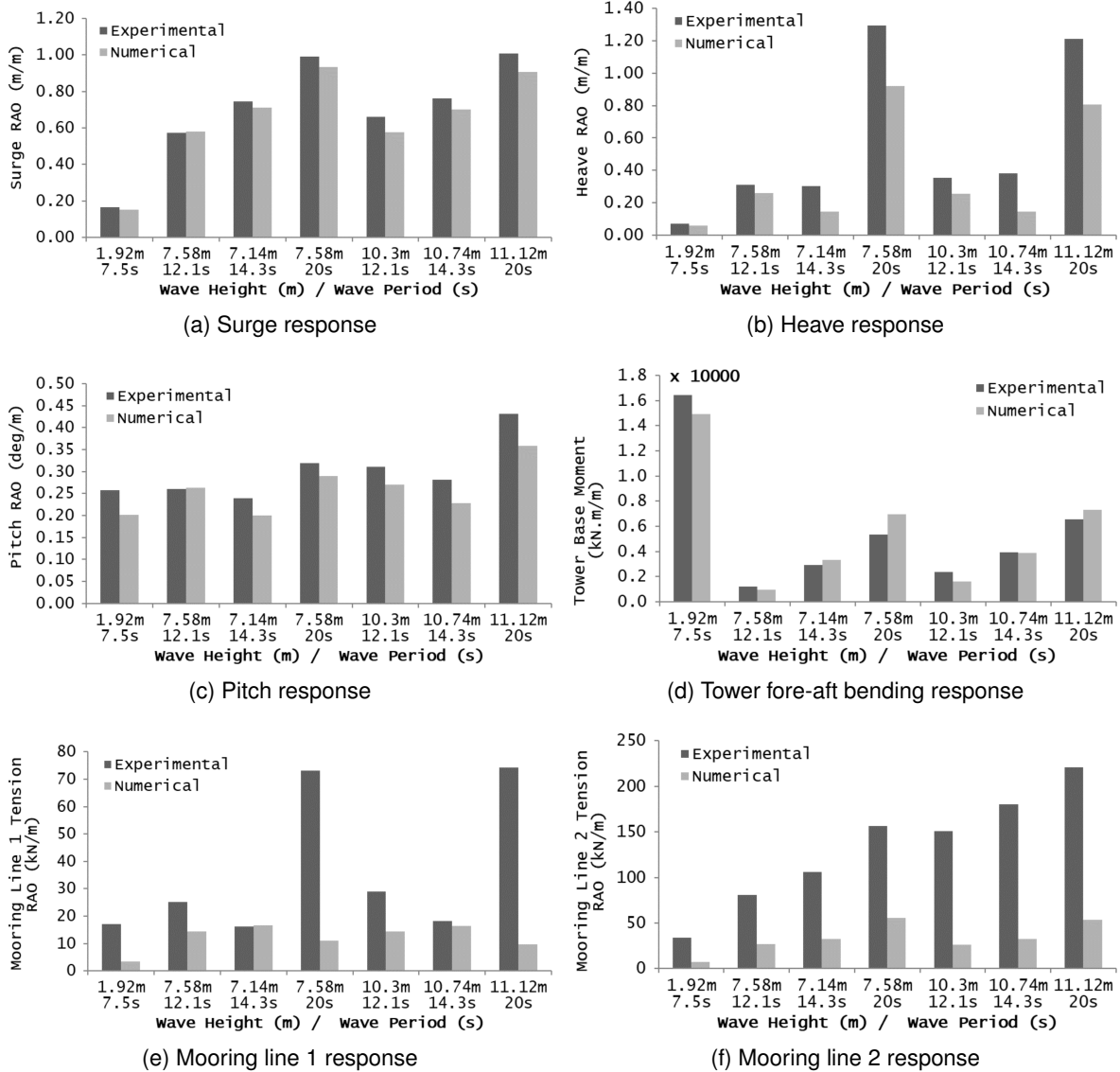


Figure 3.6: Responses of the DeepCwind platform under regular wave loading

The pitch motion in Figure 3.6c illustrates that the amplitudes are predicted better compared to the wind cases. However, the numerical estimations are still approximately 20 percent lower than the experimental data. The tower base moments in Figure 3.6d relate to the pitching motion.

The mooring line tensions for the line one and two are presented in Figure 3.6e and Figure 3.6f. Results of the numerical simulation are lower in comparison to the experiments. These simulations were carried out on FAST 7, which uses a quasi-static mooring model. The data shows that a testing a dynamic approach may be necessary to improve the results.

3.5 Concluding remarks

The chapter compared a numerical model of a trust-equivalent NREL 5MW turbine on the DeepCwind platform to experimental data under isolated wind and wave loading. Modelling tower shapes

with a 6th order polynomial and negligible differences in mode shapes compared to a 9th order polynomial suggested by previous published works. Hence, it is not an improvement over the current implementation in FAST.

In a condition where only the steady wind is present, FAST's surge predictions were satisfactory. However, the estimated pitching amplitude was lower than the experimental values. The tower-base-moment estimations provided similar results. In the absence of waves, the mooring line tensions were within a 10 percent margin. The wave responses of the platform were captured adequately in surge and pitch. In heave, they were underestimated. The tower bending moments followed platform pitching motion as expected. Unlike wind-only responses, the mooring tensions were calculated significantly lower than the experimental data. Overall, the code's performance depends on the oscillation period and the amplitude of the exciting force.

This numerical model gives identical results to previously published data and performs as predicted. Hence, it provides a base setup for the oncoming chapters. Regarding the results, the biggest opportunity for improvement seems to lay in switching to a dynamic mooring model in place of the quasi-static one.

Influence of geometric modelling simplifications on platform motion predictions

4.1 Introduction

The platform's underwater geometry defines its hydrodynamic characteristics. Once the hull form is decided, it is important to have the fully developed model. Commercial software (e.g., Rhinoceros 3D and MultiSurf) serve this purpose. However, for testing new concepts, modelling the geometries in full detail may not be economical in terms of computational costs. Accordingly, hulls are often simplified for hydrodynamic calculations through reductions such as removing the spokes of TLPs and modelling them as cylindrical columns [78]. The options for simplifications depend on the platform type [129]. A SPAR does not include a significant number of connecting parts. If they exist, inclusion or exclusion of the strakes can be alternatives. Conversely, a semisubmersibles with multiple bodies may feature braces. The WindFloat design study shows that several cross bracings and structural members were omitted in the hydrodynamic model [12].

At any rate, these alterations of the submerged geometry changes the added masses, damping coefficients, and wave exciting forces. It interests to see the extent of these variations to decide whether to consider them. With this aim, the hydrodynamic responses of two geometric models of the DeepCwind semisubmersible are examined in this chapter. All parts are included in the complete model while the simplified model excludes the connecting braces. The hydrodynamic variables are obtained using WAMIT: a commercial software that calculates wave interaction with floating or

Published in: E. Uzunoglu and C. Guedes Soares. Influence of bracings on the hydrodynamic modelling of a semisubmersible offshore wind turbine platform. In C. Guedes Soares, editor, *Renewable Energies Offshore*, pages 755–762. Taylor & Francis Group, London, UK, 2015. ISBN 978-1-138-02727-5

submerged bodies [130]. It is a panel method code that delivers exciting forces, hydrodynamic coefficients, the pressures and fluid velocities, the mean drift forces and moments in frequency domain [131]. The models are examined further in time domain using FAST. Environmental cases include free decay motion, wave effects, and combined wind-wave loading. While the bracings are essential concerning structural integrity, only their hydrodynamic effect is discussed here.

4.2 Methodology

The DeepCwind semisubmersible features 15 cross braces that connect the three buoyancy columns and the central column. There are direct connections between two buoyancy columns on the upper and lower extremities of the hull. The lower braces are under the waterline, while the upper connections are above. The three cross-bracings are partially under water. The complete model studied here is identical to the model in OC4 Phase II [48]. Accordingly, the viscous damping values are updated to the values listed in Table 4.1. Additionally, the design values of the tower and the turbine, with the alterations given in Table 4.2, are used unlike the Chapter that deals with the experimental comparison.

Both models have identical towers, blades, and nacelles. However, two approaches were used for the modelling of the platform. The complete model disregards all simplifications. Only the three buoyancy columns and the centre column are included in the simplified model. The number of panels was kept close between models when possible. The geometry without braces was developed with the approach described in [132]. This code required an equal number of panel sections along the polar axis of each column. For this reason, the sectioning of the base and the upper columns were readjusted to equal values. Additionally, removing the braces changes the discretization of the connection locations. Figure 4.1a is the complete structure and Figure 4.1b represents the simplified model. The models are prepared using a low-order grid mesh and second order effects are overlooked.

First, the two models are evaluated to obtain the added masses, potential damping coefficients and the exciting forces. These values are compared to identify the motions where the deviations are the largest. These modes are investigated further in time domain simulations to compare the responses in various conditions.

The load cases here are a subset of the OC4 Phase II code comparison study [49]. Similarly, they are divided into three sections. Free decay tests focus on the system identification phase. The

Table 4.1: Updated viscous damping values

Variable	Value	Unit
Surge quadratic drag coefficient	3.95E+5	Ns ² /m ²
Sway quadratic drag coefficient	3.95E+5	Ns ² /m ²
Heave quadratic drag coefficient	3.88E+6	Ns ² /m ²
Roll quadratic drag coefficient	3.70E+10	Nms ² /rad ²
Pitch quadratic drag coefficient	3.70E+10	Nms ² /rad ²
Yaw quadratic drag coefficient	4.08E+9	Nms ² /rad ²

Table 4.2: NREL 5MW turbine design values

Variable	Value	Unit
Overhang	5	m
Shaft tilt	5	°
Precone	2.5	°
Tower mass	249,718	kg
Nacelle mass	240,000	kg
Hub mass	110,000	kg

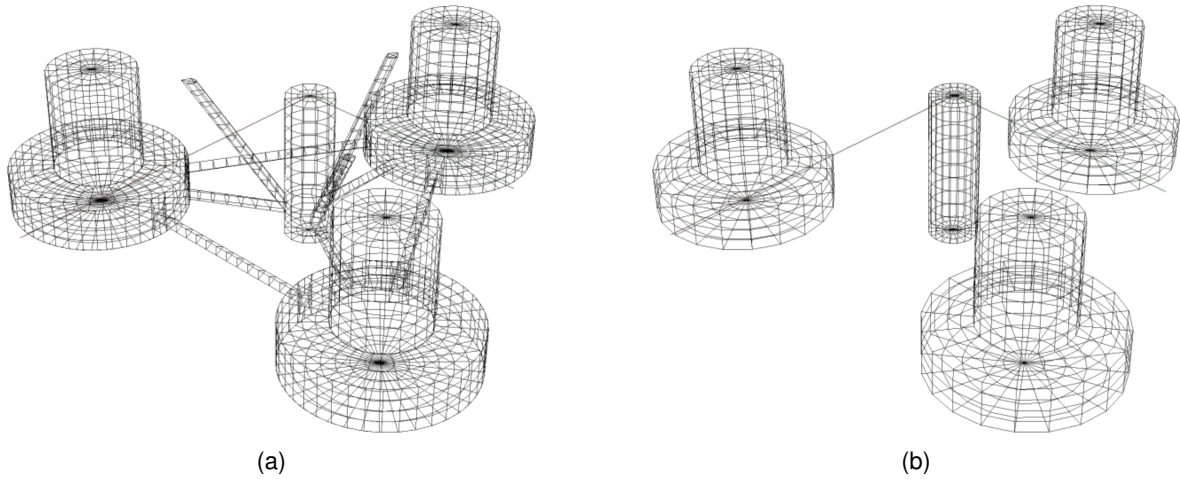


Figure 4.1: The underwater geometry of the semisubmersible model with and without the connecting braces

platform and the moorings are allowed to move while the generator, rotor, and the drivetrain are locked. In the second set, the platform's and the tower's motions are calculated. This condition is used to check responses to incoming waves without the wind. The third set considers the system with the waves and the wind.

4.3 Comparison of hydrodynamic coefficients and wave exciting forces

This section compares the results of hydrodynamic coefficients and the exciting forces on platform. It does not include the tower, nacelle and the blades. The hydrostatics were obtained assuming that the platform geometry is afloat at the given draft without providing an external mass matrix. The results from this set are used to decide which load cases should be focused on when conducting the combined loading study.

4.3.1 Added masses

The added masses in the surge, heave, pitch, and yaw modes are presented in Figure 4.2. Considering the symmetry of the platform, the results of sway equal to surge and roll equals to pitch

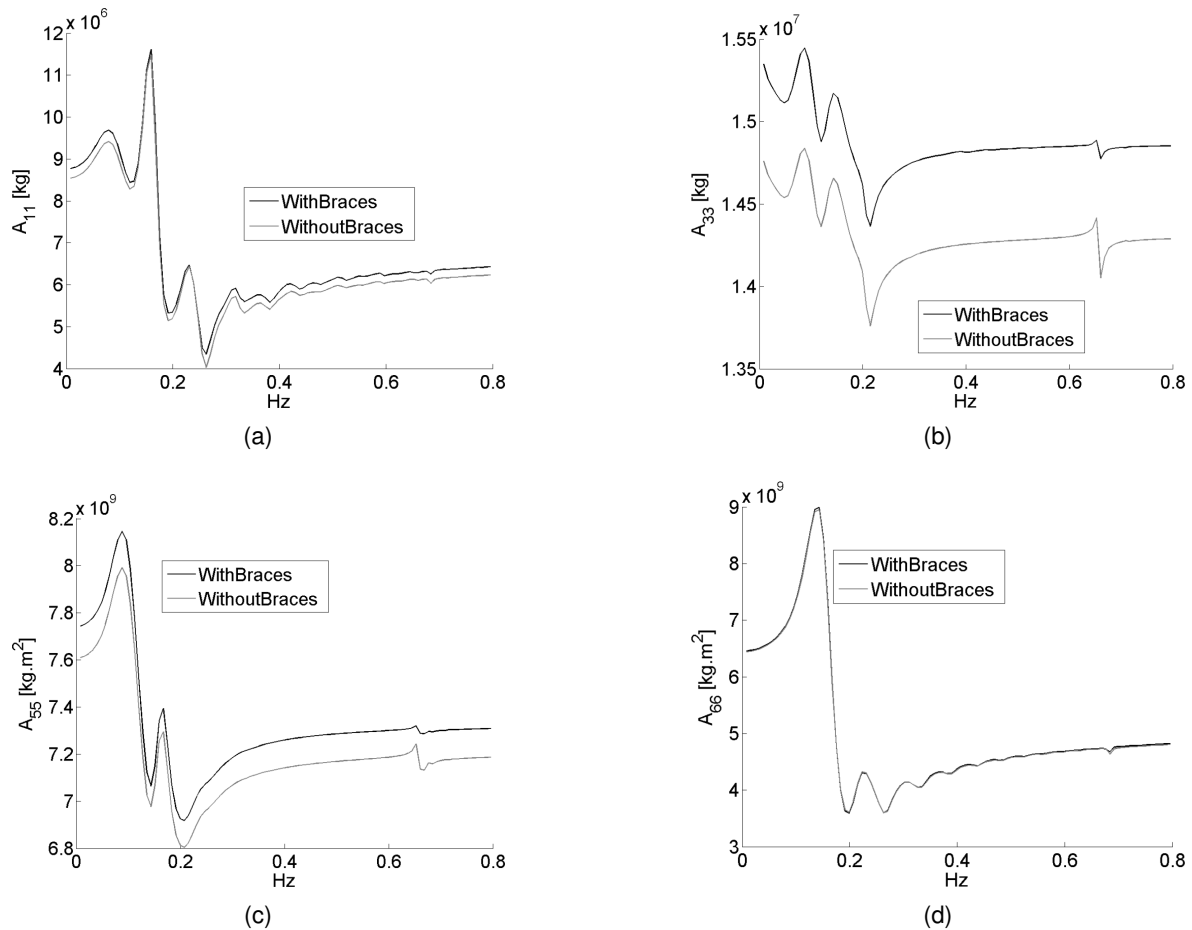


Figure 4.2: Added mass coefficients of the braceless and full models

motion, and therefore their figures are omitted. The model with braces is given in black lines, and the model without braces is represented by grey lines. The frequency axis range is up to 0.8 Hz.

When the figures are compared regarding their agreement between the two models, it is seen that the results depend on the mode of motion. Added masses in surge are significantly close. The complete model has higher values as the wetted surface area increases with bracing. In heave, the difference is approximately five percent, and this margin does not change depending on the frequency. This behaviour is different in pitch, where the data matches between sets when frequency ranges of 0.1 to 0.2 Hz are considered. There is approximately two percent difference outside this range. The yaw mode values are almost identical. Considering these sets of results, the change in heave and pitch added masses can alter the motions of the platform as they change the total mass. The extent of this effect needs clarification.

4.3.2 Damping coefficients

The surge, heave, pitch and yaw potential damping coefficients are compared in Figure 4.3. The complete and the braceless models are represented by black and grey lines. Unlike the added masses, these comparisons do not seem to be mode dependent. In all cases, the deviation between

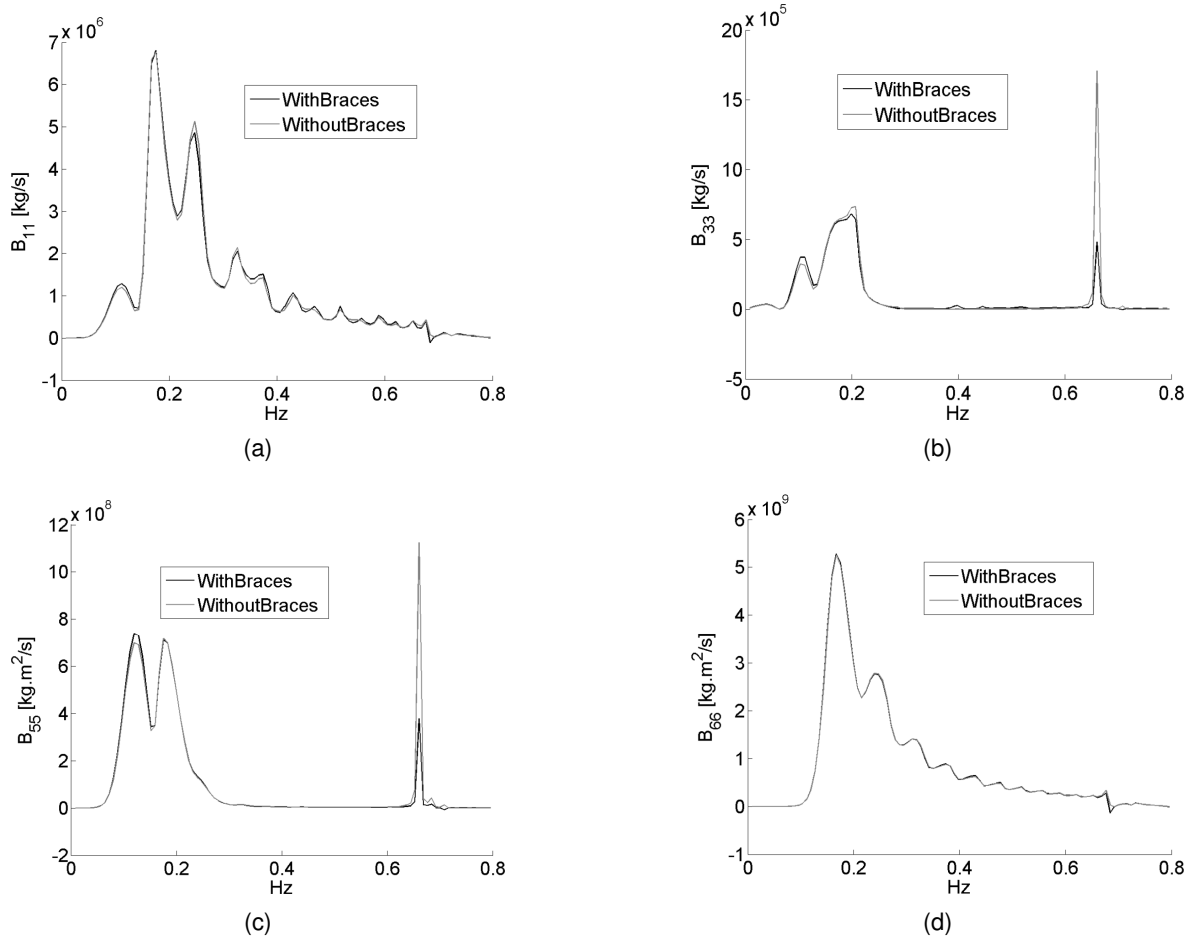


Figure 4.3: Potential damping coefficients of the braceless and complete models

sets is negligible with the most prominent variation being at the peaks. However, they do not reach one percent.

4.3.3 Exciting Forces

The exciting forces due to head waves are compared in Figure 4.4. Considering the symmetry of the platform and the direction of the waves, the prominent motions are surge, heave and pitch. For this geometry, head waves cause no roll, sway, or yaw. Therefore, those modes are omitted.

When the exciting forces are compared between the complete model (black lines) and braceless model (grey lines), they show to be in agreement. In this aspect, modelling braces does not change the forces. Accordingly, the dataset shows that they will not be the source of possible disagreements in platform motions.

4.4 Time domain evaluation

The previous section examined the hydrodynamic coefficients and the exciting forces of the models. The exciting forces and the potential damping coefficients do not show significant differences

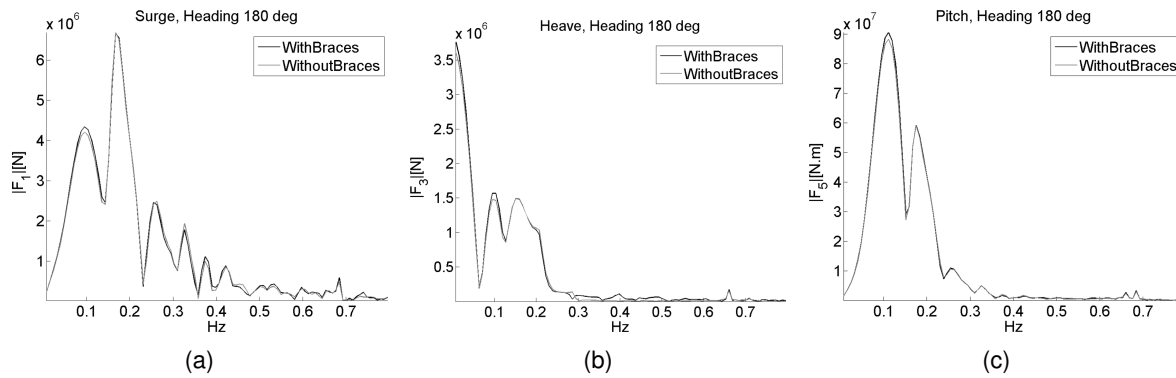


Figure 4.4: Wave exciting forces of the braceless and complete models

Table 4.3: System identification load cases

Motion	Initial condition	Time
Surge free decay	+22 m	20 min
Heave free decay	+6 m	5 min
Pitch free decay	+8 deg	5 min

between the two modelling approaches. However, the added masses are relatively different depending on the mode of motion. The time domain responses of the platform below help to identify whether these changes cause significant differences in motions.

4.4.1 System identification

From the information in Figure 4.2, the system is expected to show altered free decay behaviour as the added mass alters the total mass. The free decay was simulated by letting the motion commence without external forces to identify the natural frequencies. The data includes the surge, heave, and pitch modes. These cases assume the tower, blades, and the generator to be rigid. There are no incoming waves or wind. The allowed degrees of freedom are the six modes of motion of the platform and the moorings. The initial conditions of the free decay tests are summarised in Table 4.3.

In Figure 4.5, the comparative results of free decay motions are provided. Regarding the surge motion, the difference in the added masses does not seem to have an effect. There is a negligible shift in the phase. The amplitude of the motion shows no difference.

Heave motion shows a more substantial shift in the natural frequency of the platform. The amplitudes are unaffected. It can be stated that they would be more reflective if there were differences in damping coefficients. The pitch motion shows the most significant shift. These results repeat the patterns in added mass values. However, in terms of motion amplitudes, there are no changes.

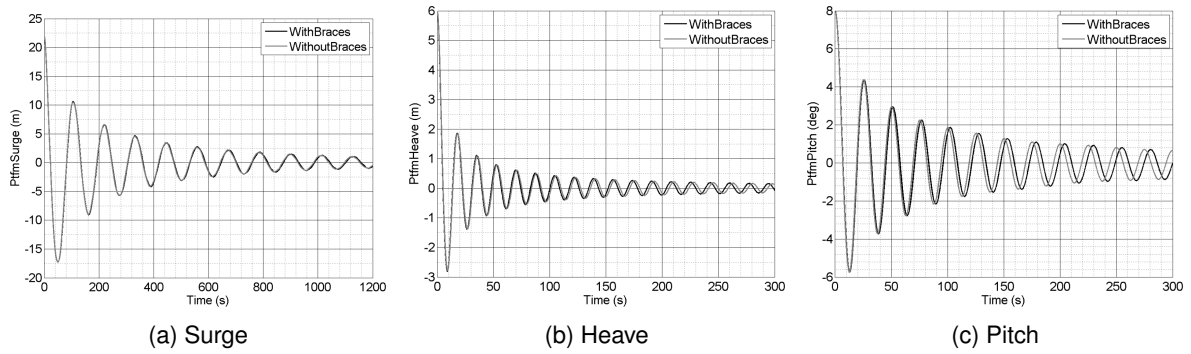


Figure 4.5: Free decay motions of the platform in surge, heave, and pitch

Table 4.4: Load cases with only waves and no wind

Load Case	Wave condition	Time
2.1. Deterministic waves	Airy wave of 6 m wave height and 10 s of period	60 s
2.2. RAO Estimation	PSD of 1 m ² /s between 0.05 – 0.25 Hz	60 min

4.4.2 Platform responses in waves

Two cases were examined with waves and no wind to understand the difference in wave responses. This section considers an otherwise flexible system with the generator, nacelle, and the rotor degrees of freedom omitted. Accordingly, the tower, platform and the mooring system are the allowed degrees of freedom. Table 4.4 lists the environmental conditions.

In Figure 4.6, the surge, heave and pitch responses of the platform in regular head waves of 6 meters, with a 10-second period are presented. There are relatively small differences in amplitudes. The phases of the motion are unaffected. These results do not reveal considerable differences in amplitudes in any of the modes.

Given the shifting natural frequencies, noticeable differences can be expected where the wave and platform resonance frequencies coincide. Figure 4.7 deals with this case by examining the response amplitude operators to a white noise spectrum of 1 m²/Hz between 0.05 and 0.25 Hz. The

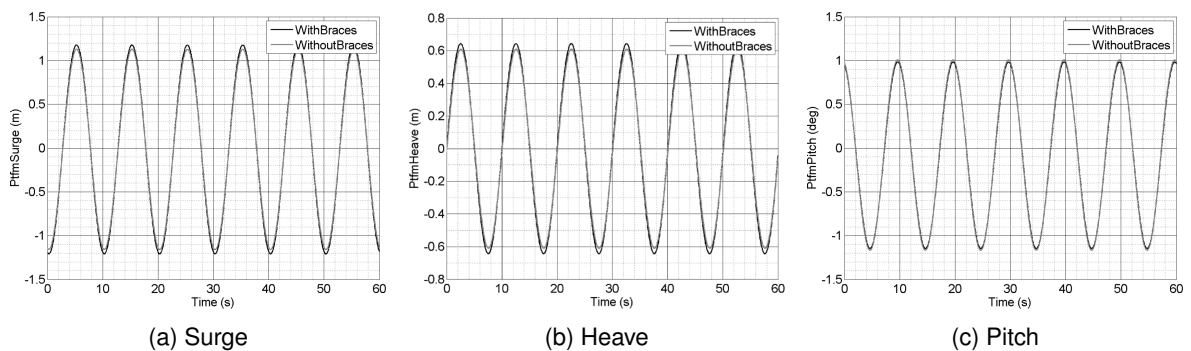


Figure 4.6: Load case 2.1, Responses of the platform to regular waves

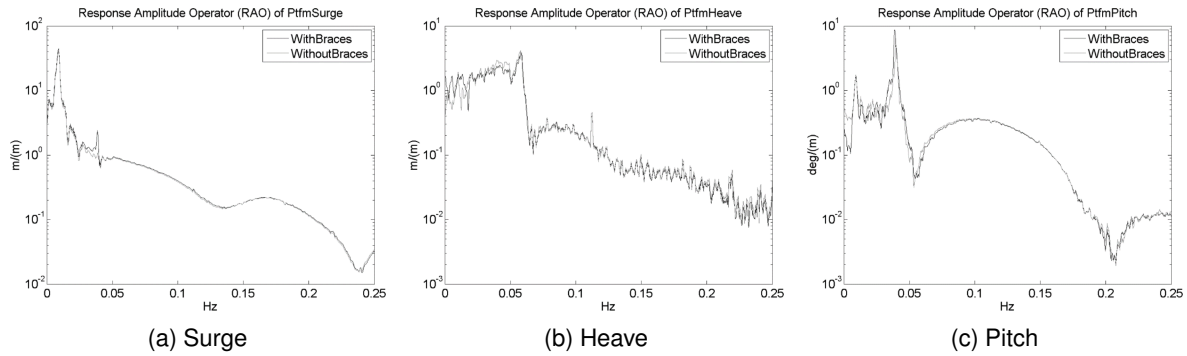


Figure 4.7: RAOs as a response to white noise amplitude of $1 \text{ m}^2/\text{Hz}$ between 0.05 Hz and 0.25 Hz, described in load case 2.2

Table 4.5: Load cases with waves and wind

Load Case	Wave condition	Wind speed at hub	Time
3.1. Below rated wind (9 rpm)	Airy waves of 6 m height and 10 s of period	Linear, 8 m/s at hub height	60 s
3.2. Stochastic, rated speed, (12.1 rpm)	JONSWAP spectrum, $H_s = 6\text{m}$, $T_p = 10\text{s}$, $\gamma = 2.87$	Turbulent (Mann Model), 11.4 m/s	60 min
3.3. Below rated wind (9 rpm)	PSD of $1 \text{ m}^2/\text{Hz}$ between 0.05 and 0.25 Hz	Linear, 8 m/s	60 min

values in the figures were smoothed using a moving average of 5 values. Therefore, the original data was retained as much as possible while increasing readability. The calculated wave responses are almost identical. When there are differences, they are seen in the frequency range below 0.05 Hz. The surge mode show some differences between 0.05 to 0.025 Hz. In heave, there is a divergence below 0.025 Hz. This area is not inside the wave excitation range. In all cases, the peak value estimations are identical, and the simplified model does not seem to miss them.

4.4.3 Coupled system dynamics

The coupled system dynamics considers the behaviour of the platform with incoming waves in the presence of wind. Load cases are listed in Table 4.5. All degrees of freedom (i.e., the platform, moorings, tower, generator, nacelle and the blades) are allowed. Three load cases are considered. Initially, a regular wave identical to the load case of 2.1 is used for comparison. It is followed by a realistic case where turbulent wind is present at the turbine's rated speed of 11 m/s. The turbine is rotating at 12.1 rpm, and stochastic waves represented by the JONSWAP spectrum are present. The third "full system dynamics" case focuses on the RAOs with the linear wind at 8 m/s. A flat white noise spectrum of $1 \text{ m}^2/\text{Hz}$ is applied. As previously done, the plotted data was smoothed using a moving average of 5 values.

Figure 4.8 with regular waves and linear wind shows elevated responses of the platform in surge and pitch, compared to the case without wind (Figure 4.6). The differences between the complete

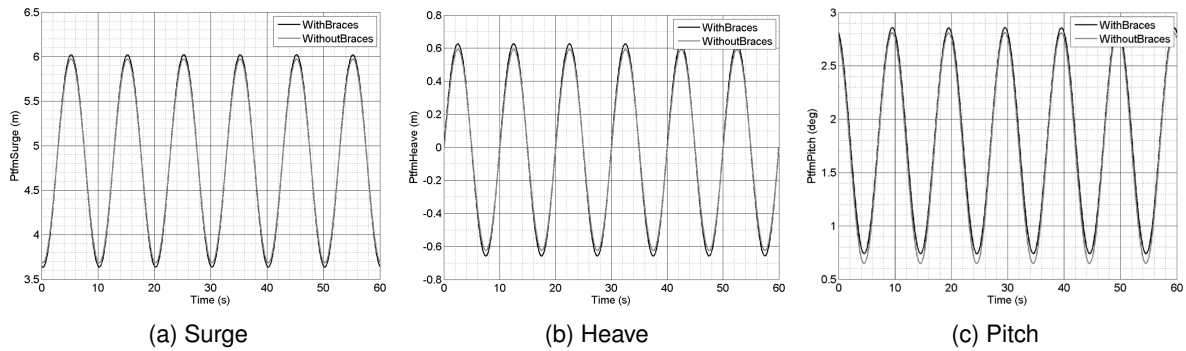


Figure 4.8: Platform responses in regular waves with wind, described in load case 3.1

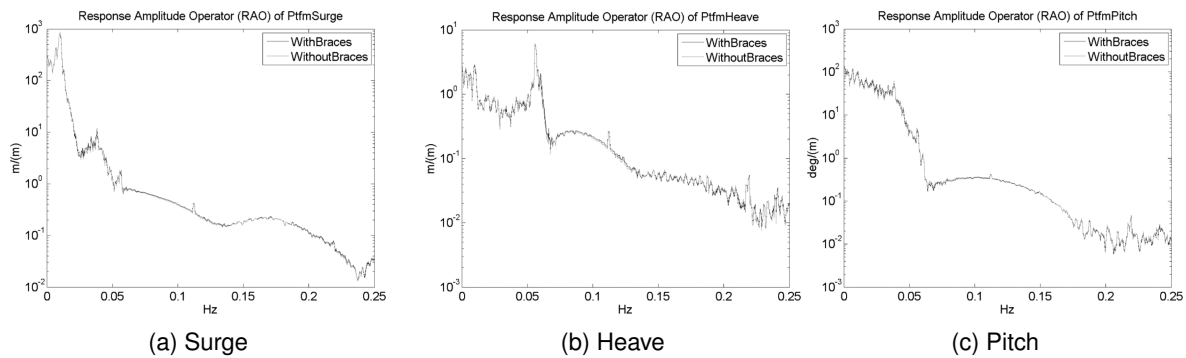


Figure 4.9: RAOs of surge, heave and pitch motions in turbulent wind and irregular waves, described in load case 3.2

and braceless models are not significant. Regarding amplitudes, the largest difference occurs in pitching, where the braceless model shows smaller minima. All phases are identical.

The results of load case 3.2 are in Figure 4.9 with stochastic wind and waves. Low frequency responses are amplified in this case. Despite the increase, the models with and without braces compare favourably. The progression from free decay to the full system dynamics show that the effect of modelling on motion predictions reduces as the number of involved variables increases.

There is a difference between the RAOs in Figure 4.9 (stochastic wind and waves) and Figure 4.10 (white noise spectrum and below rated wind speed) regarding responses. Lower wind speed results in reduced amplitudes in load case 3.3. This effect is highly prominent in surge and pitch, and less noticeable for heave. Regardless, the model with and without the braces compare favourably also in this case. Apart from the low frequency heave response, it is not possible to detect differences between these sets of data.

4.5 Concluding remarks

The chapter evaluated possible approaches to the 3D modelling of a semi-semisubmersible's hull form for hydrodynamic calculations. A complete model including the connecting braces and a simplified model that disregards the bracings were compared to understand the characteristics and

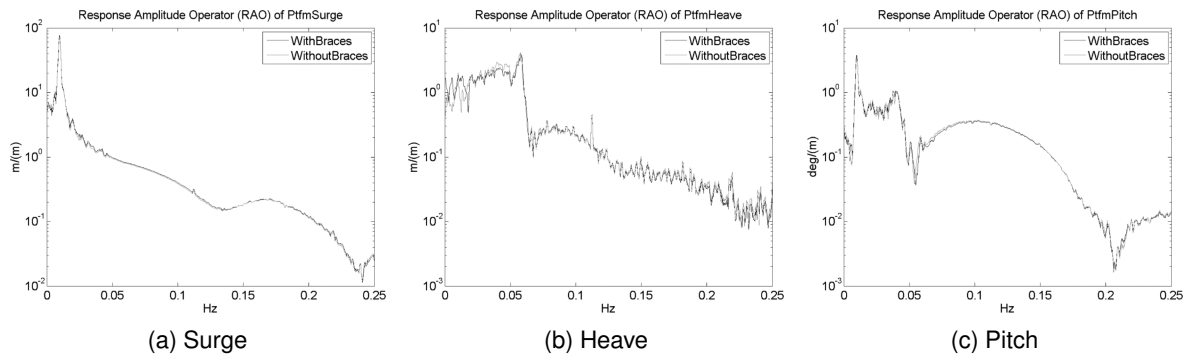


Figure 4.10: RAOs for white noise amplitude of $1 \text{ m}^2/\text{Hz}$ between 0.05 Hz and 0.25 Hz and linear wind of 8 m/s, described in load case 3.3

responses. The results show that each mode responds differently to simplifications. The affected motions were put under further evaluation to reveal their influence on system dynamics.

Free decay tests underline that if added mass is significantly affected by the modelling practices, the eigenfrequencies of the platform is altered. This condition may become prominent in resonance. However, these changes do not have a significant reflection in overall response to waves. Also under the combined loading of wind and waves, the two models consistently deliver similar results.

Comparing a variety of hulls with different configurations can provide a more accurate insight into the treated problem. Regardless, for the current set of data at hand, the results suggest that simplified geometric models may be considered for hydrodynamics calculations. While the bracings are crucial for structural integrity, they cause limited deviations for the hydrodynamic model. Hence, they may serve the purpose at initial design stages.

Model uncertainty of wave induced platform motions and mooring loads

5.1 Introduction

The oil and gas industry has previous experience coming from more than half a century of installations. However, the loading on the wind turbines is different than that of the oil-and-gas platforms. The presence of the turbine creates thrust, and the height of the tower which can reach 90 meters, acts as a lever that creates a substantial rotational force. The blade aerodynamics is also a factor. Hence, the wave loading is combined with significant aerodynamic loading. Additionally, when the platform is floating, mooring lines are required for station keeping, imposing another layer of challenge. The resulting system dynamics is highly coupled.

Several codes are available to deal with the behaviour of the floating turbines, and there have been many developments in this regard. Two possible approaches help to understand their performance. Experiment-to-code comparisons provide a basis. Alternatively, code-to-code comparisons have also been a part of the progression towards improved numerical models. The Offshore Code Comparison Collaboration Continuation within IEA Wind Task 30: Phase II [48] is an iteration of a series of similar studies. In that work, which the author was also a part of, a semisubmersible platform with identical input parameters was tested to see the correlation between the results of the participants. After limiting the variables apart from the user's knowledge of the software and the implementation of mathematical models, the difference between the results comes down to the mathematical model

Published in: On the model uncertainty of wave induced platform motions and mooring loads of a semisubmersible based wind turbine. *Ocean Engineering*, 148:277–285, 2018. doi: 10.1016/j.oceaneng.2017.11.001

itself. Quantification of these variations, the model uncertainty, aids understanding the deviations between the methods.

This chapter focuses on one of the load cases of the OC4 Phase II study, published in [49]. The chosen environmental condition includes no wind to minimise the system complexity and focuses on the hydrodynamics and the mooring. Ideally, before adding wind forces, all codes should be at a base level of agreement. Otherwise, the added complexity will likely increase the divergence. Therefore, it is important to quantify where the current state of art stands in this regard. The study aims to be as inclusive as possible by considering all submitted results of the load case. However, a mathematical filtering method was applied to identify the outliers that may skew the comparison. Only the participants that provided data for all required responses (i.e. the surge, heave, pitch motions and mooring loads) are evaluated. Preliminary analysis with a limited set of data was published in [133]. The mentioned work is extended here, and an evaluation of user errors and the mooring models are added.

5.2 Assessment of model uncertainty

When an uncertainty can be attributed to the variable nature of physical phenomena, it is termed the fundamental (intrinsic) variability. While its presence is acknowledged, it cannot be eliminated. The ocean waves are an example that represent this category. The second type of uncertainty, model (epistemic) uncertainty, relates to the knowledge about a physical process as opposed to its nature. It can be reduced by obtaining additional information about the problem [134]. The hydrodynamic and mooring codes in this study are in this group.

Increasingly complex mathematical models can be used to describe an event, however, with certain drawbacks. Increased input data and computational times are examples of limiting conditions. Consider two hypothetical models of higher and lower sophistication, both with their associated model uncertainties. Even if the sophisticated model is better predictive, the simpler model may be preferred considering other advantages. The decision depends on the problem at hand, the allowed error margins, and the available resources. For this reason, model uncertainty does not dictate which method to use. It aims to provide an understanding of the deviations. Then, a suitable method can be chosen based on several variables. In this regard, the uncertainty values are an important factor to consider, but they are not the decision. Therefore, it is important to quantify the model uncertainty of all available methods to form a basis of judgement.

The principles for the quantification of model uncertainty are known for some time and have been used to assess ship responses to waves [135, 136] and also wave energy devices [137]. The method described below extends the application to wave induced responses and mooring loads of wind turbine platforms.

5.2.1 Description of the initial data set and preliminary considerations

The OC4 Phase II comparative study had 24 participants using 19 simulation tools. The output set contained 62 channels of response data in a time series with a fixed step of 0.05 seconds. They can be summarised as the wind and wave characteristics, power generation, and system loads and responses. The entire data set evaluated the platform motions and the forces on the moorings, the tower, and the rotor. From this output, the chapter solely focuses on the motions and the mooring loads. The participant who did not submit mooring loads was eliminated, reducing the initial number to 23.

In head waves, the surge, heave, and pitch modes are prominent. Hence, the sway, roll, and yaw motions aren't discussed. Mooring loads at the fairleads were chosen as opposed to the anchors. Since the time series are difficult to interpret in irregular waves, frequency domain data through Fourier analysis is used as in [49].

When several groups submit results using the same code, the effect of the mathematical model is annulled, and the participant's approach to the modelling of the structure assumes the deciding role. Therefore, the differences in motions should be attributed to the user's handling of the software and the input data. This case is evaluated by comparing differences between identical-code results. Consequently, user-related variations will be addressed separately.

5.2.2 Obtaining the model uncertainty

In the presence of experimental values, they act as a reference point for comparison. In their absence, a method of relative evaluation is required. There are various ways of exploring the current data set in this manner. They are discussed below.

It is explained in [138] that the root mean square (RMS) value allows different probabilistic statements to be made about the motions. The probability of exceedance and the largest maximum expected to occur in N maxima in narrow-banded spectra are examples. Similarly, the model uncertainty of the responses can be directly related to the root mean square.

A response spectrum's ($S_R(\omega)$) RMS is calculated by:

$$RMS = \sqrt{\int_0^{\infty} S_R(\omega) d\omega} \quad (5.1)$$

Consider that the true RMS of responses is known. If a theoretical mathematical model returns RMS_c , a direct relation can be written to reveal the model uncertainty:

$$RMS = B.RMS_c \quad (5.2)$$

In this case, the variable B becomes the indicator of the model uncertainty [139, 140].

In the absence of experimental data, the *RMS* in the uncertainty Equation 5.2 becomes an unknown itself. To remedy the problem, instead of checking each model against the true RMS value, an alternative can be devised by providing a relative comparison of the entire group. This approach was used by [141] on wave induced loads on ships. The coefficient of variation (CoV) was utilised as a standardised measure of dispersion in sets of discrete values. As opposed to that study, the current data presents a larger set, due to the number of points to be evaluated throughout the response spectrum. There are two possibilities to applying the CoV approach in this case. The first option is to compare the value at each frequency. Alternatively, the *RMS* values representing the full spectra of each participant can be utilised to provide an overall comparison. Each approach has associated advantages and disadvantages.

When applied to the entirety of the spectrum, RMS values will fail to capture the problem regions where the codes show greater dispersion. Conversely, the interpretation is easier. For this reason, comparisons of CoV values at each frequency were first used as a method to determine the regions of disagreement. Then, for the selected regions, the RMS values of the range were used. In this approach, the formulation of the model uncertainty for an arbitrary section of the spectrum becomes:

$$B = CoV (RMS_r(1, \dots, n)) = \frac{\sigma_{RMS_r}}{\mu_{RMS_r}} \quad (5.3)$$

In the Equation above, the standard deviation and the mean value are represented with σ and μ . The *RMS_r* refers to the root mean square values of a spectral range of n participants.

5.2.3 Filtering the data set

The coefficient of variation imposes a difficulty for smaller sample sizes. To understand the problem, consider its mathematical definition given defined as the standard deviation divided by the mean:

$$CoV = \frac{\sigma}{\mu} \quad (5.4)$$

In a set of approximately 20 numbers, when a rogue value that deviates by magnitudes is present, the mean and the standard deviation will change significantly. When multiple codes with related numerical models exist, these extremes may hint at errors.

To clarify the problem, Table 5.1 presents the results regarding the surge motion of the platform between 0 and 0.5 Hz. To avoid bias, each participant is given a number from 1 to 23 (P1 to P23) after shuffling the data. A quick glance states that the values are below 10 except for P8 and P5, who have reported 104 and 16 respectively. An inclusive comparison with all participants has a mean value of 6.7. Excluding the P8 and the P5 lowers it to 1.6.

In the absence of experimental data, this type of filtering is challenging, and always partially arbitrary. However, it is also true that the presence of experiments does not explain how codes fare against each other. In that regard, the arbitrary nature does not present a problem for the fundamental

Table 5.1: Platform surge RMS values of all attending participants

P1	P2	P3	P4	P5	P6	P7	P8	P9	P10	P11	P12
0.2	0.2	0.3	0.2	16.2	1.2	0.2	103.7	0.3	0.2	7.1	0.2
P13	P14	P15	P16	P17	P18	P19	P20	P21	P22	P23	
0.2	0.2	0.2	5.4	1.9	1.6	7.3	0.2	5.6	0.2	0.2	

question in this work. Still, the level of subjectivity can be reduced by implementing a mathematical filter and setting its criteria to be as inclusive as possible. The initial values have the indicators for the definition of a possible range of acceptable results. When a set is revised by removing the upper and lower 10 percent of the highest and the lowest values, its extremes are eliminated. However, the reduced set is also likely to overlook valid results. Albeit, this new set can still deliver an acceptable range if a normal distribution is fitted to the reduced data through its the mean and standard deviation values. Then, using a large confidence interval (i.e., 98% in this case), a new maximum and minimum of a range can be defined. Consequently, the original set can be assessed to identify the values that lay outside these boundaries.

Consider the values in Table 5.1 to serve as an example. Removing the top and bottom 10th percentile removes 15 of the participants from the list. P5 and P8 are the top 10%. Continuing to extract the bottom 10% leaves only nine values (i.e., P3, P6, P9, P11, P16, P17, P18, P19, P21). This restrictive set provides the new mean (μ_c) and the standard variation (σ_c) of 3.41 and 2.90 respectively. Obtaining the 98 percent confidence interval with the critical value (V_c) 2.33 results in an acceptable range (R_c) of [-3.35, +10.17]. The formulation is as follows:

$$R_c = [\mu_c - V_c\sigma_c, \mu_c + V_c\sigma_c] \quad (5.5)$$

Checking the RMS values in Table 5.1 identifies P5 and P8 to be outside these limits. The remaining results are kept, and those two are eliminated.

The example given above was limited to the surge mode. A participant needs to comply with this filter in all studied output channels to be included. Repeating the filter in a second iteration is possible, but it may risk high bias. Hence, only a single pass was used.

5.3 Platform model, load case, and the final participants

The turbine here is the NREL 5MW reference wind turbine [33] as designed, mounted on the OC3 Hywind spar tower [36]. The tower's total weight and the distribution are slightly altered, and the details are available in the definition document [48]. In a continuation of the previous code comparison studies, OC3 [142], the platform is replaced with the semisubmersible composed of four columns. The viscous damping values repeated in Table 5.2 were assessed in an experimental programme [39] and updated subsequently in the OC4 project.

Table 5.2: Viscous damping coefficients used in the OC4 Phase II

Surge Ns ² /m ²	Sway	Heave	Roll Nms ² /rad ²	Pitch	Yaw
3.95E+5	3.95E+5	3.88E+6	3.70E+10	3.70E+10	4.08E+9

Participants of the OC4 Phase II have reported almost identical natural frequencies for the system [49] with showing slight deviations. The surge, sway, and yaw frequencies are 0.01 Hz while the roll and pitch frequencies are 0.04 Hz. The heave frequency is 0.06 Hz. Platform eigenfrequencies are close to the lower end of the wave excitation region (accepted to be as 0.04 Hz to 0.25 Hz in DNV [27]). Surge mode is an exception, and it is much lower.

The load case 2.6 is explained in the description document [48] as an inverted pendulum under the influence of wave loads. The nacelle, the drivetrain and the rotor are considered rigid, and the generator is locked. Having no wind removes the complexity of the aerodynamic responses and focuses the study solely on the hydrodynamics. The moorings, the platform, and the tower are allowed to respond in their respective degrees of freedom. The waves are defined with a white noise spectrum limited to 1 m²/Hz between 0.05 to 0.25 Hz. Ideally, choosing a flat spectrum would remove the discrepancies caused by generating the wave time series. However, there were certain differences in that regard which are also addressed later in the text. The results were submitted as a time series for the OC4 Phase II, and here they are studied through the spectral densities and response amplitude operators.

Table 5.3 presents the filtered list of participants with their codes and numerical models. Regarding hydrodynamics, there are three primary models: the Morison Equation (ME), Morison Equation combined with the potential flow theory (ME + PF), and the potential flow theory combined with quadratic damping (PF + QD). Some codes alter these models through additions such as the instantaneous water level (IWL) and the instantaneous position (IP). In Table 5.3, the primary approaches are given without parenthesis while the alterations are marked in parentheses. The mooring line models are quasi-static (QS), finite elements dynamic (FE/DYN), and lumped mass dynamic (LM/DYN).

5.4 Hydrodynamic models

Before presenting the tabulated results in the sections below, a few points are discussed here using figures to identify several topics. Figure 5.1 verifies that all participants comply with the prerequisite of a wave spectra with 1 m²/Hz amplitude between 0.05 – 0.25 Hz. Compared to a theoretical white noise signal between 0 – 0.5 Hz, the RMS values were approximately 20% higher than required. However, when compared between themselves, their deviation did not surpass 3% of their mean RMS. The increase from the theoretical value can be explained by the differences outside the excitation ranges. On both the lower and higher ends of the spectrum, there is a small (10⁻³ m²/Hz and less) amount of energy represented. When summed throughout the entire range, the discrepancy increases.

Table 5.3: Load case 2.6 data included in the uncertainty study and their respective figure markings

Code	Developer	Participant	Structural Dynamics	Hydrodynamics	Mooring
OrcaFlex	Orcina	4Subsea	T: FE P: Rigid	PF + ME	LM/Dyn
CHARM3D+FAST	TAMU+ NREL	ABS	T: Mod/MB P: Rigid	PF + ME + (MD + NA) + (IP + IWL)	FE/Dyn
Simo+ Riflex+ AeroDyn	MARINTEK+ NREL	CeSOS	T: FE P: FE	PF + ME	FE/Dyn
Bladed Advanced Hydro Beta	GH	GH	T: Mod/MB P: MB	PF + ME + (IWL)	QS
Bladed	GH	POSTECH	T: Mod/MB P: MB	ME + (IWL+ IP)	QS
Riflex-Coupled	MARINTEK	MARINTEK	T: FE P: Rigid	PF + ME + (IWL)	FE/Dyn
FAST	NREL	NREL, CENTEC, IST, Goldwind	T: Mod/MB P: Rigid	PF + QD + (QTF)	QS
DeepLinesWT	PRINCIPIA-IFPEN	PRINCIPIA	T: FE P: FE	PF + ME + (MD + QTF/NA) + (IP + IWL)	FE/Dyn
SIMPACK+ HydroDyn	SIMPACK	SWE	T: Mod/MB P: Rigid	PF + QD	QS
hydro-GAST	NTUA	NTUA	T: MB/FE P:MB/FE	PF + ME + (IWL)	FE/Dyn
UOU+FAST	UOU+NREL	University of Ulsan	T: Mod/MB P: Rigid	PF + QD	QS

—————	4Subsea-(OrcaFlex)
—————	ABS-(CHARM3D+FAST)
—————	CENTEC-(FAST)
- - - - -	CeSOS-(Simo+Riflex+HydroDyn)
- - - - -	GH _{AHB} -(AdvancedHydroBeta)
- - - - -	Goldwind-(FAST)
- - - - -	IST-(FAST)
- - - - -	MARINTEK-(RiflexCoupled)
- - - - -	NREL-(FAST)
- - - * - - - -	NTUA-(HydroGast)
- - - * - - - -	POSTECH-(Bladed)
- - - * - - - -	PRINCIPIA-(DeepLinesWT)
- - - * - - - -	SWE-(SIMPACK+HydroDyn)
- - - * - - - -	UOU-(FAST)

T= turbine
P= platform
Mod= modal
MB= multi-body
FE= finite element
N/A=not applicable

PF= potential flow theory
ME= Morison equation
MD= mean drift
QTF= quadratic transfer function
FE= finite element
NA= Newman's approximation
IP= instantaneous position
IWL= instantaneous water level

QS= Quasi Static
Dyn= dynamic
LM= lumped mass

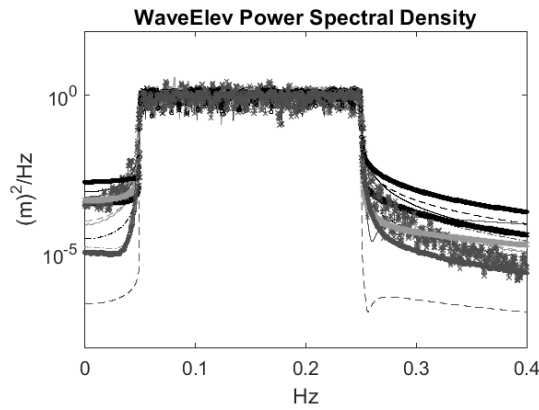


Figure 5.1: Spectral density of the wave frequency

The rounding also needs to be addressed when comparing the coefficient of variation of the motions on a frequency basis. Calculating the CoV of negligible numbers (e.g., 10^{-9} to 10^{-4}) will result in inevitably large values although they merely represent rounding errors. To remedy this issue, the response amplitude operators were preferred to obtain the CoV in place of spectral densities. This alteration makes it possible to take advantage of the physical interpretation of the RAOs. For the translational modes of surge and heave, 1 cm of motion was used as the cut-off amplitude. Similarly, 0.1 degrees was utilised for the rotational mode of pitch. This approach results in zero CoV in areas that show responses below the threshold to set the focus only on the relevant information.

Examining the spectral density of pitch in this light, Figure 5.2a illustrates the emergence of 3 separate groups up to 0.05 Hz. From there on, the results tend to consolidate, particularly in the central regions between 0.10 to 0.15 Hz. At the pitching eigenfrequency of 0.04 Hz, all codes detect the dynamic amplification, albeit at different amplitudes. This data is easier to see from the CoV values of the pitch response amplitude operators in Figure 5.2b. The low-frequency region between 0 to 0.05 separates itself from the rest. Therefore, the model uncertainty study is divided into two parts. The first part examines the full range of responses between zero and 0.25 Hz, and the second part evaluates the wave excitation range of 0.05 to 0.25 Hz. This approach helps to understand the reflection of different models in low-frequency ranges where non-linear effects are prominent in minimal wave excitation.

Figure 5.3a shows that the behaviour is not limited to pitch, and it is almost identical in the surge mode. The results are very consistent inside the wave frequency region while there is a divergence in the estimation of the peak resonant response in low frequencies. Heave mode in Figure 5.3b is a particular case where the natural frequency of the mode is inside the wave excitation range. The drop-off from the peak is different, along with the low-frequency responses. Hence, in heave mode, there are variations throughout the entire range.

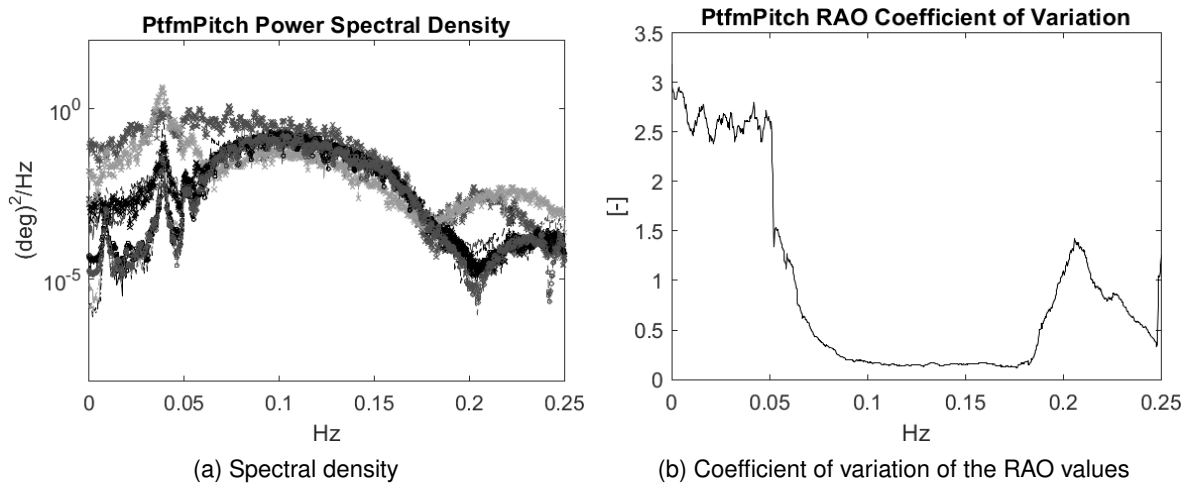


Figure 5.2: Platform pitch responses

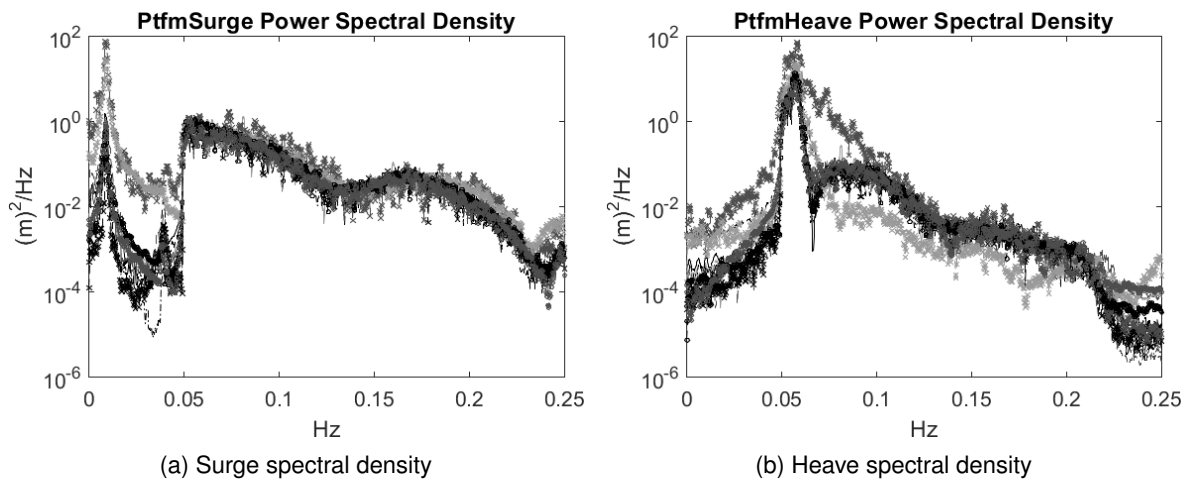


Figure 5.3: Platform surge and heave responses

5.4.1 Combined low-frequency and wave frequency ranges

In scope of this work, the combined frequency range is defined as zero to 0.25 Hz. It is evaluated in three classifications. Initially, the comparison considers only the groups that utilise the same primary hydrodynamic approach (i.e., the Morison Equation (ME), a hybrid method combining the potential flow theory with the Morison Equation (ME+PF), and Potential flow with added quadratic damping (PF+QD)). Next, these primary approaches are compared against each other. The third classification details a one on one comparison of all hydrodynamic models including the alterations such as the instantaneous position.

Table 5.4 lists the CoV and RMS values of the primary models. Only one participant depends solely on the Morison Equation. Hence, no associated coefficient of variation is given. In this case, the mean RMS value is the only indicator, and it is notable that 'ME' responses are significantly higher than the other two groups. The CoV values of the 'PF+QD' and 'ME+PF' that include potential

Table 5.4: Low-frequency and wave frequency combined range comparisons inside identical primary hydrodynamics groups

Base Model	Codes	Surge		Heave		Pitch	
		Mean RMS	CoV	Mean RMS	CoV	Mean RMS	CoV
ME	Bladed	6.89	0.00	8.72	0.00	0.33	0.00
ME + PF	OrcaFlex, "Charm3D+FAST", "Simo+Riflex+AeroDyn", "Bladed Advanced Hydro Beta", Riflex-Coupled, HydroGast, DeepLinesWT	0.58	1.38	1.68	0.41	0.12	1.12
PF + QD	FAST, "SIMPACK+HydroDyn", UOU+FAST	0.30	0.14	1.47	0.22	0.07	0.17

Table 5.5: CoV values of low-frequency and wave frequency comparisons between the mean RMS values of the primary hydrodynamics groups

Model 1	Model 2	Surge	Heave	Pitch
ME	'ME + PF'	1.19	0.96	0.66
ME	'PF + QD'	1.30	1.01	0.92
ME + PF	'PF + QD'	0.46	0.10	0.37

flow, point out that the alterations in the same approach can make a significant difference. Codes that utilise the 'ME+PF' show a CoV of 0.41 in heave responses. The surge and pitch modes show significantly higher values (i.e., 1.38 and 1.12 respectively). The differences reduce in 'PF+QD' when the drag from the Morison equation is replaced with the quadratic damping coefficient (0.14, 0.22, and 0.17 for the surge, heave and pitch). It is also important to note that all codes in the 'PF+QD' group rely on the hydrodynamics module of NREL's FAST (HydroDyn) for motions which may cause this consolidation. However, there are individual differences in the implementation such as the inclusion or exclusion of the quadratic transfer function.

The data in Table 5.5 focuses on comparing the primary models. A clear outcome is that Morison equation is set apart from the alternatives for all modes. What is also notable is that the 'ME+PF' and the 'PF+QD' deviate similarly from the 'ME' approach both in the surge and heave modes. Including potential flow seems to consolidate the variation, in this case, lowering the CoV to 46, 10, and 36 percent for surge, heave, and pitch.

While broader grouping serves to understand the overall behaviour, it disregards the alterations in each code. When the combinations are evaluated, 28 possibilities of individual comparisons arise from the entire group. They are detailed in Table 5.6. The Morison only approach utilises instantaneous water line and instantaneous position 'ME + (IWL + IP)'. It continues to be highly divergent. Comparing 'PF + ME' to 'PF + ME + (IP)' shows that adding instantaneous position into the equation causes changes between 6 to 16 percent. A similar statement holds true for the instantaneous water line in 'PF + ME + (IWL)'. The prominent difference is in the heave mode, reaching 22 percent. Replacing quadratic drag with the Morison equation results in differences of 5 percent in other modes, and 10 percent in pitch ('PF+ME' vs. 'PF+QD'). This data repeats the finding that inclusion of po-

Table 5.6: CoVs of all hydrodynamic models in low and wave frequency ranges

Model 1	Model 2	Surge	Heave	Pitch
'ME + (IWL + IP)'	'PF + ME'	1.30	1.00	0.91
'ME + (IWL + IP)'	'PF + ME + (IP)'	1.31	0.91	0.96
'ME + (IWL + IP)'	'PF + ME + (IWL)'	1.31	1.10	0.93
'ME + (IWL + IP)'	'PF + ME + (MD + NA) + (IP + IWL)'	1.29	1.04	0.94
'ME + (IWL + IP)'	'PF + ME + (QTF/NA) + (IP + IWL)'	0.68	0.68	0.17
'ME + (IWL + IP)'	'PF + QD'	1.31	1.02	0.97
'ME + (IWL + IP)'	'PF + QD + (QTF)'	1.29	1.00	0.89
'PF + ME'	'PF + ME + (IP)'	0.06	0.16	0.08
'PF + ME'	'PF + ME + (IWL)'	0.07	0.22	0.02
'PF + ME'	'PF + ME + (MD + NA) + (IP + IWL)'	0.07	0.09	0.05
'PF + ME'	'PF + ME + (QTF/NA) + (IP + IWL)'	1.11	0.48	1.01
'PF + ME'	'PF + QD'	0.05	0.05	0.11
'PF + ME'	'PF + QD + (QTF)'	0.06	0.00	0.04
'PF + ME + (IP)'	'PF + ME + (IWL)'	0.01	0.38	0.06
'PF + ME + (IP)'	'PF + ME + (MD + NA) + (IP + IWL)'	0.13	0.25	0.04
'PF + ME + (IP)'	'PF + ME + (QTF/NA) + (IP + IWL)'	1.14	0.33	1.05
'PF + ME + (IP)'	'PF + QD'	0.01	0.21	0.03
'PF + ME + (IP)'	'PF + QD + (QTF)'	0.13	0.16	0.13
'PF + ME + (IWL)'	'PF + ME + (MD + NA) + (IP + IWL)'	0.14	0.13	0.02
'PF + ME + (IWL)'	'PF + ME + (QTF/NA) + (IP + IWL)'	1.14	0.67	1.02
'PF + ME + (IWL)'	'PF + QD'	0.02	0.17	0.09
'PF + ME + (IWL)'	'PF + QD + (QTF)'	0.14	0.22	0.07
'PF + ME + (MD + NA) + (IP + IWL)'	'PF + ME + (QTF/NA) + (IP + IWL)'	1.09	0.56	1.03
'PF + ME + (MD + NA) + (IP + IWL)'	'PF + QD'	0.12	0.03	0.06
'PF + ME + (MD + NA) + (IP + IWL)'	'PF + QD + (QTF)'	0.01	0.09	0.09
'PF + ME + (QTF/NA) + (IP + IWL)'	'PF + QD'	1.13	0.53	1.06
'PF + ME + (QTF/NA) + (IP + IWL)'	'PF + QD + (QTF)'	1.09	0.48	0.98
'PF + QD'	'PF + QD + (QTF)'	0.12	0.05	0.15

tential flow mostly consolidates the results. The 'PF + ME + (QTF/NA) + (IP + IWL)' model requires attention. Considering that most results in the 'PF+ME' section are below 20%, the sudden increase to over 100 percent hints at an implementation error rather than a significant effect of the (QTF/NA) addition. This statement can be reasoned through the results of 'PF + ME + (MD + NA) + (IP + IWL)' which is very similar except for the omission of the quadratic transfer function and the inclusion of mean drift.

The data set points out that the primary indicator seems to be the inclusion of potential flow in calculations. Alterations such as instantaneous position and instantaneous water line do seem to produce differences while not being as prominent as the omission of potential flow. The theoretical limits of the Morison Equation are respected in some parts of the spectrum while disregarded in others. This case is a likely cause of its divergence from the other models. However, the comparison of the 'PF+ME' to 'PF+QD' also shows that a hybrid model that considers the Morison drag can be useful when the quadratic drag cannot be estimated.

Table 5.7: Wave frequency range comparisons inside identical primary hydrodynamics groups

Base Model	Codes	Surge		Heave		Pitch	
		Mean RMS	CoV	Mean RMS	CoV	Mean RMS	CoV
ME	Bladed	0.41	0.00	9.74	0.00	0.31	0.00
ME + PF	OrcaFlex, "Charm3D+FAST", "Simo+Riflex+AeroDyn", "Bladed Advanced Hydro Beta", Riflex-Coupled, HydroGast, DeepLinesWT	0.30	0.08	1.88	0.41	0.07	0.27
PF + QD	FAST, "SIMPACT+HydroDyn", UOU+FAST	0.32	0.16	1.64	0.22	0.08	0.17

Table 5.8: CoV values of wave frequency comparisons between the mean RMS values of the primary hydrodynamics groups

Model 1	Model 2	Surge	Heave	Pitch
ME	'ME + PF'	0.23	0.96	0.89
ME	'PF + QD'	0.16	1.0	0.84
ME + PF	'PF + QD'	0.07	0.10	0.09

5.4.2 Wave frequency range

When the frequency range is reduced to 0.05 – 0.25 Hz, the motions become a direct result of the wave excitation. Figure 5.2b, describing the CoV of the pitch RAOs, had shown that excluding low-frequency ranges increases the consistency of motion estimations significantly. The change also means that the surge and pitch resonant responses are eliminated from the motions. A similar order to the previous section is followed below to present the model uncertainty in this limited range.

The data regarding the primary groups are summarised in Table 5.7. It can be related directly to Table 5.4. The most noticeable change is in 'ME+PF', which shows a significant decrease regarding their disagreement in the surge and pitch modes. The 'PF+QD' results show smaller changes regarding the CoV values. Since the 'PF+QD' results rely on the same hydrodynamics module, it is as expected. The behaviour is similar in Tables 5.4 and 5.7.

Table 5.8 reveals that the disagreement between models drops significantly when low-frequency responses are not considered. Surge fares better than heave and pitch modes for Morison based models. The cause may be the distance of the surge eigenfrequency from the wave excitation range. The discrepancy in heave may be reasoned from the resonant responses coinciding with the wave excitation range. The heave motion in Figure 5.3b had already noted differences in model behaviour on each side of the resonance peak, which happens at the eigenfrequency of heave at 0.06 Hz. Similarly, pitch mode resonates close to the lower edge of the wave excitation. It can be estimated from this table that excluding the potential flow theory makes a notable difference around the resonant regions.

Table 5.9: CoV of all hydrodynamic models in wave frequency range

Model 1	Model 2	Surge	Heave	Pitch
'ME + (IWL + IP)'	'PF + ME'	0.22	1.00	0.85
'ME + (IWL + IP)'	'PF + ME + (IP)'	0.24	0.91	0.89
'ME + (IWL + IP)'	'PF + ME + (IWL)'	0.29	1.10	0.86
'ME + (IWL + IP)'	'PF + ME + (MD + NA) + (IP + IWL)'	0.17	1.04	0.87
'ME + (IWL + IP)'	'PF + ME + (QTF/NA) + (IP + IWL)'	0.19	0.68	1.13
'ME + (IWL + IP)'	'PF + QD'	0.25	1.02	0.90
'ME + (IWL + IP)'	'PF + QD + (QTF)'	0.12	1.00	0.81
'PF + ME'	'PF + ME + (IP)'	0.02	0.16	0.07
'PF + ME'	'PF + ME + (IWL)'	0.08	0.22	0.02
'PF + ME'	'PF + ME + (MD + NA) + (IP + IWL)'	0.05	0.09	0.03
'PF + ME'	'PF + ME + (QTF/NA) + (IP + IWL)'	0.03	0.48	0.55
'PF + ME'	'PF + QD'	0.03	0.05	0.09
'PF + ME'	'PF + QD + (QTF)'	0.10	0.00	0.06
'PF + ME + (IP)'	'PF + ME + (IWL)'	0.06	0.38	0.05
'PF + ME + (IP)'	'PF + ME + (MD + NA) + (IP + IWL)'	0.07	0.25	0.04
'PF + ME + (IP)'	'PF + ME + (QTF/NA) + (IP + IWL)'	0.05	0.33	0.49
'PF + ME + (IP)'	'PF + QD'	0.01	0.21	0.02
'PF + ME + (IP)'	'PF + QD + (QTF)'	0.12	0.16	0.13
'PF + ME + (IWL)'	'PF + ME + (MD + NA) + (IP + IWL)'	0.13	0.13	0.01
'PF + ME + (IWL)'	'PF + ME + (QTF/NA) + (IP + IWL)'	0.11	0.67	0.53
'PF + ME + (IWL)'	'PF + QD'	0.05	0.17	0.07
'PF + ME + (IWL)'	'PF + QD + (QTF)'	0.18	0.22	0.09
'PF + ME + (MD + NA) + (IP + IWL)'	'PF + ME + (QTF/NA) + (IP + IWL)'	0.02	0.56	0.53
'PF + ME + (MD + NA) + (IP + IWL)'	'PF + QD'	0.08	0.03	0.06
'PF + ME + (MD + NA) + (IP + IWL)'	'PF + QD + (QTF)'	0.05	0.09	0.09
'PF + ME + (QTF/NA) + (IP + IWL)'	'PF + QD'	0.06	0.53	0.47
'PF + ME + (QTF/NA) + (IP + IWL)'	'PF + QD + (QTF)'	0.07	0.48	0.60
'PF + QD'	'PF + QD + (QTF)'	0.13	0.05	0.15

If the potential flow theory is included in the model (i.e., 'ME+PF' and 'PF+QD'), the disagreement does not exceed 10 percent. The CoV drop of 0.46 to 0.06 is remarkable in the surge mode. The likely cause of this change is removing the resonant amplitudes at 0.01 Hz and disregarding the differences in the estimation of the peak value. Pitch similarly drops from 0.37 to 0.09. This set of results points out that the major disagreement regarding motion responses occur at lower frequencies, and there is higher consistency in the estimations due to wave excitation.

The one on one evaluation of all models in Table 5.9 shows that the uncertainty is significantly reduced from the detailed assessment in Table 5.6 that represented the combined frequency range. The comparisons to the Morison model also reduces to approximately 20 percent in the surge mode. In heave and pitch, the values are significantly higher. Therefore, the estimation of responses around resonant areas can be identified as a primary source of disagreement between models. The implementation of 'PF + ME + (QTF/NA) + (IP + IWL)' may still be doubtful since it is highly divergent from the rest of the 'PF+ME group'.

Table 5.10: CoV values of the users of NREL's FAST

Wave elevation	Surge	Heave	Pitch
0.08	0.12	0.19	0.16

5.4.3 User errors and differences in modelling practices

The set of users that preferred NREL's FAST allow to consider another perspective on the data. When focused on a single code with identical mathematics, the uncertainty is limited to the user's knowledge and the modelling practices. Theoretically, in this type of a study where all input data is fixed, there should be no differences. In practice, this is not the case as shown in Table 5.10. The data reveals that slight variations were present in the wave spectrum. It is likely that this detail has reflected in the estimation of motions where 15 percent CoV values is an average. The takeaway from this set is that the human factor in modelling practices and code usage cannot be neglected. A method of reducing this type of errors would be to provide a detailed documentation to clarify doubts. An alternative is to automate most parts of the process to leave no room for error as discussed in [143]. A very high number of variables come together to produce the results of a load case. For this reason, it is challenging to point out the root of the variations. However, user errors in complex codes remain a factor that needs to be considered.

5.5 Mooring models

The mooring models of the participants are limited to three approaches. A quasi-static (QS) model and two dynamic models based on finite elements (Dyn/FE) and lumped mass (Dyn/LM) are used. Only one dynamic code depends on the lumped mass model, while others prefer finite elements. There is a distribution of 6 dynamic and 5 quasi-static codes.

Figure 5.4 shows the spectral densities of the mooring line tension located at the incoming wave direction (Fairline 1) with the resulting RMS values in Table 5.11. The behaviour tends to show two distinct groups. The LF and WF regions do not appear to be the main concern, unlike the motions. In this case, the divergence of estimations inside the wave excitation region is even more apparent than in low-frequency regions.

Table 5.11: Mean RMS values of the mooring models

Base Model	Codes	Mooring tensions at fairlead 1	
		Mean RMS	CoV
QS	CENTEC-(FAST), Goldwind-(FAST), IST-(FAST), NREL-(FAST), POSTECH-(Bladed), SWE-(SIMPACT+HydroDyn), UOU-(FAST)	768.74	1.66
FE/DYN	ABS-(CHARM3D+FAST), CeSOS-(Simo+Riflex+HydroDyn), MARINTEK-(RiflexCoupled), NTUA-(HydroGast), PRINCIPIA-(DeepLinesWT)	1762.6	0.72
LM/DYN	4Subsea-(OrcaFlex)	864.10	0.00

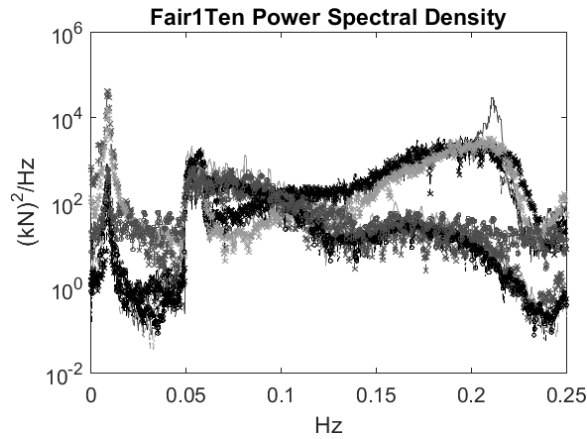


Figure 5.4: Spectral density of the tension at fairline 1

Table 5.12: CoV of the mean RMS values of the mooring models

Model 1	Model 2	CoV of Tension at Fairline 1
'QS'	'FE/DYN'	0.56
'QS'	'LM/DYN'	0.08
'FE/DYN'	'LM/DYN'	0.48

Table 5.12 compares the RMS and CoV values. In this aspect, there is a significant difference between the dynamic and quasi-static models. However, an interesting finding is that the lumped-mass dynamic approach delivers results almost identical to quasi-static codes. The coefficient of variation is 8% when compared to the 'QS' approach. The difference between the finite elements dynamic and the quasi-static estimations reach 56%. Since both models include potential flow for hydrodynamics (see Table 5.3), the divergence is unlikely to stem from the hydrodynamic models. Before, it was clarified that including the 'PF' in calculations reduces the overall disagreement between codes.

The elastic behaviour of the mooring lines is affected by their total length, which is approximately 835 meters for the semisubmersible. This information, coupled with the experimental comparison of the quasi-static mooring calculations discussed in Chapter 3 and published by [39, 53], may suggest that the QS model might be failing to capture the full extent of the mooring line dynamics.

5.6 Concluding remarks

A quantitative evaluation of the motion and mooring load estimation of the OC4 Phase II participants was provided for the DeepCwind semi-submersible wind turbine platform. A mathematical filtering method was used to avoid skewing the data with outliers. The load case was given as a white noise spectrum with only head waves and no wind.

The motions prominent in head waves (i.e., surge, heave, and pitch) were compared based on the hydrodynamics model used for obtaining them. It was clarified that the agreement between the results relates to the region of the wave spectrum. For this reason, separate evaluations were carried out in the wave frequency range and the combined range of the low-frequency and wave

frequency regions. Inside each section, initially, the groups that use similar primary approaches were compared within themselves. Then a comparison of the groups that base their approach on the same primary model was given. Finally, alterations to the main models were also examined by providing all possible combinations of the hydrodynamic models. The inclusion of potential flow theory seemed to consolidate results. However, alterations to the models affected the behaviour. The data pointed out that removing resonant areas resulted in the Morison Equation performing closer to the potential flow theory. The differences in results due to user errors and modelling practices were emphasised.

A similar methodology was utilised to extract the uncertainty in mooring models. Unlike the hydrodynamics, the mooring spectral densities did not seem to be significantly affected by the frequency range but depended on the approach taken. Quasi-static and finite elements dynamic methods emerged as two main groups with a disagreement between themselves. The lumped-mass dynamic method provided results closer to a quasi-static approach.

Automation of the time domain code for model building and sequential simulations

6.1 Introduction

The OC4 study in the previous chapter lists that 8 out of the 24 participants were using FAST [124] as their simulation tool [49]. LIFES50+ is another collaborative project reporting similar preferences where six out of nine participants have worked with FAST [144]. One reason for this preference is FAST's availability as an open source code, signifying that it may be improved by any willing researcher. That approach lead to a considerable community of users. Consequently, its current performance has been evaluated in various studies, clarifying the level of confidence that can be placed on the code [39, 53, 54].

While FAST has a significant user community and is frequently updated, most of this work is geared towards improving individual modules of the code (e.g., hydrodynamics, aerodynamics, mooring model). There isn't much emphasis placed on increasing the ease of use or removing the types of errors discussed in Chapter 5. Overall, system of usage stays identical to that of the previous versions. The current text-based input system of FAST uses one input file for each module. Regarding flexibility, there is a significant advantage that comes from text-based entry. However, as it stands, this potential is not explored. Consequently, quickly assessing a series of load cases turns out to be cumbersome. The setup requires constant interaction with multiple files for each simulation. Between

Published in: E. Uzunoglu and C. Guedes Soares. Supervisory system for the automation of model building and simulations with the wind turbine code FAST. In C. Guedes Soares, editor, *Progress in Renewable Energies Offshore*, pages 627–635. Taylor & Francis Group, London, UK, 2016. ISBN 978-1-138-62627-0

these runs, no consistency is enforced. The user is expected to revert the changes that were introduced with a load case before starting the next setup. The FAST package includes MATLAB scripts to read the input files. However, they forgo the introduction of a system. On the contrary, taking advantage of the text-based entry and a systematic approach, the code's usage may be simplified, and consistency of input data can be enforced. This change also would lead to reduced errors, fewer repetitions, and open up possibilities that come from unsupervised simulations.

The output of FAST is given in text or binary files. In almost all cases, the user is left with additional steps to confirm that the code has delivered the intended data. If a series of simulations were run, the output files multiply, requiring considerable verification time to load files and plot results. Additionally, the time series of stochastic data (e.g. irregular waves) are better represented in spectral densities and response amplitude operators. FAST's output contains all necessary information to present this data automatically.

For these reasons, it is beneficial to develop a modular structure for making models and running load cases without intervention. This approach saves time for the user and lets them concentrate on the results. This chapter provides a set of modules to deal with the input and output operations to minimise possible input errors and decrease analysis times. It focuses on simplifying the workflow and emphasises what can be readily made available. Contrary to the post-processing tools such as MCRUNCH [145] which require additional parameters, the described method aims to provide the maximum output using the minimum extra input. The modules are built to be generic, meaning that a single module is utilised for all input files and are independent of the developments in FAST. They work for all existing versions and will also work on the future versions unless the file structure is drastically changed.

The setup described below includes input and output processing. A load case matrix (i.e., rectangular form of data entry) deals with the inputs. The outputs are given as plots of channels, spectral densities, response amplitude operators, static equilibrium points, and a backup of the input data. Emphasis is placed on the system as opposed to coding practices. Model calibration using linear regression is used as a demonstration. Sequential simulations, model building, calibration, and optimisation are the uses for the proposed approach.

6.2 System setup for automation

The current section presents a discussion on how the manageability of the system may be increased with a systematic approach. It is important to note that while each module has its purpose, making everything work together is the primary goal for efficiency. The major issues that cost time are introduced below and addressed in their respective sections.

Each module of FAST has an input and output setup confined within its related file. Therefore, increasing the number of active modules increases the user's interaction with the input files. Another

alternative would be to use a centralised input file, which would cause significantly reduced manageability given the high number of variables. Output file format provides the option of choosing between an ASCII and a binary file.

6.2.1 Advantages and disadvantages of text-based input and output

The modular structure of FAST as explained above, signifies that the user will have to go through several files to set up a test case. As the number of modules increases, the number of files to edit also increases. Consider the model of a floating structure with the turbine, tower, platform, and the moorings. In the simplest case, the user needs to go through the wave and wind files to set an environmental condition. This means editing a minimum of two text files and several variables. Then FAST is run, and the output is obtained. Likely, it will have to be saved by the user into a memorably named folder to be analysed later. These steps are repeated for each simulation.

With the number of variables that FAST uses, it is rather possible to forget values that would need to be defaulted back for the next iteration. A common issue of dealing with multiple files is overlooking data that is changed less often. Without graphical output, such errors are not realized until post-processing is carried out at a later stage. FAST does not provide a method of confirming if the simulation was correct or an input step was overlooked. Importing files and plotting figures for these confirmations becomes a time-consuming process. If errors are encountered at these stages, all the input files will have to be rechecked for values that might be left out. As the last simulation might belong to any load case at the time of post-processing, each variable needs to be verified one by one.

On the other hand, the text-based input structure means that values may be calculated externally and integrated into the system through batch-processed text. A visual editing tool for automation beats the purpose if the user is asked to click input boxes and type in the values. The result may be an unintended loss of time, at the cost of simplified data entry. These systems like FAST Lognoter [146] have their advantages at the expense of flexibility. However, they may become useful for people unfamiliar with the codes. Conversely, using manipulated text files, any variable that FAST allows may be handled by external codes using parametric approaches, such as the data related to the geometry of the platform [132].

6.2.2 Systematising FAST's input-output procedure

The following paragraphs explain how to systemize the procedure so that only modelling decisions and detailed post-processing is left to the user. The summary of the progression is as follows: tabular data in the form of a matrix (termed the load case matrix from here on) is taken as the main input. For data entry purposes, if a variable was altered once, it is required to set it again for the next simulation. This proposed method enforces consistency and does not allow lapses. The case name as defined by the user is read from this load case matrix. The input files of FAST (referred as the input file from here on) are pre-processed, changing the variables to their corresponding values in the load case

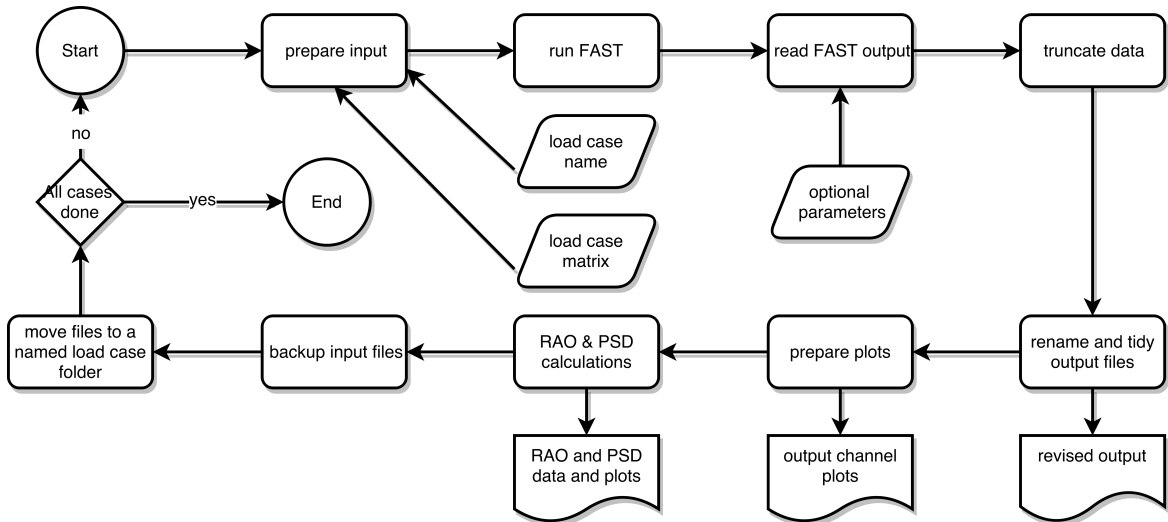


Figure 6.1: Flowchart systematization of the I/O process

matrix. FAST is run. The output is read from the files, renamed, and moved to an output folder. Any post-processing to arrive at the final data set is carried out at this stage. An example to this type of post-evaluation is extracting sections that match certain conditions of the wave height and azimuth angle. The channels are plotted with the truncated data. A backup of the input files is taken into a separate folder, omitting certain file extensions. If required, response amplitude operators are plotted. Optionally, the static equilibrium points are calculated. The next simulation is started.

In this setup, the load case matrices are prepared only once, and the simulations are set to run without user intervention. The output, plots, response amplitude operators, and backups of the input files are obtained for verification and distribution. Figure 6.1 presents an overview of the process.

6.3 Pre-processing

The pre-processing stage is composed of two parts: setting the load case matrix up and the preparation of FAST's input data. This section deals with the input file, which requires two different types of data manipulation. Using "varname" to represent the variable name, and "value" for the values, the formulation may be presented in a verbatim format in the following forms:

The primary format:

```
value - varname - comments
```

The tabular Format (A) of k rows and n columns:

```
varname 1    varname 2    ...    varname n
value(1,1)  value(1,2)  ...    value(1,n)
...          ...          ...    ...
value(k,1)  value(k,2)  ...    value(k,n)
```

In practice, a third form exists as a combination of the primary and the tabular formats. It is dealt with in the manner that it is defined (i.e., as a combination of the two formats):

varname	total_rows_of_tabular_data		comments
value(1,1)	value(1,2)	...	value(1,n)
...
value(k,1)	value(k,2)	...	value(k,n)

Beyond these three types, there are no differences particular to the modules of FAST. Addressing the data with this broad classification of three groups instead of focusing on each module's input file generalises the problem and avoids dealing with each file separately.

6.3.1 Load case matrix

The load case matrix is a tabular form of input that lists the names of variables to be altered in the first row, and their respective values in the following rows. A sample is presented in Table 6.1. The data shows that all variables such as platform surge (PtfmSurge) repeat throughout the table. At first glance, this approach may look superfluous. However, consider a scenario, where a run of cases 1.2 to 1.3c were carried out. The final input files will be left with the initial platform pitch (PtfmPitch) set to eight degrees. On another set, the user would like to test only 1.3a. In this condition, not replacing PtfmPitch back with zero would result in a load case where the initial pitch and surge are non-zero values. This is clearly not the intention of the user. Similarly, going onto 2.1 would leave an initial amplitude coming from the free decays (1.3a to 1.3d). Following onto one of the 1.3 load cases from 2.1 would cause the FAST to generate unwanted waves. Therefore, a fully filled-in matrix format is crucial in enforcing consistency between runs. Sequential simulations should not be built incrementally.

In FAST, most of the tabular input data represent the model setup rather than the load case setup. As examples, it may contain the definitions of the mooring lines, the tower, or the blade's properties. In these cases, the input is given in the same structure above but an array data format replaces each value. There are programming languages that allow this kind of input (e.g., MATLAB).

Table 6.1: Sample load case matrix representing the platform related variables of the OC4 Code Comparison studies

Load Case	Ptfm Surge	Ptfm Sway	Ptfm Heave	Ptfm Roll	Ptfm Pitch	Ptfm Yaw	Wave Mod	Wave Hs	Wave Tp
1.2	0	0	0	0	0	0	0	0	0
1.3a	22	0	0	0	0	0	0	0	0
1.3b	0	0	6	0	0	0	0	0	0
1.3c	0	0	0	0	8	0	0	0	0
1.3d	0	0	0	0	0	8	0	0	0
2.1	0	0	0	0	0	0	1	6	10

Two options are present regarding the setup of load case tables. All variables belonging to multiple input files can be set out in a single file. Alternatively, each FAST input file may have its own tabular load case file. The second option is preferable. The justification is that through this approach each variable in the load case matrix may be checked to see if it exists in FAST's input file. Consequently, trying to alter wrongly named variables may be prevented by implementing proper error reporting.

6.3.2 Altering the primary data format

Altering the primary data format of FAST files is a linear process. The input for this module is the case name, the load case matrix, and the respective FAST input file. After assuring that the input file and the load case matrix are both present, these additional checks must be asserted:

1. Each variable to be changed must be defined only once in the load case matrix.
2. Each load case should be defined only once in the load case matrix.

The remaining steps may be summarised as reading the input file and locating the variables that match the list in the load case matrix and replacing them with their new values. An exception is made when one variable name appears twice in FAST's input file. This case happens when the variable name occurs once after its numerical value and once more in the comments. An easy way of avoiding problems caused by this structure is to look for the earliest occurrence of the variable (i.e. if a variable name is present starting at the 5th character of the line, and another copy is present starting at the 21st character of the line, the line number belonging to the 5th character is taken). The pseudo-code for the algorithm is given in Table 6.2. An optional setting for this module is to pad the variable values and names with trailing blanks. In this way, the variable names line up and the file is easier to read in text editors.

6.3.3 Altering the tabular data format

The method to edit tabular data is a variation of the default format. It will be described here as a summary of steps. The problem of locating this input numerically arises from identifying the beginning and the end of the table without given information on the number of rows of the data. In this case, extracting this information is possible by utilizing the default input format of "*numeric variable – variable name – comments.*" Unless an input line follows this setup, it can be readily classified as tabular data.

To locate the beginning of the tabular format, a "search variable" that occurs right before the tabular input is defined. Then, the end of the tabular input is located by searching where "numerical variable – variable name – comments" setup begins again. Finally, the newly given table replaces the data in between.

If the data is not given in the combined format (i.e., the format where the row before the table contains data related to it), then the "search variable's" line is left intact. Otherwise, the row that

Table 6.2: Pseudocode for input editing

Algorithm for FAST input editing

1. **Read** load case matrix
2. **Assert** each variable defined only once in load case matrix (LCM)
3. **Assert** each load case is defined only once in the LCM
4. **Read** FAST input file
5. **For** k = all variables (NVAR) in LCM
6. **Find** the rows where NVAR exists in the input file
7. **Get** the earliest occurrence of NVAR as valid
8. **Add** variables and column numbers (NROW) to be altered into matrix (RMAT)
9. **End For**
10. **Case (default input type)**
11. **For** k = all rows of FAST file
12. **if** current row number exists in NROW
13. **Rewrite** the input line using RMAT. Keep variable name and comments
14. **else**
15. **Leave row** intact
16. **End If**
17. **End For**
18. **Case (tabular input type)**
19. **For** k = all rows of FAST file
20. **if** current row number exists in NROW
21. **Locate** beginning and the end of the table
22. **Rewrite** the table using new tabular data value in RMAT.
23. **Replace** the data line if it includes the number of table rows
24. **else**
25. **Leave row** intact
26. **End If**
27. **End For**
28. **Save** new file

contains data related to the table is updated to reflect the alterations. For instance, count of the total number of rows for the upcoming tabular data is changed. This format may have extra lines between the search variable and the table, and this data needs to be provided externally. This type of input is primarily used to model new structures. Tower, blade, airfoil, and mooring setup are examples. The airfoil files are not numerical, but contain text strings listing the names of the airfoil files. Here, the number of lines is read from the line defining the number of airfoil files, which is in the default FAST input format.

6.4 Post-processing

Post-processing modules include algorithms to assess the output with less effort. The requirements of this stage are as follows:

- The output data should be understandable at a glance.
- Simulations should be classified into folders with the load case names.

- Basic data such as the response amplitude operators and static equilibrium points needs to be calculated
- The input should be backed up in case the user wants to verify the files.

The modules for these works and their optional parameters are explained below.

6.4.1 Output processing

If the output is in a binary format instead of text, it is preferable to use NREL's provided MATLAB subroutine as the file is definitely in FAST's format. For the ASCII output, reading the files may look to be a straightforward case of skipping comment lines, and returning the remaining data as a matrix. However, at this point, it is better to generalise the output module. This way, if a delivery in a project (e.g., OC4 [48]) requires a different output format, it can be provided effortlessly. An added benefit of generalisation is that when it is necessary to work with altered files again, there is no need for a readjustment of the codes. The ASCII output format is:

Comments			
...			
"Time"	CH{1}name	...	CH{n}name
"s"	CH{1}units	...	CH{n}units
t	CH{1}data	...	CH{n}data
...

The generalisation of file reading is carried out by locating the row that starts with "time" and considering all previous lines as comments. This approach introduces an acceptable limitation where the comment lines cannot start with the word "time". On the other hand, it allows a generalised code that can read and assess many FAST type output files regardless of their setup. With these considerations, the output file is reprocessed with the following extra options:

1. Comment line editing: comment line count is altered to match a given number by removing or adding lines (e.g., with the purpose of delivering to projects with this constraint). Remaining comments are updated if needed.
2. Set wave position: the time series is edited to match the wave position to a certain phase. It is used for comparing records of different models in regular waves. The initiation of the data is set to start at the specified phase of the wave, and the total simulation time is truncated to a given limit. This option is included in FAST for the start of the simulation. However, the usual requirement for comparison is the phase after the transient stage. This option remedies the problem by extracting a section of a simulation that meets the criteria.

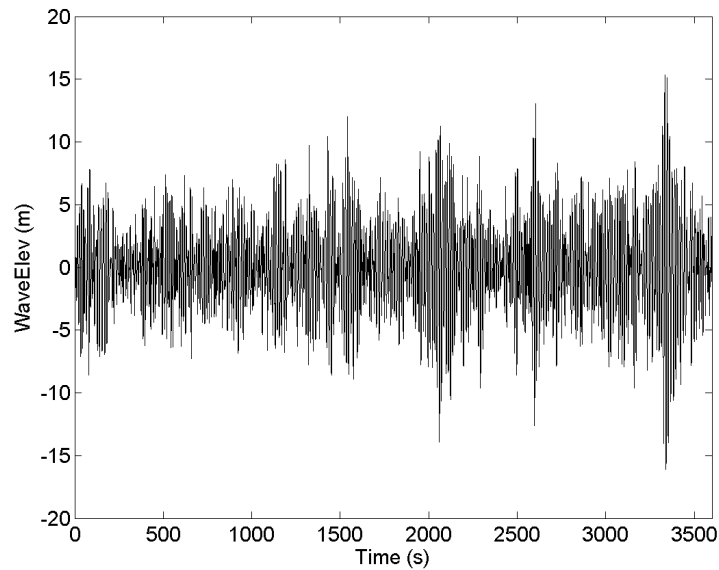


Figure 6.2: Time series plot of a wave; the headers and units are taken from the FAST output file

3. Set azimuth position: similar to waves, the turbine blade's azimuth position at the initiation of the new time series is set to the required angle. The data is then truncated to extract a given simulation time.
4. Set azimuth and wave position: Merges the two options above to extract time domain simulations beginning with a given wave phase and azimuth angle.
5. Header sorting: Presents an option to revise the final data into the specified header order. As of FAST version 8, the output order keeps changing depending on the involved modules. Hence, an extra separate subroutine here saves considerable save time on unnecessarily editing text files when comparing data sets.

6.4.2 Plotting

Since this system is built on sequential simulations and automation of the process, the output will inevitably be a folder with the results of multiple load cases. Accordingly, it is useful to provide plots so that the user can verify the simulation easily. Figure 6.2 is a sample presenting the wave elevation as a function of time. These plots are inherently available from FAST's output. The files have the headers, and the units of each channel along with the data. Hence, the headers and the units of the axes in the figure are taken from that output file. Then, the file is saved using the following naming convention (curly brackets are used to indicate variables):

$$\text{CH}\{\text{Channel\#}\}-\{\text{Channel name}\}.\text{png}$$

6.4.3 Response amplitude operators

Regular time series plots give only a limited idea on simulations that contain stochastic data. The response amplitude operators and the spectral densities are necessary to understand the behaviour of the numerical model. Given the time series, and the channel name, the power spectral density (PSD) and the response amplitude operators (RAO) are calculated with the following formulations through Fast Fourier Transforms (FFT):

$$PSD_{wave} = FFT(wave\ data) \quad (6.1)$$

$$PSD_{motion} = FFT(motion\ data) \quad (6.2)$$

$$RAO = \sqrt{\frac{PSD_{motion}}{PSD_{wave}}} \quad (6.3)$$

The channel names in the output file are used to get the units of the RAO and PSD plots. The x-axis is given in Hz, and the y-axis units are calculated using $[\{\text{channel unit}\}^2/\text{Hz}]$. The same approach applies to rad/s as the x-axis, however, demands unit conversion for the y-axis.

A practical note on the implementation of Equations 6.1, 6.2, and 6.3 as functions is to consider that the channels in the output files will change column numbers. The platform heave motion at channel 6 may end up at channel 8 on the next simulation due to the presence of some additional data. Therefore, the code needs to work with channel names instead of channel numbers.

6.4.4 Assessment of static equilibrium

Visually, static equilibrium may be checked through plots by confirming the final values of the time series. An alternative to visual inspection is to average last n values of a series. However, at the end sections, there will be some oscillatory motion and complete standstill will only be achieved after a very long transitional period. These two concerns regarding numerical confirmation may be addressed by working with a single input and three-value output approach. The input is the number of seconds (n) to be evaluated at the end of the time series. The three output values are the mean value (μ), the standard deviation (σ), and the relative standard deviation (RSD) of the sampled points. RSD is also termed the coefficient of variation:

$$RSD = \frac{\sigma}{\mu} \quad (6.4)$$

This output structure makes it possible to decide if the motion has reached a steady state, or is still oscillating. The RSD provides normalisation where the values of all channels actually differ by magnitudes. It should be calculated after rounding the output down to a limited number of significant

Table 6.3: A sample of suggested output format for numerical verification of static equilibrium

	Platform pitch (deg)	Tower base moment (kN)	Yaw bearing moment (kN)
Case 1: Unsteady system response			
μ	0.07	1765	896
σ	0.00	1620	285
%RSD	0.00	92	32
Case 2: Steady system response			
μ	0.07	1808	900
σ	0.00	7.3	0.1
%RSD	0	0	0

digits. Otherwise, rounding errors of small numbers will lead to unrealistically high RSD values for stable systems (e.g. RSD of $10^{-2}/10^{-6}$).

A sample of the proposed static equilibrium output is given in Table 6.3. Two cases are listed: a steady phase, and an oscillating phase. In case 1, the values show that although the platform is mostly stable in pitch, there is an oscillation at the tower, judging by the significant deviations in the yaw bearing and tower base moments. Case 2 represents the system in a steady state where there are only negligible oscillations at the tower base.

6.4.5 Input backup

Backups serve to verify input files and to repeat simulations. The backup module should rename the output files using the load case name and move them to an identifiable subfolder. It needs two considerations:

1. It is ineffective regarding file operations and storage space to have a complete copy of the input folder. It may contain unrelated files that don't need to be backed up.
2. The data should encompass the subfolders that include files necessary for the simulation to be repeated. These files can be the wind, hydrodynamic, and the airfoil information.

From this information, the backup subroutine needs two options: a list of subfolder names to include and a list of extensions to omit. The subfolder names should be based on inclusion (i.e., list of folders to be added) because the working folder may get larger in time. An exclusion approach would mean rewriting the list each time a folder is added to the main directory. Conversely, excluding certain file extensions is an easy way of generalisation for saving time and space on file operations. These omitted files may include the executables or large wind field files.

6.5 Application: linear regression based volume calibration process

The system of codes listed above serves several purposes. The most basic use is running a series of simulations on a model that has already been built. This application is rather simple, and the only requirement is making the load case matrix. When the matrices are available, obtaining a comparison of two or more simulations is straightforward. Sequential runs without supervision also provide access to sensitivity analysis. Additionally, with the help of external codes, it is possible to build and optimise a new numerical model.

The example here describes a different use in an iterative calculation scenario to adjust a numerical model's setup. Consider an experimental program where the weight of the turbine, tower, and the platform are reported. Additionally, heave and pitch values at the static equilibrium are given. In any experiment, the measurements include a level of uncertainty. In the case reported in [52], the weight needed small adjustments to match the measured data at equilibrium. Out of the three components (i.e., turbine, tower, and the platform), the platform was chosen as the one with the highest level of uncertainty attached to its weight. The decision was to adjust the floater's volume to obtain zero meters for the heave static equilibrium.

For this purpose, initially, the system was modelled as documented in [48] but the platform was given an arbitrary initial volume of 13,000 m³. At this value, the first FAST simulation delivers a heave static equilibrium of 0.21 meters. Taking a second iteration of 14,000 m³ returns a heave amplitude of minus 2.4 meters. Once at least two points are available, linear regression provides 13,919 m³ as the final volume of the numerical model. The third run confirms the static equilibrium happening at zero meters of heave. The pseudo-code to set this setup up is given in Table 6.4.

The approach in this section can be extended onto multi-variable optimization. In this case, computational time required by the simulations will come into question, and the applicability of optimization routines such as gradient descent will have to be evaluated under computational power constraints.

6.6 Concluding remarks

The chapter described a set of codes that aim to facilitate the usage of NREL's FAST and make it more efficient. The text-based system provides time savings by allowing input to be entered automatically compared to typing manually. A single algorithm covers all data files and is compatible with the past and current versions of FAST. The method will also work on the future versions provided that the system of data entry is not drastically changed.

Imposing a matrix type data entry for input enforces consistency between simulations and reduces possible errors. The pre-processing and post-processing system makes use of a minimum input with maximum output approach. Therefore, it differentiates itself from other post-processing codes that

Table 6.4: Pseudocode for mode calibration

System example for model calibration

1. **Read** load case matrix
 2. **Assert** each variable defined only once in load case matrix (LCM)
 3. **Assert** each load case is defined only once in the LCM
 4. **Set** initial volume to 1300
 5. **Set** heave tolerance to 0.005
 6. **While** heave > heave tolerance
 7. **Prepare** FAST input files
 8. **Run** FAST with the iteration volume
 9. **Read** FAST output files
 10. **Plot** data
 11. **Get** static equilibrium
 12. **Confirm** static equilibrium
 13. **If** RSD > 0.05
 14. **Extend** simulation time in LC matrix
 15. **Set** heave = 1
 16. **Backup** input
 17. **Go** to 6
 18. **End if**
 19. **Backup** input
 20. **Add** data points for linear regression (heave, volume)
 21. **Calculate** new volume with linear regression
 22. **Add** new volume to LCM
 23. **Change** iteration volume to new value in LCM
 24. **End While**
-

require additional input to function. The system delivers plots of all data, backs up information, calculates the response amplitude operators, spectral densities, and numerically assesses static equilibrium positions as an addition to the standard text output.

The usage was demonstrated on an iterative model calibration process. In this scenario, the codes were asked to match a floater's experimental volume by adjusting the heave static equilibrium. This provided method serves for sequential simulations, model building, and optimization. It adds flexibility and it is easy to implement.

Multi-purpose parametric modelling for hydrodynamic calculations

7.1 Introduction

This chapter presents a numerical approach to creating quadrilateral meshes for hydrodynamic calculations and obtaining mass properties from the same mesh. This type of double objective model will be referred to as a multi-purpose model from here on. While it is mainly intended as a replacement for the commonly used spreadsheet methods in initial design of floaters, the mass calculations apply to any grid mesh. Matrix data are used to input the geometry. Partial solutions of a section of the model provide the mass and volume distribution in space. Integration for the entirety of the structure delivers the model weight, volume, and inertia. The output is then fed to WAMIT to validate the model's use in hydrodynamic calculations. The tool was initially developed for the design of offshore platforms for wind turbines [132, 147], but it allows to model a wider range of structures. To illustrate this point and its usage, the examples throughout the text are diversified. The validation of the code is performed through comparisons with Rhino3D combined with its PanelingTools plug-in, ANSYS, and MultiSurf models for volume, mass, and hydrodynamic properties. It should be noted that the number of software packages needed for comparisons also emphasizes the current lack of a consolidated solution. The concluding section contains a measure of performance to evaluate the method's efficiency in providing the 3D model and mass properties to be used in a system that requires iterative model building.

7.2 On modelling practices for hydrodynamic calculations

In settled industries such as shipbuilding, the design process begins with the cumulative knowledge from previous experience and may progress into improving an existing geometric form [148, 149]. Conversely, in novel applications such as floating offshore wind turbine platforms, the most favourable implementation is still under discussion [150, 151, 80]. In all cases, mathematical modelling of static and dynamic behaviour requires a correct representation of the mass and inertia. If the structure is afloat, underwater geometry related hydrodynamic coefficients become additional requirements. These properties are closely linked with the geometry of the platform, hence, involve CAD software to get reliable estimates. The same reasons that make the use of these sophisticated tools and software favourable at later design stages present a complication at the earlier design stages. When the knowledge is limited to a concept, preparing a set of iterations of 3D models for parametric studies as in [78] can become tedious. Another problem is the specialisation of tools. Some codes are made to perform a specific calculation well while expecting input from another source. For instance, WAMIT [130] is a verified code in hydrodynamic calculations, provided that the six by six mass matrix is correctly delivered. Erred mass will simply lead to errors in estimated motion responses. Accordingly, this data needs to be prepared externally. The procedure needs to be repeated for each iteration of the concept.

To remedy this problem in new designs, researchers usually revert to avoiding sophisticated 3D modelling tools entirely and rely on spreadsheet calculations and simplifications, as outlined in [81] and utilised in ([79, 82]. This case creates a substantial gap between the higher-complexity surface models such as non-uniform rational basis spline (NURBS) and the simple hand calculations on a spreadsheet. The issue is not only present at initial stages but also repeats itself from another perspective for optimisation studies. The two interlinked sides need to be considered in this regard: mass properties and hydrodynamics.

Obtaining the mass and inertia on a spreadsheet is less problematic when a partial analytical solution exists. Accordingly, one approach is to introduce simplifications to describe the model, removing some of its parts, effectively reducing it to a form that is broken down into solvable components (e.g., cylinders) [87, 152, 12]. This is not a generic solution, as it is inapplicable for a body that cannot be easily expressed as a set of basic shapes. Regarding hydrodynamics, a solution to the coefficients can be obtained from tabular data for members [96, 108]. However, if the platform requires a potential flow solution, they will not be accurate as it is discussed in an experiment-to-code comparison [58]. In that case, it is still necessary to build a 3D model despite the preliminary hand calculations. Furthermore, the entire breakdown and calculation process needs to be repeated if the structure is altered, as the solution is specific to a given body.

From the point of optimisation, another problem arises. A recently published work describing the evaluation of semisubmersible hulls for weight and heave motion [93] states that one of its main contributions is including mass as an optimization variable, unlike previous studies which took it as a

constant [84, 90, 91]. After starting from Bezier & B-Spline curves, the study assumes that the mass equals a statistically obtained constant multiplied by the surface area of a simplified version of the 3D model. The reduced geometry is given as a set of rectangular prisms without the curvatures and other details of the hydrodynamic model. In essence, the approach is a reversal to the spreadsheet calculation inside a complex system. The inertia is not mentioned; therefore, the study is limited to the heave mode in a manner similar to [85]. It should also be noted that a shortcoming of statistical data is that they do not exist for novel structures (e.g., wind turbine platforms, wave energy converters).

Another study that considers both mass and inertia, [92] assumes the mass and the radius of gyration to be based on percentages of the main dimensions, and takes a fixed position for the centre of gravity. The rationale behind this decision is not explained. For tension leg platforms, using an assumption of mass as in [90] is especially problematic considering the relation between the tendon tension and the structural weight. In the absence of proper inertia estimations, the pitching and rolling effects on the tensions are also overlooked. In this regard, with a large number of dependencies, it is clear that the mass properties should preferably be calculated, as opposed to assumed. While this estimation may be more complicated for structures designed for significantly variable cargo (e.g., tankers, bulk carriers, oil-and-gas platforms), a representative mass matrix with a higher precision can be obtained for fixed-loading type structures (e.g., floating wind turbine platforms).

From a purely hydrodynamical point of view, once the mass properties are calculated, the estimation of responses will require evaluating a suitably prepared mesh as in [153, 154]. The coefficients of the equations of motion rely on the underwater geometry, and even smaller changes reflect in motion dynamics [155, 128]. Hence, simplifications also lead to consequences such as altering the natural frequencies [156]. In sum, it is beneficial to devise a consolidated approach to the problem. A solution would be to implement the estimations of mass properties into the 3D meshes used in hydrodynamics while keeping the file format compatible. Additionally, the calculation method should be mathematically simple so that it can be implemented by other researchers in any programming language and should avoid commercial CAD tools. It is also preferable to use a numerical input format as it has advantages regarding parametrisation for iterative design. In that regard, specialised approaches exist for parametrising bodies such as ships [157]. However, with an increased number of unknowns in fields such as the design of floating wind turbine platforms, flexibility assumes a larger role. Hence, the solution should not be limited to an individual form.

7.3 Representation of a 3D geometry with quadrilaterals

The quadrilateral meshes utilised in panel method tools such as WAMIT are defined by the x , y , and z coordinates of each panel's four vertices (i.e., 12 values per panel). When two of the adjacent four vertices coincide, the polygon forms a triangle. The entirety of the structure is then represented as a combination of individual panels. The ordering of the vertices defines the surface normal direction, using the right-hand rule. In Figure 7.1, the coordinate system is presented. The darker shaded arrow demonstrates the normal facing the fluid domain, while the lighter shaded arrow

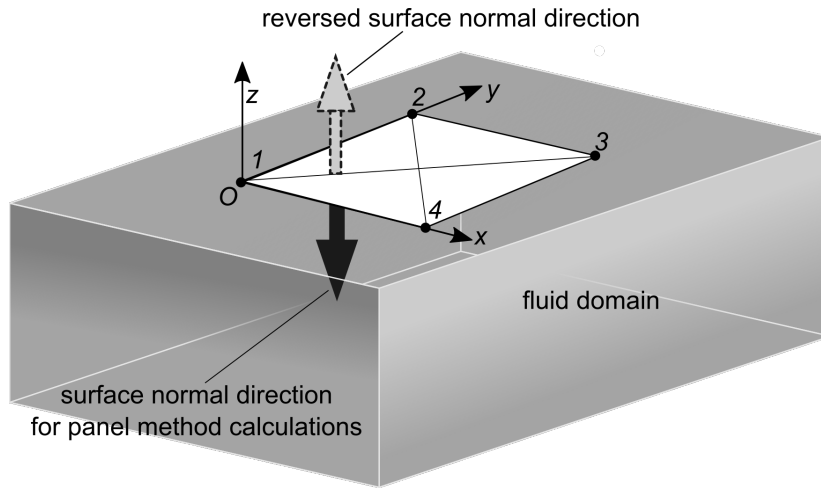


Figure 7.1: Origin, axis, surface normals, and vertex ordering

is the inverted normal. Panel method solutions require the normals to face the fluid domain. The inverse normal will be used to simplify mass property calculations.

The modelling process described below is divided into radius based and face based approaches. Radius based models encompass cylinders, cones, frustums, spheres and similar shapes that can be described as a function of their radii at a given height. Face based models have a broader range of applications. A triangular prism with an open bottom uses three faces. A rectangular prism consists of six faces. Eventually, the idea may be extended to a sphere as a set of connected quadrilateral panels. In this context, radius based models are a subset of face based models. In practice, having the radius based model option simplifies and speeds up the modelling. For this reason, both approaches are explained, starting with the radius based approach.

7.3.1 Radius based approach

Consider a quadrant of a disc, with the radius and the arc length divided as illustrated in Figure 7.2a. The polygon's z coordinates are identical, resulting in a flat disc on the xy-plane. Input data of this case are the radius (r), the number of segments between two consecutive edges (i.e., inner edge with a zero radius and the outer edge radius of r), the Z coordinate, and the reference angle (i.e., 90 degrees for a quadrant, φ_c). The number of segments on the radius (s_r) and the arc (s_p) are utilized to define the increments of r_{inc} and φ_{inc} respectively:

$$\varphi_{inc} = \frac{\varphi_c}{s_p} \quad (7.1)$$

$$r_{inc} = \frac{r_i}{s_r} \quad (7.2)$$

The information above suffices to express the location of the four vertices in Cartesian coordinate system as a function of Equations 7.1 and 7.2 and set the origin to $O(X_0, Y_0)$:

$$X_{i_1} = \cos(\varphi_i + \varphi_{inc}) \cdot (r_i - r_{inc}) + X_0 \quad (7.3a)$$

$$Y_{i_1} = \sin(\varphi_i + \varphi_{inc}) \cdot (r_i - r_{inc}) + Y_0 \quad (7.3b)$$

$$Z_{i_1} = Z_i + Z_{inc} \quad (7.3c)$$

$$X_{i_2} = \cos(\varphi_i) \cdot (r_i - r_{inc}) + X_0 \quad (7.4a)$$

$$Y_{i_2} = \sin(\varphi_i) \cdot (r_i - r_{inc}) + Y_0 \quad (7.4b)$$

$$Z_{i_2} = Z_i + Z_{inc} \quad (7.4c)$$

$$X_{i_3} = \cos(\varphi_i) \cdot (r_i) + X_0 \quad (7.5a)$$

$$Y_{i_3} = \sin(\varphi_i) \cdot (r_i) + Y_0 \quad (7.5b)$$

$$Z_{i_3} = Z_i \quad (7.5c)$$

$$X_{i_4} = \cos(\varphi_i + \varphi_{inc}) \cdot (r_i) + X_0 \quad (7.6a)$$

$$Y_{i_4} = \sin(\varphi_i + \varphi_{inc}) \cdot (r_i) + Y_0 \quad (7.6b)$$

$$Z_{i_4} = Z_i \quad (7.6c)$$

With the initial angle φ_i and radius r_i , the quadrant in Figure 7.2a can be modelled iteratively. The disc begins with a reference angle of $\varphi_i = 0$, and utilizes $\varphi_{inc} = 45$. The next iteration arrives to $\varphi_{i+1} = 0 + 45$. The progression is identical for the radius.

Adding an incremental value of Z as Z_{inc} extends the application to cylinders. An equal radius throughout the model with a height increment forms the walls of the cylinder quadrant in Equation 7.2b. When the number of vertical sections in z-axis is given in, s_z , the incremental value of height results in:

$$Z_{inc} = \frac{Z_i - Z_{i+1}}{s_z} \quad (7.7)$$

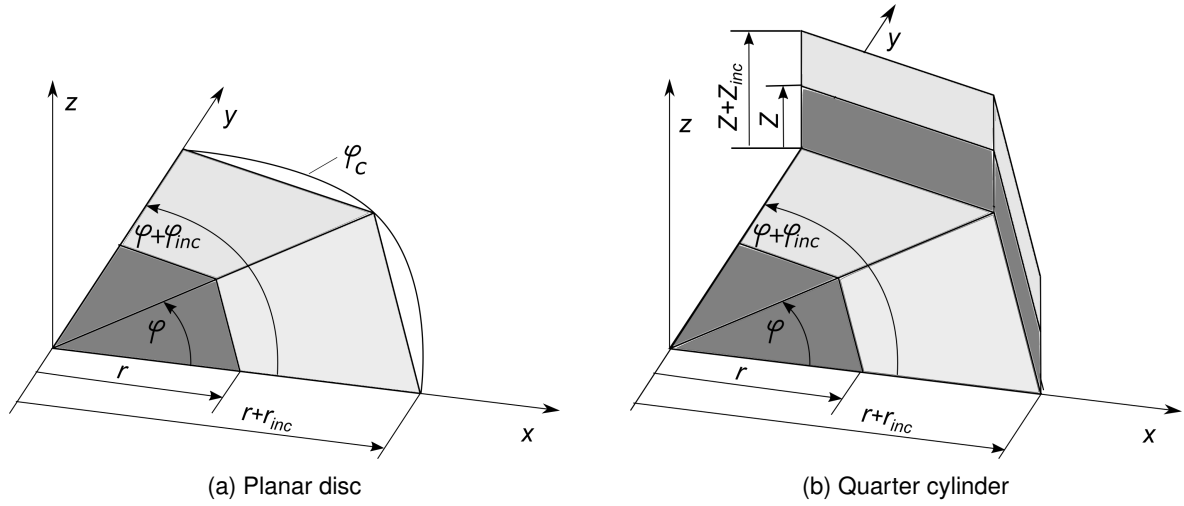


Figure 7.2: Simplified models of a disc and a cylinder quadrant

Mathematically, the side walls and the base can be treated in an identical manner. The base is a side wall that starts with a radius of zero, and increases to r at a constant depth. On the other hand, the side walls are equivalents of the base, with equal radii at different depths. This approach results in reducing the sectioning input to a single variable:

$$s_z = s_r \Rightarrow Z_{inc} = \frac{Z_i - Z_{i+1}}{s_r} \quad (7.8)$$

A systematic input format to the formulation above is possible using matrices. For n number of edges, the radius, z location, and the number of sections can be collected into a $[3 \times n]$ matrix. Each row describes the radius and the depth of the edge i , and the number of sections to build between these two consecutive edges. Presented in this format, a $[3 \times 2]$ matrix defines a series of panels. This matrix is termed as the P matrix (i.e., Panel Matrix):

$$P_j = \begin{bmatrix} r_i & D_i & s_r \\ r_{i+1} & D_{i+1} & s_{r+1} \\ \dots & \dots & \dots \\ r_n & D_n & s_n \end{bmatrix} \quad (7.9)$$

It is functional to separate the body-wide properties from the P matrix. The reference angle, number of angular sections (s_p), and the x and y origin ($0(x_0, y_0)$) are input externally as a local settings matrix (L). Consolidating the panel matrix of body j into the local matrix, the format takes the following form:

$$L_j = [P_j \quad s_p \quad \varphi_c \quad (x_0, y_0)] \quad (7.10)$$

Following the methodology above, the panels in Figure 7.2a at $z = -20$ meters, are represented by the following P and L matrices:

$$P_1 = \begin{bmatrix} 0 & -20 & 2 \\ 5 & -20 & 2 \end{bmatrix} \quad (7.11)$$

$$L_1 = [P_1, \quad s_r = 2, \quad \varphi_c = 90, \quad (x_0, y_0) = (0, 0)] \quad (7.12)$$

Equation 7.11 reads as follows: A surface is formed between an edge with a radius of zero and an edge with a radius of five, both at -20 meters. The surface is subdivided into panels with two radial segments ($P_1(1, 3) = 2$). The value at $P_1(2, 3) = 2$ is void as no edges follow in the third row. L_1 defines that there are two angular sections revolving 90 degrees. The origin in x and y-axes is $(x_0, y_0) = (0, 0)$. To obtain the cylinder in 7.2b, a third line is added to the P matrix and with an identical L_1 :

$$P_2 = \begin{bmatrix} 0 & 20 & 1 \\ 5 & 20 & 2 \\ 5 & 0 & 0 \end{bmatrix} \quad (7.13)$$

When modelling with increasing z or r values, Equations 7.3a enforce surface normals to face the negative z , positive x , and positive y directions, which were found convenient for naval engineering. Introducing multiple L and P matrices describes multiple bodies. The process is summarized with a flowchart in Figure 7.3 for $j = [1, \dots, m]$ bodies.

7.3.2 Face based approach

Assume an arbitrary quadrilateral face with the vertices $V1(x_1, y_1, z_1)$, $V2(x_2, y_2, z_2)$, $V3(x_3, y_3, z_3)$ and $V4(x_4, y_4, z_4)$. The number of segments of the edges between $V1$ to $V2$, and $V2$ to $V3$ are provided, and opposing sides are identically sectioned. When the locations of the internal points are calculated, a subdivided surface is obtained.

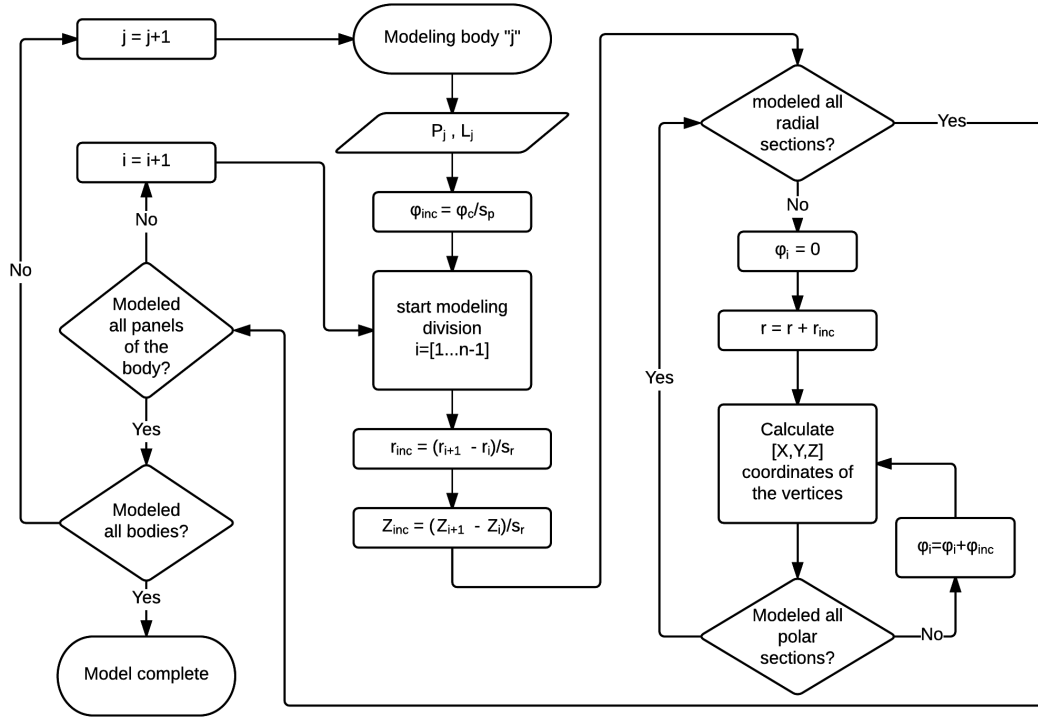


Figure 7.3: Flowchart of radial based modelling

Consider dividing a larger face into the three sub-surfaces illustrated in Figure 7.4. Given the four initial vertices (V_1, V_2, V_3, V_4) and the number of segments in the shorter dimension (s_2), the polygon composed of V_1, V_2, V_{23} and V_{14} can be deduced from the generalized formulation below:

$$V_{S_1} = V_1 + \frac{(V_4 - V_1)}{s_2} \cdot (n_{sub} - 1) \quad (7.14a)$$

$$V_{S_2} = V_2 + \frac{(V_3 - V_2)}{s_2} \cdot (n_{sub} - 1) \quad (7.14b)$$

$$V_{S_3} = V_2 + \frac{(V_3 - V_2)}{s_2} \cdot n_{sub} \quad (7.14c)$$

$$V_{S_4} = V_1 + \frac{(V_4 - V_1)}{s_2} \cdot n_{sub} \quad (7.14d)$$

The sub-surfaces are numbered with " n_{sub} ". The lowermost sub-face in Figure 7.4 results from equating $n_{sub} = 1$ and $s_2 = 3$:

$$[V_{S_1}, V_{S_2}, V_{S_3}, V_{S_4}] = [V_1, V_2, V_{23}, V_{14}] \quad (7.15)$$

When the number of segments in the longer dimension is denoted by s_1 , a top edge increment (\vec{l}_T) and a bottom edge increment (\vec{l}_B) can be defined:

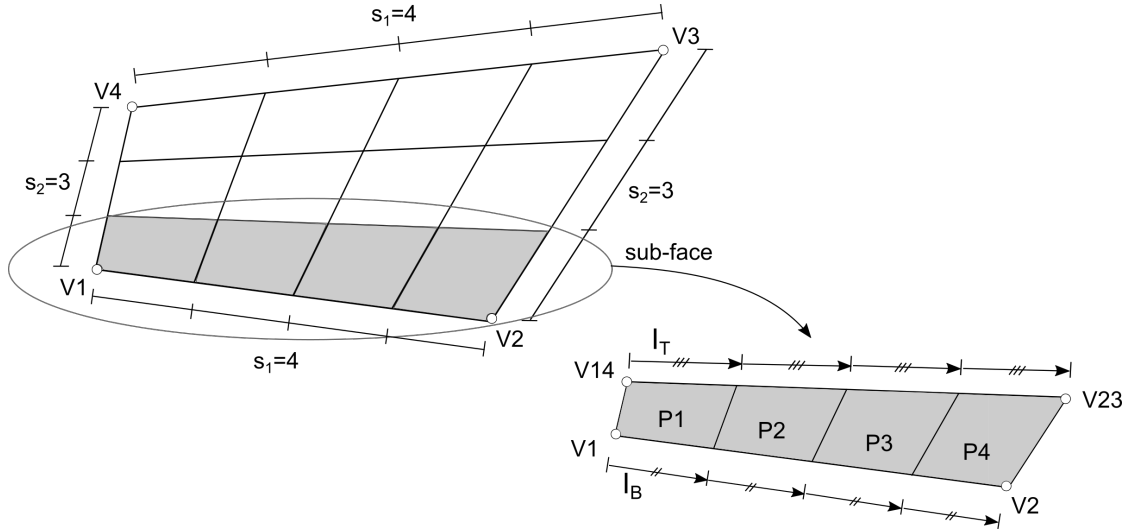


Figure 7.4: A quadrilateral face composed of three sub-faces

$$\vec{l}_T = \frac{V23 - V14}{s_1} \quad \vec{l}_B = \frac{V2 - V1}{s_1} \quad (7.16)$$

It is then clear that iteratively dragging the two initial vertices ($V1$ and $V14$) along the edges of the sub-face by the increments l_B and l_T defines the vertices of individual panels. The generalized formulae below deducts the coordinates using (n_{panel}) to indicate the panel number.

$$V1_{P_i} = V1 + \vec{l}_B(n_{panel} - 1) \quad (7.17a)$$

$$V2_{P_i} = V2 + \vec{l}_B(n_{panel}) \quad (7.17b)$$

$$V3_{P_i} = V14 + \vec{l}_T(n_{panel}) \quad (7.17c)$$

$$V4_{P_i} = V14 + \vec{l}_T(n_{panel} - 1) \quad (7.17d)$$

A $[4 \times 3]$ matrix can contain the four vectors consisting of the x,y and z coordinates of the vertices. To define the segments between $V1$ to $V2$, and $V2$ to $V3$ (i.e. s_1 and s_2 respectively), an additional column is required. As the opposing edges are sectioned identically, two values remain in a $[4 \times 4]$ matrix for orienting the surface normals.

Each panel has three possibilities for the x, y, z-components of the surface normal vector. The first two happen when the component direction is identical or the reverse of the axes' orientation (e.g., $\vec{n} = [0.32, 0, -0.67]$, where the x component equals to 0.32 having the same orientation with the axis). Consequently, defining an axis and the required normal vector direction in reference to the given axis normal is an effective way of ensuring the intended orientation. The third case is when the surface normal component becomes zero (e.g, a polygon flat on the xy-plane, where the values of the normals in x and y directions are zero). Under these circumstances, only the the remaining (e.g., z-axis in the example above) orientation can be evaluated. Consequently, it is beneficial to define

two axes in $P(3, 4)$ and $P(4, 4)$ to be evaluated if one is zero. This approach allows to use the same matrix multiple times without alterations when rotations are introduced. Let the input matrix take the following form:

$$P = \begin{bmatrix} x_1 & y_1 & z_1 & s_1 \\ x_2 & y_2 & z_2 & s_2 \\ x_3 & y_3 & z_3 & o_{axis1} \\ x_4 & y_4 & z_4 & o_{axis2} \end{bmatrix} \quad (7.18)$$

The intended surface normals are set with o_{axis_1} and o_{axis_2} . Defining the normal vector $\vec{n} = [x_f, y_f, z_f]$ of a panel and mapping axes x , y and z to the numbers $k = [1, 2, 3]$ respectively, the operation below sets the orientation of the face in the intended direction:

$$\text{sgn}(o_{axis_k}) = \text{sgn}(\vec{n}(o_{axis})) \rightarrow Q_F = Q_F \quad (7.19a)$$

$$\text{sgn}(o_{axis_k}) \neq \text{sgn}(\vec{n}(o_{axis})) \rightarrow Q_F = \chi \cdot (Q_F) \quad (7.19b)$$

A mathematical function, " χ ", is introduced to flip the first three columns of the matrix upside down. This operation is the equivalent of turning the points in the opposite order (e.g. counter-clockwise if they were defined clockwise initially). The flip does not alter the number of sections between the vertices as they end up defining the same spacing. Therefore, the fourth column is kept intact. An example is provided for a unit square bottom face (B_F), parallel to the xy -plane, with the normal intended to be set in $-z$ direction:

$$B_F = \begin{bmatrix} 0 & 0 & 0 & 3 \\ 1 & 0 & 0 & 1 \\ 1 & 1 & 0 & -3 \\ 0 & 1 & 0 & 1 \end{bmatrix} \quad (7.20)$$

Using the right-hand rule, and following the order in which the points are defined in B_F , the surface normal will be set originally in the $+Z$ direction. Flipping the first three columns of the matrix upside down provides the following matrix, with the surface normal set in the negative z direction. As stated, the additional value at $P(4, 4)$ is beneficial for iterative scripts where the panel definition is used at multiple times inside the model. The code will not use it in this case.

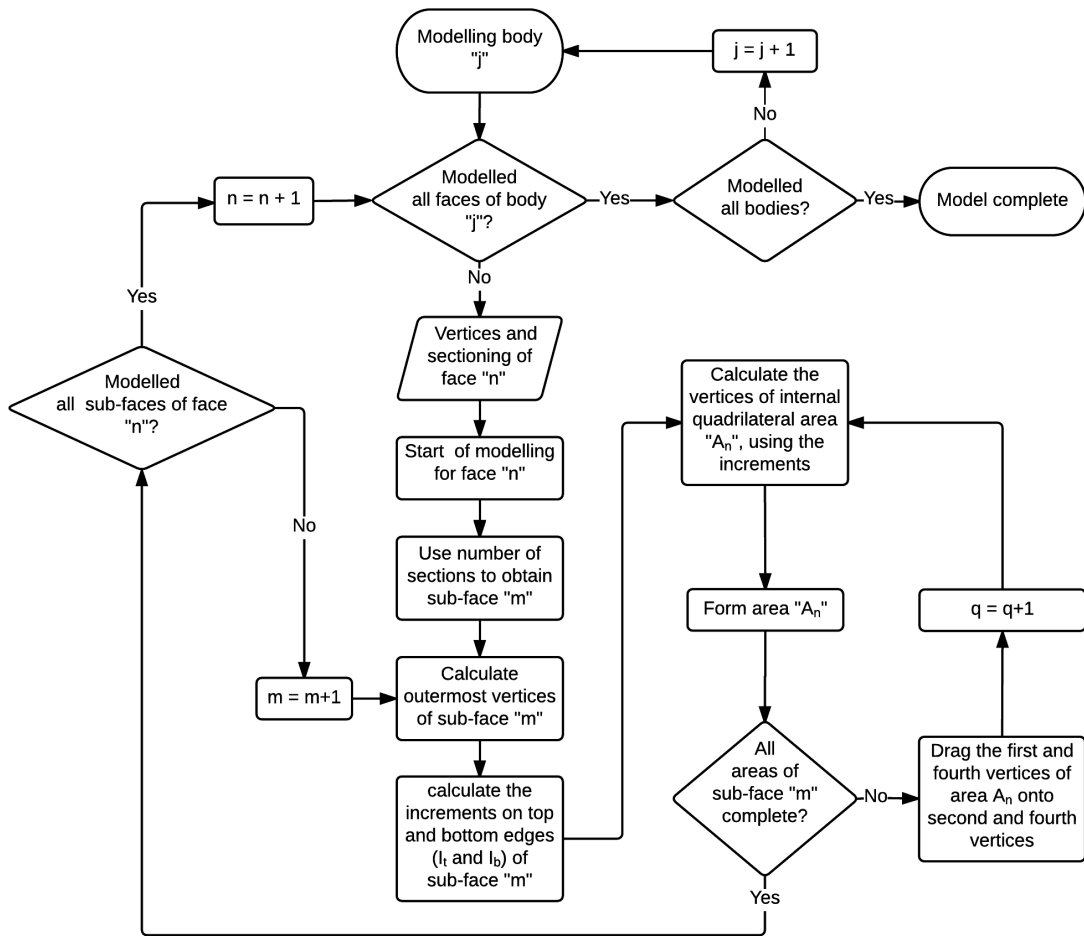


Figure 7.5: Flowchart of face based modelling

$$\chi \cdot B_F = \begin{bmatrix} 0 & 1 & 0 & 3 \\ 1 & 1 & 0 & 1 \\ 1 & 0 & 0 & -3 \\ 0 & 0 & 0 & 1 \end{bmatrix} \quad (7.21)$$

The approach above builds the bodies as a collection of faces that are composed of sub-faces as illustrated in the flowchart in Figure 7.5. A cube is modelled with the top (F_T), the bottom (F_B) and the four sides (F_1, F_2, F_3, F_4). The faces are collected into a local matrix (L_f) to form a body:

$$L_f = [F_1, F_2, F_3, F_4, F_T, F_B] \quad (7.22)$$

7.3.3 Rotation and translation in 3D space

The same matrices can be used multiple times to simplify building the models. For instance, in the case of a cube, a single matrix can be utilized if it can be moved and rotated in 3D space. Translating

points is easily achieved by adding the x_m, y_m and z_m distances to the original matrix data and does not necessitate further discussion. The origin, the axis, and the angle are the requirements for rotation. Additionally, the final position depends on the order when multiple rotations are performed (e.g., about the z axis first, then y, and then z).

The solution to rotations of a point about the axes of the coordinate system, the Euler's rotation matrix, is detailed in [158]. However, regarding functionality, rotating about an arbitrarily defined axis is easier for the user. For instance, alternative coordinate axes may be chosen as the centre of the base of a cylinder, or the geometric centre of a rectangular prism. For this purpose, the solution can be extended onto rotations about an arbitrary point in the coordinate axes.

In this case, the origin of the coordinate system is moved to the origin of the rotation. The new point is then used to perform the rotations about the new coordinate axes. At the final stage, the model is translated to its original location. The equations below summarize the rotations of the point coordinates (x, y, z) about the point (a, b, c) by an angle θ in a given axis. Rotated coordinates are presented as (x', y', z') and the rotation axis is denoted by the subscript (e.g., x'_X is rotation about the x-axis):

$$\begin{bmatrix} x'_X \\ y'_X \\ z'_X \end{bmatrix} = \begin{bmatrix} x(1 - \cos \theta) + x \cos \theta \\ b(1 - \cos \theta) + y \cos \theta + (c - z) \sin \theta \\ c(1 - \cos \theta) + z \cos \theta + (y - b) \sin \theta \end{bmatrix} \quad (7.23)$$

$$\begin{bmatrix} x'_Y \\ y'_Y \\ z'_Y \end{bmatrix} = \begin{bmatrix} a(1 - \cos \theta) + x \cos \theta + (c - z) \sin \theta \\ y(1 - \cos \theta) + y \cos \theta \\ c(1 - \cos \theta) + z \cos \theta + (a - x) \sin \theta \end{bmatrix} \quad (7.24)$$

$$\begin{bmatrix} x'_Z \\ y'_Z \\ z'_Z \end{bmatrix} = \begin{bmatrix} a(1 - \cos \theta) + x \cos \theta + (b - y) \sin \theta \\ b(1 - \cos \theta) + y \cos \theta + (x - a) \sin \theta \\ z(1 - \cos \theta) + z \cos \theta \end{bmatrix} \quad (7.25)$$

7.3.4 Multi-body models, symmetry, and the consolidated input format

Up to this point, the formulations focused on forming a single body. The local matrices defined in the Equations 7.10 and 7.22 build parts of the geometry by collecting panel matrices together. The type of modelling (i.e., radius based or face based) is clear by the size of the panel matrix. Radius based models are contained within $[3 \times n]$ matrices, and face based geometries use $[4 \times n]$.

Additional modelling data can be defined as follows: the number of arc segments and the reference angle are summed up as rad_i . Rotations depend on the origin ($O_R(x, y, z)$) and the order (R_O) along with the angles (R_x, R_y, R_z). The translation distance (D) is required for moving panels. The

material density and the plate thickness (ρ and t) are required for weight and inertia calculations. Finally, for the panel matrices indicated by P_i , the local matrix takes the following generalized form:

$$L = [(P_1, P_2, \dots, P_i), rad_i, R_x, R_y, R_z, O_R, R_O, D, t, \rho] \quad (7.26)$$

The variables that apply to the entirety of the model can be integrated into a "global settings" matrix, denoted by G . With the same approach used for the local matrices that consolidate the panel matrices, global matrices collect and integrate local matrices. Therefore, structures composed of multiple bodies are made possible. Symmetry information in x and y-axes is included as Boolean (true or false) input. When the file name is added, the global matrix is written as:

$$G = [FileName, (L_j \ L_{j+1} \ \dots \ L_n), X_{symmetry}, Y_{symmetry}] \quad (7.27)$$

In brief, the modelling procedure is described as nesting panel matrices into local matrices that are nested into a single global matrix:

$$Model = G[L_1(P_j, \dots, P_n), L_2(P_k, \dots, P_t), \dots, L_m(P_l, \dots, P_q)] \quad (7.28)$$

7.4 Calculation of the mass properties of the mesh

7.4.1 Centre of gravity and weight

To calculate the mass, volume, and inertia of the mesh, it is possible to borrow from the finite elements approach by integrating the properties of individual panels throughout the structure. The solution proposed below follows the same order. Panel properties are described first, followed by the mass properties.

A polygon's centre of gravity in 3D space can be calculated with triangulation. For a quadrilateral, the triangulation equals removing a vertex. Vertices 1,2,3 and 1,3,4 are valid triangles in Figure 7.6. Repeating two adjacent vertices forms a line and an area equal to zero for triangles expressed as quadrilaterals. Therefore, the formulation still applies. Assume that the panels of the structure are thin sheets with zero thickness; hence, with an attributed area but zero volume. The centre of mass of this polygon is the result of a weighted average of the two triangles forming the quadrilateral panel. In this case, the problem turns into locating the centroid of a 3D planar triangle. Considering that each vertex i is represented by $V_i = (x_i, y_i, z_i)$, the geometric centre of a triangle (C_{tri}) is calculated as the intersection point of its medians.

$$C_{tri}(x_c, y_c, z_c) = \frac{V_1 + V_2 + V_3}{3} \quad (7.29)$$

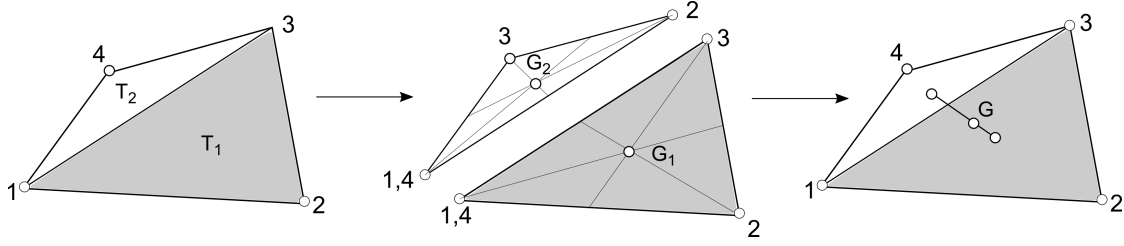


Figure 7.6: Triangulation of a quadrilateral

The area of the triangle is represented by a cross product of its two edges and the normal vector (\vec{n}):

$$A_{tri} = \left| \frac{\vec{n} \cdot ((V_2 - V_1) \times (V_3 - V_1))}{2} \right| \quad (7.30)$$

A weighted average using the Equations 7.29 and 7.30 gives the centre of geometry of the quadrilateral:

$$C_{quad}(x_c, y_c, z_c) = \frac{\sum_{m=1}^2 A_{tri_m} C_{tri_m}(x_c, y_c, z_c)}{\sum_{m=1}^2 A_{tri_m}} \quad (7.31)$$

The total area of the panel is the sum of the areas of the two triangles forming it:

$$A_p = \sum_{m=1}^2 A_{tri_m} \quad (7.32)$$

To add the thickness into the calculations, consider that a sheet of metal (i.e., panel mesh) is lying flat on a table (i.e., fluid domain) with the surface normal direction oriented towards the table. The mesh represents the bottom surface. In this case, the location of the centre of gravity is offset from the centre of geometry of the face by the inverse of surface normal multiplied by the half of its thickness. The surface normal can be calculated with Newell's method [159, 160]. For a polygon with m vertices, the normal vector defined by $\vec{n} = [n_x \ n_y \ n_z]$ is obtained as follows:

$$n_x = \sum_{i=1}^m (y_i - y_{(i+1)}) \cdot (z_i + z_{(i+1)}) \quad (7.33a)$$

$$n_y = \sum_{i=1}^m (z_i - z_{(i+1)}) \cdot (x_i + x_{(i+1)}) \quad (7.33b)$$

$$n_z = \sum_{i=1}^m (x_i - x_{(i+1)}) \cdot (y_i + y_{(i+1)}) \quad (7.33c)$$

Panel method calculations require that the section facing the fluid domain be modelled (e.g., the table in the example given above). Consequently, the thickness faces "inwards", opposing the surface

normal. For this reason, it becomes computationally efficient to calculate a reverse normal and use it in structural calculations. The updated vector may also be implemented into the Equation 7.30 by negating it to avoid multiple calculations. This normal can be termed the structural normal vector \vec{n}_s and is obtained by multiplying \vec{n} with minus unity and normalizing:

$$\vec{n}_s = -\frac{\vec{n}}{|\vec{n}|} \quad (7.34)$$

Finally, the centre of mass (C_M) as a function of the centre of geometry of the panel (C_{quad}), the thickness (t), and the structural surface normal (\vec{n}_s) becomes:

$$C_M(x, y, z) = 0.5 \cdot t \cdot \vec{n}_s + C_{quad}(x_c, y_c, z_c) \quad (7.35)$$

The total weight of the panel (M_p) is calculated using the area (A_p), thickness (t), and the density (ρ):

$$M_p = A_p \cdot t \cdot \rho \quad (7.36)$$

The structure's total weight, W_t , is found by summing up the weights of the panels:

$$W_t = \sum_1^m M_{p_m} \quad (7.37)$$

Through C_M , the location of each panel's centre of gravity was known. Merging Equations 7.35 and 7.37 locates the centre of gravity of the structure ($C_G(x_g, y_g, z_g)$):

$$C_G(x_g, y_g, z_g) = \sum_1^m \frac{M_{p_m} \cdot C_{M_m}}{M_{p_m}} \quad (7.38)$$

7.4.2 Inertia

Using the location of the centre of gravity $C_M(x_c, y_c, z_c)$ and the mass (M_p), the structural inertia is calculated about the x, y, and z-axes as follows:

$$I_{xx} = \sum_m M_{p_m} (y_{c_m}^2 + z_{c_m}^2) \quad (7.39a)$$

$$I_{yy} = \sum_m M_{p_m} (x_{c_m}^2 + z_{c_m}^2) \quad (7.39b)$$

$$I_{zz} = \sum_m M_{p_m} (x_{c_m}^2 + y_{c_m}^2) \quad (7.39c)$$

The products of inertia about the axes are given as follows:

$$I_{yz} = \sum_m M_{\rho_m} (y_{c_m} z_{c_m}) \quad (7.40a)$$

$$I_{zx} = \sum_m M_{\rho_m} (x_{c_m} z_{c_m}) \quad (7.40b)$$

$$I_{xy} = \sum_m M_{\rho_m} (x_{c_m} y_{c_m}) \quad (7.40c)$$

The inertial values about the centre of gravity of the structure are obtained through the parallel axis theorem. An alternative option is to replace the centre of gravity in Equations 7.39a and 7.40a with the values referenced from the centre of gravity of the structure ($C_G(x_g, y_g, z_g)$). This approach is equal to temporarily translating the origin to the centre of gravity.

7.4.3 Volume

The enclosed volume of a structure can be calculated by integrating the projected areas of individual panels up to the xy , xz , or yz -planes. The distance between the plane and the panel is obtained from the centre of geometry of the panel (C_{quad}). Directly multiplying the area by the distance to axis errs for the following reason: consider a cube of 6 faces, with the edge length of a . One vertex is located at the origin. The volume of the cube equals to a^3 . However, the sum of areas of the faces multiplied by the distance from the centre of the panels to an axis yields $3a^3$. This error is corrected by taking the projection of each vertex onto the plane and calculating the area of projection times the distance to the planes of origin. An example is given here for integrating towards the xy -plane. Projection onto the xy -plane is possible by setting the Z coordinate of the 12 vertices to zero:

$$P_{xy} = \begin{bmatrix} x_1 & y_1 & 0 \\ x_2 & y_2 & 0 \\ x_3 & y_3 & 0 \\ x_4 & y_4 & 0 \end{bmatrix} \quad (7.41)$$

The unit normal of the xy -plane is in the Z direction:

$$\vec{n}_{xy} = \begin{bmatrix} 0 & 0 & 1 \end{bmatrix} \quad (7.42)$$

Considering that each vertex i is represented by $V_i = (x_i, y_i, z_i)$, the projection area of each panel is calculated by:

$$A_{PROJ} = \vec{n}_{xy} \frac{(V_3 - V_1) \times (V_4 - V_2)}{2} \quad (7.43)$$

The distance between the panel's centre of geometry and the xy-plane (i.e., C_{quad_z}) is measured from the Z value of the geometric centre of the panel C_{quad} . Multiplication of the area and the distance provides the volume coming from the panel in z direction:

$$Vol_{z_p} = A_{PROJ} \cdot C_{quad_z} \quad (7.44)$$

Other directions are delivered by pairing \vec{n}_{yz} with C_{quad_x} and \vec{n}_{xz} with C_{quad_y} . The resulting values are Vol_x and Vol_y respectively. When the volume coming from each panel is known, the total volume is obtained by integration:

$$Vol_{z_t} = \sum_1^m Vol_{z_p} \quad (7.45)$$

7.5 Examples of application

A number of geometries are demonstrated in this section. Simple shapes such as the frustum are given with the matrices that create them. For complex structures, the method is described. The idea of parametrisation of the input data is applied and discussed. The matrices below use an alternative notation to contract them. The semicolon operator (;) signifies the next row of the matrix. Global matrices only contain information related to file naming and symmetry; hence, they are omitted.

7.5.1 Examples of application for the radius based models

Previously, Equation 7.11 was given to describe a cylinder quadrant. An extension of application is the frustum in Figure 7.7. Symmetry is used to revolve 360 degrees. The centre of origin is offset by $(x, y) = (3, 5)$ units:

$$P_f = \begin{bmatrix} 0 & 20 & 5; & 3.250 & 20 & 5 \\ 2 & 0 & 10; & 0 & 0 & 5 \end{bmatrix} \quad (7.46)$$

$$L_f = \left[P_f, \text{ arc segments} = 10, \text{ reference angle} = 90, X_0 = 3, Y_0 = 5 \right] \quad (7.47)$$

The idea of changing radii as a function of depth applies similarly to obtain a sphere. The model starts at certain z value with zero radius. As the height is incremented, the its radius increases until it equals the radius of the sphere. Subsequently, the steps are reversed until zero radius is obtained:

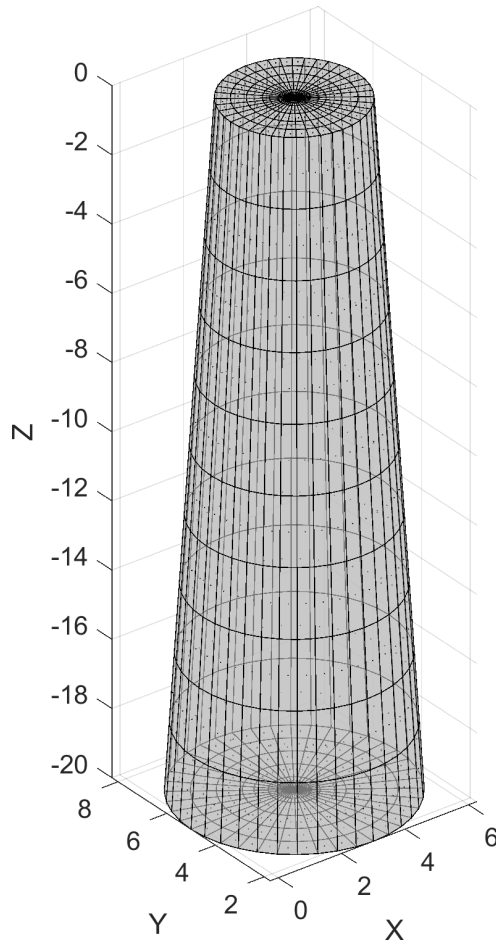


Figure 7.7: Frustum

$$P_{sphere} = \begin{bmatrix} 0.00 & 5.0 & 1; & 0.87 & 4.8 & 1; & 1.20 & 4.6 & 1 \\ 1.43 & 4.4 & 1; & 1.60 & 4.2 & 1; & 1.73 & 4.0 & 1 \\ 1.83 & 3.8 & 1; & 1.91 & 3.6 & 1; & 1.96 & 3.4 & 1 \\ 1.99 & 3.2 & 1; & 2.00 & 3.0 & 1; & 1.99 & 2.8 & 1 \\ 1.96 & 2.6 & 1; & 1.91 & 2.4 & 1; & 1.83 & 2.2 & 1 \\ 1.73 & 2.0 & 1; & 1.60 & 1.8 & 1; & 1.43 & 1.6 & 1 \\ 1.20 & 1.4 & 1; & 0.87 & 1.2 & 1; & 0.00 & 1.0 & 1 \end{bmatrix} \quad (7.48)$$

$$L_{sphere} = \left[P_{sphere}, \text{PolarSections} = 10, \text{revAngle} = 90, X_0 = 0, Y_0 = 0 \right] \quad (7.49)$$

Equation 7.48 gives the sphere in Figure 7.8. It can be largely simplified by parameterizing the sphere section's radius as a function of its height and scripting it out.

To obtain a torus through a similar parameterization, consider the side walls of an upright cylinder. When the radius of this wall is increased towards its centre and decreased back to its initial value back at the extremities (i.e., top and bottom), a convex shape is obtained, forming the outer ring of

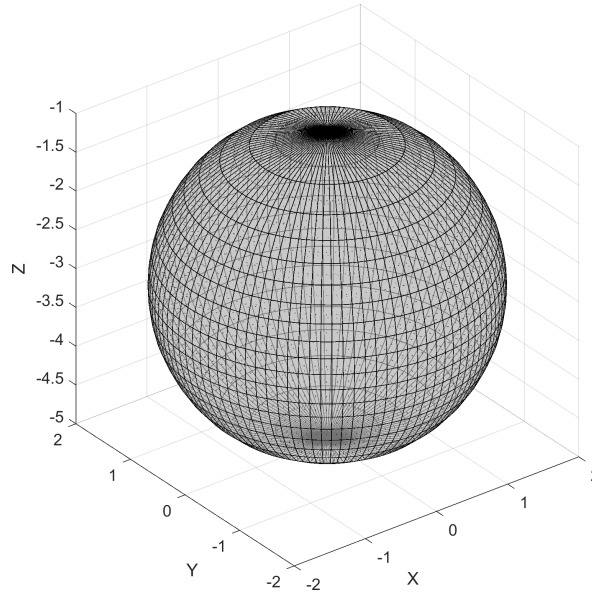


Figure 7.8: Sphere

a torus. The idea is reapplied with a decreasing radius, resulting in the inner ring. The shape is revolved about the origin to complete the model.

The P matrix of the outer ring is similar to the P matrix of the sphere in Equation 7.48 with the minor radius (r_{sphere}) increased by the major radius (R_{torus}). With a centre radius of 10 units, the matrix is written as follows, using the sphere's panel matrix of $j = [1, \dots, 21]$ rows:

$$P_{outer}(1, j) = \sum_{j=1}^{21} (P_{sphere(1, j)} + R_{torus}) \quad (7.50)$$

The radii of the inner ring as a function of the outer radii:

$$P_{inner}(1, j) = \sum_{j=1}^{21} (P_{outer}(1, j) - 2R_{torus}) \quad (7.51)$$

Combining the matrices and rotating 45 degrees in both the X and Y axes delivers the torus in Figure 7.9:

$$L_{torus} = \left[[P_{inner}, P_{outer}], \text{PolarSections} = 10, \text{revAngle} = 360, X_r = 45, Y_r = 45 \right] \quad (7.52)$$

The same idea applies to all radius based shapes and borrows from the approach used by the "revolve" command available in most CAD software. A classic example for the usage of the command's usage is the glass shape in Figure 7.10. A multi-body example can be given with the semisubmersible floating wind turbine platform [49]. It consists of three buoyancy columns with altering radii, and the turbine is located on the central column. Cross braces connect the parts and they are rotated

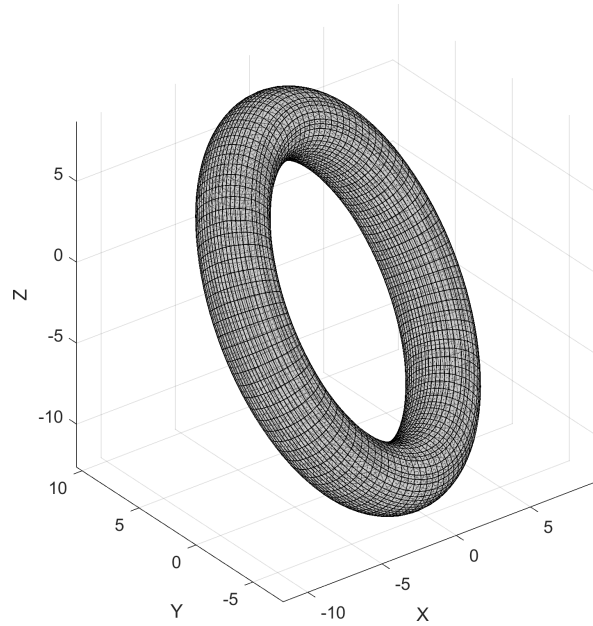


Figure 7.9: Torus rotated 45 degrees in Y and X axes

cylinders. Since all of the columns are identical, only one P matrix with six rows suffices to model the three buoyancy columns. They are separately positioned in the L matrices. A similar approach is also taken for the braces. The model is presented in Figure 7.11.

7.5.2 Examples of application for the face based models

A basic face based shape is a rectangular prism. It consists of 6 faces, modelled in their respective P matrices and put into a single L matrix. Let the edges of the box have the lengths of a units in the x -axis, b units in the y -axis and c units in the z -axis. The origin is set to $O(0,0,0)$. The six faces are written as follows:

$$F_{top} = \begin{bmatrix} 0 & 0 & +0 & 10; & a & 0 & +0 & 10 \\ a & b & +0 & 3; & 0 & b & +0 & 1 \end{bmatrix} \quad (7.53)$$

$$F_{bottom} = \begin{bmatrix} 0 & 0 & -c & 10; & a & 0 & -c & 10 \\ a & b & -c & -3; & 0 & b & -c & 1 \end{bmatrix} \quad (7.54)$$

$$F_{front} = \begin{bmatrix} a & 0 & +0 & 10; & a & 0 & -c & 10 \\ a & b & -c & 1; & a & b & +0 & 1 \end{bmatrix} \quad (7.55)$$

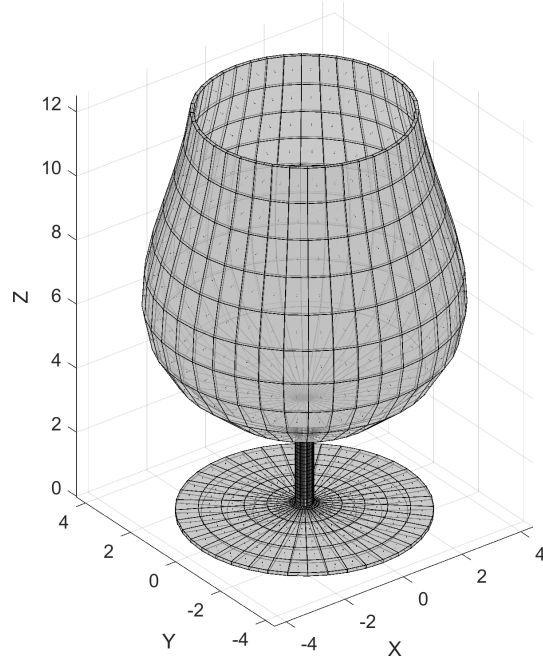


Figure 7.10: Glass

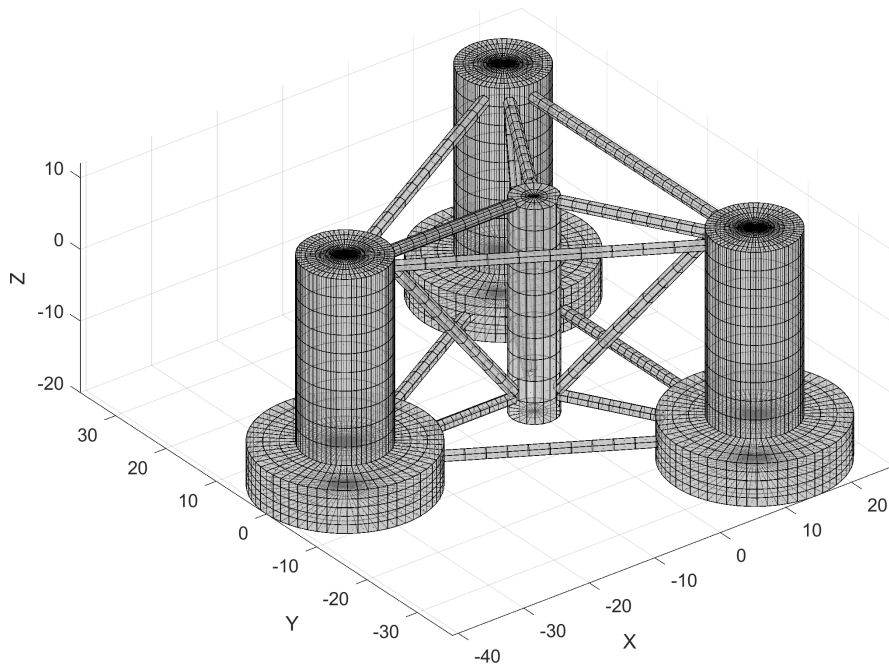


Figure 7.11: The DeepCwind semisubmersible floating wind turbine platform

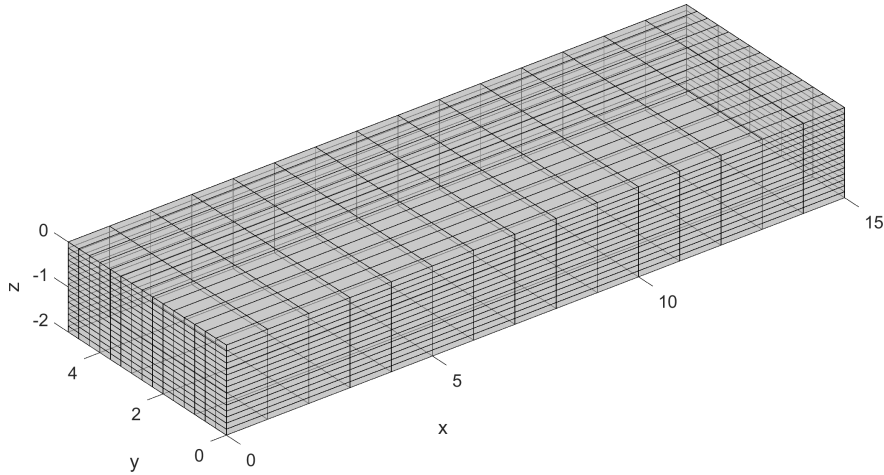


Figure 7.12: A rectangular prism with 6 faces

$$F_{back} = \begin{bmatrix} 0 & 0 & +0 & 10; & 0 & 0 & -c & 10 \\ 0 & b & -c & -1; & 0 & b & +0 & 1 \end{bmatrix} \quad (7.56)$$

$$F_{left} = \begin{bmatrix} 0 & b & +0 & 10; & a & b & +0 & 10 \\ a & b & -c & 2; & 0 & b & -c & 1 \end{bmatrix} \quad (7.57)$$

$$F_{right} = \begin{bmatrix} 0 & 0 & +0 & 10; & a & 0 & +0 & 10 \\ a & 0 & -c & -2; & 0 & 0 & -c & 1 \end{bmatrix} \quad (7.58)$$

In the Equation 7.53, the surface normals of the box are defined. The top face normal is oriented in +z direction ($F_{top}(3,3) = 3$). Similarly, $F_{bottom}(3,3) = -3$, denotes the reverse of the z-axis orientation. In place of writing out the six matrices, using the move command and only adjusting the normals would reduce the matrices to three. After setting $a = 15$, $b = 5$, and $c = 2$, the resulting box is in Figure 7.12.

The versatility of modelling using faces stems from the possibility of parameterizing and scripting. The midship section in Figure 7.14 is an extended example to the barge given above. It may serve to obtain an estimate of weight and inertia of the section. The components such as the deck and the bottom plates are quadrilaterals identical to the top and the bottom of the prism. The stiffeners are added iteratively by offsetting the copy of a single stiffener multiple times. The bilge is built with a function of radius. The process may be summarized as repeating Equation 7.53 with altered parameters within a script.

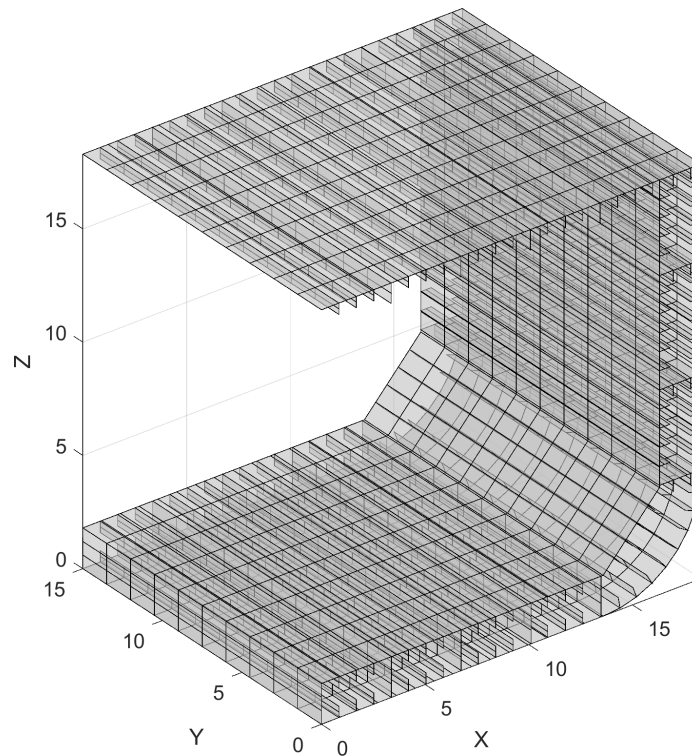


Figure 7.13: Midship section of a tanker

A ship's hull form is an alternative example. A table of offsets used in naval architecture provides the width of a transversal section as a function of depth. When the depth values of adjacent transversal sections are connected longitudinally, the result is the ship's hull form. The bulkheads in Figure 7.14 may be added by connecting the opposing vertices transversally instead of longitudinally. The hull form model may be used for hydrostatic and hydrodynamic calculations. With this model, it is also possible to obtain the distributed weight of the hull along its length, required for bending moment calculations.

Brunelleschi's Octagonal Dome in Florence is presented in Figure 7.15 and illustrates an example from architecture. In this case, the changing radius of the dome is read from an external file, which registers the real measurements of the dome. A single side of the octagon is built, copied and moved within a script. The rotations are performed about the origin for the support system and about their first defined point for the edges/sides.

7.6 Validation of mass property calculations and the panel method model

The volume, the centre of gravity, the weight, the inertia calculations and the panel method model are validated below. To compare the weight and inertial data, models for the box and the frustum were built in ANSYS. Rhino3D can open the meshes in the GDF file format. Therefore, it was used to get a comparison of volume. The use of sectional volume (i.e., the volume up to a certain depth, which can be expanded onto sectional weight) is discussed.

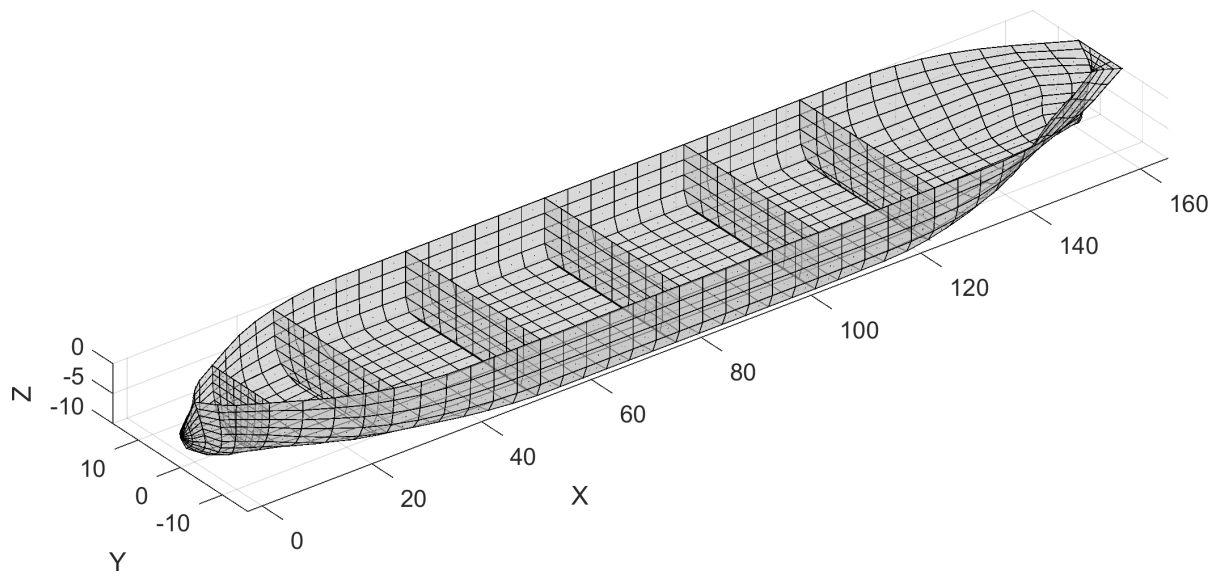


Figure 7.14: Hull geometry of a ship

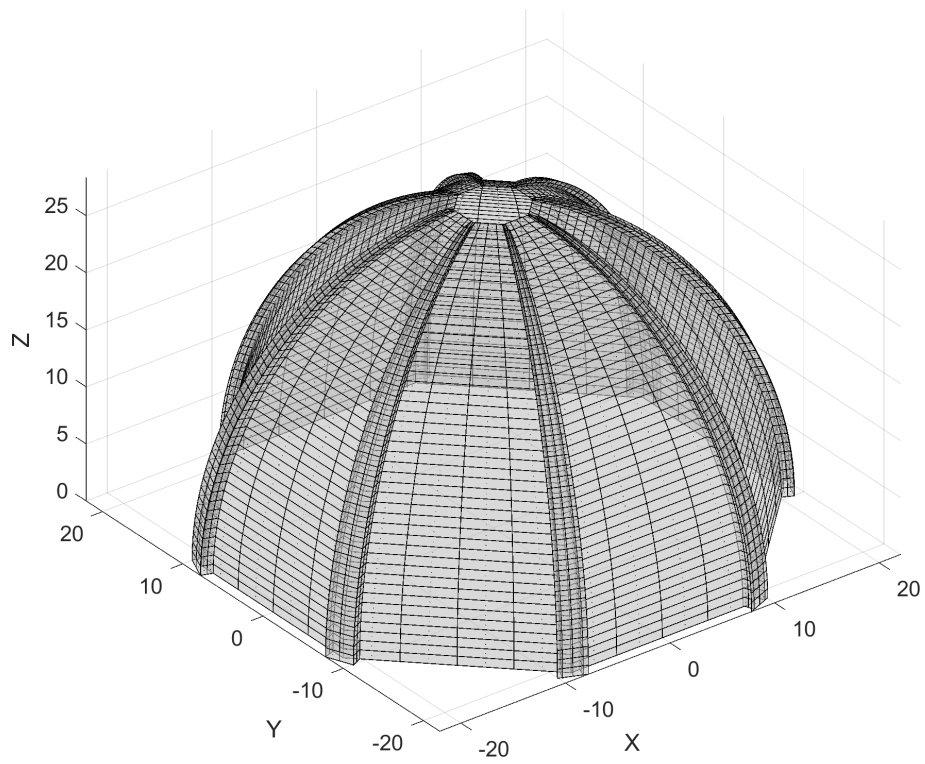


Figure 7.15: Brunelleschi's Octagonal Dome in Florence

Table 7.1: Comparisons of volume measurements between Rhino3D and ParMod

	ParMod	Rhino3D	Analytical	ParMod/Rhino comparison
Frustum	440.84	440.84	441.13	0.00%
Rotated Torus	785.95	785.95	789.57	0.00%
Sphere	33.18	33.18	33.51	0.00%
Box	150.00	150.00	150.00	0.00%
Glass	37.03	36.23	–	2.21%
Semisubmersible	13895	13842	–	0.38%
Ship hull	21152	21152	–	0.00%
Dome	26564	26578	–	-0.05%

For the panel method comparison, a cylinder model was built in Rhino3D with the sizing described in [78], and both were run in WAMIT [130]. Units are omitted. Providing that there is consistency between codes, they are not indicators. Information relating to the code’s usage practices are mentioned where appropriate.

7.6.1 Volume

The Table 7.1 lists the results of volume calculations with ParMod, Rhino, and when possible, analytical formulae. The current approach is listed under the abbreviation of ParMod (parametric modeller). The comparison of methods must be carried out on identical models and a rounded shape represented by a collection of a finite number of panels loses some volume (e.g., a cylinder divided into four segments is a diamond shape, with a lower volume). Therefore, comparisons are provided against Rhino3D’s measurements as opposed to the analytical values. Analytical values are included to present an idea on the loss of volume due to panelling and serve to validate the geometry of the model itself.

In Table 7.1, the glass, the semisubmersible, and the dome show slight differences. The remaining results are identical. Despite the intuition, the glass is the most complex shape in the list. It has an inner surface, modelled with the opposite surface normal of the outer surface. It was purposefully built to measure the possible errors. The difference in measurement is 2.21 percent in that case. For the other two cases, Rhino3D could not measure when all areas are not enclosed, therefore the models needed adjustments (e.g., The Dome had to be capped). The values reflect the alterations in the models.

Volume calculations as a function of depth are useful in stability studies of floating structures. Figure 7.16 delivers this type of a computation for the box and a semisubmersible. The figure also illustrates that to obtain a good distribution, the number of sections should go past a certain value. In the z direction, the calculated volume is correct at the maximum depth. Intermediate values are lost as there is only a single section for integration (see Figure 7.12: bottom and top faces). This figure shows that when getting the distributed values, the direction with the most number of sections is preferable. The semisubmersible’s z integration is similar, despite the cross-braces resulting in an

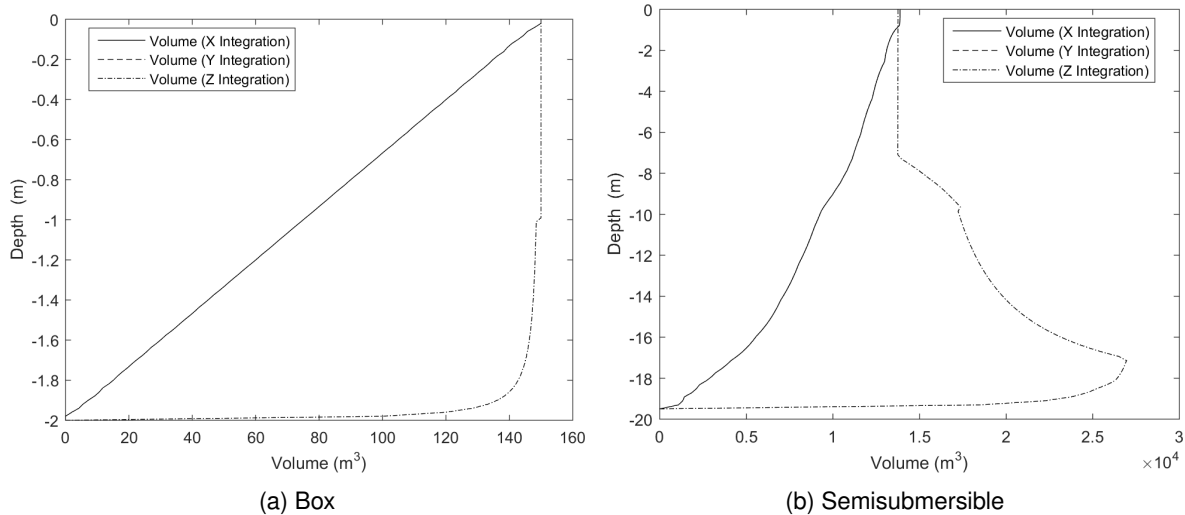


Figure 7.16: Simplified models of a disc and a cylinder quadrant

Table 7.2: Weight calculations of the box and the frustum

	Weight			CoG (x,y,z)	
	ParMod	ANSYS	%	ParMod	ANSYS
Frustum	1.772E+05	1.772E+05	0.00	(5.0, 10.0, -11.25)	(5.0, 10.0, -11.25)
Box	9.028E+04	9.028E+04	0.00	(7.5, 2.5, -1.0)	(7.5, 2.5, -1.0)

increased number of z-sections. The volumes at the water level (i.e., 0 depth) are identical for the x, y, and z integrations when all of the panels are considered.

7.6.2 Centre of gravity, weight and inertia

The centre of gravity, weight and inertia comparisons are presented for the frustum and the box (Figures 7 and 12), using a thickness of 0.05 and 0.06 respectively. The density of steel was used as the material density value (7850). Table 2 lists the weight and the centre of gravity estimations. Both are identical to ANSYS. The two sets of inertias are provided in the Tables 7.3 and 7.4. The inertial values are given for the origin and the centre of gravity (CoG). For both, the inertial values at the origin are identical. When the inertia at the centre of gravity is examined, the results differ around 0.5 percent. It is probable that there is a difference in rounding of the values of the centre of gravity. In that case, the inertial values would reflect the difference when multiplied by the distance squared.

7.6.3 Panel method calculations

In the field of hydrodynamics, the coefficients play an important role, and their calculation depends on the underwater geometry. These added masses and potential damping values can be calculated from a suitably developed mesh. The added masses are denoted by A, while the potential damping is denoted by B. The subscript 11 is used for the surge mode, and 55 denotes pitch. This section illustrates the usage without discussing modelling practices.

Table 7.3: Structural inertia calculations of the frustum about the origin and the centre of gravity (CoG)

	ParMod		ANSYS		Difference	
	Origin	CoG	Origin	CoG	Origin	CoG
lxx	4.78E+07	7.65E+06	4.78E+07	7.68E+06	0.00%	-0.39%
lyy	3.45E+07	7.65E+06	3.45E+07	7.68E+06	0.00%	-0.39%
lzz	2.34E+07	1.22E+06	2.34E+07	1.23E+06	0.00%	-0.82%
lxy	-8.86E+06		-8.86E+06		0.00%	
lyz	1.99E+07		1.99E+07		0.00%	
lzx	9.96E+06		9.96E+06		0.00%	

Table 7.4: Structural inertia calculations of the box about the origin and the centre of gravity (CoG)

	ParMod		ANSYS		Difference	
	Origin	CoG	Origin	CoG	Origin	CoG
lxx	1.01E+06	3.55E+05	1.01E+06	3.56E+05	0.00%	-0.28%
lyy	7.22E+06	2.05E+06	7.22E+06	2.06E+06	0.00%	-0.48%
lzz	7.91E+06	2.26E+06	7.92E+06	2.27E+06	0.00%	-0.44%
lxy	-1.69E+06		-1.69E+06		0.00%	
lyz	2.26E+05		2.26E+05		0.00%	
lzx	6.77E+05		6.77E+05		0.00%	

Figure 7.17 presents the panel method calculation results of a cylinder mesh modelled in ParMod and Rhino3D. A platform with a 19-meter radius, at a draft of 20 meters, located at a 200-meter water depth was chosen, for which a set of results are readily available in [78]. This set shows no differences between the ParMod and Rhino models.

In models of higher complexity, it is likely that there will be certain differences depending on the modelling practice (e.g., the number of panels) and the results will reflect that. Figure 7.18 shows a comparison for the semisubmersible in Figure 7.11. The MultiSurf set was published in [39]. The values compare favourably with slight shifts in peak amplitudes.

7.7 Performance assessment

Average run times are important when the tool is used inside a larger system for design, in an iterative setting. It should require the minimal amount of time to deliver the model and its mass properties. Inside a loop, the available time should preferably be reserved for other calculations such as the panel method code's run time, or any additional module. Therefore, this section focuses only on the mass property and modelling times. The goal of providing this data is to clarify that the approach is minimally resource-intensive to avoid hindering the design process.

The performance depends on the number of panels used for the structure. Modern computers provide enough computational power to deliver fast results in simple arithmetic operations. The bottlenecks prove to be file writing and the trigonometric functions used for rotations. Consequently,

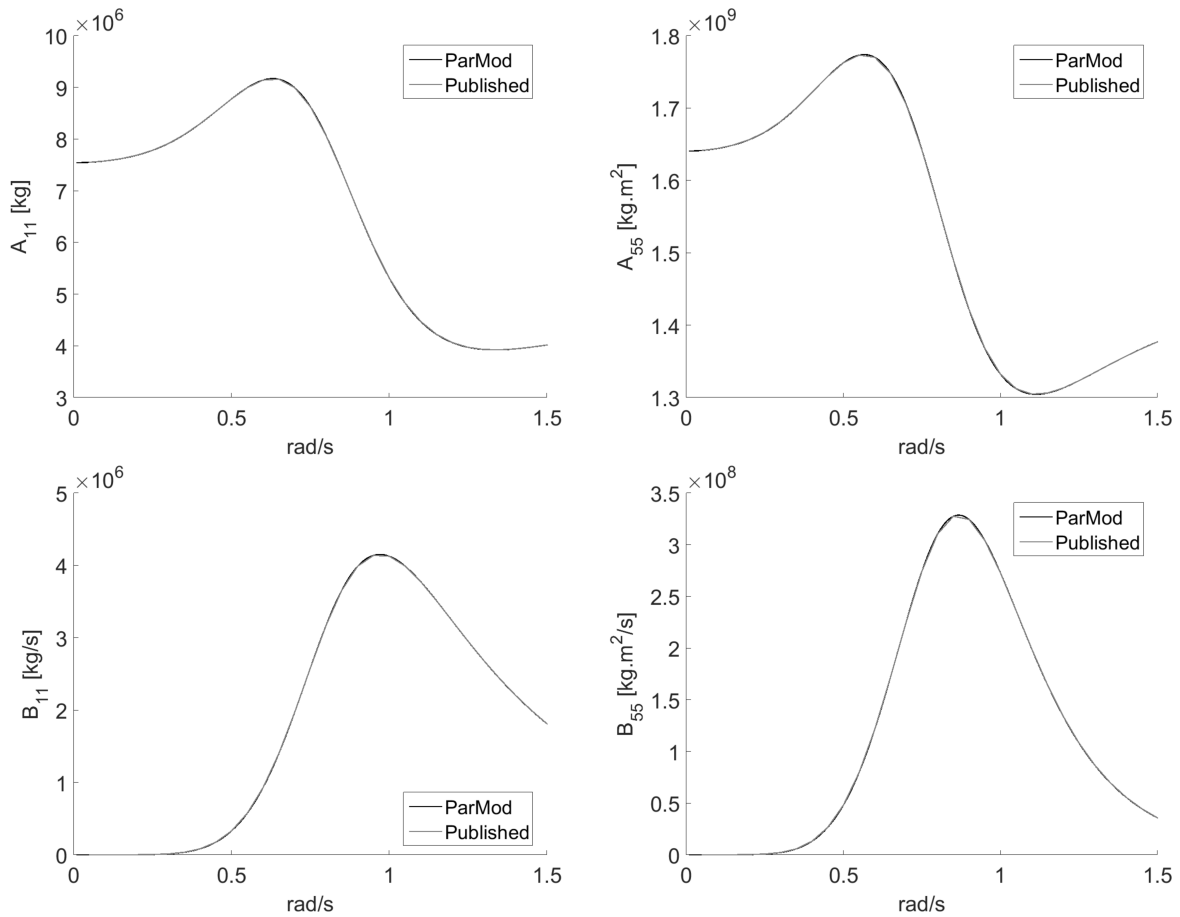


Figure 7.17: Comparison of hydrodynamic coefficients of a cylinder, obtained with WAMIT.

a breakdown of modules is necessary to understand expected the runtime. Furthermore, measuring the performance requires additional calculation time. For that reason, multiple measurements were taken with and without the performance measurement code. The final runtime is given without the performance measurement. The modules' assessments have to include the additional code's contribution. Therefore, the totals are not equal.

Details are presented in Table 7.5 for the semisubmersible and the torus. The torus also includes a rotated version. Rotating it 45 degrees in both x and y-axes ensures that each panel is rotated at least once. Therefore, approximately there is a total of 9600 rotations performed. As explained above, file operations and rotations emerge as the degraders of performance. Overall, one second per 1000 panels is a reasonable average runtime as seen in Table 7.6.

7.8 Concluding remarks

The chapter provided an efficient numerical solution for obtaining a multi-purpose 3D model of structures, returning their mass properties while providing a suitable mesh model for panel method calculations. The input data was described based on matrices. Therefore, geometries may be scripted out without visual intervention. Parameterizing the model was explained to provide a basis for building variations of a model in iterative calculations. A range of examples was given to

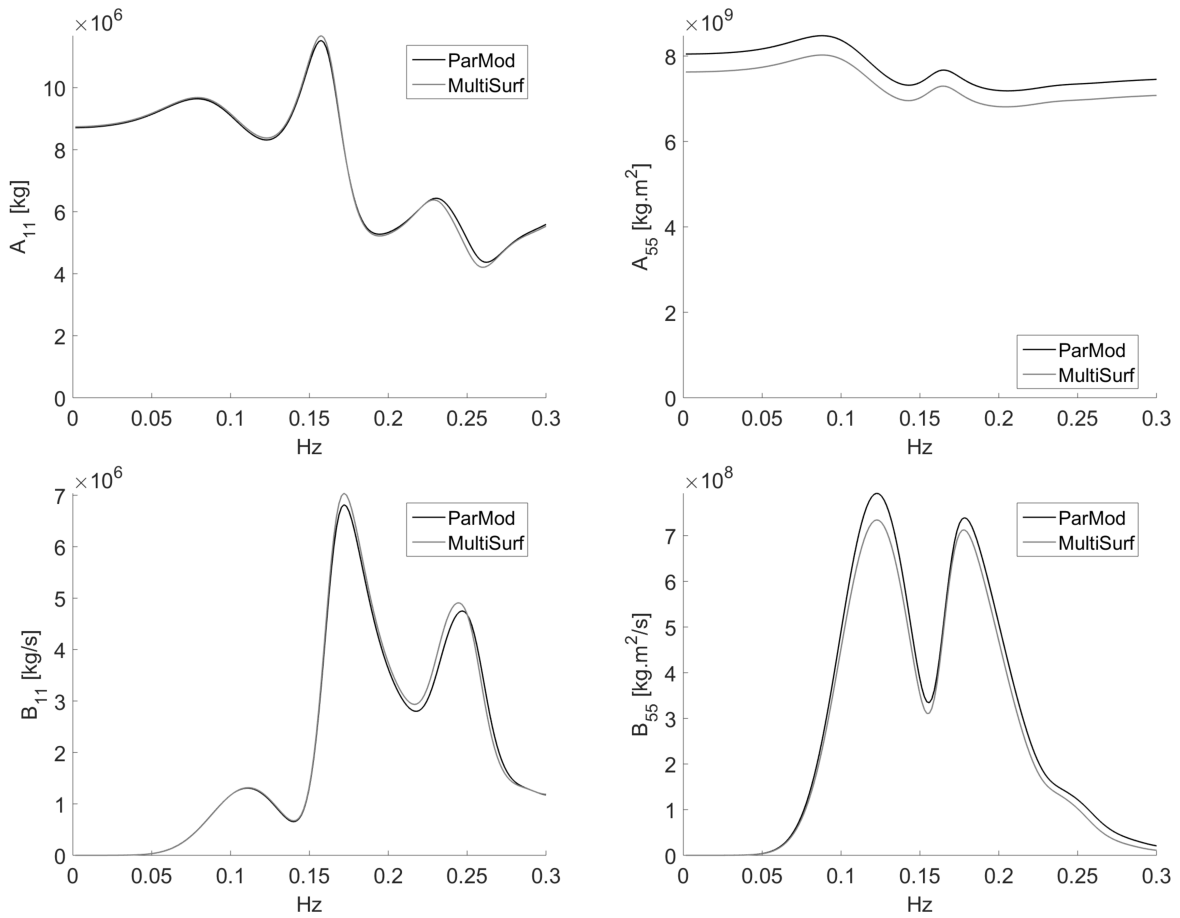


Figure 7.18: Comparison of hydrodynamic coefficients of the semisubmersible platform, obtained with WAMIT.

Table 7.5: Performance breakdown of the modules in seconds

	Semisubmersible (1633 panels)	Torus (4800 panels)	Rotated torus (4800 panels)
Panel properties (CoG, Weight)	0.54	1.52	1.44
3D Rotations	0.04	0.00	1.31
File I/O	0.45	0.79	0.79
Surface normals	0.25	0.36	0.69
Other operations	0.41	0.74	0.65

Table 7.6: Total run times with (W) and without (WO) performance measurement in seconds

	Semisubmersible (1633 panels)	Torus (4800 panels)	Rotated torus (4800 panels)
WO	1.37	2.83	4.09
W	1.68	3.41	4.88

demonstrate the usage of the code. The list included a frustum, a sphere, a torus, a glass, a rectangular prism, a midship section, an offshore platform, a ship hull, and a dome to illustrate variety. The code was evaluated on these samples to calculate the mass properties of weight, inertia, volume and the centre of gravity. A validation of the calculation method was given through comparisons with commercial software. Panel method validation was carried out on a cylinder and a semi-submersible offshore platform.

Overall, this approach delivers mass data within a 0.5% margin compared to ANSYS. Volume calculations are in a similar range when compared to Rhino3D evaluations. In WAMIT, for a cylinder, the model prepared with a combination of Rhino3D and PanelingTools gave identical results with the presented method. For a semisubmersible wind turbine platform prepared in MultiSurf, the data compared favourably to published results. The performance indicators summarise that the expected runtime is approximately one second per 1000 panels to provide mesh model and solve it for mass. These numbers are unlikely to be a hindrance to the design systems that would include this type of calculations. Accordingly, this method can be integrated into early design states to replace spreadsheets and manual calculations, or used for obtaining distributed mass properties from available mesh grids.

Application of the design system on a tension leg platform

8.1 Introduction

This chapter lays out the foundation of a design system using the multi-purpose 3D modeller in Chapter 7. It studies a hypothetical tension leg platform as a worked example with a geometry closer to the conventional TLP hull forms. In here, the purpose is to demonstrate the method of systematisation to test out ideas rapidly as opposed to presenting a favourable platform; the proposed setup requires minimal or no alterations when applied to another TLP. It is assumed that only the tower and the rotor-nacelle assembly's mass, and the turbine's thrust values are known before starting the design. Accordingly, the system can be applied with minimal input at the frequency domain stage.

The design system acts as a moderator to calculate the necessary input (e.g., mass data, hydrostatics, mooring setup and stiffness matrix) to build a mathematical model of the structure. It feeds this data to two separate software. Potential flow calculations from WAMIT [130] are extended for the frequency domain assessment with the turbine. FAST [50] is used for the time domain solution. The automated building of the FAST model is carried out by the code described in Chapter 6. After discussing the level of agreement between the two mathematical solutions, an evaluation is given for a range of platform's main dimensions. The selected hull is then examined at the coast of Spain, Galicia, using scatter diagrams that represent the probable sea states and wind speeds. Formulae are provided to evaluate the occurrence of mooring line tension loss as opposed to leaving this crucial factor to the time domain stage. A measure of performance regarding time is also given to discuss the computational requirements.

Published in: A system for the hydrodynamic design of tension leg platforms of floating wind turbines. *Ocean Engineering*, 171:78–92, 2019. doi: 10.1016/j.oceaneng. 2018.10.052

8.2 Design practices and considerations

The numerical studies on existing platforms (e.g., [38, 25, 123]) contribute to the understanding of response dynamics. The knowledge gained from this type of in-depth assessment forms a basis for motion prediction codes where the emphasis is on improving particular modules of a software (e.g., a better mooring implementation [161]). Conversely, the design process of an envisioned platform starting from a blank-sheet scenario (i.e., a case where nothing is known or given apart from an idea) is a different problem that needs to be addressed. Summarising from previous chapters, spreadsheets are commonly used to find an estimate of the mass properties [93, 83]; then, various simplifications are introduced to get the hydrodynamic coefficients such as making use of tabular data for cylinders as in [96, 79]. An early assessment of the motions can be obtained through closed-form equations [81].

Considering the entirety of the design process, these approaches offer lower precision compared to building 3D models for the mass and hydrodynamics. For instance, for the spreadsheet in [162], it is explained that the mass calculations were based on statistical averages of steel weight listed in [81] for oil and gas platforms. The applicability of oil and gas platform data to wind turbine hulls was not evaluated. The inertia was estimated from this assumed mass after approximating the hull shape as a set of prisms and cylinders. Other variables such as added masses and waterplane area characteristics for hydrostatic calculations were treated in the same manner. Without a 3D model, the hydrodynamic variables needed to leave out the potential flow solution even if the structure requires it. This case results in possible discrepancies due to simplifications [58, 47]. Similarly, deviations in the mass matrix lead to significantly different predictions of motion as discussed in [34].

Another immediate disadvantage of these approaches is that the entire calculation procedure needs to be revised if the structure is changed. For instance, on a spreadsheet, the formulation for mass, hydrostatics, and hydrodynamics (e.g., added mass) should be replaced if a prismatic barge is considered instead of a cylindrical buoy. Methods such as genetic algorithms that aim to study the design space without “for loops” [88, 152] do not address these problems and they are still limited to elementary shape combinations. Regardless of the method, generic (i.e., applicable to a variety of hull forms as opposed to being limited to one form) solutions become difficult as it may not be possible to break down the components of any hull into basic shapes. Additionally, these processes require considerable time to test out ideas. This case is especially true for complex hull forms that move beyond cylinders and their variations.

As opposed to the solution above, a generic interconnected system can allow obtaining the motion dynamics of a novel concept in the shortest time possible with an acceptable level of accuracy. Studies that offer partial solutions exist for topics such as fatigue life optimisation of an existing hull [84, 90]. However, expanding onto new designs brings other challenges. There are no base values to assume as constants as in the case of optimisation studies on existing structures (e.g., the mass and inertia of the platform, and the mooring setup [84, 90, 92]). Accordingly, new designs will benefit

from integrated modular approaches where each component deals with a specific problem and can be updated and improved as necessary. These modules should be able to work with each other without user intervention (e.g., stopping to obtain and copy data from another software, or carrying out manual calculations) to speed up the process. Hence, automation needs to be considered not as a target but as a requirement, and it will additionally serve to remove possible human errors discussed in [47]. Approximate solutions with a satisfactory degree of precision should be given rapidly in frequency domain. This way, time domain simulations that require a longer computational time commitment are reserved to valid candidates that comply with a set of criteria.

8.3 System development

In scope of this work, building a system signifies developing a self-sufficient procedure. Once a parametric model is developed, the internal codes and all external implementations must work with each other without necessitating further user involvement. Unless they interact seamlessly, the use of multiple models and software (e.g., software A for mass properties and B for hydrodynamics) signifies that the procedure is interrupted, requiring an additional time commitment for moving data (e.g., manually copy-pasting into a spreadsheet from another program). For this reason, the process below tries to cover all necessities of the initial design process and only utilises external codes that allow text-based input as opposed to visual input.

The structure is defined with a script to develop the multi-purpose parametric 3D model. The utilised format serves two purposes. The entire model including the turbine, tower and the platform is used for the mass property calculations. It is truncated at the waterline and fed into a panel method code to obtain the hydrodynamic coefficients, wave exciting forces, and the response amplitude operators. The waterplane area is also extracted at this stage and serves as an intermediate between mass and hydrodynamic models. The platform's natural frequencies and coupled responses to combined wind and wave loading are approximated with the potential flow solver's output. This data is then used to build a time domain model. These stages are explained below.

8.3.1 Mass properties

As described in Chapter 7, ParMod's input format is numerical. Matrices of $[3 \text{ by } n]$ are used to develop radius-based (e.g., cylinders, spheres, torus) parts by defining the radius, position, and the number of sections of the shape. The $[4 \text{ by } n]$ matrices describe face-based components (e.g., barges, ship shapes) of a body providing the vertices, and the sectioning. The output is a mesh of quadrilateral panels defined by the three coordinates of their four vertices (i.e., x y and z Cartesian coordinates). This geometry is represented by an $[n \text{ by } 12]$ matrix where n denotes the total number of panels that describe the hull. When this format is extended by adding two more columns for thickness and density (i.e. making an $[n \text{ by } 14]$ matrix), it can be used to estimate the weight and inertia of the model. A solution is obtained to deliver the mass matrix of the entire structure by combining the position of the centre of gravity of each panel with the thickness and density.

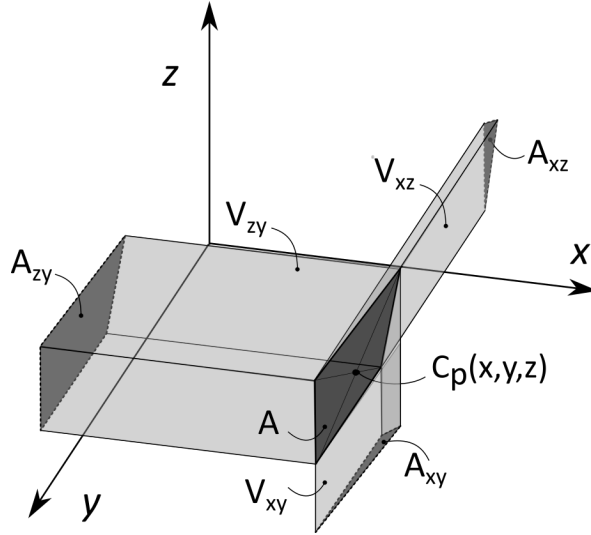


Figure 8.1: Contribution of an individual panel to the model's centre of buoyancy

The [6x6] mass matrix is written in the following form for a structure with a mass denoted by (m) and centre of gravity (x_g, y_g, z_g) in their respective axes:

$$M = \begin{bmatrix} m & 0 & 0 & 0 & mz_g & -my_g \\ 0 & m & 0 & -mz_g & 0 & mx_g \\ 0 & 0 & m & my_g & -mx_g & 0 \\ 0 & -mz_g & -my_g & I_{xx} & I_{xy} & I_{xz} \\ mz_g & 0 & -mx_g & I_{yx} & I_{yy} & I_{yz} \\ -my_g & mx_g & 0 & I_{zx} & I_{zy} & I_{zz} \end{bmatrix} \quad (8.1)$$

The hull's displacement is obtained by projecting the area of each panel onto the reference planes and integrating the values from its geometric centre up to the reference system axes. The geometric centres of the n number of volumes below the waterline provide the centre of buoyancy (see Figure 8.1 for the illustration of an individual panel's contribution):

$$CoB(x, y, z) = \frac{\sum_1^n CoB_i(x_i, y_i, z_i) \cdot V_i(x_i, y_i, z_i)}{\sum_1^n V(x, y, z)} \quad (8.2)$$

8.3.2 The hydrostatic restoring matrix and the hydrodynamic panel model

The hydrostatics require the extraction of the waterplane area and serve as an intermediate between the mass and the hydrodynamic models. Thus, an algorithm is necessary to truncate the structure at the waterline intercept and to obtain the underwater geometry. Then, the hydrostatic stability calculations can be obtained with a method similar to [163].

Consider a quadrilateral polygon with some of its vertices (e.g., P1, P2, P3, and P4) located partially below a given line. One, two, or three vertices may reside above the line as illustrated in Figure

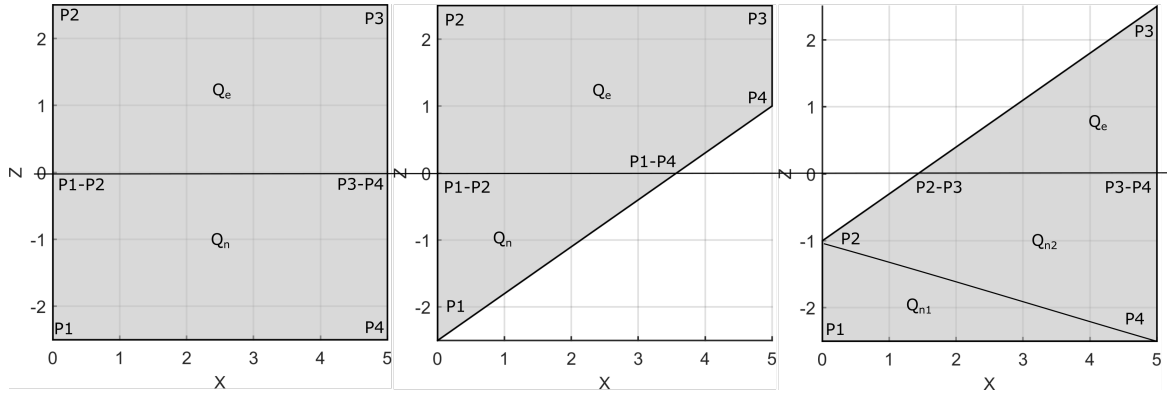


Figure 8.2: Truncating an individual quadrilateral panel from the waterline ($Z=0$), the subscripts e and n denote eliminated sections and new quadrilaterals respectively.

8.2. Evaluating the mesh in clockwise (P1 to P4) and then counter-clockwise (P4 to P1) directions and looking for edges that cross over the limit locates the intersections (e.g., P1-P2 represents the intersection between P1 and P2). Then, truncated quadrilaterals can be formed using these new points and the vertices that were already below the limit. The surface normal should also be ensured to remain identical to its former value. In the case where there are three points above the waterline, the remaining triangle can be expressed by repeating the last vertex. For cases with only one vertex above the waterline, two panels are written as represented by the areas Q_{n1} and Q_{n2} in Figure 8.2.

The procedure of evaluating the interpolations as described and keeping underwater panels generates the hydrodynamic mesh. To obtain the waterplane area and its moments, the water-level vertices are extracted with a known clockwise or counter-clockwise order that defines a closed polygon. This shape can be produced by sorting the vertices by their four-quadrant inverse tangents about a distance from an internal location. Assume that the x_c and y_c are internal points of a given polygon. The four-quadrant inverse tangent is commonly denoted by “atan2” in a variety of computer languages. For each vertex $n(x, y)$, the order (O_v) is associated to:

$$O_v = \text{atan2}(x - x_c, y - y_c) \quad (8.3)$$

Arranging the vertices according to their O_v values results in a polygon that defines the waterplane area. If there are multiple components that intercept the waterline (e.g., a four-column semisubmersible) this process is repeated for each component.

Figure 8.3 is an example of the process described above that illustrates the mass, hydrodynamic, and waterplane model of the semisubmersible given in the previous chapters. Once the waterplane area is represented as a closed polygon, its moments of inertia can be found by summing the contribution from each segment according to Greene’s theorem. The area and the centroid (i.e., the centre of floatation) of the polygon can be calculated using formulations for a set of known coordinates. The linearised [6x6] hydrostatic restoring matrix is written using this data in the following form [164, 165]:

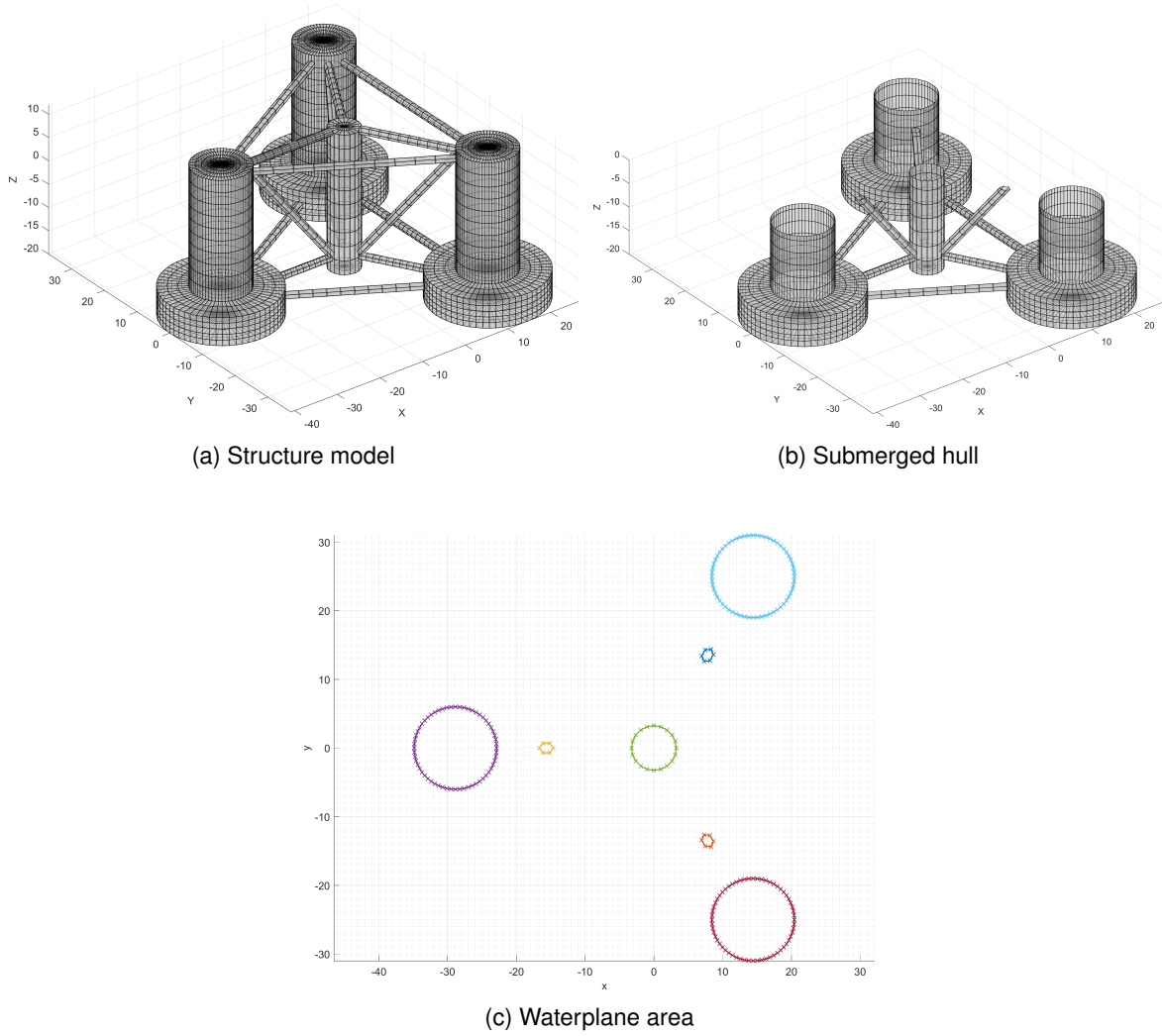


Figure 8.3: The mass, hydrodynamics, and waterplane area models illustrated on the OC4 semisubmersible platform

$$C_h = g \begin{bmatrix} 0 & 0 & 0 & 0 & 0 & 0 \\ 0 & 0 & 0 & 0 & 0 & 0 \\ 0 & 0 & \rho A_{wp} & \rho A_{wp} y_f & \rho A_{wp} x_f & 0 \\ 0 & 0 & \rho A_{wp} y_f & \rho (V_{z_b} + I_{xx}^w) - m z_g & \rho I_{xy}^w & -\rho V_{x_b} + m x_g \\ 0 & 0 & \rho A_{wp} x_f & -\rho I_{xy}^w & \rho (V_{z_b} + I_{yy}^w) - m z_g & -\rho V_{y_b} + m y_g \\ 0 & 0 & 0 & 0 & 0 & 0 \end{bmatrix} \quad (8.4)$$

In Equation 8.4, the term A_{wp} represents the waterplane area, x_f and y_f are the centres of floatation. The waterplane inertia terms are I_{xx}^w and I_{yy}^w for roll and pitch respectively. V_{s_b} denotes the centre of buoyancy where the subscript s is replaced with x, y, and z to identify the axes. The gravitational acceleration and the water density are g and ρ respectively. The mass of the structure is given as m, and the centres of gravity are denoted with x_g , y_g , and z_g in their respective Cartesian axes.

Table 8.1: The properties of spiral strand mooring line material as a function of its diameter

Steel area (m ²)	Weight in water (kg/m)	Breaking strength (N)	Stiffness (N)
3.74E-4 d ²	0.79 d ²	5.60E5 d ²	5.93E7 d ²

8.3.3 Mooring setup

In tension leg platforms, the mooring lines are the primary source of stiffness in restricted modes, and their setup is a crucial part of the design process. For reasonable solutions, the availability of mooring line diameters should be considered at early design stages. This approach opposes finding an equivalent radius that complies with the class society rules and assuming that this number can be covered with several mooring lines as it was done in [79].

The Handbook of Offshore Engineering [81] mentions that the diameter of the largest chain mooring line constructed as of 2005 measured 159 mm. While there are surely changes in the recent years, the fact that there are size limits does not change. Beyond the maximum value, the number of mooring lines needs to be increased as opposed to the diameter. Accordingly, the added lines will lead to a structure with higher complexity regarding production. For instance, at 160 mm, the TLPWT1 tension leg platform presented in [79] requires a minimum of 9 mooring lines per fairlead (i.e., 36 mooring lines in total) to cover the 1.4-meter equivalent diameter. The platform's designed natural frequencies are also higher due to the extreme stiffness provided by this mooring setup. However, the mentioned scenario may be impractical under preferable production terms. In such cases, the structure needs to be redesigned since the eigenfrequencies will reflect the changes in the mooring setup. There will be other complexities as the thickness of an individual line also becomes problematic. For these reasons, it would be advisable to consider the total number of mooring lines at early design stages.

Here, the assumption is that 50 to 150 millimetres are acceptable ranges of mooring line diameters. Their related material properties are presented in Table 8.1. These values are used for designing the structure within limitations using spiral strand material with a maximum of 4 mooring lines per fairlead. The load encountered by each line is:

$$F_{line} = g \frac{\nabla \rho - W_t}{n_t} \quad (8.5)$$

The displacement is represented by ∇ , W_t is the weight of the structure, and n_t is the number of mooring lines. API RP2T [166] recommends a safety factor of 1.67 up to twice the initial tension, resulting in:

$$2F_{line} < \frac{F_{break}}{1.67} \quad (8.6)$$

Within these limits, the design algorithm follows an iterative procedure. It starts with one mooring line per fairlead and a diameter of 50 millimetres. If the line cannot comply with the safety margin, it increases the diameter in steps of 10 mm up to 150 mm. When this limit is surpassed, it increases the number of mooring lines. The designs that need more than a limit number of mooring lines is classified as uncompliant.

With known material properties and setup, the [6x6] mooring stiffness matrix (C_m) can be obtained from the formulae given in [84]:

$$C_m = \sum \begin{bmatrix} \frac{F_{line}}{L_m} & 0 & 0 & 0 & -z_l \frac{F_{line}}{L_m} & 0 \\ 0 & \frac{F_{line}}{L_m} & 0 & z_l \frac{F_{line}}{L_m} & 0 & 0 \\ 0 & 0 & \frac{EA}{L_m} & 0 & 0 & 0 \\ 0 & z_l \frac{F_{line}}{L_m} & 0 & (y_l^2) \frac{EA}{L_m} & 0 & 0 \\ -z_l \frac{F_{line}}{L_m} & 0 & 0 & 0 & (x_l^2) \frac{EA}{L_m} & 0 \\ 0 & 0 & 0 & 0 & 0 & (x_l^2 + y_l^2) \frac{EA}{L_m} \end{bmatrix} \quad (8.7)$$

The positions of an individual mooring line in Cartesian coordinates are represented by x_l , y_l and z_l respectively. The mooring line's stretched length is denoted by L_m . The unstretched length (L_u) is given by:

$$L_u = \frac{L_m}{1 + \frac{F_{line}}{EA}} \quad (8.8)$$

The weight in air per meter can be obtained from the weight in water increased by the buoyancy applied to the line per unit length. This value and the unstretched length are used in later stages for building the finite element mooring line setup of the FAST time domain model.

8.3.4 Platform motion dynamics

At the stage of calculating the motion dynamics, a structural model is already prepared, truncated from the waterline, and the mooring setup is completed. Passing the underwater mesh, the externally calculated mass matrix, and the mooring line stiffness matrix to WAMIT delivers the wave response amplitude operators, exciting forces, and the hydrodynamic coefficients in frequency domain. It is possible to devise a preliminary checkpoint for the structure from this data, starting with the natural frequencies.

Eigenfrequencies

The following formulae are given for the natural frequencies of an undamped single degree of freedom system oscillating in water:

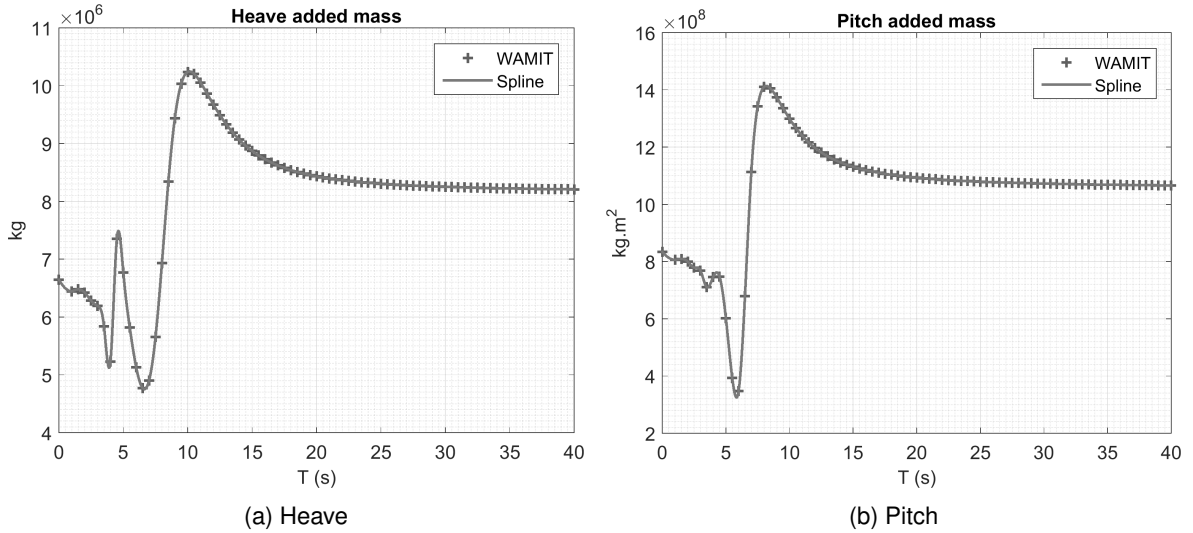


Figure 8.4: Spline interpolation of heave and pitch added masses calculated with 0.5-second intervals by WAMIT

$$C_t = C_h + C_m \quad (8.9)$$

$$\omega_n = \sqrt{\frac{C_t}{M_t + A_{ij}}} \quad (8.10)$$

The restoring terms (C_h and C_m) and the mass matrix were discussed previously. However, the added masses (A_{ij}) were not mentioned. There are simplified formulations and tables for estimating these values (e.g., [96]). However, they may not be sufficient especially for hull shapes that adhere to a potential flow solution as stated in [58]. For this reason, it's beneficial to use the readily available solution obtained from the panel method code. To do so, the hydrodynamic data is imported, and a curve-fitting algorithm is used to estimate the in-between values. This approach does not necessitate all points to be given by the panel method code. Consider the heave and pitch added masses in Figure 8.4 as an example. The WAMIT data was obtained in half second intervals. Between 2.5 and 5 seconds, a likely range for the tension leg platform eigenfrequencies, the values change rapidly. However, the interpolations provide an estimation for all data points.

Equation 8.10 serves to calculate the natural frequencies iteratively. An initial estimate is made using the zero frequency added masses. When the difference between the resulting eigenfrequency and the added mass's selected frequency is less than a tolerance value, the solution is accepted. Otherwise, the calculation is repeated using the added mass value of the current iteration's natural frequency. Solving for the six degrees of freedom results in the uncoupled and undamped eigenfrequencies of the system. The platform needs to be designed outside the 4 to 25 seconds range to avoid first-order wave excitation [27].

Pitch motion and mooring line angle in operational conditions

In TLPs, to avoid complexities at the anchors, the mean offset caused by the operating turbine and the waves should not surpass 6 to 8 percent of the water depth according to [81] which corresponds to approximately 5 degrees. Since the RAO is known at this point, the surge caused by the waves in operational conditions at a frequency of ω_o and wave height of H_o can be calculated by:

$$x_{wave_{11}} = RAO_{11}(\omega_o) \cdot H_o / 2 \quad (8.11)$$

If the turbine is accepted to operate at a constant thrust ($F_{turbine}$) with a shaft angle of θ , the related horizontal motion caused by the turbine can be estimated by:

$$x_{wind_{11}} = \frac{F_{turbine} \cos(\theta)}{C_t(1, 1)} \quad (8.12)$$

The total offset in operational conditions then becomes:

$$x_{t_{11}} = x_{wave} + x_{wind} \quad (8.13)$$

Defining D as the installation water depth, the 6% limit can be checked through:

$$x_t < 0.06D \quad (8.14)$$

Similarly, the pitching angle due to waves ($\varphi_{wave_{55}}$), wind ($\varphi_{wind_{55}}$), and their total ($\varphi_{t_{55}}$) is equal to:

$$\varphi_{wave_{55}} = RAO_{55}(\omega_o) \cdot H_o / 2 \quad (8.15)$$

$$\varphi_{wind_{55}} = a \cdot F_{turbine} \cdot \cos(\theta) / C_t(5, 5) \quad (8.16)$$

$$\varphi_{t_{55}} = \varphi_{wave} + \varphi_{wind} \quad (8.17)$$

In Equation 8.16, a is the moment arm that causes the pitching motion.

Set-down

Set-down is a specific dynamic of tension leg platforms. The surge mode of a TLP forces its mooring lines into an angle at the fairleads. Since the line length stays constant disregarding the elasticity, the resulting motion is heaving in the direction of the seabed. In a sense, it is a coupling between surge and heave modes. It can be argued that the surge motion of TLPs becomes more

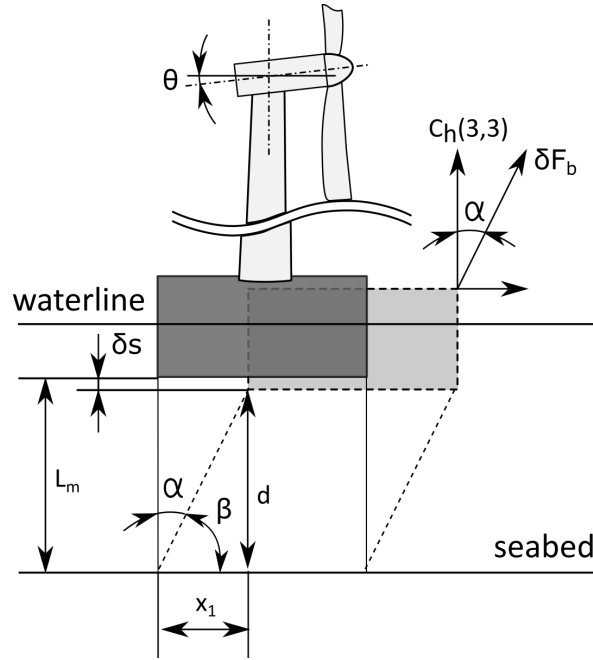


Figure 8.5: Tension leg platform dynamics in set down

relevant in floating wind turbine platforms as opposed to oil and gas platforms. It is not caused only by the waves and the wind forces on the hull; it is actively enforced by the turbine thrust.

Assume that the surge motion caused by the waves and the wind is already known with the Equation 8.13 for the platform given in Figure 8.5. Through geometrical relationships, the set-down distance is:

$$\delta s = L_m - \sqrt{L_m^2 - x_{11,t}^2} \quad (8.18)$$

Approximating the mooring line responses

A failure state for a tension leg platform is the loss of mooring line tension, termed as going slack. This case causes large bending moments in the tethers and a snatch load when they come back into tension. Accordingly, it is relevant to get an estimation of mooring responses at early design stages. While the dynamics are complicated, there are various possibilities to devise a simplified approach for approximation purposes.

One of the alternatives is to consider the mooring line as a spring with known elasticity properties. To illustrate the approach for design in head waves, assume that the roll is minimal, and the heave and pitch are the prominent motions. The heave motion at a given frequency is:

$$x_{33} = RAO_{33}(\omega) \cdot \frac{H}{2} \quad (8.19)$$

Operating at a shaft angle of θ degrees, there is also a component of the turbine thrust that leads to heave. The resulting total becomes:

$$x_{33,t} = x_{33} + \sin(\theta) \cdot \frac{F_{turbine}}{C_t(3,3)} \quad (8.20)$$

For a total pitching angle of φ_{t55} , the vertical motion at the location of the fairlead ($x_{fairlead}$) is:

$$x_{t55} = \sin(\varphi_{t55}) \cdot x_{fairlead} \quad (8.21)$$

The total vertical motion caused by heave and pitch becomes:

$$\delta Z = x_{t33} + x_{t55} \quad (8.22)$$

The heave and pitch motions (x_{33}) and (x_{55}) in Equations 8.19 and 8.15 will happen with a phase shift of ϵ degrees. In regular waves, this shift can be considered by:

$$\delta Z_{max} = \sqrt{x_{33}^2 + x_{55}^2 + 2x_{33}x_{55} \cdot \cos(\epsilon)} \quad (8.23)$$

A conservative calculation would be to assume that heave and pitch motions occur in phase.

When the mooring line is considered to act as a spring that has moved δz meters from its original length of L_m , the loss of tension at the mooring line is given by Hooke's law for a stretched cable:

$$F_{loss} = \delta z \cdot \frac{EA}{L_m} \quad (8.24)$$

For the sake of completeness, the increased buoyancy force (F_b) due to the heaving motion and the component of the surge force that applies on the angled mooring line (F_{sm}) can be added (see Figure 8.5 for α):

$$F_b = \cos(\alpha) \cdot \rho \cdot g \cdot C_h(3,3) \cdot \delta z \quad (8.25)$$

$$F_{sm} = F_{11} \cdot \sin(\alpha) \quad (8.26)$$

Finally, the loss of mooring line tension becomes:

$$\delta F_m = F_b + F_{sm} - F_{loss} \quad (8.27)$$

Table 8.2: Tower and RNA mass properties as modelled and documented

		Documented	Modelled
Tower mass	[kg]	249,718	249,760
Height of the tower's CG	[m]	43.4	43.4
Hub and blades mass	[kg]	56,780	Point mass as documented
Nacelle mass	[kg]	240,000	Point mass as documented

8.3.5 Building a parametric model and systemising the design process

Figure 8.6 summarises the design process where the dark grey shaded boxes represent FAST and WAMIT as external codes. The parametric modelling tool (ParMod) described in Chapter 7 assumes a central role in building the 3D model and providing the output for the mass properties, hydrostatics, and the underwater hull. The interaction between ParMod's modules in the development and assessment of the multi-purpose model are illustrated in Figure 8.7. The mooring setup is an external code that performs as described in the previous section. Since the turbine and the tower are pre-designed, their specifications are inputs to the parametric modeller.

The system evaluation stage utilises the output from WAMIT to get the added masses to calculate the eigenfrequencies. It also approximates the platform and mooring line responses using the wave RAOs of WAMIT and considers an additional response to the turbine. This information is used for a frequency domain design check. If the design complies with the requirements, it is classified as a candidate and a time domain model is built. Otherwise, it is discarded. The time domain motions of possible candidates can then be studied. As generally known, and will be discussed later, frequency domain results are faster to obtain. For this reason, time domain simulations are reserved only for designs that pass the frequency domain check.

The 3D model includes the tower, RNA, and the platform, where only the platform is parametrised within the script. The tower model is a cylinder with a thickness of 2.7 centimetres at the bottom and a diameter of 6.5 meters, and 1.9 centimetres at the top with a diameter of 3.87 meters. These measurements result in the mass given for the NREL 5MW tower [48]. Table 8.2 lists the documented values in comparison to the output from the 3D model where tower's mass and centre of gravity gives an idea about the precision of the mass model. The masses of the blades, nacelle, and the hub are considered (i.e., RNA) as point weights, located at their centres of gravity. They are unmeshed in Figure 8.8 that shows the entire model.

The platform consists of four buoyancy columns placed on pontoons and a central column with the turbine atop. The naming of the components is given in Figure 8.9. The outer ring size (i.e., length and beam) and the keel depth (i.e., draft) were chosen as the parameters to vary. The dimensions related to these two main variables as listed in Table 8.3. When a variation is built inside the design process, all measurements are rounded to their nearest 5 cm increments (e.g., if a dimension was calculated as 0.241 meters, it is selected as 0.25 meters).

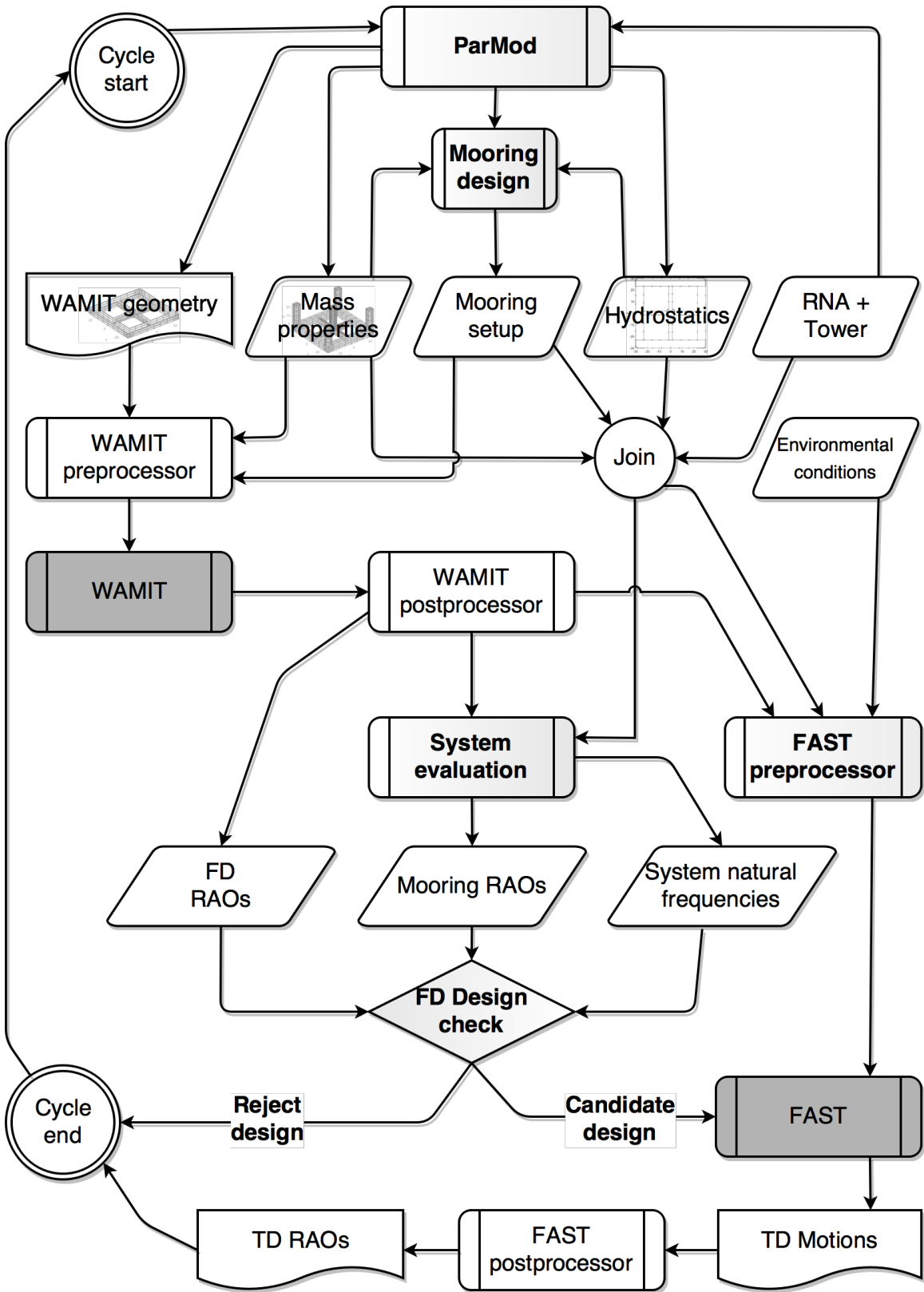


Figure 8.6: Interaction between the modules throughout the design cycle, dark grey shaded components represent external codes

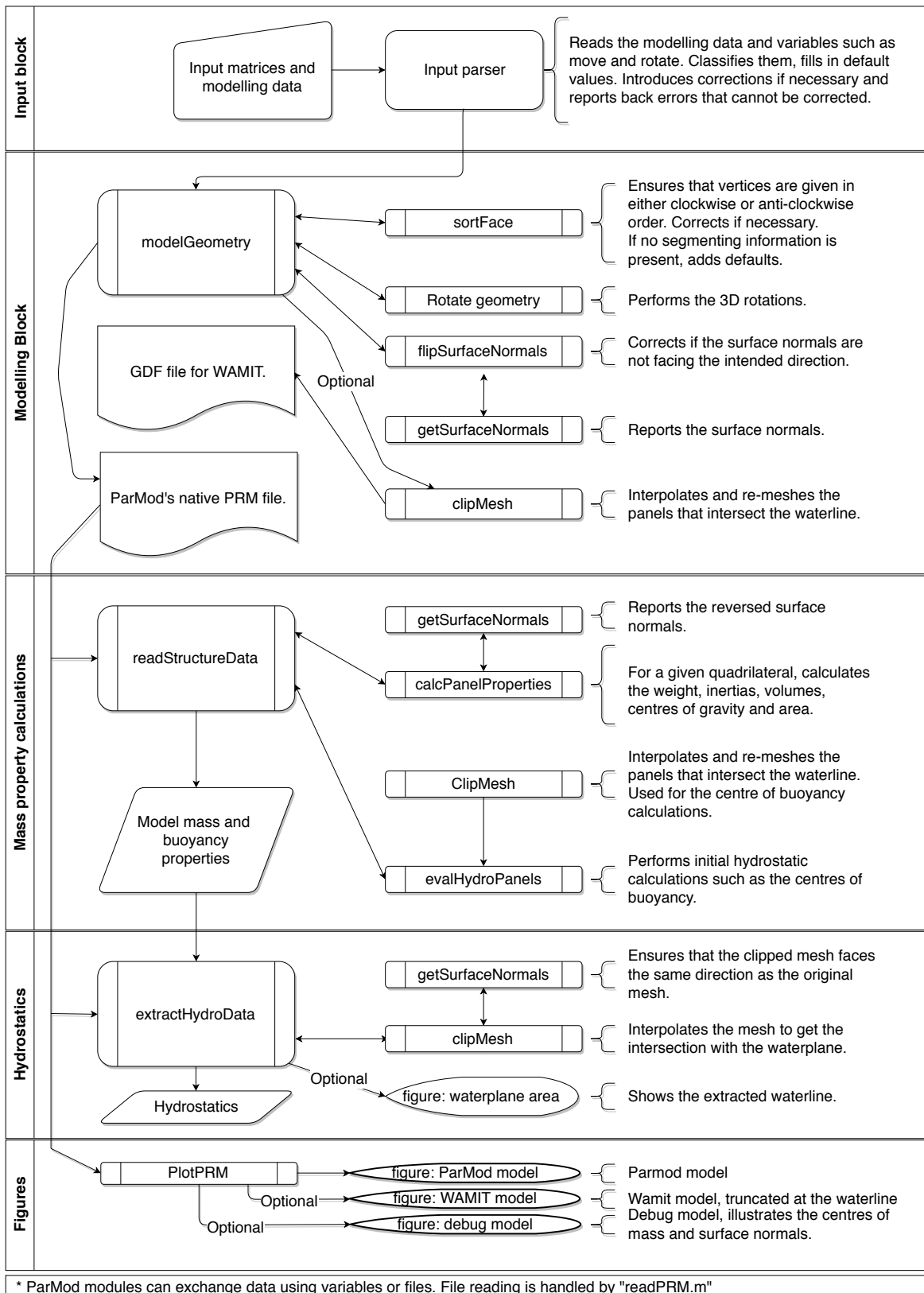


Figure 8.7: Interaction between ParMod's modules in the development and assessment of the multi-purpose model

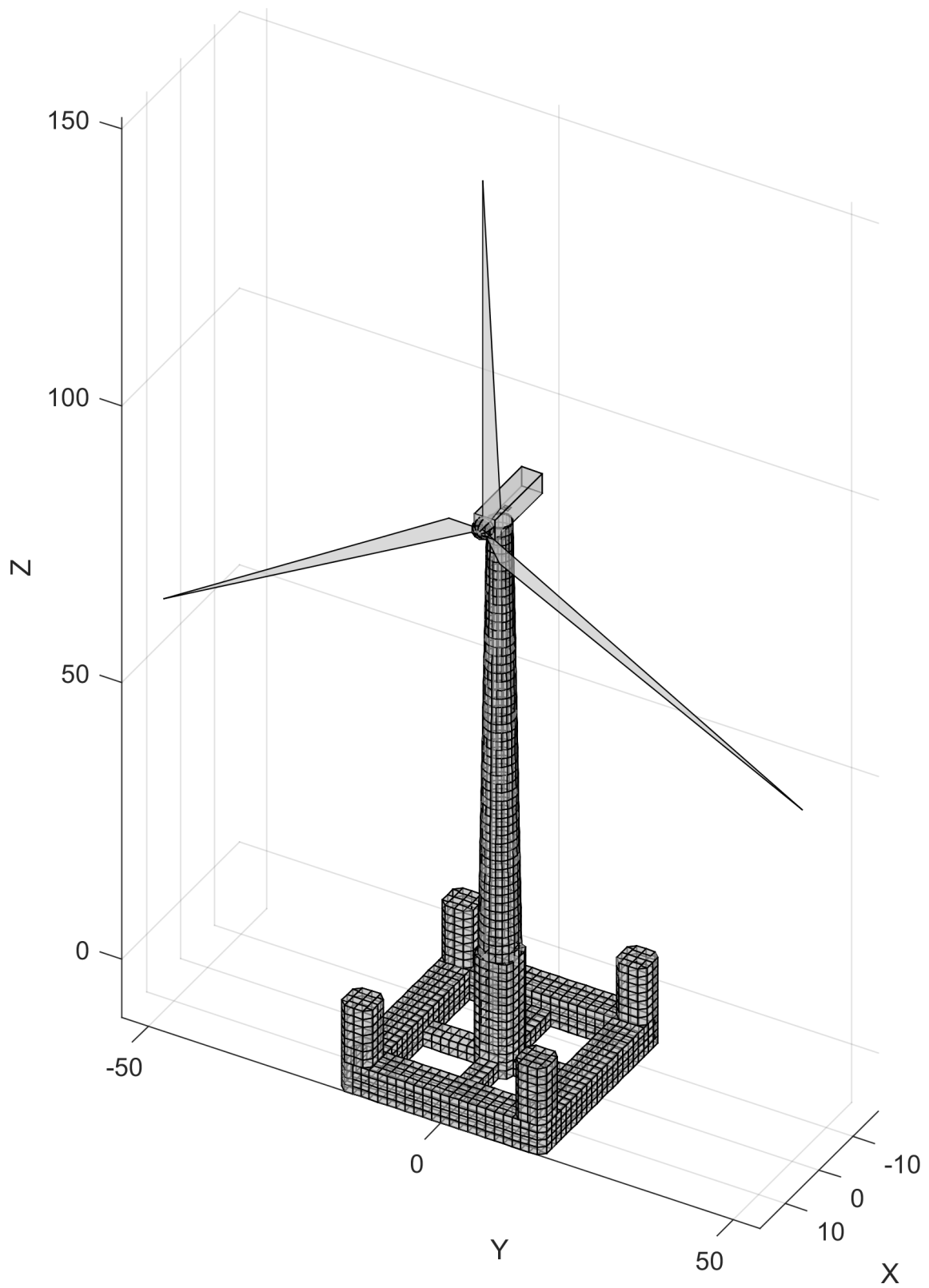


Figure 8.8: The model of the platform, tower and the RNA. The meshed components are considered as distributed mass

Table 8.3: Parameters used for the platform dimensions

Input parameters	Value
Outer ring	[15.00, 15.25, ..., 19.75, 20.00]
Keel depth	[10.00, 10.50, ..., 14.50, 15.00]
Relative sizing	
Pontoon width	[pontoon height]
Ring column width	[pontoon width]
Ring column corner radius	[pontoon width]/5
Connection height	[pontoon height]/2
Connection width	[pontoon height]/2
Central column corner radius	[central column width]/4
Fixed sizing	
Pontoon height	5.25 m
Central column width	6.50 m
Central column height above WL	10.00 m
Ring column height above WL	5.00 m

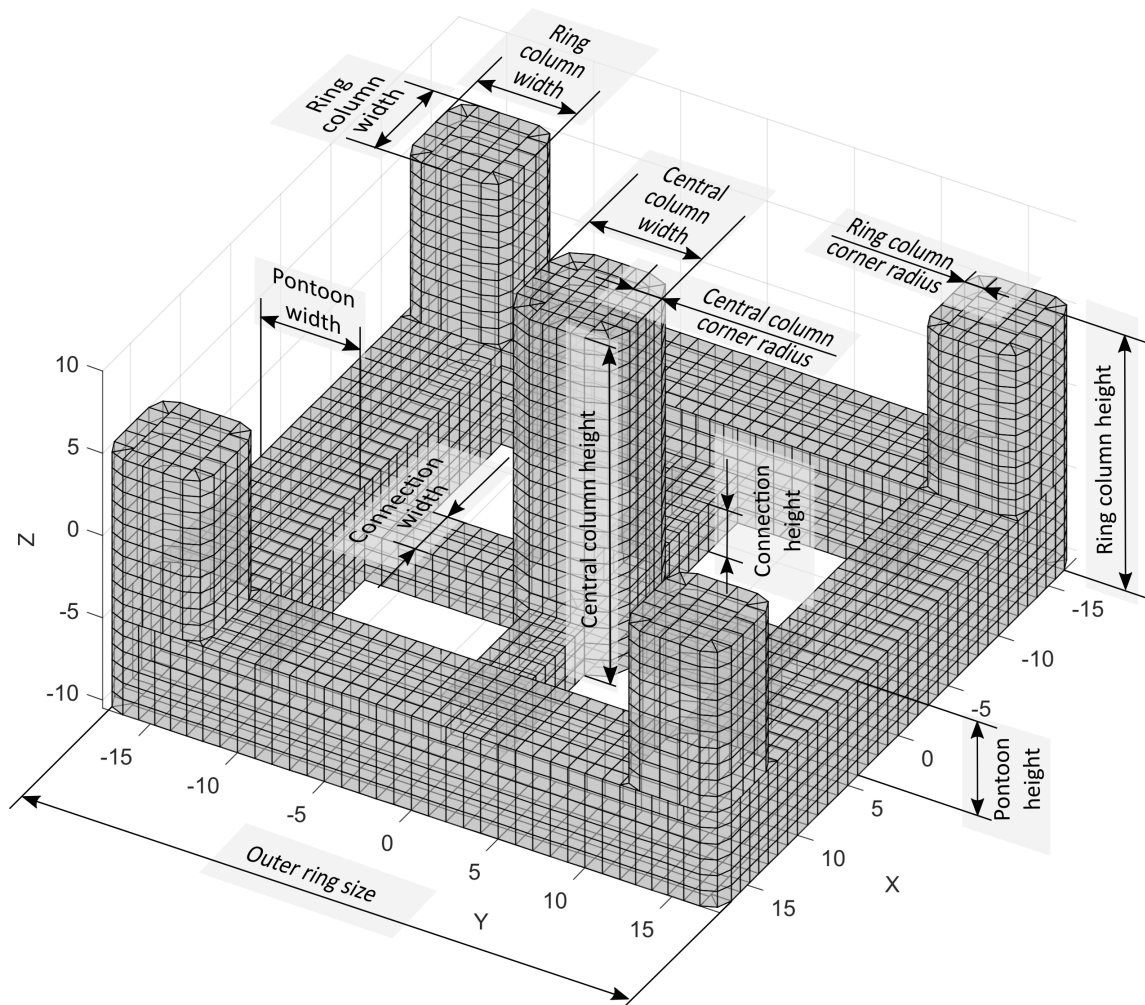


Figure 8.9: The parameterised dimensions of the platform

Table 8.4: Hydrostatic calculations of WAMIT and ParMod, CoB stands for the centre of buoyancy

	WAMIT	ParMod	Units
CoB	(0, 0, -7.115)	(0, 0, -7.115)	[m]
Volume	4492.6	4492.6	[m ³]
$C_h(3,3)/(g,\rho)$	138.24	138.24	[-]
$C_h(4,4)/(g,\rho)$	-41053.90	-40915.27	[-]
$C_h(4,6)/(g,\rho)$	166.46	166.46	[-]
$C_h(5,5)/(g,\rho)$	-41012.94	-40915.27	[-]

The FAST processor explained in Chapter 6 builds the time domain model and performs the simulations for the given set of environmental conditions. It requires numerical input for the mass properties and mooring setup along with WAMIT's output for the hydrodynamic forces, coefficients, and the restoring matrix. The mooring responses in time domain are calculated by a finite element model (FEAMooring [122]).

8.4 Motions under linear excitation in frequency and time domain

A set of results is given here for a TLP with the outer ring size of 17.5 meters, and a keel depth of 10.5 meters as initial estimates. The other dimensions are calculated from the relationships presented in Table 8.3. Eigenfrequencies and motion responses under linear excitation are assessed to obtain the level of agreement between the time domain and frequency domain regarding motion dynamics.

As a precursor to motion responses, the verification of the hydrostatic restoring calculations of the design code is discussed here using WAMIT as a reference. The panel code output could have been used directly as in the case of added masses. However, the comparison clarifies that the platform mesh is evaluated identically by both ParMod and WAMIT. The capability of internal calculations also adds flexibility to the approach. It should be restated that the restoring terms of WAMIT depend on the mass property input of the parametric modelling code through the relationships given in Equation 8.4.

Table 8.4 shows identical centre of buoyancy and the volume results. The differences below 0.2% between the pitch and roll restoring terms are likely due to rounding errors. Otherwise, a panel method code would deliver the same coefficients for any structure with both x and y-symmetry. It should be noted that, for a platform modelled upright, there is also a roll to yaw coupling term due to the eccentricity of the turbine in the longitudinal axis.

8.4.1 Static equilibrium and the platform eigenfrequencies

The static equilibrium in time domain is taken as the mean value of the last 100 seconds of a 1100 second simulation without wind and waves. The small differences presented in Table 8.5 do

Table 8.5: Static equilibrium assessment

	Surge (m)	Sway (m)	Heave (m)	Roll (degrees)	Pitch (degrees)	Yaw (degrees)	Line 1 (kN)	Line 2 (kN)
FAST	-0.001	0	-0.002	0	-0.006	0	1694	1680
ParMod	0	0	0	0	0	0	1692	1692

Table 8.6: Platform eigenfrequency estimations of the three numerical models [s]

	FAST	FAST_{rigid}	ParMod
Surge	50.00	50.00	46.41
Sway	50.00	50.00	46.41
Heave	2.50	2.50	2.46
Roll	4.29	3.33	3.36
Pitch	4.29	3.33	3.36
Yaw	25.00	25.00	25.35

not have significant physical meaning considering the units. They only serve to conclude that the design code correctly built the time domain model. Conversely, showing considerable differences in here would signify that one of the models contains errors. It is useful to note that the mooring lines 1 and 2 are located at opposed sides of the pitching axis. Since the turbine's weight applies with a longitudinal offset, some small initial pitch angle is expected. This value will reflect as differences in mooring line forces which are not considered by the design code. When comparing motion dynamics between time and frequency domains in the rest of the work, the mooring line with the lowest tension is selected.

The method of estimation for the platform eigenfrequencies in Equation 8.10 is practical in initial stages. However, in application to wind turbine platforms, some limits need to be addressed. Table 8.6 compares the natural frequencies calculated from the Equation 8.10 and two time-domain models simulated in free decay by FAST. To illustrate the root of the differences, one of the time domain simulations accept that the tower is flexible, and the second model considers it to be rigid (denoted by FAST and FAST_{rigid}).

The data shows a level of divergence for the pitch and roll modes for the flexible tower. The differences reduce significantly when the tower is considered as a rigid structure. With a tower height of approximately 90 meters, flexibility becomes a defining factor in estimating natural frequencies through simplified formulae. Additionally, the coupling between the surge and pitch (see Equation 8.1) shifts the surge mode's natural frequency away from its uncoupled value. These limitations should be acknowledged, and it should be expected that the time domain model's results will differ. This limitation can be addressed at the frequency domain design stage by adding margins. The coefficient of variation (CoV) serves as a measure of model uncertainty explained in Chapter 5 and exemplified in [134] to obtain these values.

Table 8.7: Wave only RAOs for a 10s period regular wave

	Units	WAMIT	FAST	FAST _{rigid}	CoV
Surge	[m/m]	0.92	0.94	0.95	0.01
Heave	[m/m]	0.04	0.04	0.04	0.00
Pitch	[deg/m]	0.11	0.13	0.12	0.07
Mooring	[kN/m]	273	256	249	0.05

8.4.2 Motion dynamics

The NREL 5 MW reference turbine's rated wind speed is 11.4 m/s at hub height, where it also delivers the highest thrust [33]. The Beaufort scale would point to a likely corresponding wave height of 3 to 4 meters for this wind speed. A 10 second period is probable for this wave height taking the Portuguese shoreline as a reference [167, 168]. Hence, an 11.4 m/s of wind speed at a 4-meter wave height and 10 second period in head waves was chosen to compare the motion dynamics in time and frequency domains. Wind and wave directions are accepted to be aligned. In the discussions below, it should be noted that percentages can be misleading even due to rounding of values. For this reason, the coefficient of variation serves better than percentages.

Table 8.7 compares the response amplitude operators for an environmental condition with only waves. FAST simulations were carried out for 120 seconds after giving an initial transient stage of 1000 seconds. There are small differences in the estimations of motions. The effect of tower elasticity on pitching seems to be visible. However, it is not as prominent as it was in the case of eigenfrequencies. There is an approximate difference of 6 percent in mooring line responses. This is expected, as the pitch RAO is slightly different, and it is a direct contributor to the mooring responses.

An alternative approach to evaluating mooring line estimations is to ask the design code to find a hypothetical wave that would cause complete loss of tension. This wave can then be simulated with the time domain code using the finite element approach for comparison. In this type of a study, Equation 8.27 calculates that a slack mooring will be caused by a wave height of 6.74 meters at a period of 7 seconds. Figure 8.10 provides the time series for this wave and clarifies that these types of evaluations are possible when the platform motions are known. It should be noted that this is an unlikely wave height and period combination, and the aim here is to verify the calculation method. For instance, while a wave with a 2-second period and 10 meters of height can be defined mathematically for testing purposes, it is almost impossible to encounter in the ocean.

The platform's responses to wind forces with a running turbine are summarised in Table 8.8. In this case, a theoretical case where there are no waves but a wind of 11.4 m/s is considered. The results suggest that the frequency domain approach is overestimating surge by 10 percent. Given the connection between the surge and heave modes due to set down, heave response is also overestimated as expected by 3 centimetres. Conversely, pitch mode is slightly underestimated as well as the minimum mooring line tension. The data shows that the elasticity of the tower is less of a concern with a constant exciting force after a static equilibrium position is reached.

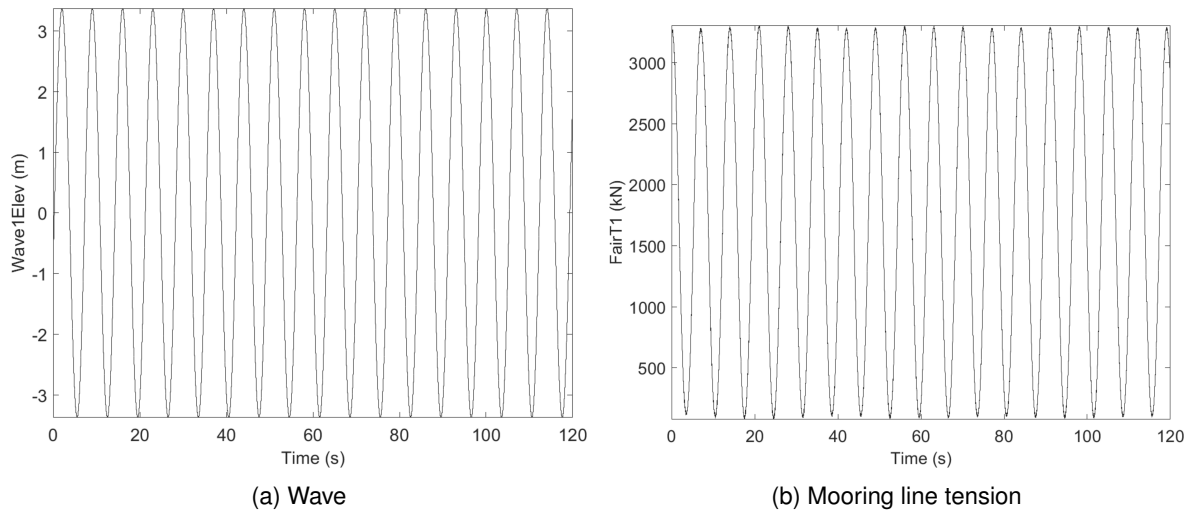


Figure 8.10: Mooring line responses in a time domain simulation with a wave height of 6.74 meters at a period of 7 seconds

Table 8.8: Motions of the TLP under 11.4 m/s linear wind excitation

	Units	Design Code	FAST	FAST _{rigid}	CoV
Surge	[m]	7.49	6.76	6.77	0.06
Heave	[m]	0.15	0.12	0.12	0.13
Pitch	[deg]	0.26	0.30	0.30	0.08
Min. line tension	[kN]	1142	1340	1350	0.09

Table 8.9 summarises calculation results for a linear wind of 11.4 m/s combined with a wave height and period of 4 meters and 10 seconds respectively. The coupled responses show the largest differences, which is expected as the system's overall complexity increases. There is a difference of 6% in surge. The heave and pitch responses are approximately 15% apart. Regarding heave results, the reported totals are a combination of two components: set down due to surge and heave due to wave excitation. When evaluated separately, it is seen that the total heave of 0.23 meters includes a set down of 14 centimetres related to the surge mode. The differences in the estimated heave and pitch responses reflect on the lowest mooring tension by predicting a 12 percent higher minimum tension compared to the finite element model.

This data summarises that the overall differences between the estimations of heave and pitch are under 5 cm and less than a quarter of a degree. Surge responses are overestimated at the frequency design stage. This finding signifies that the operational mooring line angles will also be estimated conservatively. The pitch mode seems to cause the primary preliminary design challenge for obtaining the slack mooring case. It is, however, understood that if a design cannot comply with the criteria in frequency domain stage, it is likely to fail the time domain stage. Hence, a checkpoint with a safety margin is needed to verify designs at frequency domain evaluations.

Table 8.9: Platform responses to regular wave height of 4 m and a period of 10 seconds, with a linear wind of 11.4 m/s

	Units	Design Code	FAST	FAST _{rigid}	CoV
Surge	[m]	9.33	8.78	8.84	0.03
Heave	[m]	0.23	0.28	0.29	0.12
Set-down	[m]	0.14	-	-	-
Pitch	[deg]	0.48	0.58	0.55	0.10
Min. line tension	[kN]	926	830	761	0.09

Table 8.10: Occurrences of sea states and related wind speeds during the period of January 2008 to December 2010 in Galicia (H_s in m, U_w in m/s, T_p in s)

		T_p													
U_w	H_s	5.5	6.0	6.5	7.0	7.5	8.0	8.5	9.0	9.5	10.0	10.5	11.0	11.5	
0.3	0.0	273	130	108	66	36	22	7	1	0	0	0	0	0	
3.4	0.5	543	590	677	679	520	287	167	108	41	24	8	3	9	
5.5	1.0	172	432	686	1026	1062	947	659	441	211	142	85	55	24	
6.7	1.5	5	142	446	491	636	1062	1304	873	482	334	140	75	63	
8.0	2.0	0	0	50	237	264	257	323	712	713	484	280	175	154	
9.4	2.5	0	0	0	41	178	152	138	185	523	598	381	198	210	
10.8	3.0	0	0	0	0	21	136	108	78	126	340	478	308	292	
12.3	3.5	0	0	0	0	0	17	43	72	113	120	206	304	462	
13.9	4.0	0	0	0	0	0	0	2	49	23	31	34	147	470	
15.0	4.5	0	0	0	0	0	0	0	6	27	10	11	34	342	
16.0	5.0	0	0	0	0	0	0	0	0	9	5	3	22	297	
17.2	5.5	0	0	0	0	0	0	0	0	0	3	1	4	166	
18.1	6.0	0	0	0	0	0	0	0	0	0	0	0	0	107	
19.0	6.5	0	0	0	0	0	0	0	0	0	0	0	0	123	
19.8	7.0	0	0	0	0	0	0	0	0	0	0	0	0	51	
21.4	7.5	0	0	0	0	0	0	0	0	0	0	0	0	26	
22.0	8.0	0	0	0	0	0	0	0	0	0	0	0	0	11	

8.5 Assessing responses in stochastic environments

Dynamic analysis can evaluate whether the structure can withstand the wind and waves (i.e., for a tension leg platform, this signifies limiting the occurrence of slack moorings) given the environment data. However, for high numbers of structures or environmental conditions, time domain simulations are rather time-consuming. On the contrary, a frequency domain solution is almost instantaneous to obtain. Applying this idea, a possible approach to the assessment of environmental sets is discussed here using the scatter diagram for Galicia given in Table 8.10 [167, 168]. Since the wind speeds were not made available, they were estimated as a function of the wave height based on the Beaufort scale. The turbine's related thrust value for wind speeds above the cut-out speed is taken from [33].

The previous section discussed the estimation of mooring responses under linear excitation and did not account for stochastic variability. Comparing the results under an identical wind speed to wave height pair can link the linear and stochastic conditions. The same environmental setup in the linear waves and wind study in Table 8.9 was used for this purpose. Accordingly, the wind speed is

Table 8.11: Safety margin estimations between a linear wind / regular waves case and a stochastic case, wind speed is 11.4 m/s and wave height and period are 4 m at 10 s

	Units	Design code	FAST
Environment model	[-]	Regular waves + linear wind	Stochastic wind and waves
Lowest line tension	[kN]	927	516
Initial tension	[kN]	1692	1680
Reduction	[%]	55	31

11.4 m/s at hub height (Von Karmal spectrum), and the significant wave height is 4 meters with a peak period of 10 seconds (JONSWAP spectrum) also in the stochastic case.

Table 8.11 compares the linear and the “corresponding-peak-value” stochastic cases. The linear excitation results in a mooring line tension drop to approximately 55% of the initial value. FAST sees a reduction to 30% of the initial tension throughout a time series of 1200 seconds. The difference between these two values, 25 percent, can be used as a variability margin. This value signifies that the mooring lines are not expected to lose more than 75% of their initial tension in the frequency domain design check to comply with the safety criteria. For a realistic scenario, a higher margin is preferable; the time domain code can also underestimate motions as seen in Chapter 3 or [39, 53]. Probabilistic approaches and model uncertainty studies carried out against experiments (e.g., [140]) can help to decide these values.

The wind and the waves are the two major exciting forces of this system. While the platform is always exposed to wave excitation, there are two possible responses to the wind. The turbine can be running or parked. The resulting dynamics will be different in these two cases. Therefore, the response evaluation can also be carried out for these two scenarios. In Table 8.12, the areas marked with “T+W” show that the turbine can run in the given condition without encountering slack mooring cases. The area marked with only “W” (8 and 7.5-meter wave heights) signifies that a running turbine forces the mooring tensions below the allowed margins due to added pitching. As a verification, Table 8.13 presents the minimum mooring line tensions attained in 1200 second time domain simulations for the given wave heights, corresponding wind speeds, and a wave period of 11.5 seconds. While the mooring lines don’t go into compression, environment table is correct in detecting where they can be considered to carry no tension.

There are two paths to take at this point. Any structure that can’t survive the waves should be eliminated from the design space. Then, the orthodox approach would be to consider only the structures that pass the criteria for “T+W”. Alternatively, the turbine’s cut-out speeds can be adjusted if this lowers the risk sufficiently and is economically viable. For the NREL 5MW turbine, taking the sea states in Table 10 as the reference, the cut-out speed would need to be lowered below 20 m/s from its design value of 23 m/s.

Table 8.14 presents the downtime breakdown for Galicia with an altered cut-out speed. The region where the expected wind speed is below 3 m/s is classified as the turbine’s “no wind downtime”. It shows that the yearly probability of the turbine not running due to reduced cut-out speeds would be

Table 8.12: Platform’s compliance with the 25% safety margin. (T+W) signifies compliance with a running the turbine and. (W) signifies that the platform can comply only with a parked turbine. (H_s in meters, T_p in seconds)

H_s	T_p												
	5.5	6.0	6.5	7.0	7.5	8.0	8.5	9.0	9.5	10.0	10.5	11.0	11.5
0.0	-	-	-	-	-	-	-	-	-	-	-	-	-
0.5	T+W	T+W	T+W	T+W	T+W	T+W	T+W	T+W	T+W	T+W	T+W	T+W	T+W
1.0	T+W	T+W	T+W	T+W	T+W	T+W	T+W	T+W	T+W	T+W	T+W	T+W	T+W
1.5	T+W	T+W	T+W	T+W	T+W	T+W	T+W	T+W	T+W	T+W	T+W	T+W	T+W
2.0	-	-	T+W	T+W	T+W	T+W							
2.5	-	-	-	T+W	T+W	T+W	T+W						
3.0	-	-	-	-	T+W	T+W	T+W	T+W	T+W	T+W	T+W	T+W	T+W
3.5	-	-	-	-	-	T+W	T+W	T+W	T+W	T+W	T+W	T+W	T+W
4.0	-	-	-	-	-	-	T+W	T+W	T+W	T+W	T+W	T+W	T+W
4.5	-	-	-	-	-	-	-	T+W	T+W	T+W	T+W	T+W	T+W
5.0	-	-	-	-	-	-	-	-	T+W	T+W	T+W	T+W	T+W
5.5	-	-	-	-	-	-	-	-	-	T+W	T+W	T+W	T+W
6.0	-	-	-	-	-	-	-	-	-	-	-	-	T+W
6.5	-	-	-	-	-	-	-	-	-	-	-	-	T+W
7.0	-	-	-	-	-	-	-	-	-	-	-	-	T+W
7.5	-	-	-	-	-	-	-	-	-	-	-	-	W
8.0	-	-	-	-	-	-	-	-	-	-	-	-	W

Table 8.13: Lowest mooring line tension attained in a 1200-second time domain simulation

Wave height [m] at 11.5 s period	6.5	7.0	7.5	8.0	
Wind speed [m/s]	19.0	19.8	21.4	22.0	
Minimum line tension [kN]					
	Turbine operational	225	136	4	1.5
	Turbine parked	396	305	227	146

rather low (below 0.2 percent). Hence, it may become advantageous to park the turbine earlier than the designed cut-out speed compared to installing a larger structure. These types of ideas may be less relevant for a 5MW turbine. However, as the 10 MW margin is approached, the turbine thrust values will become even more significant in defining the motions. In those cases, the cut-out speeds can be considered as an optimisation variable.

8.6 Design criteria evaluation and platform sizing

Once the motions of a platform are calculated with an acceptable level of certainty, a favourable structure can be designed. This evaluation is done through an algorithm that enforces a set of criteria and looks for the lightest compliant structure. Since a tension leg platform inherently has smaller responses especially in restricted modes, minimising the motions is not the goal. While, any criteria can be assessed at this stage (e.g., minimum tendon fatigue as in [90]), the outcome will always be a preferable sizing for the selected purpose.

Table 8.14: Turbine’s probable operational conditions in response to the sea states of Galicia during the period of January 2008 to December 2010

Condition	probability
no wind downtime (waves <0.5 meters)	2.3%
turbine parked for safety	0.2%
turbine running	97.5%

Table 8.15: Frequency domain evaluation criteria

Assessment condition	limit	units
Surge and sway natural periods ($t_{\eta_{1,2}}$)	$0.95 \cdot t_{\eta_{1,2}} > 25$	[s]
Heave, pitch, and roll natural periods ($t_{\eta_{3,4,5}}$)	$1.20 \cdot t_{\eta_{3,4,5}} < 4$	[s]
Yaw natural period (t_{n_6})	$t_{n_6} \geq 25$	[s]
Mooring line anchor angle in operation (α)	$\alpha < 5$	[deg]
Slack mooring safety margin	25	[%]
Environment verification	“T+W” in all probable sea states of Galicia	[-]
Minimised cost function	Platform mass	[t]

Frequency domain checkpoint uses the model uncertainty (coefficient of variation) values in Table 5.5 to account for modelling simplifications (e.g., the effect of tower elasticity on the natural frequencies). The surge mode has a 5% margin (i.e., when the frequency domain period is lowered by 5 percent, it stays above 25 seconds). The pitch and roll modes allow a 20% shift (i.e., when the frequency domain periods are increased 20% they stay below 4 seconds). The environment table of Galicia (Table 8.10) should have the turbine running (“T+W”) with a 25% slack mooring margin. The surge condition in operation asks that the mooring line angles at the anchors do not surpass 5 degrees. As all variations include API’s mooring line breaking criteria by design, it is not rechecked. The platform’s steel weight is the selected cost function. Mathematically, a cost function is defined as “the variable to be minimised”. Therefore, the selection process looks for the lightest structure that satisfies the safety criteria. Given the links between steel mass and monetary cost, the purpose of the algorithm may be summarized as picking the least expensive platform in this regard that adheres to the defined criteria. This information is summarised in Table 8.15.

Two of the main dimensions in Figure 8.9 are used in the sizing study. This number is selected for the ease of 3D plotting for illustrative purposes. Without this consideration, all main dimensions can be set as variables. The outer ring size is varied between 15 and 20 meters in intervals of 0.25 meters. The keel depth is altered between 10 to 15 meters in steps of 0.50 meters, equalling to 231 variations.

The surface plots in Figure 8.11 shows the results regarding the motions and mooring line setup. The surge motion favours smaller structures with deeper drafts. Conversely, the heave and pitch responses increase as the platform gets smaller. For each iteration, the algorithm adjusts the mooring line diameters and the setup. Depending on the platform size, it designs one or two mooring lines per fairlead to stay below the line breaking safety margin. The tension per line corresponds to the

Table 8.16: Finalized platform properties after evaluation

Variable	Value	Units
Outer ring size	19.25	[m]
Keel depth	13.00	[m]
Mass	2232	[t]
Number of mooring lines	8	[-]
Mooring line diameter	0.12	[m]
Surge and sway eigen periods	41.67	[m]
Heave eigen period	2.50	[s]
Pitch and roll eigen periods	3.75	[s]
Yaw eigen period	25	[s]
Maximum mooring line angle at the anchors	2.4	[deg]

number of mooring lines. The platform and structure (i.e., platform + RNA) mass values are given in Figure 8.12. As expected, the platform mass increases with the size up to a maximum of 2400 tons.

After evaluating all alternatives according to the criteria in Table 8.15, the algorithm points to a draft of 13 meters and an outer ring size of 19.25 meters as the lightest functional platform in Galicia. The time domain responses to a sea state with 8-meter significant wave height and 22 m/s of wind are presented in Figure 8.13. The mooring line tensions (Fair1Ten) show no slack mooring occurrences. The maximum surge motion is 8.18 meters, corresponding to a 2.34-degree mooring line angle at the anchors and complying with the 5-degree limit. Table 8.16 summarises that the platform fundamental frequencies stay outside the first order excitation area, it functions in Galicia, and complies with the anchor angle.

8.7 Time requirements for design space evaluation

Measuring performance is challenging in most cases since it is directly related to the hardware. Still, a comparison of time domain and frequency domain solutions on identical systems (a laptop PC with a 2.5 GHz CPU in this case) provides an idea. It was explained that the design tool builds the 3D model, manages the external software and pre-processes the data for the FAST's time domain model. Hence, it handles the extra input/output work along with the design itself. It is, therefore, useful to list the performance as a breakdown of modules instead of the total runtime.

The averaged breakdown of module runtimes is given in Table 8.17. The data shows that the WAMIT module runs the longest (16.30 seconds). The remaining 2 seconds are used for building the 3D model, calculating its mass properties, hydrostatics, obtaining the coupled frequency domain solution, and the time domain model. Pre/post-processing files and design related calculations (e.g., the mooring setup and calculating area tables) take approximately 1 second. The design process from preparation of the input to the end of the calculations about 15 to 25 seconds for each variation of the structure depending on platform size. Larger models inevitably need a higher number of panels with a constant mesh size (e.g., 2 meters). The design space evaluation of the 231 variations takes approximately an hour. Certain alterations can tweak the performance: the mesh is about 2100

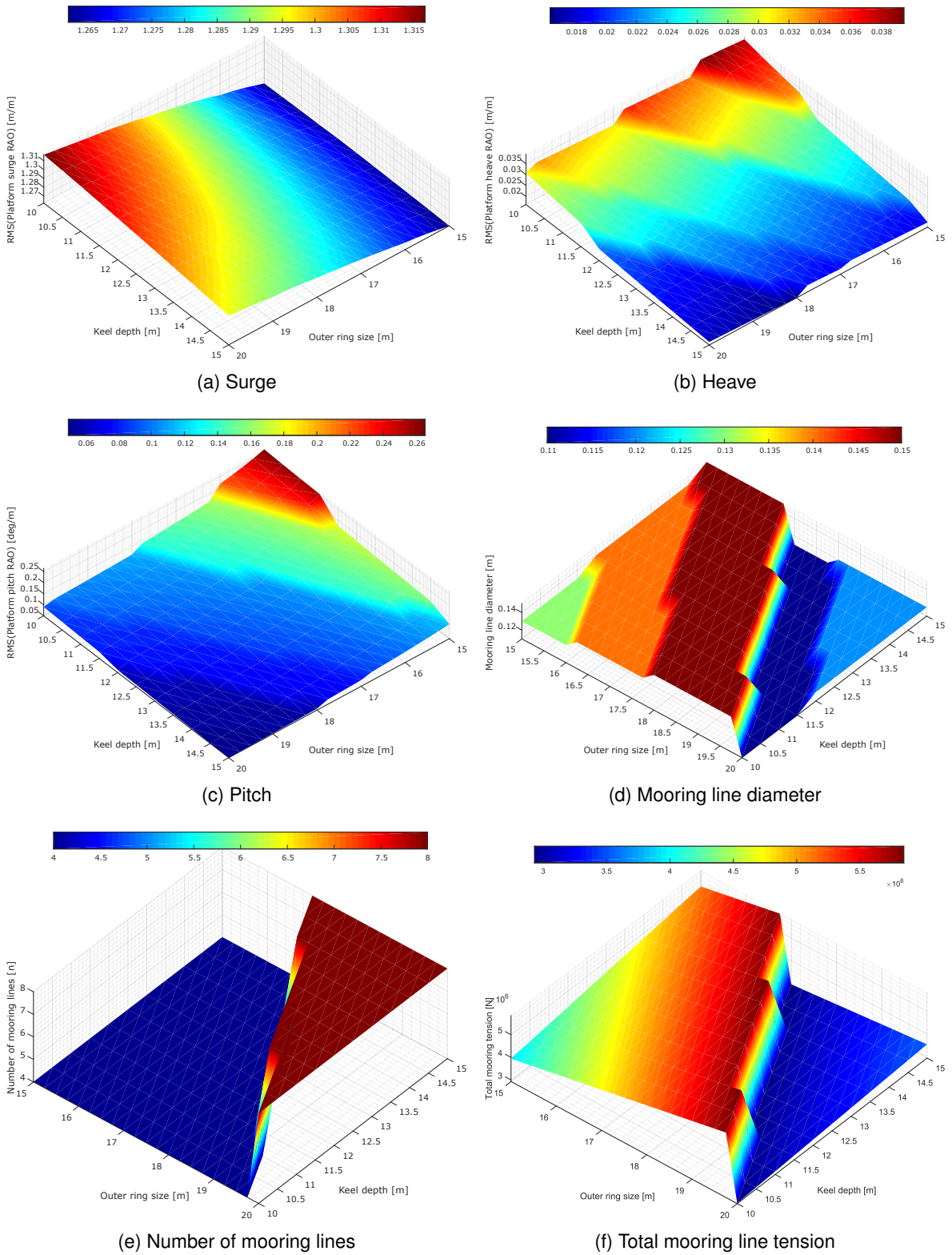


Figure 8.11: Motion responses, mooring line setup and tensions of the 231 TLP variations

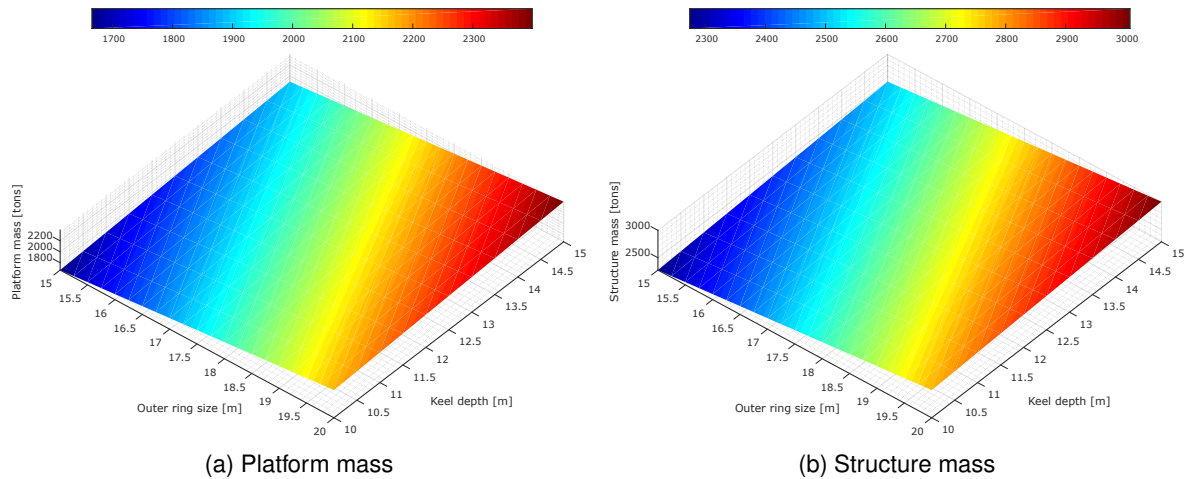


Figure 8.12: Platform mass and the total mass including the RNA for the 231 TLP variations

Table 8.17: Performance breakdown of the modules and codes used inside the design process of a single variation

Process	Time (s)
WAMIT	16.30
Modelling the 3D mesh	0.18
Mass property calculations	0.66
Hydrostatics	0.05
Time domain model building	0.20
Other calculations and pre/post processing	0.91
Total runtime per variation	18.32

panels for the tower, turbine, and the platform. This speed can be increased using a lower number of panels depending on the necessary precision. Also, inside a loop, it is not needed to remodel parts with constant values such as the tower and the turbine.

The time domain simulations depend on the calculation intervals as opposed to the panel size. Especially for higher waves, a smaller time step is necessary for FAST to reach a numerically stable solution that adheres to its assumptions. To simulate a 1000-second environmental condition with wind and waves, it requires approximately 3.5 hours of runtime. If a larger time step leads to a stable solution, this time can be reduced. At any rate, given the timings, it would be recommended to save this process for the later stages of design where the behaviour of the structure is already approximated with sufficient confidence.

8.8 Concluding remarks

A systematic approach to the hydrodynamic design of a tension leg platform to host the NREL 5 MW turbine was presented. The stages were explained over a worked example. Model development, hydrostatics, mooring setup, and estimation of motion dynamics in frequency domain were discussed. The time domain model built in FAST was used to compare simulations and the frequency

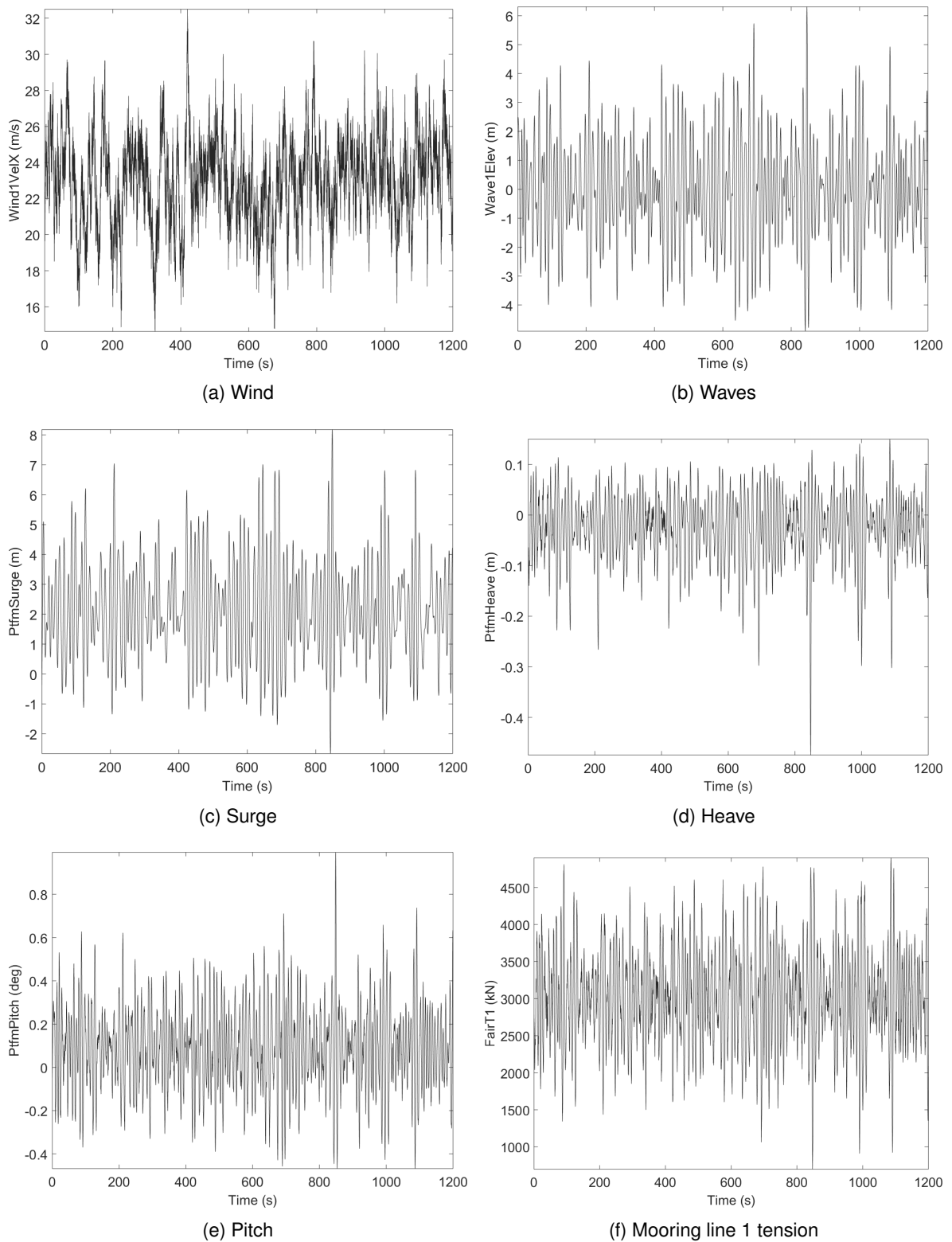


Figure 8.13: Time domain responses of the platform with 19.25 meters outer ring size and 13 meters of keel depth to 8 meters of significant wave height and 22 m/s of stochastic wind

domain calculations. The differences were used to account for stochastic cases which were utilised to assess the structure's performance in Galicia, Spain. Then, an evaluation process was illustrated for selecting the main dimensions for the smallest functional platform.

This process can be used in early design stages to approximate the responses of a platform. The method utilises the same parameterised 3D mesh for mass, hydrostatic, and hydrodynamics calculations and provides a direct connection between the models. It avoids the use of lookup tables for hydrodynamic coefficients, simplified shapes in spreadsheets for mass properties, and closed-form solutions for motions, hence, increasing the precision. It also reduces time spent in early design stages compared to building multiple 3D models in various software for each of these variables.

While this work will not replace the role of human creativity in innovative fields, it will allow room to investigate concepts efficiently. Once a script for any parametric TLP hull is written into this system, further user intervention is unnecessary. Large sets of data can be obtained in an automated manner. The output data can serve further as a basis for multi-criteria optimisation studies. This setup can be extended to other hull forms such as semi-submersibles by adding catenary mooring and ballasting algorithms and implementing appropriate selection criteria. Integrating an early economic assessment is also beneficial.

Pitch actuator fault induced yaw motion in storms

9.1 Introduction

Floating platforms have several compliant degrees of freedom such as yaw. In places where higher wind speeds are available, they will also be exposed to extreme weather conditions more frequently. When these two elements are combined, the responses in these scenarios come into question. There is also the fact that offshore structures are at a disadvantage regarding the maintenance schedule as the weather may limit access to the platform. They operate unmanned, which conveys that an immediate response to failures may not be possible. For this reason, they should be able to survive storm conditions without damage until the maintenance is done. Multiple studies [169, 170] and class society rules [66, 67, 27] discuss these conditions.

Regarding reliability, the increasing sizes of the wind turbines is major factor as their components are affected by higher loads. One Failure Modes and Effects Analysis (FMEA) study shows that the number of failures per turbine per year correlates to the increase in generated power [171]. For instance, the rate of brake failures almost doubles for a 1 MW turbine in comparison to a 300-kW wind turbine. Pitch system problems increase seven-fold. In this list of possible failures, pitch systems were the third most failed components of wind turbines, placed after blade and gearbox failures. Brake systems were at the 7th place.

Considering the coupled dynamics of the turbines, the effect of a fault in one of the system components does not necessarily have to stay limited to that component. It was previously noted that when blade pitch failure combines with the 1-year extreme conditions, a barge type platform shows

Published in: Yaw Motion of Floating Wind Turbine Platforms Induced by Pitch Actuator Fault in Storm Conditions. *Renewable Energy*, 134:1056–1070, 2019. doi:10.1016/j.renene.2018.11.076

large amplitude limit cycle motions. This motion was described as instability in yaw mode [172, 173] and its occurrence was linked to the motions of the turbine blades. Over the years, the topic was also discussed for tension leg platforms [79, 174]. For the barge, it was stated that the problem was eliminated when the high speed-shaft brake (HSS Brake) was applied. It was also assumed that the absence of viscous damping in the numerical model might have been the reason for this motion to occur in simulations [173]. The issue was not examined in detail since it could not be clarified whether the problem is real or virtual in the absence of model tests to obtain viscous damping values. The application of the HSS brake will serve to stop the blades from rotating, but will not directly cause or stop the platform's yaw motion. Therefore, links between the two factors exist and need to be evaluated. It should also be clarified whether the absence of the hydrodynamic viscous damping was a significant cause as suspected.

It is shown here that the case repeats itself on a semisubmersible platform in the presence of experimentally obtained viscous damping coefficients, with an applied HSS brake. After a description of the model, a comparison of operating conditions and 50-year extreme environmental loads in IEC standards, North Sea and at storm conditions at the coast of Portugal is presented as a basis for motions without faults. Then they are examined in the presence of blade pitch actuator fault. Factors that lead to the problem are broken down into components. In this regard, the linearised hydrostatic matrix of floating wind turbines is reviewed since a frequently applied form overlooks roll-yaw coupling terms [50, 22, 78]. The reasoning behind the large amplitude motions in fault conditions is explained and preventative measures are suggested.

9.2 The system and the environmental conditions

9.2.1 Description of the turbine, tower, and the platform

The system consists of the NREL's 5MW hypothetical wind turbine [33], combined with the OC3 Hywind tower [36], hosted by the DeepCwind semisubmersible [48]. The numerical model was built in NREL's open source simulation code FAST v7 [50]. The platform model was utilised in the collaborative code comparison projects OC4 Task 30 [49] and studied further in the experiment-to-code studies [52]. Hence, this numerical model's performance in comparison to the experimental data is known as presented in Chapter 3. While the experiments did not include faulty blade scenarios in storm conditions, this case presents an opportunity in furthering the study of environmental cases with a previously validated model. Accordingly, this numerical model with known confidence levels can serve as a benchmark to assess environmental conditions in the absence of experimental data.

The data relevant to this chapter are repeated here for convenience as they will later be discussed in detail. The mass properties of the semisubmersible are in Table 9.1. The hydrodynamic properties of added mass, potential damping, and the hydrostatic restoring coefficients were obtained with the panel method code WAMIT presented in Chapter 4 for the model with braces. The referred data

Table 9.1: Properties of the semisubmersible platform

Variable	Value
Platform mass, including ballast	1.344E+7 kg
Platform roll and pitch inertias	6.827E+9 kg·m ²
Platform yaw inertia	1.226E+10 kg·m ²
Maximum high-speed shaft brake torque	28.12 kN·m
RNA and tower's centre of mass (x, y, z)	[0.28, 0, 70.5] m
The platform's centre of mass (x, y, z)	[0, 0, -13.46] m

Table 9.2: Viscous damping coefficients

Surge	Sway	Heave	Roll	Pitch	Yaw
Ns ² /m ²			Nms ² /rad ²		
3.95E+05	3.95E+05	3.88E+06	3.70E+10	3.70E+10	4.08E+09

verifies that excitation forces in the roll and yaw modes are zero in head waves as expected from a longitudinally symmetrical structure.

The viscous damping values in Table 9.2 were obtained experimentally [39] and updated for the OC4 Phase II code comparison study [49]. Three catenary mooring lines enforce the station-keeping with a spread of 120 degrees. Table 9.3 lists the restoring forces of the mooring lines and the hydrostatics. The natural frequencies of the tower and the platform are given in Table 9.4.

The hub-centred coordinate system presented in Figure 9.1 shows the blade numberings from 1 to 3 and possible static equilibrium positions where blade 1 is taken as the faulted component. The positions of the two remaining blades are readily available as they are set apart with a constant 120-degree angle in reference. Unless stated otherwise, the faulty blade is initially pointing upwards in the z-direction (i.e., 0 or 360 degrees of azimuth angle) at the beginning of simulations and arrives at its calculated position after a transient stage of 600 seconds.

When allowed to rotate freely from an arbitrary position in the absence of external forces, the static equilibrium positions of blade 1 would be about 180 or zero degrees of azimuth angles (e.g., blade 1 pointing up or down in z-direction) given one open and two feathered blades of equal weights. This position would slightly shift depending on the location of the centre of mass of the open blade: simulations without wind and waves lead to blade equilibrium positions at approximately 1-degree and 179-degree azimuth angles. These two static equilibrium positions are significant in the sense that they introduce minimal yawing due to wind forces, given the highly symmetric geometry of the

Table 9.3: Hydrostatic and mooring restoring forces

	Surge and Sway N/m	Heave N/m	Roll and pitch Nm/rad	Yaw Nm/rad
Hydrostatics	0	3.84E+04	3.78E+08	0
Mooring	7.08E+04	1.91E+04	8.37E+10	1.17E+08
Total	7.08E+04	5.75E+04	8.41E+10	1.17E+08

Table 9.4: Natural frequencies of the structure [Hz]

Surge	Sway	Heave	Roll	Pitch	Yaw	Tower Fore-Aft	Tower Side-to-Side
0.009	0.009	0.057	0.037	0.037	0.013	0.43	0.42

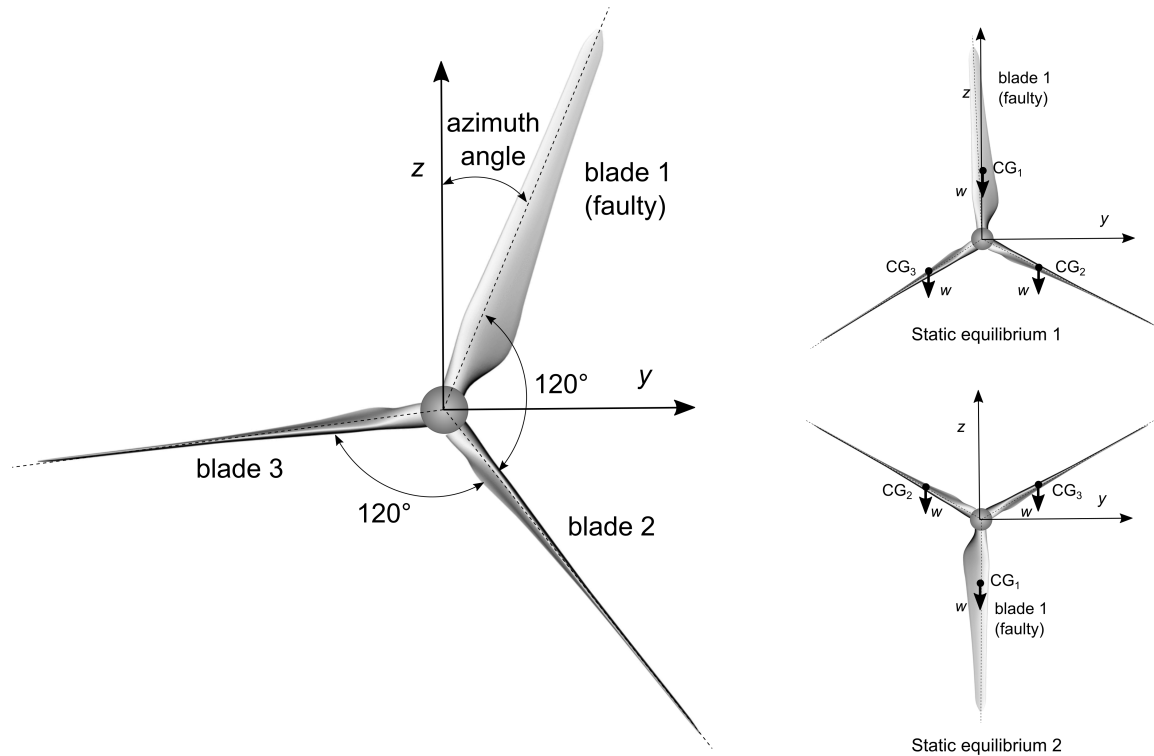


Figure 9.1: The hub-centred coordinate system and the blade numberings

rotor about the yaw axis. On the other hand, rotor positions closer to a 90-degree azimuth angle would place the open blade on the right side of the z-axis with the remaining two blades on the left side of the yaw axis. In this case, the asymmetric geometry would be expected to result in larger yaw angles due to the wind forces on the blades.

9.2.2 Environmental conditions

Four environmental cases are considered in unidirectional head waves with the rotor facing the wind. The rated wind operational conditions, denoted with OPR, are presented first to act as the base of comparison with extreme events. In OPR, the blades are rotating at 12.1 rpm, with turbulent wind at the rated speed of 11.4 m/s. The significant wave height is 6 meters with a period of 10 seconds. The second case is a 50-year extreme wind and wave combination set according to IEC standards [175, 176]. It is referred to as the IEC condition and the wind data available to the participants of the OC4 project [49]. The wind speed at the hub is 45.7 m/s, with a significant wave height of 15 meters at the peak period of 19.2 seconds. The third case is similar to the IEC regarding the wind characteristics. It represents the North Sea conditions [169] and is denoted by NS. The wind speed at hub height is 49 m/s, the peak period and the significant wave height are 13.2 seconds and 14.1

meters respectively. The fourth case examines an area of practical importance: Aguçadoura, located on the Portuguese coast where the WindFloat semi-submersible [12] was installed in 2011. This environment is designated as the PT₅₀ condition. The wind in this location was generated utilising the Kaimal spectrum for the IEC class 2 as proposed by DNV [27], at a speed of 23.2 m/s. The significant wave height is 8.5 meters and the peak period is 19.2 seconds. The wind speeds are lower since the measurements were taken closer to the shore. The value is slightly below the cut-out speed for the NREL 5MW turbine. The PT area was explicitly included in the study to clarify if similar fault related issues can be replicated at lower wind speeds.

The North Sea (NS₅₀), IEC (IEC₅₀), and the Portuguese Coast (PT₅₀) diverge in certain aspects. The IEC₅₀ and NS₅₀ have different peak periods. PT₅₀ has a lower wave height and an equal peak period to that of the IEC₅₀. In all load cases, the peakedness factor of JONSWAP wave spectra was assumed to follow the relationship between the wave height and wave period as described in [177]. This consideration results in the JONSWAP peakedness parameters of 1.05, 5.86, and 7.0 for the IEC₅₀, NS₅₀, and PT₅₀ conditions respectively. Given that a lower parameter causes a broader spread in the frequency range of the spectrum, the encountered wave ranges vary. The Portuguese coast and the IEC₅₀ have shorter wave frequency ranges in comparison to the operational condition and the NS₅₀.

In environmental loads above their operational limit, the turbines are designed reduce the loads and prevent damage by effectively shutting down. The blades feather to cause minimal torque at the shaft, and the brake system engages to stop the blades from rotating. FAST's HSS brake model is based on the Coulomb model of sliding friction where the braking torque is a function of the shaft speed. The magnitude of the brake torque is constant while the shaft speed is non-zero. When the shaft speed is zero, the torque takes on any value between its limiting constants to prevent motions of the shaft. The shaft can move only if external torques exceed the braking torque limits [178]. If the brake or the pitching system fails, the responses will follow the altered dynamics.

The sets consider two possibilities to study these preventative measures. In the first case, the wind and the waves subject the turbine to extreme loading and the safety systems are accepted to work as expected. The second set repeats the storm loads with the pitch actuator of one of the blades failing while the other two keep functioning. Table 9.5 summarises the environmental conditions where the functional cases are denoted by the subscript 50, and the subscript A (i.e., accidental) indicates the fault conditions. The runtime of each simulation was 4200 seconds, where the first 600 seconds are eliminated as transient stages.

9.3 Motion responses in fault-free storm conditions

This brief revision of the operating conditions serves as a basis to understand the reactions of the platform under storm loads. The primary objective is to clarify the motions in the relevant modes and excitation ranges throughout frequency spectra in Figure 9.2. In head waves and aligned wind, the

Table 9.5: Summary of the environmental conditions

	Ω [rpm]	Wind Spectrum [-]	U_w [m/s]	H_s [m]	T_p [s]	HSS Brake [-]	Blade 1 initial pitch [deg]
OPR	12.1	Mann	11.4	6.0	10.0	[-]	(0, 0, 0)
IEC ₅₀	0.0	Mann	47.5	15.0	19.2	[X]	(90, 90, 90)
NS ₅₀	0.0	Kaimal	49.0	14.1	13.2	[X]	(90, 90, 90)
PT ₅₀	0.0	Kaimal	23.2	8.5	19.2	[X]	(90, 90, 90)
IEC _A	0.0	Mann	47.5	15.0	19.2	[X]	(0, 90, 90)
NS _A	0.0	Kaimal	49.0	14.1	13.2	[X]	(0, 90, 90)
PT _A	0.0	Kaimal	23.2	8.5	19.2	[X]	(0, 90, 90)

significant responses are surge, heave, and pitch. The pitch motion is most evident between 0.05 – 0.15 Hz. The mean value of pitch was approximately 3 degrees, with a standard deviation of 0.65 degrees. These values signify that the floater pitches to an operational angle, and deviates minimally around that point. The yaw angles are negligible, and resonant areas show the only significant responses, occurring around the yaw eigenfrequency (0.012 Hz). This is the behaviour expected from a floater with a symmetric underwater hull in head waves. The tower side-to-side moment shows a similar dynamic amplification related peak at 0.42 Hz. However, these values stay significantly away from the frequencies of the first order wave excitation range of 0.05 – 0.25 Hz.

In the storm condition, all blades are feathered to 90 degrees, and the high-speed shaft brake is applied to stop the hub's rotation. In this case, given in Figure 9.3, the low-frequency surge motion is visible also in the absence of a running turbine. The elevated responses are close to the surge natural frequency of 0.009 Hz. The heave mode yields a similar case with a dynamic amplification of the motion at 0.06 Hz. Pitch natural frequency stays outside the wave excitation range in all cases.

When operating, the turbine is one of the factors that force the platform to pitch. In storm conditions, with the turbine parked, the waves combined with the weight and location of the rotor-nacelle assembly causes higher amplitude pitch motions. As expected, there is almost no yaw motion apart from dynamic amplification. The tower base side-to-side moments are given as a basis for later comparisons between the faulty and functional conditions.

Comparing the IEC₅₀, NS₅₀, and PT₅₀ shows a known aspect of the frequency range distribution of the spectra. In extreme conditions, waves shift towards lower frequency ranges. Coinciding natural and exciting frequencies can occur if the design was not thoroughly evaluated for storm conditions. In calmer seas, the spectrum spreads out to higher frequency ranges, mitigating this problem for the semi-submersible. DNV accepts the possible linear wave excitation range of 5 to 25 seconds (0.04 – 0.20 Hz) for floating wind turbines [179]. The results show that, based on the installation area, values outside this range might also be important to avoid dynamic amplification related issues in storms. The structure enters pitch resonance in both the IEC₅₀ and PT₅₀ conditions, occurring around 0.04 Hz. The milder PT₅₀ waves also lead to significant resonant responses.

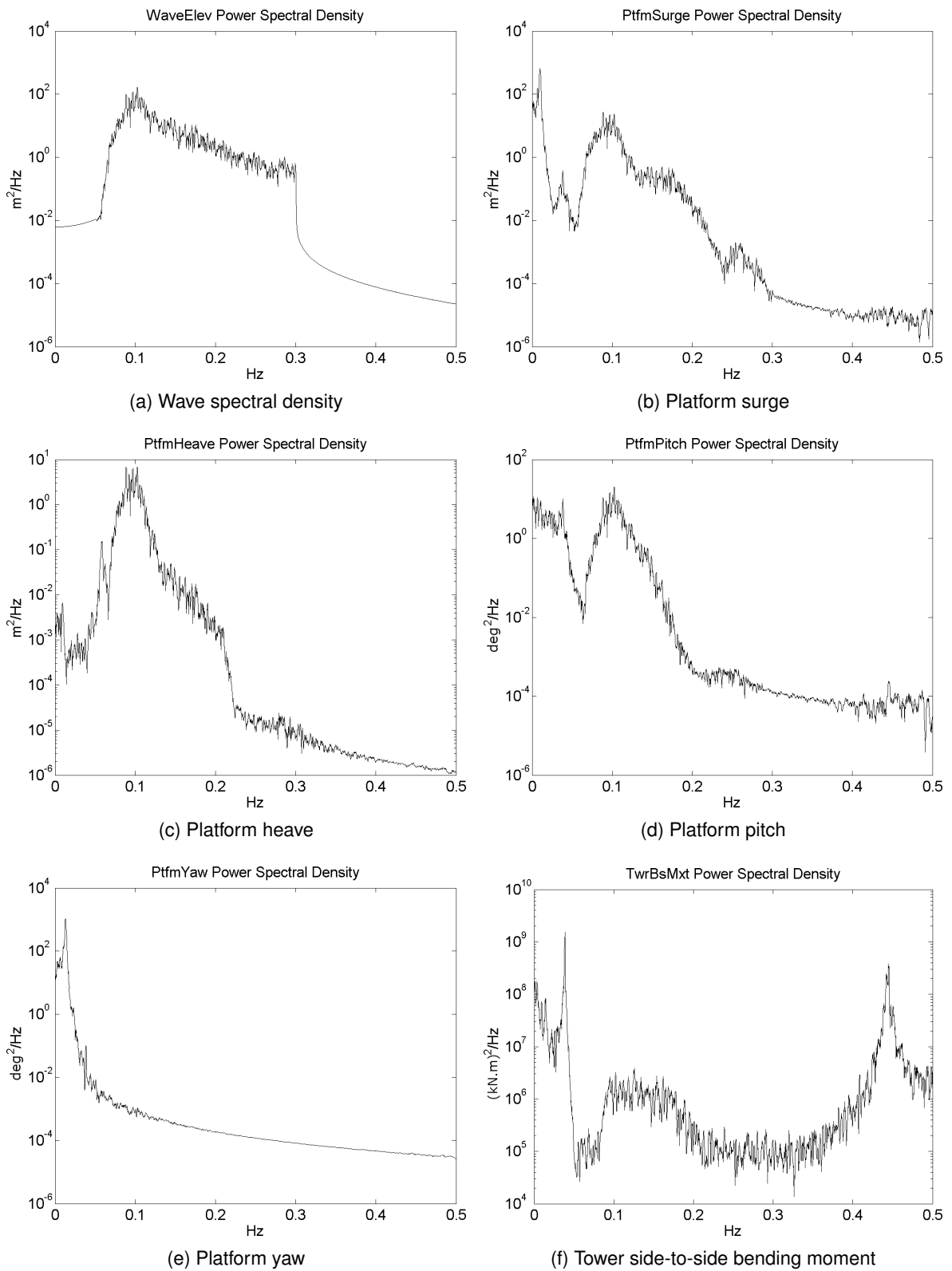
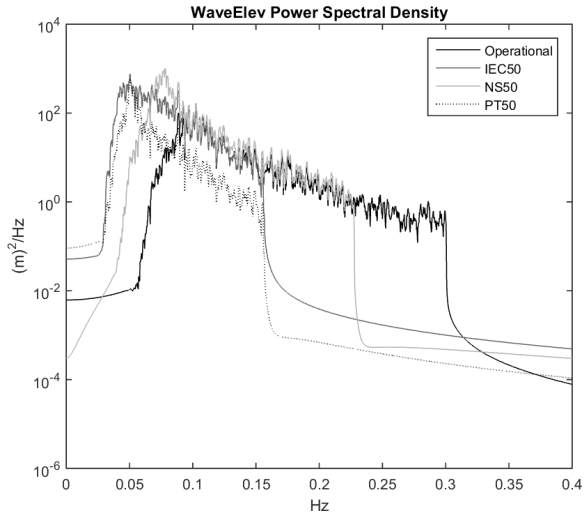
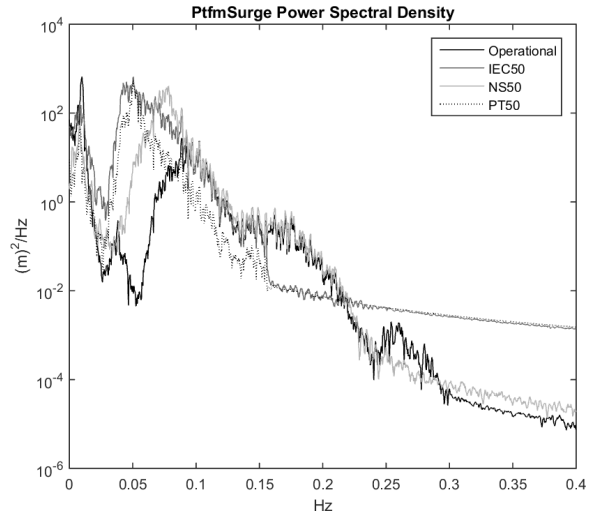


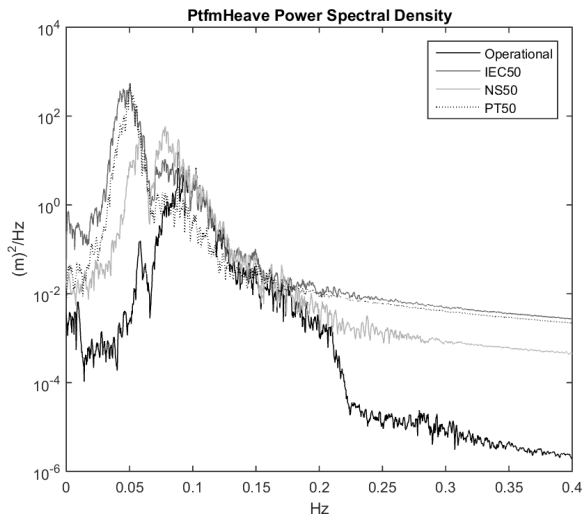
Figure 9.2: Platform responses and tower base side-to-side moments in operational conditions



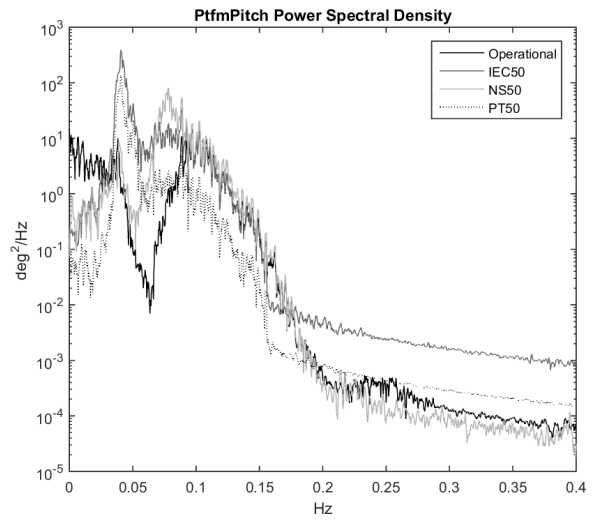
(a) Wave spectral density



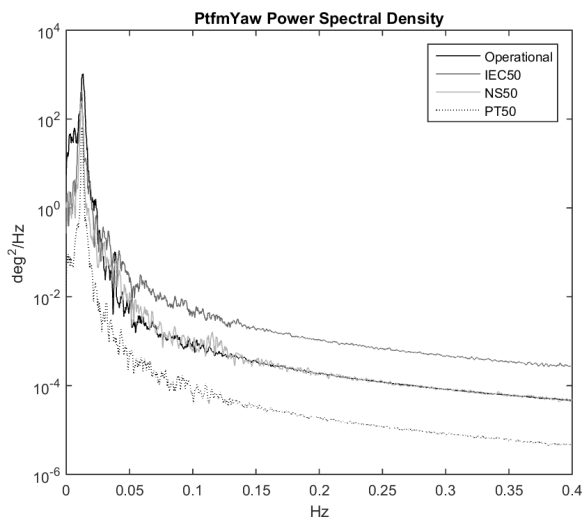
(b) Platform surge



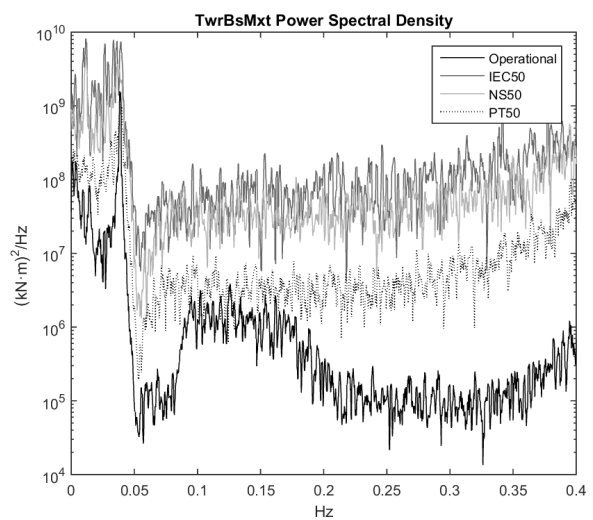
(c) Platform heave



(d) Platform pitch



(e) Platform yaw



(f) Tower side-to-side bending moment

Figure 9.3: Platform responses and tower base side-to-side moments in storm conditions

9.4 Blade pitch actuator fault induced yaw motion

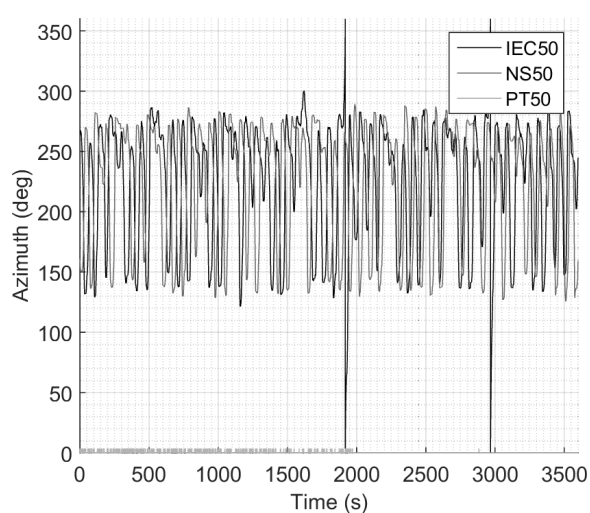
9.4.1 Responses of the platform in fault condition

A feathered blade should result in the minimum possible amount of torque at the shaft. This moment should be countered by torque provided by the high-speed shaft brake when engaged, causing only negligible variations in the azimuth angle of the blades. If there happens to be a difference in these moments, the blade will keep rotating. Figure 9.4 shows that this is the case with an applied HSS-brake in both the North Sea and the IEC conditions when one of the blades fails to feather. At the Portuguese coast (PT), the azimuth angle of the first blade stays at approximately zero degrees (i.e., the initial angle at the beginning of the time series) as expected. There is no yaw motion; platform sways less than a meter. Limited rolling motion is present. The tower base side-to-side forces are negligible. Conversely, the North Sea and IEC both show yaw angles surpassing 20 degrees, and reaching 30 degrees on occasions. Similarly, roll motion reaches 6 degrees and results in radically increased side-to-side forces at the tower base in both IEC_A and NS_A. The platform sways 4 to 6 meters from its average position. In this type of response, even if the platform's yaw motion does not cause problems, the increase in tower base moments may become a problem or mooring related complications may arise. In head waves and upwind on a symmetric structure, while wind forces will contribute to yawing to a degree, they are unlikely to be the sole cause of the rolling and yawing motions. It is understood that other factors beyond the direct effect of wind and waves should also be examined.

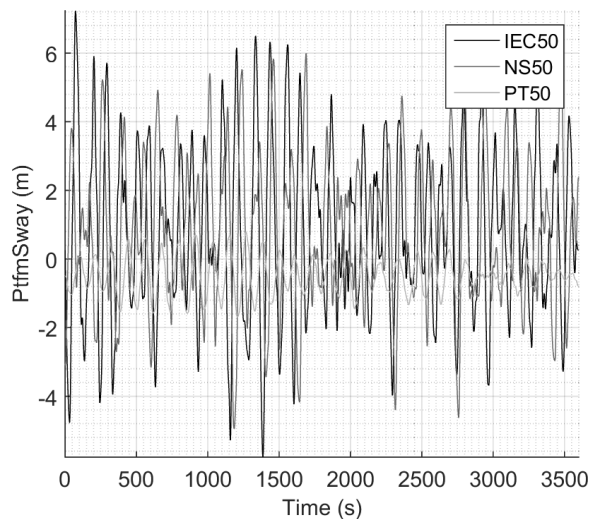
The maximum brake torque that the NREL 5MW turbine can provide is 28.12 kN.m. The lightest grey line in Figure 9.4e clarifies that this value is rarely reached in the PT₅₀ condition. Conversely, both the NS₅₀ and IEC₅₀ show the maximum value consistently. When the brake cannot stop the rotating blade, its function is reduced to slowing it down by applying a torque in the opposite direction to the shaft motion.

When the behaviour is examined, it is seen that the blades of the IEC₅₀ and NS₅₀ rotate not unidirectionally, but bi-directionally, imitating a displaced pendulum. The azimuthal angle covers 275 to 140 degrees, an approximate range of 135 degrees. Additionally, the differences between the minimum and maximum values of the azimuth angles do not decrease throughout the time series, showing that the motion is not damping out. It can be intuitively understood that this motion will contribute to the rolling mode.

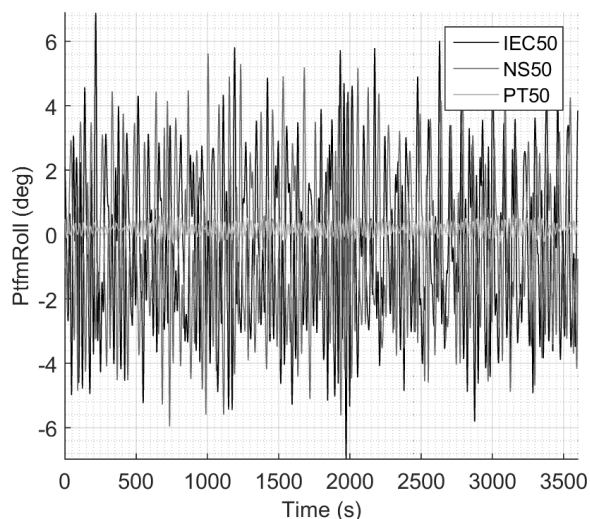
The effect of the un-feathered blade can be further evaluated by comparing the behaviour of the platform with and without the feathering fault. Figure 9.5 for the NS₅₀ provides this comparison where the subfigures (a), (c) and (e), represent the case with feathered blades (identified with (fb)). Subfigures (b), (d), and (f) demonstrate the cases where the feathering fails (identified with (af) for actuator fault). In both scenarios, the maximum torque of the HSS-brake is reached. Even when the actuator works and blade feathers, the blades still rotate. However, their reactions are different.



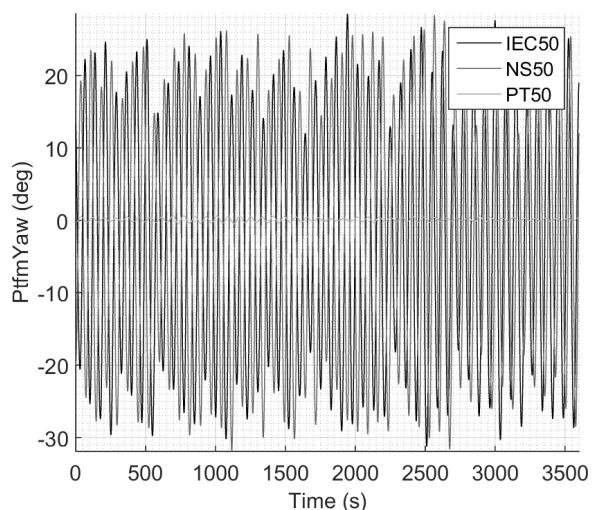
(a) Blade 1 azimuth angle



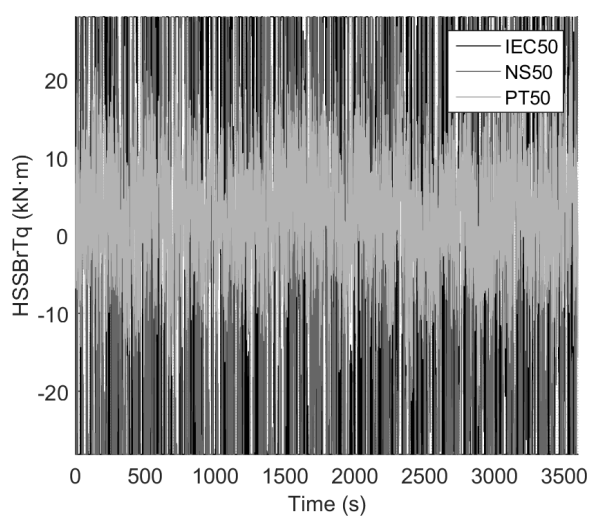
(b) Platform sway



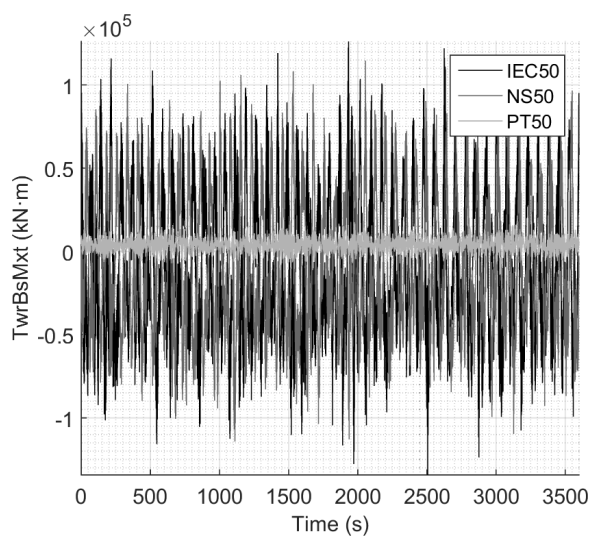
(c) Platform roll



(d) Platform yaw



(e) High speed shaft brake torque



(f) Tower side-to-side bending moments

Figure 9.4: Time series of the yaw motion caused by the blade feathering fault under IEC, North Sea and Portuguese coast storm conditions

Table 9.6: The effect of the faulty blade position on the yawing motion in NS_A environment [deg]

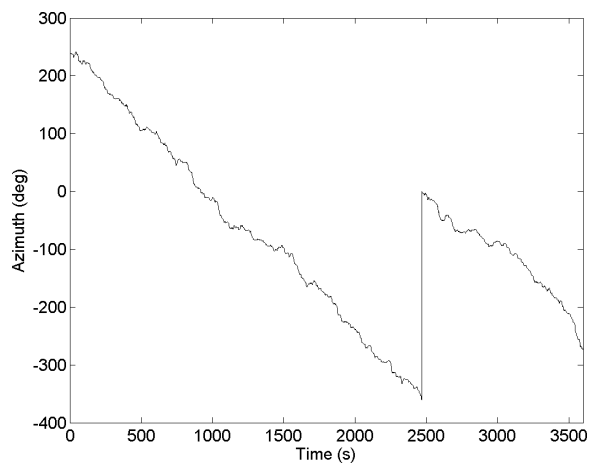
Variable	Blade rotating bidirectionally	Blade azimuth fixed at 210 deg	Blade azimuth fixed at 280 deg
Mean value	-2.3	-2.2	-4.7
Standard deviation	17.0	1.9	2.7
Maximum amplitude	30.2	5.7	7.2
Total rotation	60.3	10.2	15.2

The rotation with a feathered blade is unidirectional and slower. The platform shows roll angles lower than a degree and less than two degrees of yaw. Indicatively, the behaviour of the blades does not resemble the pendulum-type motion encountered in the fault condition.

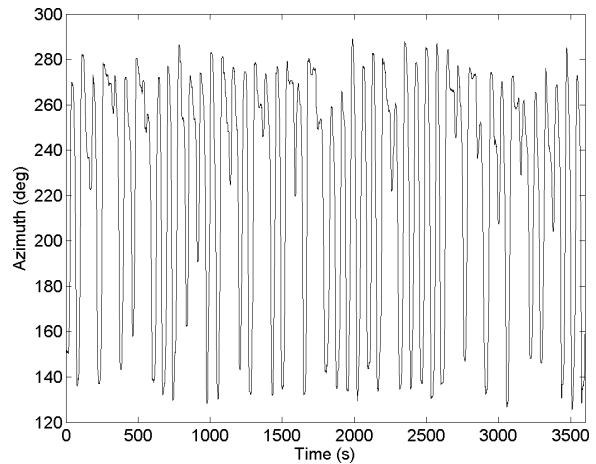
In the faulted condition, the brake stays at its maximum torque longer (the constant maximum and minimum values in Figure 9.5 (h)). For an amount of time, the rotor turns in one direction until it reaches the maximum or the minimum azimuth angle. It then stops and reverses the direction. The brake reacts by applying moments in the opposite direction until it reaches its maximum torque. It stays at this constant value for an amount of time until the cycle is repeated. The roll and yaw motions increase from 2 and 6 degrees to 6 and 30 degrees respectively. From these figures given for both cases, it is understood that the brake is not designed to hold in storm conditions of this severity. However, that situation only becomes a problem when the turbine rotates bidirectionally.

A question is how far the system yaws due to the wind forces on the open blade alone. From Figure 9.5, it is seen that the average position of the blade 1 is approximately at 210 degrees, alternating between 140 and 280 degrees. A hypothetical scenario where the faulted blade is fixed to 210 (i.e., mean value) and 280 degrees (i.e., the furthest point away from the z axis) can help to look at the contribution of the wind forces on the yaw motion. Table 9.6 gives a comparison in three NS₅₀ conditions: the bidirectionally rotating blade as presented in Figure 9.5, blade 1 fixed at 210 degrees, and blade 1 fixed at 280 degrees. The HSS brake torque was increased to a value that is never surpassed during the 210 and 280-degree simulations to ensure that the rotor stays in position.

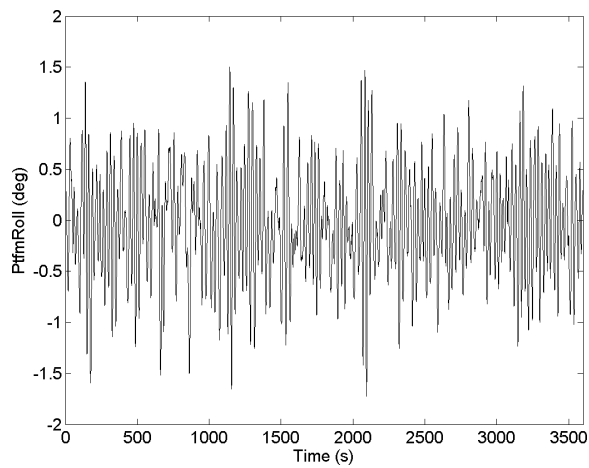
The mean values are similar in all cases. When the blade is forced to stay at 280 degrees where it is furthest away from the axis, it creates the largest moment, resulting in a mean value of -4.7 degrees. The standard deviation values clarify the differences in the behaviour of the platform. The bidirectional blade motion continually causes large amplitudes of yawing (17 degrees). In the 210 and 280 cases, the platform rotates to the mean value and starts oscillating in small angles about the point (2 to 3 degrees). The largest amplitude attained in the simulations is 30 degrees with the bidirectional motion, while it does not surpass 7.7 degrees in the other cases. The yaw motion covers about 60 degrees (i.e., approximately 30 degrees to each side of the mean value) as opposed to 15 degrees for the 280-degree azimuth angle of the blade. Comparing the standard deviation and maximum amplitudes show that larger angles are reached momentarily in the 210 and 280 cases. However, the platform's general behaviour is to reach a certain angle and oscillate about that position. While the maximum amplitudes differ, the responses are similar. On the other hand, the bidirectional



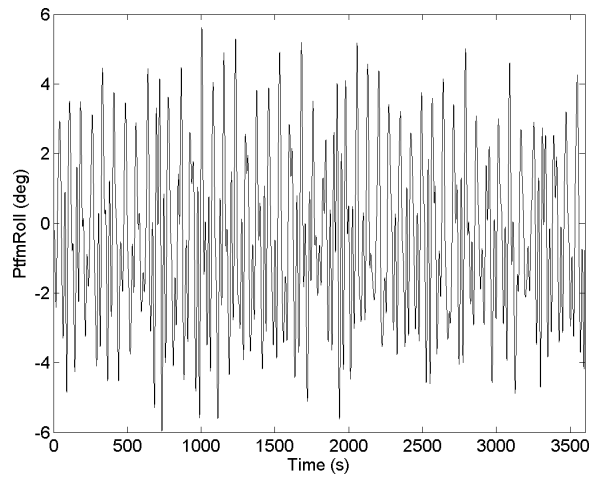
(a) Blade 1 azimuth angle (fb)



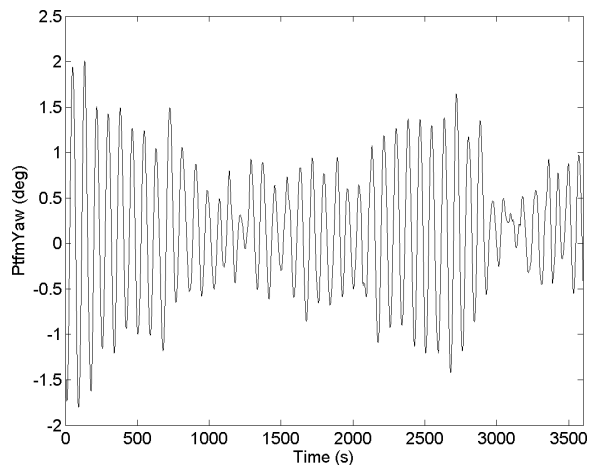
(b) Blade 1 azimuth angle (af)



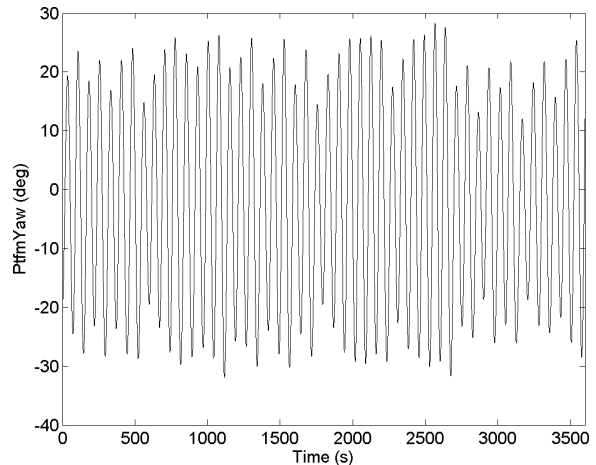
(c) Platform roll motion (fb)



(d) Platform roll motion (af)



(e) Platform yaw motion (fb)



(f) Platform yaw motion (af)

Figure 9.5: Comparison of the blade 1 azimuth angle, platform motions, and the HSS-brake behaviour in the North Sea Storm (NS₅₀) conditions. Feathered blades and actuator fault are denoted by (fb) and (af) respectively.

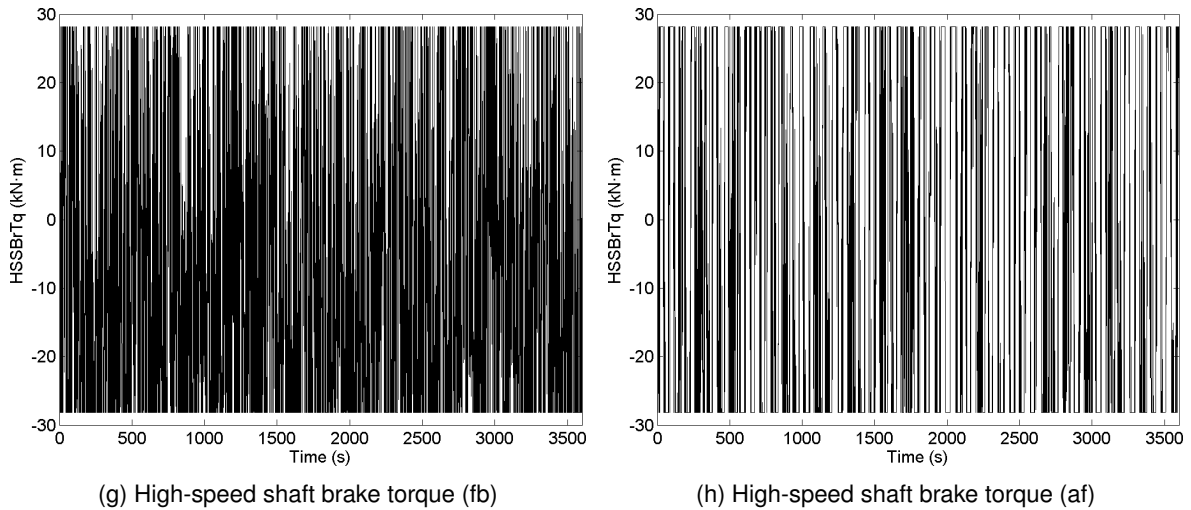


Figure 9.5: continued, Comparison of the blade 1 azimuth angle, platform motions, and the HSS-brake behaviour in the North Sea Storm (NS₅₀) conditions. Feathered blades and actuator fault are denoted by (fb) and (af) respectively.

Table 9.7: Thrust forces on the rotor in intact and faulty conditions [kN]

	NS ₅₀	NS _A	IEC ₅₀	IEC _A	PT ₅₀	PT ₅₀
Mean value	173.0	506.7	166.1	489.9	110.1	226.3
Standard deviation	63.5	127.9	76.9	123.1	36.1	49.2
Maximum value	432.4	983.2	437.4	1102.0	245.4	420.8

case exhibits larger amplitudes of continuous yawing. It should also be noted that the 280 position is momentarily reached before the blade starts rotating back to its mean position. Therefore, the system is exposed to these forces only instantaneously. With bidirectional motion, the blade is generally in a position between 280 and 150 degrees.

This bi-directional motion results in a turbine that functions in an unintended manner in storm conditions. The main idea behind locking the low-speed shaft and disallowing rotations of the blades is to reduce the forces that may cause problems. The comparisons in Table 7 show that the faulty blade scenario exposes the platform up to three times larger thrust forces in the IEC and NS cases. The value doubles for the lower storm speed of the PT condition. While the turbine's approximately 800 kN maximum thrust value is not reached, the blade fault significantly reduces the effectiveness of the parked turbine.

9.4.2 Yaw motion in lower wind speeds and partial brake failure

This section examines whether it is possible to replicate this motion at lower wind speeds. Figure 9.6 shows the time series of the environmental condition with the HSS brake applied and two of the three blades feathered in PT₅₀. In this case, the roll and yaw motions stay below a 1-degree angle. Platform sways less than 1.5 meters. The amplitudes of the forces at the base of the tower range from 100 to 200 kN and the brake frequently stays below its torque limit of 28.12 kN·m. In

Table 9.8: Yaw motion as a function of the blade starting position [deg]

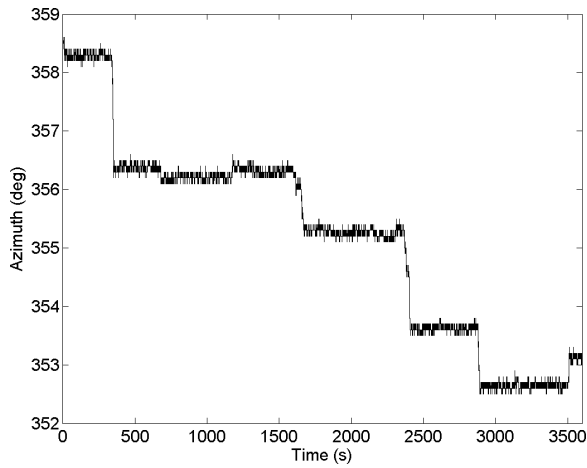
	Blade 1 initiated at zero degrees	Blade 1 initiated at 193 degrees
Mean value	-0.26	-0.26
Standard deviation	1.03	1.05
Maximum amplitude	2.57	2.54
Total rotation	4.94	4.98

the instances that it reaches this value, the azimuth angle of the blade changes minimally. The total angle of rotation is approximately 5 degrees changing between 358 to 353 degrees exhibiting long durations (e.g., 1000 seconds) of fixed azimuth angles. During the simulation's runtime, the blade rotates mostly unidirectionally.

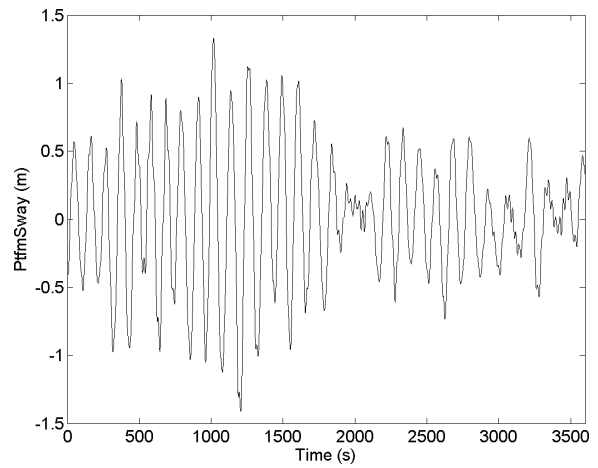
The brake torque shows that 5 kN.m is a repeatedly surpassed amplitude. This observation can be utilised to design a system where the brake fails partially. In a real-world scenario, this type of an effect equates to a worn out or faulty brake system. When simulations are repeated after reducing the maximum torque to 5 kN.m, the motion dynamics change as presented in Figure 9.7. In this case, the first reaction is that the open blade starts to move towards the 180 degrees of azimuth angle, pointing at the minus z-axis direction, where static equilibrium would occur without external forces. Then it starts to exhibit the pendulum motion between 215 and 170 degrees. The covered angle of 45 degrees is significantly lower than the 135 degrees found in the previous cases of NS_A and IEC_A. Under these circumstances, the yaw angle approximately triples to reach 2.7 degrees from 0.8 degrees. While the magnitudes of the motion are not significant, the change in dynamics is relevant.

For azimuth angles of approximately zero degrees, the blade that faces the wind in the open state is pointing in the positive z-direction (Figure 9.1). However, Figure 9.7 shows the mean position of blade 1 to be 193 degrees of azimuth angle. It is understood that the blade initially travels from the positive z-direction to towards the negative z-direction at the beginning of simulations, initiating the motion. Table 9.8 represents the comparisons for two cases where the simulations are initiated with zero and 193-degree (i.e., the mean value in Figure 9.7) blade 1 azimuth angles. The data show negligible differences in the results. The mean value, standard deviation, the maximum amplitude of motion, and the total yawing motion are not dependent on the initial position of the blade 1. Regardless of the initial setup, the blade tends to travel to a location close to its static equilibrium at the start of simulations, and the system exhibits the same motions from there on. These differences were not visible in the time series, and the motions were indistinguishable under identical wind and wave time series. Consequently, the initial position of the blade is not a factor in this motion.

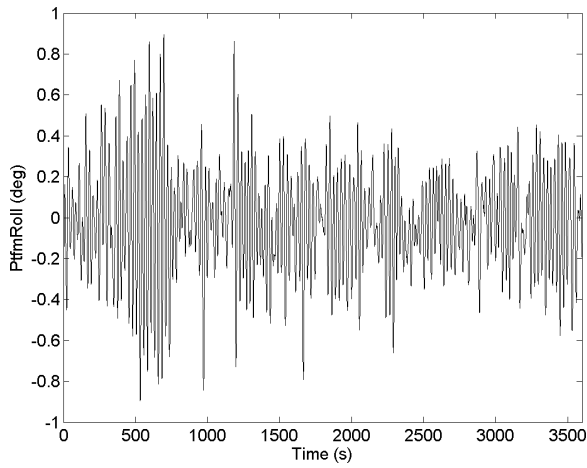
These cases clarify some of the questions on the motion dynamics. It becomes apparent that the blade failing in an un-feathered position is insufficient for the continuous yawing motion to start. The bi-directional rotation of the blades due to insufficient brake torque occurs to be the primary factor



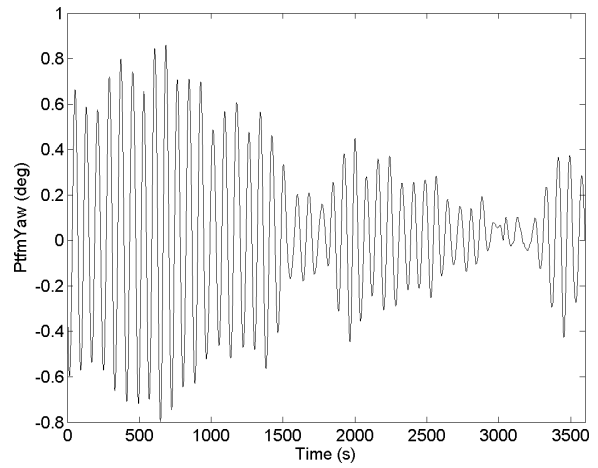
(a) Blade 1 azimuth angle



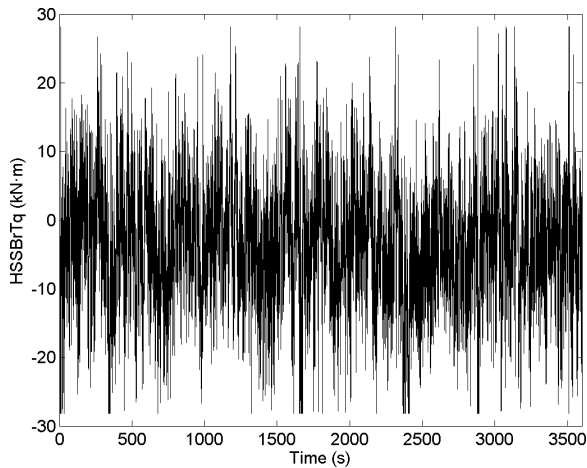
(b) Platform sway motion



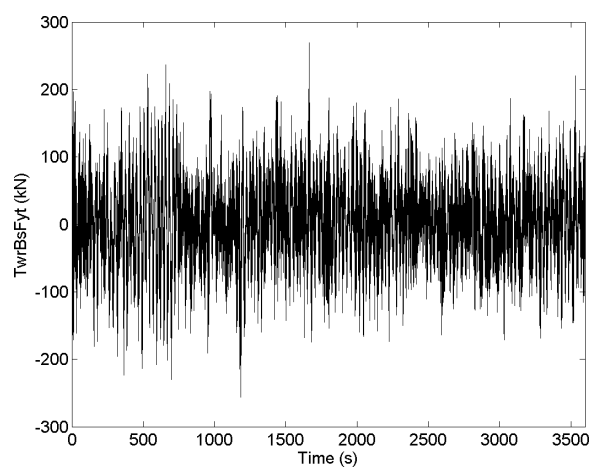
(c) Platform roll motion



(d) Platform yaw motion

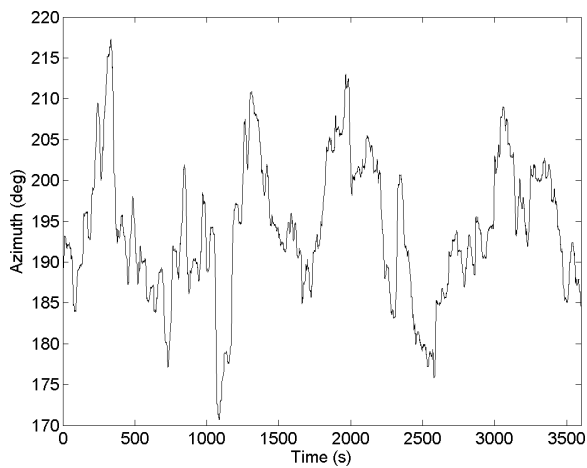


(e) High speed shaft brake torque

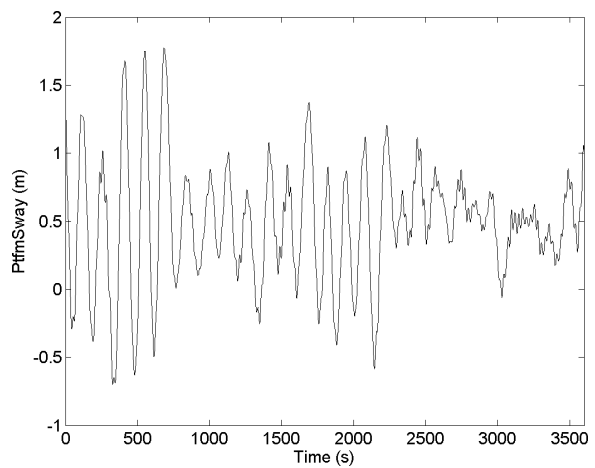


(f) Tower base side-to-side forces

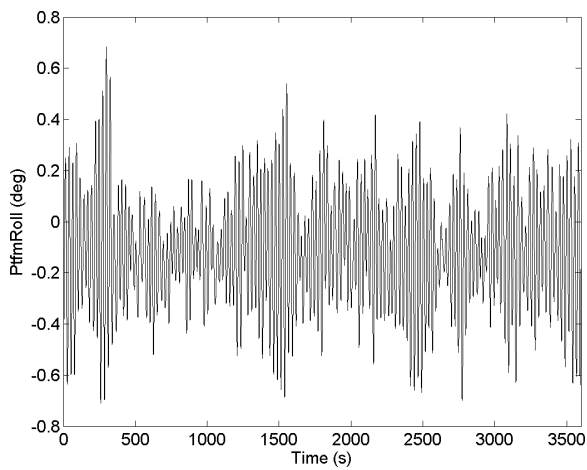
Figure 9.6: Behaviour of the platform influenced by the blade feathering fault and applied HSS brake in PT_{50} conditions



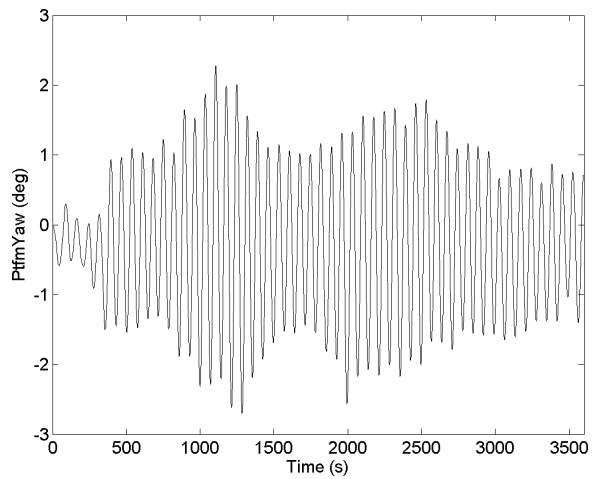
(a) Blade 1 azimuth angle



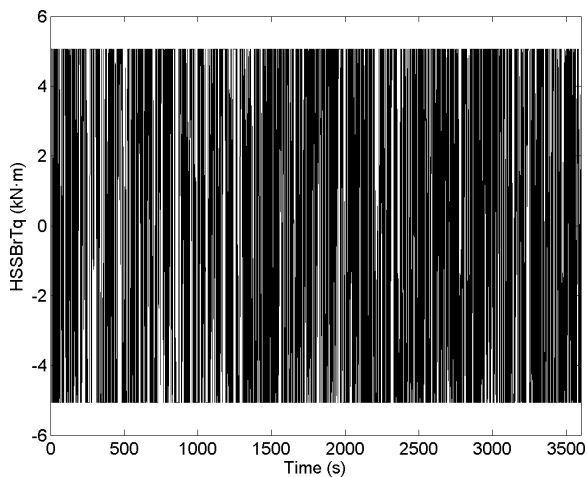
(b) Platform sway motion



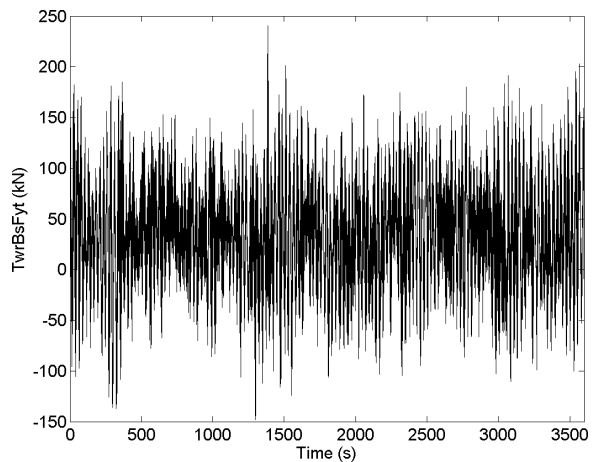
(c) Platform roll motion



(d) Platform yaw motion



(e) High speed shaft brake torque



(f) Tower base side-to-side forces

Figure 9.7: Yaw motion induced by reduced maximum HSS brake torque in PT_{50} conditions. Blade 1 initial azimuth angle is zero degrees.

in the change of dynamics. Even under a lower wind speed, the increase in the yaw amplitude is conceivable.

9.5 Factors that contribute to the yaw motion

Bidirectionally applying lateral forces will result in roll motion. To understand why the yaw is severely affected, the correlation between the yaw and roll modes, the motion dynamics, and the hydrostatic stiffness need to be discussed further. In the case of a wind turbine in head waves and aligned wind the exciting forces acting on the platform can be broken down into the hydrodynamic $F_{k_h}^E$ and aerodynamic $F_{k_a}^E$ components.

$$F_k^E = F_{k_a}^E + F_{k_h}^E, \quad k = 1, \dots, 6 \quad (9.1)$$

Given that the environmental setup consists only of head waves applied on a symmetric structure, hydrodynamic excitation of sway, roll, and yaw due to waves is zero or negligible. This case holds true until the platform rotates significantly to result in a change of geometry for the encountered waves.

$$F_{k_h}^E = 0, \quad k = [2, 4, 6] \quad (9.2)$$

The aerodynamic exciting forces are due to the exposure of the platform, rotor, and the tower to wind forces and they increase as detailed previously in Table 9.7 when the pitch actuator fails.

The inertial properties and damping values were presented in Tables 9.1 and 9.2 respectively. The platform's roll inertia is 6.83E09 kg·m² and the yaw inertia is 1.23E10 kg·m² (56% higher). These values mean that higher forces are required to start yaw motion. Conversely, the structure's yaw damping is smaller by a magnitude (4.08E+09 Nms²/rad²) than the damping of roll and pitch modes (3.35E10 Nms²/rad²). Once yaw starts, it is difficult to damp the motion out. Consider the [6x6] hydrostatic matrix repeated in the equation below:

$$C_h = g \begin{bmatrix} 0 & 0 & 0 & 0 & 0 & 0 \\ 0 & 0 & 0 & 0 & 0 & 0 \\ 0 & 0 & \rho A_{wp} & \rho A_{wp} y_f & \rho A_{wp} x_f & 0 \\ 0 & 0 & \rho A_{wp} y_f & \rho (V_{z_b} + I_{xx}) - mz_g & \rho I_{xy} & -\rho V x_b + m x_g \\ 0 & 0 & \rho A_{wp} x_f & -\rho I_{xy} & \rho (V_{z_b} + I_{yy}) - mz_g & -\rho V y_b + m y_g \\ 0 & 0 & 0 & 0 & 0 & 0 \end{bmatrix} \quad (9.3)$$

The term A_{wp} represents the waterplane area, x_f and y_f are the centres of floatation. The water-plane inertia terms are I_{xx} and I_{yy} for roll and pitch respectively. V_s denotes the centre of buoyancy where the subscript s is replaced with x , y , and z to identify the axes. The gravitational acceleration and the water density are g and ρ respectively. The mass of the structure is given in m and the

centres of gravity are denoted with x_g , y_g , and z_g in their respective Cartesian axes. The matrix shows that the yaw restoring moments solely depend on the mooring lines. A comparison of the total restoring forces of mooring and the hydrostatics reveals that yaw restoring only amounts to 0.14 percent of roll ($8.41E10$ vs $1.17E08$ for roll and yaw respectively, given in Table 9.3).

To understand the relationship between roll and yaw, the value C_{46} of the hydrostatic matrix presents the base knowledge (i.e., $-\rho V x_b + m x_g$). The coupled restoring force depends on the locations of the centres of buoyancy and gravity in the x-axis. Consider only the horizontal plane and its origin of $O(0,0)$. The DeepCwind platform's centre of buoyancy is located at the point where the x and y axes meet. However, for the NREL 5 MW wind turbine, the rotor nacelle assembly's centre of mass is offset from this position (the main dimensions in Table 9.1). The platform and the tower's masses, on the other hand, are again centred at the origin. Hence, the entire structure's mass has an offset value in the x-axis. Consequently, at any given moment apart from the static equilibrium position, there will be a coupling of the hydrostatic terms between roll and yaw, which is one of the factors in the motions.

The coupling is not limited to hydrostatics. Figure 9.8 illustrates the forces caused by the weight of the rotor nacelle assembly (RNA) of a platform in roll motion. The solid lines represent the global Cartesian axes, and the dashed lines are the platform axes. The weight of the turbine is broken down into its force components that cause yaw and pitch. The yaw moment of the RNA is the lateral component of the nacelle weight multiplied by the moment arm (i.e., the distance of to the location of the centre of gravity of the nacelle from the origin of the platform yaw axis). The mathematical connection can be identified by writing out the entire [6 by 6] mass matrix:

$$M = \begin{bmatrix} m & 0 & 0 & 0 & mz_g & -my_g \\ 0 & m & 0 & -mz_g & 0 & mx_g \\ 0 & 0 & m & my_g & -mx_g & 0 \\ 0 & 0 & -mz_g & I_{xx} & I_{xy} & I_{xz} \\ mz_g & 0 & 0 & I_{yx} & I_{yy} & I_{yz} \\ -my_g & mx_g & 0 & I_{zx} & I_{zy} & I_{zz} \end{bmatrix} \quad (9.4)$$

In a similar manner to the hydrostatic matrix, there are couplings also in the mass matrix whenever there is a longitudinal offset of the centre of gravity. Hence, neither the hydrostatics nor the mass couplings are limited to wind turbine platforms but are present for all structures that have a non-zero x_g term (e.g., buoys, ships, offshore platforms). From Equation 9.4, the couplings can be seen between sway and yaw $M(2, 6)$, heave and pitch $M(3, 5)$, roll and yaw $M(4, 6)$ & $M(6, 4)$, and roll to sway. Considering the Figures 9.5 and 9.6 and the information in Equations 9.3 and 9.4, the initiated motion of roll will inevitably result in yaw and sway for the given setup of the system. In sum, roll excitation also contributes to yaw excitation due to couplings.

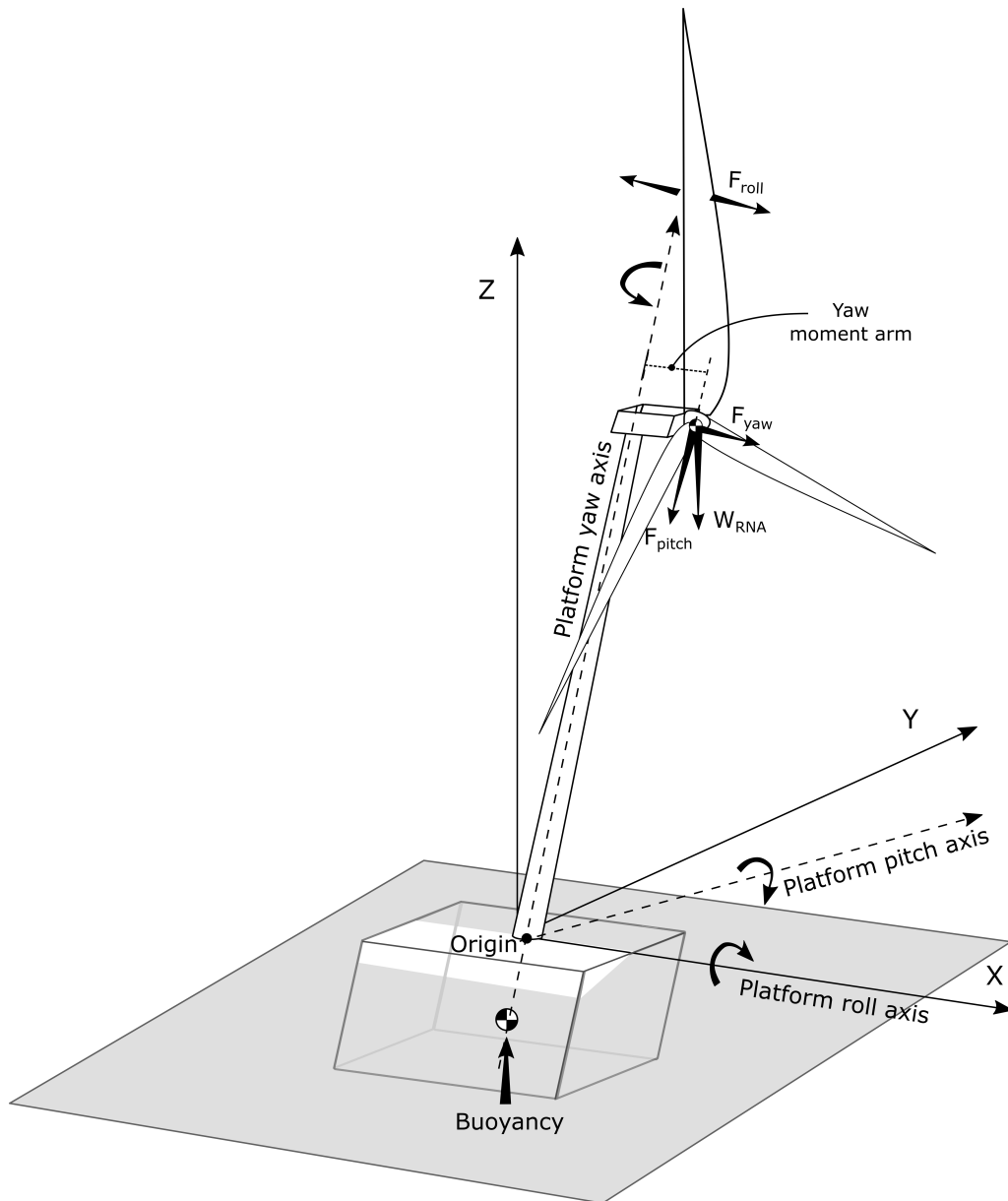


Figure 9.8: Forces acting on the platform in roll motion

The third factor and a common culprit in amplified motions is resonance. It is possible to examine its presence through the oscillatory motion of swinging blades in Figure 9.5 for the North Sea condition. Figure 9.9 provides the details of the blade motions between 2000 and 3000 seconds. The peaks that were counted as complete cycles of the pendulum are marked with diamonds. In an irregular motion, there can be different interpretations on which peaks should be included. However, in this case, providing an average value to the motion's period is sufficient to present the idea. The calculated frequency from this data is 0.014 Hz. Reminding that the yaw eigenfrequency was given as 0.012 Hz, these two values are considerably close. The yaw period of the model is 82.3 s while the blade's motion occurs at 72 s. When the bidirectional motion of the blades incites the rolling motion, the couplings, low yaw damping, and motions at the proximity of the resonance area will lead to the amplified motions seen in Figures 9.4 and 9.5.

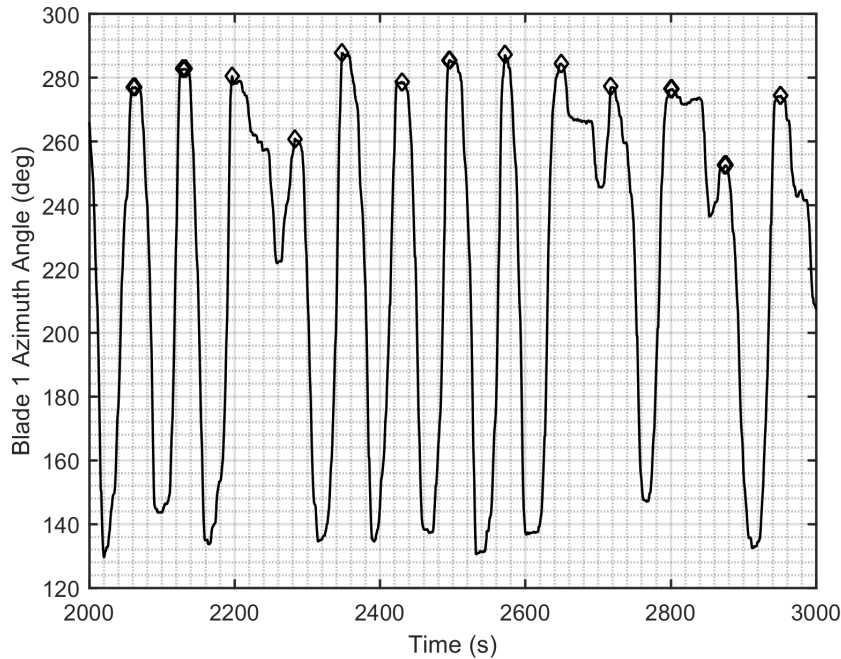


Figure 9.9: Blade 1 azimuth angles in NS₅₀ between 2000 and 3000 seconds. The peaks used for frequency measurements are marked in diamond shapes

When designing the blades and the platform, this type of fault-case behaviour is challenging to include in the prediction of resonance. Consequently, it is difficult to estimate the resulting motions. A combination of the inertial values, hydrostatics, aerodynamics, and low viscous yaw damping are at the roots of the problem. This assessment is not limited to the DeepCwind platform, but applicable to all structures with a longitudinal offset value of the centre of gravity. The workaround, in this case, would stop the motion from being initiated in the first place, by ensuring that the HSS-brake is powerful enough to hold the faulty rotor in position.

9.6 Concluding remarks

This chapter presented the yaw responses of a 5MW offshore wind turbine mounted on the DeepCwind type semi-submersible platform in storms. The platform motions in operational conditions were compared to the 50-year extreme scenarios defined by the IEC standards, the North Sea, and the storm winds at the coast of Portugal. All environmental conditions comprised unidirectional head waves and turbulent wind. The scenarios were then extended to include the effect of pitch actuator faults on yaw motion. The comparison of operational conditions to extreme environments show that higher wave amplitudes are linked to wave spectra with lower frequency ranges that coincide with the platform's natural frequencies.

Examining the fault conditions reveals that the failure of blade pitch mechanisms cause yawing motion of the platform when the HSS brake performance is insufficient. Excitation close to the yaw natural frequency combined with the coupling between modes was discussed as the primary cause

of the motion. The six by six mass and hydrostatic restoring matrices were presented to clarify the connections. It was underlined that the hydrostatic restoring terms include a coupling between roll and yaw modes given that a floating structure has an offset centre of gravity in the longitudinal axis.

With higher distances from the shore, the wind speeds are closer to the values defined for the North Sea condition as opposed to the milder Portuguese coast. Accordingly, the motions will also be more significant. Therefore, these circumstances combined with a storm condition may become an issue for floating wind turbines. Including experimentally measured yaw viscous damping values in the simulations did not solve the problem. A suggested workaround was to design the high-speed shaft brake to hold its position in storm conditions also with an unfeathered blade. This kind of revision would prevent the undesirable effects and lower the chances of probable damage to the system. The case may not be an issue for onshore and fixed bottom wind turbines as they are not compliant in the yaw mode. However, it may be of practical importance in floating offshore wind turbines. The significant yawing motion in extreme weather may cause component damage and increased tower base moments and forces. Similarly, other complications can arise in mooring lines and power cables.

CHAPTER 10

Conclusions

One of the main advances of the last century was the introduction of the assembly line into mass production. In 1913, the seemingly simple act of connecting the sequential elements reduced the time to build an automobile from 12 hours to two and a half hours. After a century, the progression of that idea reflects on almost every item currently in use. As the human thinking focused on developing systems (e.g., serially locating robotic arms to place the screws for thousands of parts) instead of carrying out repetitive tasks (e.g., hiring larger workforces to install the screws and move parts between workstations), the efficiency increased immensely. That turning point has set a basis for our current standing regarding technological advancement and economy.

Conversely, these ideas of systematisation have been overlooked in design processes, favouring specialisation and higher precision. There are numerous software packages to solve parts of the problem. The expectation is that the input is prepared separately for each one, and their outputs are brought together to provide the complete solution. Referring back to the production analogy, the commonly applied methods require a secondary workforce to feed the specialised tools and get the results back.

This situation is understandable from the point that each component of the design stage requires specific knowledge on the topic (e.g., hydrodynamics, aerodynamics, geometric modelling, mooring responses). Nevertheless, how the entirety of the system comes together should be kept in view. Otherwise, the disconnection between its parts leads to oversimplification, errors, and loss of time as simplified methods replace them.

This work attempted to address these topics on the design of offshore platforms by developing a set of integrated tools, and laying out the workflow. It emerged as a means to an end to carry

out the hydrodynamic analysis of a new floating wind turbine. Hence, the idea arose from a need after noting the limits of spreadsheet-type methods and the difficulties in using a set of specialised software in initial phases. This explicit definition of requirements led back to the equation of motion. Then, the aim was to solve its components with an acceptable level of accuracy while staying within an interconnected framework.

The interconnection serves two purposes: error removal and efficiency. Hand calculations introduce the human factor into the design process along with the unpredictability that it brings. Additionally, it turns a continuous process into an interrupted one, increasing time requirements. Hence, this involvement needs to be directed towards cases where it is beneficial. While systematisation is the main idea behind this work, selecting the right tool for the job should always be the starting point.

Despite their prominence, manual calculations on spreadsheets cannot precisely solve geometry based variables for complex shapes. They are also non-generic, and one solution will not apply to the next problem. Three-dimensional models can address these shortcomings provided that they can be parameterised. With this outlook, the decision was to develop a 3D parametric modelling tool with a numerical input format suitable for hydrodynamic calculations. Developing meshes that can simultaneously deliver the mass properties and can be evaluated by a potential flow solver proposed a multi-purpose solution to address the interconnectedness problem. An added benefit is that the implemented formulae to evaluate quadrilateral panels are an analytical solution for 3D polygons. They can also be used for other quadrilateral or triangular meshes including the ones developed with a different method.

Systems with interrelated dependencies can be validated only after knowing that each piece performs satisfactorily. It should also be ensured that the variable with the least number of dependencies is studied first (e.g., motions should be checked only after verifying that both the mass data and hydrodynamic coefficients are correct). These principles were followed in here. For instance, firstly, the volume and mass calculations were checked against several commercial software. Then, the other components were evaluated as the complexity builds up. In a case that all parts are functional, the time efficiency remained to be the problem which was addressed separately.

The worked example of a tension leg platform was used to present the system. These structures have highly coupled dynamics between the mooring lines and the hull. Accordingly, they are good examples to demonstrate motion dynamics related issues such as the detection of slack moorings and line breaking tensions. At the initial design stages, they are difficult to address with simplified hand calculations. Conversely, they can be assessed for a wide range of environmental conditions in rather short times following the steps described in the previous chapters.

The goal was to present an approach to this type of a problem as opposed to recommending a specific platform design. The setup described here will work on all tension leg platforms in an identical manner. The framework also allows room for its capabilities to enlarge and meet future requirements including those of different platform types. Following that route, this dissertation focused

on developing and connecting the parts of a design system where the person can start with only the idea. Particular contributions are summarised as follows:

- Model uncertainty of the codes used in the estimation of platform motions is quantified. It allows making informed decisions on the hydrodynamic and mooring models that are used in the calculation of platform motions.
- An accurate generic solution to the mass matrix is presented. This approach removes the requirement of breaking down hulls into elementary components for hand calculations. Commercial software and CAD tools are not required for this purpose. It also applies to existing quadrilateral or triangular meshes.
- Potential flow solver is implemented at the early design stages as opposed to a final stage solution. Thus, tabular lookup data is not necessary for structures that adhere to the potential flow theory, and the precision of the hydrodynamic calculations increase compared to closed-form equations and similar approaches.
- The developed system handles the hydrodynamic design stages in an integrated and automated manner, reducing human error in the presence of a high number of variables.
- The solution is modular. Therefore, it lays out the basis of a system that can be altered and expanded for many hull forms, designs, and functional requirements. This work provides the opportunity to build on a solid foundation.

The number of unknowns in early design stages often directs people towards limiting solutions. However, the initial commitment to building a functional system improves and simplifies all future work. The main idea is to offload the chore of repetitive calculations onto computers that are better suited for these types of tasks. Reallocating the human resource in this manner saves time, increases precision, and ultimately makes room for creativity and innovation.

10.1 Suggestions for future research

From its initiation, this work was developed in an open-ended modular structure so that it can be extended. In other words, what was presented here is a single application of a wider range of possibilities. Each module of this systematic form can be improved when better options become available. New modules can also be added to meet the changing requirements. Within these considerations, the following areas would be of immediate interest:

- Ultimately, the reason for installing offshore platforms comes down to economics. They are expensive structures designed to serve a purpose in the safest possible way. Accordingly, it is beneficial to implement an early estimation module to see if a concept is profitable.

- Similar to the slack mooring state of the TLP, the semisubmersible and the SPAR designs bring different challenges. There are also in-between stages such as wet-towing to position. Extended design routines can address these requirements.
- Depending on the type of the structure, technical challenges such as higher order effects may become important. The tendon resonant responses of tension leg platforms, and drift forces on semisubmersibles are examples. The assessment of these phenomena may be considered along with other problems such as fatigue loads.
- The developed tools provide a high number of output variables ranging from the steel mass to the mooring line responses. Dealing with this data in the most efficient format is the topic of optimization. Comprehensive subroutines for this purpose would expand the area of application.

10.2 Author's publications

10.2.1 On offshore platforms

Journals

1. E. Uzunoglu and C. Guedes Soares. Yaw Motion of Floating Wind Turbine Platforms Induced by Pitch Actuator Fault in Storm Conditions. *Renewable Energy*, 134:1056–1070, 2019. doi:10.1016/j.renene.2018.11.076
2. E. Uzunoglu and C. Guedes Soares. A system for the hydrodynamic design of tension leg platforms of floating wind turbines. *Ocean Engineering*, 171:78–92, 2019. doi: 10.1016/j.oceaneng.2018.10.052.
3. E. Uzunoglu and C. Guedes Soares. Parametric modelling of marine structures for hydrodynamic calculations. *Ocean Engineering*, 160:181–196, 2018. doi: 10.1016/j.oceaneng.2018.04.049.
4. E. Uzunoglu and C. Guedes Soares. On the model uncertainty of wave induced platform motions and mooring loads of a semisubmersible based wind turbine. *Ocean Engineering*, 148:277–285, 2018. doi: 10.1016/j.oceaneng.2017.11.001.
5. A. N. Robertson, F. Wendt, J. M. Jonkman, W. Popko, H. Dagher, S. Gueydon, J. Qvist, F. Vittori, J. Azcona, E. Uzunoglu, C. Guedes Soares, R. Harries, A. Yde, C. Galinos, K. Hermans, J. B. de Vaal, P. Bozonnet, L. Bouy, I. Bayati, R. Bergua, J. Galvan, I. Mendikoa, C. B. Sanchez, H. Shin, S. Oh, C. Molins, and Y. Debruyne. OC5 Project Phase II: Validation of Global Loads of the DeepCwind Floating Semisubmersible Wind Turbine. *Energy Procedia*, 137:38–57, 2017. doi: 10.1016/j.egypro.2017.10.333.

Book chapters

1. E. Uzunoglu, D. Karmakar, and C. Guedes Soares. Floating Offshore Wind Platforms. In L. Castro-Santos and V. Diaz-Casas, editors, *Floating Offshore Wind Farms*, chapter 4, pages 53–76. Springer International Publishing, Switzerland, 1st edition, 2016. ISBN 978-1-138-00124-4. doi: 10.1007/978-3-319-27972-5_4.
2. E. Uzunoglu and C. Guedes Soares. Supervisory system for the automation of model building and simulations with the wind turbine code FAST. In C. Guedes Soares, editor, *Progress in Renewable Energies Offshore*, pages 627–635. Taylor & Francis Group, London, UK, 2016. ISBN 978-1-138-62627-0.
3. E. Uzunoglu and C. Guedes Soares. A numerical model for compartment assessment of offshore structures with cylindrical hulls. In C. Guedes Soares, editor, *Maritime Technology and Engineering*, pages 693–700. Taylor & Francis Group, London, UK, 2016. ISBN 978-1-138-02727-5.
4. E. Uzunoglu and C. Guedes Soares. On the model uncertainty of wave induced responses of a floating semisubmersible wind system. In C. Guedes Soares, editor, *Progress in Renewable Energies Offshore*, pages 785–794. Taylor & Francis Group, London, UK, 2016. ISBN 978-1-138-62627-0.
5. K. Raed, E. Uzunoglu, and C. Guedes Soares. Uncertainty associated with the estimation of drag and inertia coefficients of fixed vertical cylinders. In C. Guedes Soares, editor, *Progress in Renewable Energies Offshore*, pages 767–774. Taylor & Francis Group, London, UK, 2016. ISBN 978-1-138-62627-0.
6. K. G. Vijay, D. Karmakar, E. Uzunoglu, and C. Guedes Soares. Performance of barge-type floaters for floating wind turbine. In C. Guedes Soares, editor, *Progress in Renewable Energies Offshore*, pages 637–645. Taylor & Francis Group, London, UK, 2016. ISBN 978-1-138-62627-0.
7. E. Uzunoglu and C. Guedes Soares. Parametric modelling of multi-body cylindrical offshore wind turbine platforms. In C. Guedes Soares and T. A. Santos, editors, *Maritime Technology and Engineering*, pages 1185–1193. Taylor & Francis Group, London, UK, 2015. ISBN 978-1-138-00124-4.
8. E. Uzunoglu and C. Guedes Soares. Comparison of numerical and experimental data for a DeepCwind type semi-submersible floating offshore wind turbine. In C. Guedes Soares, editor, *Renewable Energies Offshore*, pages 747–754. Taylor & Francis Group, London, UK, 2015. ISBN 978-1-138-02871-5.
9. E. Uzunoglu and C. Guedes Soares. Influence of bracings on the hydrodynamic modelling of a semi-submersible offshore wind turbine platform. In C. Guedes Soares, editor, *Renewable*

Energies Offshore, pages 755–762. Taylor & Francis Group, London, UK, 2015. ISBN 978-1-138-02727-5.

Conferences

1. A. Robertson, J. Jonkman, F. Vorpal, W. Popko, J. Qvist, L. Froyd, X. Chen, J. Azcona, E. Uzunoglu, C. Guedes Soares, C. Luan, H. Yutong, F. Pengcheng, A. Yde, T. Larsen, J. Nichols, R. Buils, L. Lei, T. A. Nygaard, D. Manolas, A. Heege, S. Ringdalen Vatne, H. Ormberg, T. Duarte, C. Godreau, H. F. Hansen, A. W. Nielsen, H. Riber, C. Le Cunff, F. Beyer, A. Yamaguchi, K. Jin Jun, H. Shin, W. Shi, H. Park, M. Alves, and M. Guérinel. Offshore Code Comparison Collaboration Continuation Within IEA WIND Task 30: Phase II Results Regarding a Floating Semisubmersible Wind System. In *33rd International Conference on Ocean, Offshore and Arctic Engineering (OMAE)*, San Francisco, California, USA, 2014. doi: 10.1115/OMAE2014-24040. OMAE2014-24040.

10.2.2 On other topics

Journals

1. E. Uzunoglu and C. Guedes Soares. Automated processing of free roll decay experimental data. *Ocean Engineering*, 102:17–26, 2015. doi: 10.1016/j.oceaneng.2015.04.016.
2. E. Uzunoglu, S. Ribeiro e Silva, C. Guedes Soares, A. Marón, and C. Gutierrez. The effect of asymmetric cross-sections on hydrodynamic coefficients of a C11 type container vessel. *Ocean Engineering*, 113:264–275, 2016. doi: 10.1016/j.oceaneng.2015.12.049.
3. E. Uzunoglu, S. Ribeiro e Silva, C. Guedes Soares, Zamora R., and L. Perez-Rojas. Numerical and Experimental Study of the Parametric Rolling of a Fishing Vessel in Regular Head Waves. *International of Journal Maritime Engineering, Transactions RINA*, 155(Part A4):A181–A188, 2013.

Book chapters

1. J. Rörup, Y. Garbatov, Y. Dong, E. Uzunoglu, G. Parmentier, A. Andoniu, Y. Quéméner, K. Chen, S. Vhanmane, A. Negi, et al. Round robin study on spectral fatigue assessment of butt-welded joints. In C. Guedes Soares and P. A. Teixeira, editors, *Maritime Transportation and Harvesting of Sea Resources*. Taylor & Francis Group, London, UK, 2018. ISBN 978-0-8153-7993-5.
2. E. Uzunoglu, S. Ribeiro e Silva, and C. Guedes Soares. Numerical and experimental study of parametric rolling of a container ship in regular and irregular head waves. In C. Guedes Soares and T. A. Santos, editors, *Maritime Technology and Engineering*, pages 1047–1056. Taylor & Francis Group, London, UK, 2015. ISBN 978-1-138-02727-5.

Conferences

1. S. Ribeiro e Silva, E. Uzunoglu, C. Guedes Soares, A. Marón, and C. Gutierrez. Investigation of the Hydrodynamic Characteristics of Asymmetric Cross-Sections Advancing in Regular Waves. In *30th International Conference on Ocean, Offshore and Arctic Engineering (OMAE)*, Rotterdam, The Netherlands, 2011. doi: 10.1115/OMAE2011-50322. OMAE2011-50322.
2. E. Uzunoglu, S. Ribeiro e Silva, J. L. Mantari, and C. Guedes Soares. Prevention of Parametric Rolling Onboard Fishing Vessels. In *1st International Symposium on Naval Architecture and Maritime*, pages 383–391, Istanbul, Turkey, 2011.
3. S. Ribeiro e Silva, C. Guedes Soares, A. Turk, J. Prpic-Orsic, and E. Uzunoglu. Experimental Assessment of the Parametric Rolling On a C11 Class Container Ship. In *Proceedings of the HYDRALAB III Joint User Meeting*, pages 267–270, Hanover, Germany, 2010.

References

- [1] Mr. Brush's Windmill Dynamo. *Scientific American*, 63(25):389–389, 1890.
- [2] J. K. Kaldellis and D. Zafirakis. The wind energy (r)evolution: A short review of a long history. *Renewable Energy*, 36(7):1887–1901, 2011. ISSN 09601481. doi: 10.1016/j.renene.2011.01.002.
- [3] GWEC. Global Wind Report 2016. Technical report, Global Wind Energy Council, Brussels, Belgium, 2017.
- [4] GWEC. Global Wind Report 2017. Technical report, Global Wind Energy Council, Brussels, Belgium, 2018.
- [5] WindEurope Business Intelligence. The European offshore wind industry, Key trends and statistics. Technical report, WindEurope, 2017.
- [6] S. Butterfield, W. Musial, J. Jonkman, and P. Sclavounos. Engineering challenges for floating offshore wind turbines. In *Copenhagen Offshore Wind Conference*, Copenhagen, Denmark, 2005.
- [7] Det Norske Veritas (DNV). *Offshore standard DNV-OS-C301, Stability and watertight integrity*. Det Norske Veritas AS, 2011.
- [8] Det Norske Veritas (DNV). *Floating wind turbine structures, DNV-OS-J103*. Det Norske Veritas AS, 2018.
- [9] L. Castro-Santos and V. Diaz-Casas. Life-cycle cost analysis of floating offshore wind farms. *Renewable Energy*, 66:41–48, 2014. doi: 10.1016/j.renene.2013.12.002.
- [10] C. Chen, X. Mei, and T. Mills. Effect of heave plate on semisubmersible response. In *The 17th International Offshore and Polar Engineering Conference*, Lisbon, Portugal, 2007. International Society of Offshore and Polar Engineers (ISOPE). ISOPE-I-07-044.

- [11] C. Lopez-Pavon and A. Souto-Iglesias. Hydrodynamic coefficients and pressure loads on heave plates for semi-submersible floating offshore wind turbines: A comparative analysis using large scale models. *Renewable Energy*, 81:864–881, 2015. doi: 10.1016/j.renene.2015.04.003.
- [12] D. Roddier, C. Cermelli, A. Aubault, and A. Weinstein. WindFloat: A floating foundation for offshore wind turbines. *Journal of Renewable and Sustainable Energy*, 2(3):33104, 2010. doi: 10.1063/1.3435339.
- [13] C. Cermelli, D. Roddier, and A. Aubault. WindFloat: A floating foundation for offshore wind turbines—Part II: hydrodynamics analysis. In *28th International Conference on Ocean, Offshore and Arctic Engineering (OMAE)*, pages 135–143. American Society of Mechanical Engineers (ASME), 2009. doi: 10.1115/OMAE2009-79231. OMAE2009-79231.
- [14] Fukushima Offshore Wind Consortium. Fukushima Floating Offshore Wind Farm Demonstration Project (Fukushima FORWARD). Technical report, Tokyo, Japan, 2014.
- [15] M. Karimirad and C. Michailides. V-shaped semisubmersible offshore wind turbine: An alternative concept for offshore wind technology. *Renewable Energy*, 83:126–143, 2015. doi: 10.1016/j.renene.2015.04.033.
- [16] J. A. Mercier, R. G. Goldsmith, and L. B. Curtis. The Hutton TLP: A Preliminary Design. *Journal of Petroleum Technology*, 34(01):208–216, 1982. doi: 10.2118/10647-PA.
- [17] H. Bradshaw, E. G. Stokes, and M. J. Leece. Hutton TLP installation. In *Offshore Technology Conference*, Houston, Texas, USA, 1985. Offshore Technology Conference. doi: 10.4043/4913-MS. OTC-4913-MS.
- [18] M. Jeon, S. Lee, and S. Lee. Unsteady aerodynamics of offshore floating wind turbines in platform pitching motion using vortex lattice method. *Renewable Energy*, 65:207–212, 2014. doi: 10.1016/j.renene.2013.09.009.
- [19] T. Tran and D. Kim. The platform pitching motion of floating offshore wind turbine: a preliminary unsteady aerodynamic analysis. *Journal of Wind Engineering and Industrial Aerodynamics*, 142:65–81, 2015. doi: 10.1016/j.jweia.2015.03.009.
- [20] S. E. Kibbee, J. Chianis, K. B. Davies, and B. A. Sarwono. The Seastar Tension-Leg Platform. In *4th Offshore Technology Conference*, pages 243–256, Houston, Texas, USA, 1994. doi: 10.4043/7535-MS. OTC 7235.
- [21] S. E. Kibbee, S. J. Leverette, K. B. Davies, and R. B. Matten. Morpeth SeaStar Mini-TLP. In *Offshore Technology Conference*, Houston, Texas, USA, 1999. doi: 10.4043/10855-MS. OTC-10855-MS.

- [22] D. Matha. Model development and loads analysis of an offshore wind turbine on a tension leg platform with a comparison to other floating turbine concepts. Technical Report NREL/TP-5000-60573, National Renewable Energy Laboratory (NREL), Golden, CO, USA, 2009.
- [23] J. Amate, G. D. Sánchez, and G. González. Development of a semi-submersible barge for the installation of a tlp floating substructure. TLPWIND® case study. *Journal of Physics: Conference Series*, 749(1):012016, 2016. doi: 10.1088/1742-6596/749/1/012016.
- [24] R. James and M. Costa Ros. Floating offshore wind: Market and technology review. Technical report, Carbon Trust, UK, 2015.
- [25] Y. Nihei, K. Iijima, M. Murai, and T. Ikoma. A Comparative Study of Motion Performance of Four Different FOWT Designs in Combined Wind and Wave Loads. In *33rd International Conference on Ocean, Offshore and Arctic Engineering (OMAE)*, San Francisco, California, USA, 2014. American Society of Mechanical Engineers (ASME). doi: 1115/OMAE2014-24643. OMAE2014-24643.
- [26] S. E. Hirdaris, W. Bai, D. Dessi, A. Ergin, X. Gu, O. A. Hermundstad, R. Huijsmans, K. Iijima, U. D. Nielsen, J. Parunov, N. Fonseca, A. Papanikolaou, K. Argyriadis, and A. Incecik. Loads for use in the design of ships and offshore structures. *Ocean Engineering*, 78:131–174, 2014. doi: 10.1016/j.oceaneng.2013.09.012.
- [27] Det Norske Veritas (DNV). *Design of Floating Wind Turbine Structures, DNV-OS-J103*. Det Norske Veritas AS, 2013.
- [28] C. Guedes Soares, J. Bhattacharjee, and D. Karmakar. Overview and prospects for development of wave and offshore wind energy. *Brodogradnja*, 65(2):87–109, 2014.
- [29] M. J. Muliawan, M. Karimirad, Z. Gao, and T. Moan. Extreme responses of a combined spar-type floating wind turbine and floating wave energy converter (STC) system with survival modes. *Ocean Engineering*, 65:71–82, 2013. doi: 10.1016/j.oceaneng.2013.03.002.
- [30] L. Chen, F. L. Ponta, and L. I. Lago. Perspectives on innovative concepts in wind-power generation. *Energy for Sustainable Development*, 15(4):398–410, 2011. doi: 10.1016/j.esd.2011.06.006.
- [31] F. P. Brennan, J. Falzarano, Z. Geo, E. Lendet, M. Le Boulluec, C. W. Rim, J. Sirkar, L. Sun, H. Suzuki, A. Thiry, F. Trarieux, and C. M. Wang. Offshore Renewable Energy. In F. W and B. F. P, editors, *International Ship and Offshore Structures Congress (ISSC) 2012*, volume 2, pages 153–200, Rostock, Germany, 2012. Committee V.4.
- [32] E. Uzunoglu, D. Karmakar, and C. Guedes Soares. Floating Offshore Wind Platforms. In L. Castro-Santos and V. Diaz-Casas, editors, *Floating Offshore Wind Farms*, chapter 4, pages 53–76. Springer International Publishing, Switzerland, 1st edition, 2016. ISBN 978-1-138-00124-4. doi: 10.1007/978-3-319-27972-5_4.

- [33] J. Jonkman, S. Butterfield, W. Musial, and G. Scott. Definition of a 5MW reference wind turbine for offshore system development. Technical Report NREL/TP-500-38060, National Renewable Energy Laboratory (NREL), Golden, CO, USA, 2009.
- [34] K. P. Thiagarajan and H. J. Dagher. A review of floating platform concepts for offshore wind energy generation. *Journal of Offshore Mechanics and Arctic Engineering*, 136(2), 2014. doi: 10.1115/1.4026607. OMAE-13-1010.
- [35] W. L. Moon III and C. J. Nordstrom. Tension leg platform turbine: A unique integration of mature technologies. In *Proceedings of the 16th Offshore Symposium, Texas Section of the Society of Naval Architects and Marine Engineers (SNAME)*, pages A25–A34, Houston, Texas, USA, 2010.
- [36] J. Jonkman and W. Musial. Offshore Code Comparison Collaboration (OC3) for IEA Task 23 offshore wind technology and deployment. Technical Report NREL/TP-5000-48191, National Renewable Energy Laboratory (NREL), Golden, CO, USA, 2010.
- [37] J. Jonkman. Definition of the Floating System for Phase IV of OC3. Technical Report NREL/TP-500-47535, National Renewable Energy Laboratory (NREL), Golden, CO, USA, 2008.
- [38] A. N. Robertson, J. M. Jonkman, A. J. Goupee, A. J. Coulling, I. Prowell, J. Browning, M. D. Masciola, and P. Molta. Summary of conclusions and recommendations drawn from the DeepCwind scaled floating offshore wind system test campaign. In *32nd International Conference on Ocean, Offshore and Arctic Engineering (OMAE)*, Nantes, France, 2013. American Society of Mechanical Engineers (ASME). doi: 10.1115/OMAE2013-10817. OMAE2013-10817.
- [39] A. J. Coulling, A. J. Goupee, A. N. Robertson, J. M. Jonkman, and H. J. Dagher. Validation of a FAST semi-submersible floating wind turbine numerical model with DeepCwind test data. *Journal of Renewable and Sustainable Energy*, 5(2):23116, 2013. doi: 10.1063/1.4796197.
- [40] A. Jain, A. J. Goupee, A. N. Robertson, R. W. Kimball, J. M. Jonkman, and A. H. P. Swift. FAST code verification of scaling laws for DeepCwind floating wind system tests. In *22nd International Offshore and Polar Engineering Conference*, pages 355–365, Rhodes, Greece, 2012. ISOPE-I-12-032.
- [41] H. R. Martin, R. W. Kimball, A. M. Viselli, and A. J. Goupee. Methodology for wind/wave basin testing of floating offshore wind turbines. *Journal of Offshore Mechanics and Arctic Engineering*, 136(2):20905, 2014. doi: 10.1115/1.4025030. OMAE-13-1001.
- [42] B. J. Koo, A. J. Goupee, R. W. Kimball, and K. F. Lambrakos. Model tests for a floating wind turbine on three different floaters. *Journal of Offshore Mechanics and Arctic Engineering*, 136(2):020907, 2014. doi: 10.1115/1.4024711. OMAE-13-1004.
- [43] R. Kimball, A. Goupee, A. Coulling, and H. Dagher. Model test comparisons of TLP, spar-buoy and semi-submersible floating offshore wind turbine systems. In *Society of Naval Architects Marine Engineering (SNAME) Annual Meeting*, pages 24–26, Providence, RI, USA, 2012.

- [44] Det Norske Veritas (DNV). *Design of offshore wind turbine systems, DNV-OS-J101*. Det Norske Veritas AS, 2013.
- [45] J. Azcona, F. Vittori, U. Schmidt, F. Savenije, G. Kapogiannis, X. Karvelas, D. Manolas, S. Voutsinas, F. Amann, R. Faerron-Guzmán, and F. Lemmer. Design Solutions for 10MW Floating offshore Wind Turbines. Technical Report Deliverable D 4.3.7, INNWIND, 2017.
- [46] A. Cordle and J. Jonkman. State of the art in floating wind turbine design tools. In *The 21st International Offshore and Polar Engineering Conference*, pages ISOPE–I–11–112. International Society of Offshore and Polar Engineers (ISOPE), 2011.
- [47] E. Uzunoglu and C. Guedes Soares. On the model uncertainty of wave induced platform motions and mooring loads of a semisubmersible based wind turbine. *Ocean Engineering*, 148:277–285, 2018. doi: 10.1016/j.oceaneng.2017.11.001.
- [48] A. Robertson, J. Jonkman, M. Masciola, H. Song, A. Goupee, A. Coulling, and C. Luan. Definition of the Semisubmersible Floating System for Phase II of OC4. Technical Report NREL/TP-5000-60601, National Renewable Energy Laboratory (NREL), Golden, CO, USA, 2014.
- [49] A. Robertson, J. Jonkman, F. Vorphal, W. Popko, J. Qvist, L. Froyd, X. Chen, J. Azcona, E. Uzunoglu, C. Guedes Soares, C. Luan, H. Yutong, F. Pengcheng, A. Yde, T. Larsen, J. Nichols, R. Buils, L. Lei, T. A. Nygaard, D. Manolas, A. Heege, S. Ringdalen Vatne, H. Ormberg, T. Duarte, C. Godreau, H. F. Hansen, A. W. Nielsen, H. Riber, C. Le Cunff, F. Beyer, A. Yamaguchi, K. Jin Jun, H. Shin, W. Shi, H. Park, M. Alves, and M. Guérinel. Offshore Code Comparison Collaboration Continuation Within IEA WIND Task 30: Phase II Results Regarding a Floating Semisubmersible Wind System. In *33rd International Conference on Ocean, Offshore and Arctic Engineering (OMAE)*, San Francisco, California, USA, 2014. doi: 10.1115/OMAE2014-24040. OMAE2014–24040.
- [50] J. M. Jonkman. Dynamics modeling and loads analysis of an offshore floating wind turbine. Technical Report NREL/TP-500-41958, National Renewable Energy Laboratory (NREL), Golden, CO, USA, 2007.
- [51] A. J. Goupee, B. J. Koo, R. W. Kimball, K. F. Lambrakos, and H. J. Dagher. Experimental comparison of three floating wind turbine concepts. *Journal of Offshore Mechanics and Arctic Engineering*, 136(2):020906, 2014. doi: 10.1115/1.4025804.
- [52] A. N. Robertson, F. Wendt, J. M. Jonkman, W. Popko, H. Dagher, S. Gueydon, J. Qvist, F. Vittori, J. Azcona, E. Uzunoglu, C. Guedes Soares, R. Harries, A. Yde, C. Galinos, K. Hermans, J. B. de Vaal, P. Bozonnet, L. Bouy, I. Bayati, R. Bergua, J. Galvan, I. Mendikoa, C. B. Sanchez, H. Shin, S. Oh, C. Molins, and Y. Debruyne. OC5 Project Phase II: Validation of Global Loads of the DeepCwind Floating Semisubmersible Wind Turbine. *Energy Procedia*, 137:38–57, 2017. doi: 10.1016/j.egypro.2017.10.333.

- [53] E. Uzunoglu and C. Guedes Soares. Comparison of numerical and experimental data for a DeepCwind type semi-submersible floating offshore wind turbine. In C. Guedes Soares, editor, *Renewable Energies Offshore*, pages 747 – 754. Taylor & Francis Group, London, UK, 2015. ISBN 978-1-138-02871-5.
- [54] M. Hall and A. Goupee. Validation of a lumped-mass mooring line model with DeepCwind semisubmersible model test data. *Ocean Engineering*, 104:590–603, 2015. doi: 10.1016/j.oceaneng.2015.05.035.
- [55] A. Bossler. Floating Offshore Wind Foundations: Industry Consortia and Projects in the United States, Europe and Japan. Technical report, Main(e) International Consulting, LLC, Maine, USA, 2013.
- [56] European Commission. Renewable Energy Progress Report, Report from the Commission to the European parliament, the Council, the European economic and social committee and the Committee of the regions. Technical Report COM(2015) 293, European Commission Publications Office, 2015.
- [57] European Commission. Renewable Energy Progress Report, Report from the Commission to the European parliament, the Council, the European economic and social committee and the Committee of the regions. Technical Report COM(2017) 57, European Commission Publications Office, 2017.
- [58] F. Adam, C. Steinke, F. Dahlhaus, and J. Großmann. GICON®-TLP for Wind Turbines – Validation of Calculated Results. In *The 23th International Offshore and Polar Engineering Conference*, Alaska, USA, 2013. International Society of Offshore and Polar Engineers (ISOPE). ISOPE–I–13–093.
- [59] C. Hu, M. Sueyoshi, C. Liu, Y. Kyojuka, and Y. Ohya. Numerical and experimental study on a floating platform for offshore renewable energy. In *32nd International Conference on Ocean, Offshore and Arctic Engineering (OMAE)*, Nantes, France, 2013. American Society of Mechanical Engineers (ASME). doi: 1115/OMAE2013-11133. OMAE2013-11133.
- [60] M. Umaya, T. Noguchi, M. Uchida, M. Shibata, Y. Kawai, and R. Notomi. Wind power generation-development status of offshore wind turbines. *Mitsubishi Heavy Industries Technical Review*, 50(3):29–35, 2013.
- [61] The White House Council. Executive Order 13693, Planning for Federal Sustainability in the Next Decade. Technical Report EO 13693, The White House Council on Environmental Quality, 2015.
- [62] GL. *Rules and Guidelines – IV Industrial Services –Part 2: Guideline for the Certification of Offshore Wind Turbines*. Germanischer Lloyd (GL), Hamburg, Germany, 2012.

- [63] IEC. *IEC 61400-3: Wind turbines - Part 3: Design requirements for offshore wind turbines*. International Electrotechnical Commission (IEC), Geneva, Switzerland, 2009.
- [64] ABS. *Guide for building and classing bottom-founded offshore wind turbine installations, #176*. American Bureau of Shipping (ABS), Houston, Texas, USA, 2010.
- [65] K. O. Ronold, V. L. Hansen, M. Godvik, E. Landet, E. R. Jørgensen, and A. L. H. Hopstad. Guideline for Offshore Floating Wind Turbine Structures. In *29th International Conference on Ocean, Offshore and Arctic Engineering (OMAE)*, pages 381–388, Shanghai, China, 2010. American Society of Mechanical Engineers (ASME). doi: 10.1115/OMAE2010-20344. OMAE2010-20344.
- [66] BV. *Classification and certification of floating offshore wind turbines, BV Guidance Note NI 572*. Bureau Veritas (BV), Houston, Texas, USA, 2010.
- [67] BV. *Classification and certification of floating offshore wind turbines, BV Guidance Note NI 572*. Bureau Veritas (BV), Houston, Texas, USA, 2015.
- [68] ABS. *Guide to Building and Classing Floating Offshore Wind Turbine Installations, #195*. American Bureau of Shipping (ABS), Houston, Texas, USA, 2014.
- [69] ClassNK. *ClassNK guidelines for offshore floating wind turbine structure*. Kyokai Nippon Kaiji (ClassNK), Tokyo, Japan, 2012.
- [70] A. L. H. Hopstad, K. O. Ronold, C. Sixtensson, and J. Sandberg. Standard development for floating wind turbine structures. In *Proceedings of European wind energy conference (EWEA)*, pages 3–7, Vienna, Austria, 2013.
- [71] IEC. *IEC 61400-3-2, Wind Turbines part 3-2: Design requirements for floating offshore wind turbines*. International Electrotechnical Commission (IEC), Geneva, Switzerland, 2014.
- [72] S. Srinivas, W. Musial, B. Bailey, and M. Filippelli. Assessment of offshore wind system design, safety, and operation standards. Technical Report NREL/TP-5000-60573, National Renewable Energy Laboratory (NREL), Golden, CO, USA, 2014.
- [73] C. Lopez-Pavon, R. A. Watai, F. Ruggeri, A. N. Simos, and A. Souto-Iglesias. Influence of Wave Induced Second-Order Forces in Semisubmersible FOWT Mooring Design. *Journal of Offshore Mechanics and Arctic Engineering*, 137(3):V008T09A027, 2015. doi: 10.1115/1.4030241. OMAE-13-1064.
- [74] N. S. Alexandre, F. Ruggeri, R. A. Watai, A. Souto-Iglesias, and C. Lopez-Pavon. Slow-drift of a floating wind turbine: An assessment of frequency-domain methods based on model tests. *Renewable Energy*, 116:133–154, 2018. doi: 10.1016/j.renene.2017.09.059.
- [75] D. Karmakar and C. Guedes Soares. Reliability based design loads of an offshore semi-submersible floating wind turbine. In C. Guedes Soares and L. Peña, editors, *Developments in*

Maritime Transportation and Exploitation of Sea Resources, pages 919–926. Taylor & Francis Group, London, UK, 2014.

- [76] B. Yeter, Y. Garbatov, and C. Guedes Soares. Evaluation of fatigue damage model predictions for fixed offshore wind turbine support structures. *International Journal of Fatigue*, 87:71–80, 2016. doi: 10.1016/j.ijfatigue.2016.01.007.
- [77] B. Yeter, Y. Garbatov, and C. Guedes Soares. Fatigue reliability assessment of an offshore supporting structure. In C. Guedes Soares and T. A. Santos, editors, *Maritime Technology and Engineering*, pages 671–680. Taylor & Francis Group, London, UK, 2015. ISBN 978-1-138-00124-4.
- [78] C. Tracy. *Parametric Design of Floating Wind Turbines*. Master's thesis, Massachusetts Institute of Technology (MIT), 2007.
- [79] E. E. Bachynski and T. Moan. Design considerations for tension leg platform wind turbines. *Marine Structures*, 29(1):89–114, 2012. doi: 10.1016/j.marstruc.2012.09.001.
- [80] H. Yanqing, L. Conghuan, D. Hongyan, C. Zhengshun, and Z. Puyang. Stability and dynamic response analysis of a submerged tension leg platform for offshore wind turbines. *Ocean Engineering*, 129:68–82, 2017. doi: 10.1016/j.oceaneng.2016.10.048.
- [81] S. Chakrabarti. *Handbook of Offshore Engineering (2-volume set)*. Elsevier, 1st edition, 2005. ISBN 978-0-08-044381-2.
- [82] M. Leimeister, E. E. Bachynski, M. Muskulus, and P. Thomas. Rational Upscaling of a Semi-submersible Floating Platform Supporting a Wind Turbine. In *WindEurope Summit*, Hamburg, Germany, 2016. PO.128.
- [83] M. Leimeister, E. E. Bachynski, M. Muskulus, and P. Thomas. Rational upscaling of a semi-submersible floating platform supporting a wind turbine. *Energy Procedia*, 94:434–442, 2016. doi: 10.1016/j.egypro.2016.09.212.
- [84] G. F. Clauss and L. Birk. Hydrodynamic shape optimization of large offshore structures. *Applied Ocean Research*, 18(4):157–171, 1996. doi: 10.1016/S0141-1187(96)00028-4.
- [85] L. Birk. Application of constrained multi-objective optimization to the design of offshore structure hulls. *Journal of Offshore Mechanics and Arctic Engineering*, 131(1):11301, 2008. doi: 10.1115/1.2957919.
- [86] P. Sclavounos, C. Tracy, and S. Lee. Floating Offshore Wind Turbines: Responses in a Seastate, Pareto Optimal Designs and Economic Assessment. *27th International Conference on Offshore Mechanics and Arctic Engineering (OMAE)*, pages 31–41, 2008. doi: 10.1115/OMAE2008-57056. OMAE2008-57056.

- [87] M. T. Andersen, D. Hindhede, and J. Lauridsen. Influence of model simplifications excitation force in surge for a floating foundation for offshore wind turbines. *Energies*, 8(4):3212–3224, 2015. ISSN 19961073. doi: 10.3390/en8043212.
- [88] M. Hall, B. Buckham, and C. Crawford. Evolving offshore wind: A genetic algorithm-based support structure optimization framework for floating wind turbines. In *MTS/IEEE OCEANS*, pages 1–10, Bergen, Norway, 2013. Institute of Electrical and Electronics Engineers (IEEE). doi: 10.1109/OCEANS-Bergen.2013.6608173.
- [89] J. H. Kim, S. Y. Hong, and H. J. Kim. The shape design and analysis of floating offshore wind turbine structures with damper structure and shallow draft. In *The 23rd International Offshore and Polar Engineering Conference*, pages ISOPE–I–13–025, Alaska, USA, 2013. International Society of Offshore and Polar Engineers (ISOPE).
- [90] J. Y. Lee, B. J. Koo, Samsung Heavy Industries Co. Ltd, G. Clauss, and TU Berlin. Automated Design of a Tension Leg Platform with Minimized Tendon Fatigue Damage and its Verification by a Fully Coupled Analysis. *Ship Technology Research*, 54(1):11–27, 2007. doi: 10.1179/str.2007.54.1.003.
- [91] J. Y. Lee and S. J. Lim. Hull Form Optimization of a Tension-Leg Platform Based on Coupled Analysis. *Proceedings of the 18th International Offshore and Polar Engineering Conference*, pages 100–107, 2008.
- [92] R. Z. Venzon, T. P. Tancredi, and B. L. R. de Andrade. Hull optimization of semisubmersible with multidirectional seakeeping criteria evaluated with neural network response surface. In C. Guedes Soares and F. López Peña, editors, *Developments in Maritime Transportation and Exploitation of Sea Resources*, pages 147–155, London, UK, 2014. Taylor & Francis Group. ISBN 978-1-138-00124-4.
- [93] Y. Park, B.-S. Jang, and J. D. Kim. Hull-form optimization of semi-submersible FPU considering seakeeping capability and structural weight. *Ocean Engineering*, 104:714–724, 2015. doi: 10.1016/j.oceaneng.2015.04.009.
- [94] B. Le Méhauté. *An introduction to hydrodynamics and water waves*. Springer-Verlag Berlin Heidelberg, 1976. ISBN 978-3-642-85567-2. doi: 10.1007/978-3-642-85567-2.
- [95] G. B. Airy. Tides and waves. In *Encyclopaedia Metropolitana*, volume 5, pages 241–396. William Clowes and Sons, 1845.
- [96] G. Clauss, E. Lehmann, and C. Östergaard. *Offshore Structures: Volume I: Conceptual Design and Hydromechanics*. Springer-Verlag, 1st edition, 1992. ISBN 978-1-4471-3193-9.
- [97] M. St. Denis and W. J. Pierson Jr. On the Motions of Ships in Confused Seas. *Transactions of the Society of Naval Architects and Marine Engineers*, 61:280–357, 1953.

- [98] G. G. Stokes. On the theory of oscillatory waves. *Transactions of the Cambridge Philosophical Society*, 8:441–473, 1847. doi: 10.1017/CBO9780511702242.013.
- [99] J. Wheeler. Method for Calculating Forces Produced by Irregular Waves. *Journal of Petroleum Technology*, 22(03):359–367, 1970. ISSN 0149-2136. doi: 10.2118/2712-PA. SPE-2712-PA.
- [100] K. Hasselmann, T. P. Barnett, E. Bouws, H. Carlson, D. E. Cartwright, K. Enke, J. A. Ewing, H. Gienapp, D. E. Hasselmann, P. Kruseman, A. Meerburg, P. Müller, D. J. Olbers, K. Richter, W. Sell, and H. Walden. *Measurements of Wind-Wave Growth and Swell Decay during the Joint North Sea Wave Project (JONSWAP)*. Number 12 in A(8). Deutschen Hydrographischen Institut, Hamburg, Germany, 1973.
- [101] C. Guedes Soares. Representation of double-peaked sea wave spectra. *Ocean Engineering*, 11(2):185 – 207, 1984. doi: 10.1016/0029-8018(84)90019-2.
- [102] K. Torsethaugen and S. Haver. Simplified double peak spectral model for ocean waves. In *The 14th International Offshore and Polar Engineering Conference*, Toulon, France, 2004. International Society of Offshore and Polar Engineers (ISOPE). ISOPE-I-04-289.
- [103] MARINTEK. SIMO User Manual. Technical report, Norwegian Marine Technology Research Institute (MARINTEK), 2012.
- [104] J. M. Jonkman. Dynamics of offshore floating wind turbines – model development and verification. *Wind Energy*, 12(5):459–492, 2009. doi: 10.1002/we.347.
- [105] E. V. Lewis, editor. *Principles of Naval Architecture Second Revision, Volume III, Motions in Waves and Controllability*. Society of Naval Architects and Marine Engineers, Jersey City, New Jersey, USA, 1989. ISBN 978-0939773022.
- [106] O. M. Faltinsen. *Sea loads on ships and offshore structures*. Cambridge University Press, Cambridge, UK, 1990. ISBN 0-521-45870-6.
- [107] J. Morison, J. Johnson, and S. Schaaf. The Force Exerted by Surface Waves on Piles. *Journal of Petroleum Technology*, 2(5):149–154, 1950. doi: 10.2118/950149-G. SPE-950149-G.
- [108] T. Sarpkaya and M. Isaacson. *Mechanics of wave forces on offshore structures*. Van Nostrand Reinhold Company, New York City, New York, USA, 1981. ISBN 9780442254025.
- [109] G. H. Keulegan and L. H. Carpenter. Forces on cylinders and plates in an oscillating fluid. *Journal of Research of the National Bureau of Standards*, 60(5):423–440, 1958. ISSN 0091-0635. doi: 10.6028/jres.060.043.
- [110] C. Östergaard and T. E. Schellin. Comparison of experimental and theoretical wave actions on floating and compliant offshore structures. *Applied Ocean Research*, 9(4):192–213, 1987. doi: 10.1016/0141-1187(87)90002-2.

- [111] J. F. Manwell, J. G. McGowan, and A. L. Rogers. *Wind energy explained: theory, design and application*. John Wiley&Sons Ltd, UK, 2009. ISBN 9780470015001. doi: 10.1002/9781119994367.
- [112] F. W. Diederich and J. A. Drischler. Effect of spanwise variations in gust intensity on the lift due to atmospheric turbulence. Technical Report NACA-TN-3920, National Advisory Committee for Aeronautics (NACA), Langley Aeronautical Lab., Langley Field, Virginia, USA, 1957.
- [113] J. Patrick, J. Moriarty, and A. Hansen. AeroDyn theory manual. Technical Report NREL/TP-500-36881, National Renewable Energy Laboratory (NREL), Golden, CO, USA, 2005.
- [114] M. O. L. Hansen, J. N. Sørensen, S. Voutsinas, N. Sørensen, and H. A. Madsen. State of the art in wind turbine aerodynamics and aeroelasticity. *Progress in aerospace sciences*, 42(4): 285–330, 2006. doi: 10.1016/j.paerosci.2006.10.002.
- [115] T. Burton, D. Sharpe, N. Jenkin, and E. Bossanyi. *Wind Energy Handbook*. John Wiley & Sons, Ltd, Sussex, United Kingdom, 2001. ISBN 9780874216561. doi: 10.1007/s13398-014-0173-7.2.
- [116] J. G. Leishman and T. S. Beddoes. A Semi-Empirical Model for Dynamic Stall. *Journal Of The American Helicopter Society*, 34(3):3–17, 1989. doi: 10.4050/JAHS.34.3.
- [117] T. Fan, D. Qiao, J. Yan, C. Chen, and J. Ou. An improved quasi-static model for mooring-induced damping estimation using in the truncation design of mooring system. *Ocean Engineering*, 136:322–329, 2017. doi: 10.1016/j.oceaneng.2016.05.042.
- [118] M. Masciola, J. Jonkman, and A. Robertson. Implementation of a multisegmented, quasi-static cable model. In *The 23rd International Offshore and Polar Engineering Conference*, Anchorage, Alaska, USA, 2013. International Society of Offshore and Polar Engineers (ISOPE). ISOPE-I-13-127.
- [119] J. Azcona, X. Munduate, L. González, and T. A. Nygaard. Experimental validation of a dynamic mooring lines code with tension and motion measurements of a submerged chain. *Ocean Engineering*, 129:415–427, 2017. doi: 10.1016/j.oceaneng.2016.10.051.
- [120] O. M. Aamo and T. I. Fossen. Finite element modelling of mooring lines. *Mathematics and Computers in Simulation*, 53(4-6):415–422, 2000. doi: 10.1016/S0378-4754(00)00235-4.
- [121] C. T. Kwan and F. J. Bruen. Mooring Line Dynamics: Comparison of Time Domain, Frequency Domain, and Quasi-Static Analyses. In *Offshore Technology Conference*, Houston, Texas, USA, 1991. Offshore Technology Conference. doi: 10.4043/6657-MS. OTC-6657-MS.
- [122] M. T. Andersen, F. F. Wendt, A. N. Robertson, J. M. Jonkman, and M. Hall. Verification and Validation of Multisegmented Mooring Capabilities in FAST v8. In *The 26th International Offshore and Polar Engineering Conference*, Rhodes, Greece, 2016. ISOPE-I-16-432.

- [123] E. Oguz, D. Clelland, A. H. Day, A. Incecik, J. A. López, G. Sánchez, and G. G. Almeria. Experimental and numerical analysis of a TLP floating offshore wind turbine. *Ocean Engineering*, 147:591–605, 2018. doi: 10.1016/j.oceaneng.2017.10.052.
- [124] J. M. Jonkman and M. Buhl Jr. FAST User’s Guide. Technical Report NREL/TP-500-38230, National Renewable Energy Laboratory (NREL), Golden, CO, USA, 2005.
- [125] A. J. Goupee, B. Koo, K. Lambrakos, and R. Kimball. Model tests for three floating wind turbine concepts. In *Offshore Technology Conference*, Houston, Texas, USA, 2012. doi: 10.4043/23470-MS. OTC-23470-MS.
- [126] A. D. Wright and L. J. Fingersh. Advanced control design for wind turbines, Part I: Control Design, Implementation, and Initial Tests. Technical Report NREL/TP-500-42437, National Renewable Energy Laboratory (NREL), Golden, CO, USA, 2008.
- [127] E. Uzunoglu and C. Guedes Soares. Automated processing of free roll decay experimental data. *Ocean Engineering*, 102:17–26, 2015. doi: 10.1016/j.oceaneng.2015.04.016.
- [128] E. Uzunoglu, S. Ribeiro e Silva, C. Guedes Soares, A. Marón, and C. Gutierrez. The effect of asymmetric cross-sections on hydrodynamic coefficients of a C11 type container vessel. *Ocean Engineering*, 113:264–275, 2016. doi: 10.1016/j.oceaneng.2015.12.049.
- [129] V. Dinh and B. Basu. On the Modeling of Spar-Type Floating Offshore Wind Turbines. *Key Engineering Materials*, 569–570:636–643, 2013. doi: 10.4028/www.scientific.net/KEM.569-570.636.
- [130] C. H. Lee and J. N. Newman. Computation of wave effects using the panel method. In S. Chakrabarti, editor, *Numerical Models in Fluid Structure Interaction*, volume 42, pages 211–251. WIT Press, Southampton, UK, 2005. ISBN 978-1-85312-837-0.
- [131] C. H. Lee and J. N. Newman. WAMIT User Manual, Versions 6.3, 6.3 PC, 6.3 S, 6.3 S-PC. Technical report, WAMIT, Inc., Chestnut Hill, MA, USA, 2006.
- [132] E. Uzunoglu and C. Guedes Soares. Parametric modelling of multi-body cylindrical offshore wind turbine platforms. In C. Guedes Soares and T. A. Santos, editors, *Maritime Technology and Engineering*, pages 1185–1193. Taylor & Francis Group, London, UK, 2015. ISBN 978-1-138-00124-4.
- [133] E. Uzunoglu and C. Guedes Soares. On the model uncertainty of wave induced responses of a floating semisubmersible wind system. In C. Guedes Soares, editor, *Progress in Renewable Energies Offshore*, pages 785–794. Taylor & Francis Group, London, UK, 2016. ISBN 9781138626270.
- [134] C. Guedes Soares. Quantification of Model Uncertainty in Structural Reliability. In C. Guedes Soares, editor, *Probabilistic methods for Structural Design*, volume 56 of *Solid Mechanics and*

Its Applications, pages 17 – 37. Springer Netherlands, 1st edition, 1997. ISBN 978-94-010-6366-1. doi: 10.1007/978-94-011-5614-1.

- [135] C. Guedes Soares and T. Moan. Model uncertainty in the long-term distribution of wave-induced bending moments for fatigue design of ship structures. *Marine Structures*, 4(4):295–315, 1991. doi: 10.1016/0951-8339(91)90008-Y.
- [136] C. Guedes Soares. Effect of transfer function uncertainty on short-term ship responses. *Ocean Engineering*, 18(4):329–362, 1991. doi: 10.1016/0029-8018(91)90018-L.
- [137] K. Rezanejad and C. Guedes Soares. Effect of spectral shape uncertainty in short term performance of a Oscillating Water Column device. In C. Guedes Soares, editor, *Renewable Energies Offshore*, pages 479–487. Taylor & Francis Group, London, UK, 2015. ISBN 978-1-138-02871-5.
- [138] C. Guedes Soares. Effect of spectral shape uncertainty in the short term wave-induced ship responses. *Applied Ocean Research*, 12(2):54–69, 1990. doi: 10.1016/S0141-1187(05)80030-6.
- [139] M. S. Longuet-Higgins. On the Statistical Distribution of the Heights of Sea Waves. *Journal of Marine Research*, 11(5):245–266, 1952.
- [140] C. Guedes Soares and T. Moan. Uncertainty analysis and code calibration of the primary load effects in ship structures. In I. Konishi, A. H. Ang, and M. S. Shinozuka, editors, *Proceedings of the 4th International Conference on Structural Safety and Reliability (ICOSAR '85)*, volume 3, pages 501–512, Kobe, Japan, 1985. International Association for Structural Safety and Reliability, New York, NY.
- [141] C. Guedes Soares. On the uncertainty in long-term predictions of wave induced loads on ships. *Marine Structures*, 12(3):171–182, 1999. doi: 10.1016/S0951-8339(99)00025-8.
- [142] J. Jonkman and W. Musial. Offshore Code Comparison Collaboration (OC3) for IEA Task 23 offshore wind technology and deployment. Technical Report NREL/TP-5000-48191, National Renewable Energy Laboratory (NREL), Golden, CO, USA, 2010.
- [143] E. Uzunoglu and C. Guedes Soares. Supervisory system for the automation of model building and simulations with the wind turbine code FAST. In C. Guedes Soares, editor, *Progress in Renewable Energies Offshore*, pages 627–635. Taylor & Francis Group, London, UK, 2016. ISBN 9781138626270.
- [144] A. Krieger, G. K. V. Ramachandran, L. Vita, P. G. Alonso, J. Berque, and G. Aguirre. Qualification of innovative floating substructures for 10MW wind turbines and water depths greater than 50m. Technical Report Deliverable D7.2 Design Basis, LIFES50+, 2015.
- [145] M. Buhl Jr. MCrunch User's Guide for Version 1.00. Technical Report NREL/TP-500-43139, National Renewable Energy Laboratory (NREL), Golden, CO, USA, 2008.

- [146] J. E. Gutierrez, B. Zamora, J. García, and M. R. Peyrau. Tool development based on FAST for performing design optimization of offshore wind turbines: FASTLognoter. *Renewable Energy*, 55:69–78, 2013. doi: 10.1016/j.renene.2012.12.026.
- [147] E. Uzunoglu and C. Guedes Soares. A numerical model for compartment assessment of offshore structures with cylindrical hulls. In C. Guedes Soares and P. A. Teixeira, editors, *Maritime Technology and Engineering*, pages 693–700. Taylor & Francis Group, London, UK, 2016. ISBN 9781138030008.
- [148] A. Papanikolaou. Holistic ship design optimization. *Computer-Aided Design*, 42(11):1028–1044, 2010. doi: 10.1016/j.cad.2009.07.002.
- [149] M. Ventura and C. Guedes Soares. Geometric modelling and product data management in ship design. In C. Guedes Soares, Y. Garbatov, N. Fonseca, and A. Teixeira, editors, *Marine Technology and Engineering*, volume 2, pages 1019–1044. Taylor & Francis Group, London, UK, 2011. ISBN 9780415628914.
- [150] H. Bagbanci, D. Karmakar, and C. Guedes Soares. Review of offshore floating wind turbines concepts. In C. Guedes Soares, Y. Garbatov, S. Sutulo, and T. Santos, editors, *Maritime Engineering and Technology*, pages 553–562. Taylor and Francis Group, UK, 2012. ISBN 9780415621465.
- [151] H. Bagbanci, D. Karmakar, and C. Guedes Soares. Comparison of Spar and Semisubmersible Floater Concepts of Offshore Wind Turbines Using Long-Term Analysis. *Journal of Offshore Mechanics and Arctic Engineering*, 137(6):137–147, sep 2015. doi: 10.1115/1.4031312.
- [152] M. Hall, B. Buckham, and C. Crawford. Hydrodynamics-based floating wind turbine support platform optimization: A basis function approach. *Renewable Energy*, 66:559–569, 2014. doi: 10.1016/j.renene.2013.12.035.
- [153] H. Jafaryeganeh, J. M. Rodrigues, and C. Guedes Soares. Influence of mesh refinement on the motions predicted by a panel code. In C. Guedes Soares and T. A. Santos, editors, *Maritime Technology and Engineering*, pages 1029–1038. Taylor & Francis Group, London, UK, 2014. ISBN 9781138027275.
- [154] J. M. Rodrigues and C. Guedes Soares. Exact pressure integrations on submerged bodies in waves using a quadtree adaptive mesh algorithm. *International Journal for Numerical Methods in Fluids*, 76(10):632–652, 2014. doi: 10.1002/flid.3948.
- [155] S. Sutulo, J. M. Rodrigues, and C. Guedes Soares. Hydrodynamic characteristics of ship sections in shallow water with complex bottom geometry. *Ocean Engineering*, 37(10):947–958, 2010. doi: 10.1016/j.oceaneng.2010.03.008.
- [156] E. Uzunoglu and C. Guedes Soares. Influence of bracings on the hydrodynamic modelling of a semi-submersible offshore wind turbine platform. In C. Guedes Soares, editor, *Renew-*

able Energies Offshore, pages 755–762. Taylor & Francis Group, London, UK, 2015. ISBN 9781138028715.

- [157] K. H. Ko, T. Park, K. Kim, Y. Kim, and D. H. Yoon. Development of panel generation system for seakeeping analysis. *Computer-Aided Design*, 43(8):848–862, 2011. doi: 10.1016/j.cad.2011.04.013.
- [158] H. Goldstein, C. Poole, and J. Safho. *Classical Mechanics*. Pearson Education Limited, Essex, UK, 3rd edition, 2013. ISBN 9780201657029.
- [159] M. E. Newell, R. G. Newell, and T. L. Sancha. A new approach to the shaded picture problem. In *Proceedings of the ACM National Conference*, pages 443–450, 1972.
- [160] E. E. Sutherland, R. F. Sproull, and R. A. Schumacker. A Characterization of Ten Hidden-Surface Algorithms. *ACM Computing Surveys (CSUR)*, 6(1):1–55, 1974. doi: 10.1145/356625.356626.
- [161] M. Hall, B. Buckham, and C. Crawford. Evaluating the importance of mooring line model fidelity in floating offshore wind turbine simulations. *Wind Energy*, 17(12):1835–1853, 2014. doi: 10.1002/we.1669.
- [162] E. Bachinsky. *Design and Dynamic Analysis of Tension Leg Platform Wind Turbines*. Doctoral Thesis, Norwegian University of Science and Technology (NTNU), 2014.
- [163] S. Schalck and J. Baatrup. Hydrostatic stability calculations by pressure integration. *Ocean Engineering*, 17(1-2):155–169, 1990. doi: 10.1016/0029-8018(90)90019-3.
- [164] C. H. Lee. WAMIT Theory Manual. Technical Report No. 95-2, Massachusetts Institute of Technology (MIT), Cambridge, Massachusetts, USA, 1995.
- [165] M. Khair Al-Solihat and M. Nahon. Nonlinear Hydrostatic Restoring of Floating Platforms. *Journal of Computational and Nonlinear Dynamics*, 10(4):041005, 2015. doi: 10.1115/1.4027718.
- [166] API. *American Petroleum Institute (API) Recommended Practice 2T, Planning, Designing, and Constructing Tension Leg Platforms*. American Petroleum Institute (API), Washington, D.C., USA, 2010.
- [167] D. Silva, A. R. Bento, P. Martinho, and C. Guedes Soares. High resolution local wave energy modelling in the Iberian Peninsula. *Energy*, 91:1099–1112, 2015. doi: 10.1016/j.energy.2015.08.067.
- [168] D. Silva, A. R. Bento, P. Martinho, and C. Guedes Soares. Corrigendum to “high resolution local wave energy modelling in the iberian peninsula” [energy 91 (2015) 1099–1112]. *Energy*, 94:857–858, 2016. doi: 10.1016/j.energy.2015.11.033.

- [169] E. E. Bachynski, M. Etemaddar, M. I. Kvittem, C. Luan, and T. Moan. Dynamic analysis of floating wind turbines during pitch actuator fault, grid loss, and shutdown. *Energy Procedia*, 35:210–222, 2013. doi: 10.1016/j.egypro.2013.07.174.
- [170] Z. Jiang, M. Karimirad, and T. Moan. Dynamic response analysis of wind turbines under blade pitch system fault, grid loss, and shutdown events. *Wind Energy*, 17(9):1385–1409, 2014. doi: 10.1002/we.1639.
- [171] H. Arabian-Hoseynabadi, H. Oraee, and P. J. Tavner. Failure modes and effects analysis (FMEA) for wind turbines. *International Journal of Electrical Power & Energy Systems*, 32(7):817–824, 2010. doi: 10.1016/j.ijepes.2010.01.019.
- [172] G. Bir and J. Jonkman. Aeroelastic Instabilities of Large Offshore and Onshore Wind Turbines. *Journal of Physics: Conference Series*, 75:012069, 2007. doi: 10.1088/1742-6596/75/1/012069.
- [173] J. M. Jonkman and M. L. Buhl Jr. Loads analysis of a floating offshore wind turbine using fully coupled simulation. In *Wind Power Conference and Exhibition*, Los Angeles, CA, USA, 2007.
- [174] A. R. Henderson, K. Argyriadis, J. Nichols, and D. Langston. Offshore wind turbines on TLPs - Assessment of floating support structures for offshore wind farms in German waters. In *10th German Wind Energy Conference (DEWEK)*, pages 2–7, Bremen, Germany, November 2010.
- [175] IEC. *IEC 61400-1 Wind Turbines - Part 1: Design requirements*. International Electrotechnical Commission (IEC), Geneva, Switzerland, 2005. ISBN 2-8318-8161-7.
- [176] T. J. Larsen. Turbulence for the IEA Annex 30 OC4 Project. Technical Report Risø-I-3206, Risø National Laboratory for Sustainable Energy Technical University of Denmark, 2011.
- [177] K. Torsethaugen, T. Faanes, and S. Haver. Characteristics for Extreme Sea States on the Norwegian Continental Shelf. Technical Report NHC-2-84123, Norwegian Hydrodynamics Laboratories, Trondheim, Norway, 1985.
- [178] J. M. Jonkman and M. L. Bulh Jr. New Developments for the NWTC's FAST Aeroelastic HAWT Simulator. In *42nd Aerospace Sciences Meeting and Exhibit*, Reno, Nevada, USA, 2004.
- [179] DNV GL. *Global performance analysis of deepwater floating structures, DNVGL-RP-F205*. DNV GL AS, 2017.